Porous Metal-Adeninate Crystalline Materials: Design, Synthesis and Emerging Properties

by

Jihyun An

B.S., Seoul National University, 2004

M.S., University of Pittsburgh, 2008

Submitted to the Graduate Faculty of

Arts and Sciences in partial fulfillment

of the requirements for the degree of

Doctor of Philosophy

University of Pittsburgh

2010

UNIVERSITY OF PITTSBURGH

SCHOOL OF ARTS AND SCIENCES

This thesis was presented

by

Jihyun An

It was defended on

August 31, 2010

and approved by

Dr. Toby Chapman, Associate Professor, Chemistry

Dr. Alex Star, Assistant Professor, Chemistry

Dr. Götz Veser, Associate Professor, Chemical and Petroleum Engineering

Thesis Director: Dr. Nathaniel Rosi, Assistant Professor, Chemistry

Porous Metal-Adeninate Crystalline Materials: Design, Synthesis and Emerging Properties

Jihyun An, Ph.D.

University of Pittsburgh, 2010

The research is aimed at designing and synthesizing porous biomolecule-based materials for potential environmental and biological applications. We developed synthetic methods to control the coordination chemistry between adenine and metal ions with the aim of organizing adenine into structurally well-defined porous materials. As a result, several interesting metal-adeninate frameworks, based on various metal-adeninate coordination modes, have been synthesized and characterized. They exhibit not only interesting structures but also unique physical properties.

The research has shown that adenine is a versatile biomolecular ligand for the construction and design of crystalline supramolecular and extended porous solid-state materials including MOFs. Metal-adeninate materials can be permanently porous and can selectively adsorb and store various gas molecules. Anionic-MOFs can be used as materials for gas sorption, drug storage and release, and the sensitization of lanthanides by tuning the functionality and pore metrics of anionic-MOFs via cation exchange. Finally, a new strategy to design and construct mesoporous MOFs with unprecedented pore volumes from metal-adeninate secondary building units (SBUs) has also been discovered.

TABLE OF CONTENTS

LIST OF TABLES

LIST OF SUPPORTING TABLES

LIST OF FIGURES

LIST OF SUPPORTING FIGURES

LIST OF SCHEMES

1.0 INTRODUCTION

Synthesizing structurally well-defined materials via coordination-directed molecular assembly has attracted and challenged chemists and materials scientists. For example, there has been an effort to synthesize porous materials with metal ions and organic molecules by using a molecular building block approach. Such materials are called metal organic frameworks (MOFs), metal organic polyhedra, or coordination polymers.[1]

1.1 METAL-ORGANIC FRAMEWORKS

MOFs[2-5] are polymeric crystalline compounds comprising metal ions/clusters that serve as vertices and organic ligands that serve as linkers that connect the vertices into periodic structures (Scheme 1). In a typical MOF synthesis, crystalline materials can form when a mixture of metal salt and ligand are reacted together either at room temperature or under solvothermal conditions. MOF syntheses, therefore, are inherently modular, as one can incorporate the metal ion/cluster or organic linker of their choosing. This approach is attractive for a number of reasons: the functionality of the framework can be tuned by carefully choosing the metal ion and organic components and the pore metrics of the framework can be carefully tuned by modulating the length and shape of the organic linker molecule. The most commonly used linkers typically have either Lewis-basic nitrogen or oxygen sites that bind to the metal cations. These include multitopic carboxylated linkers and pyridyl linkers, for example.

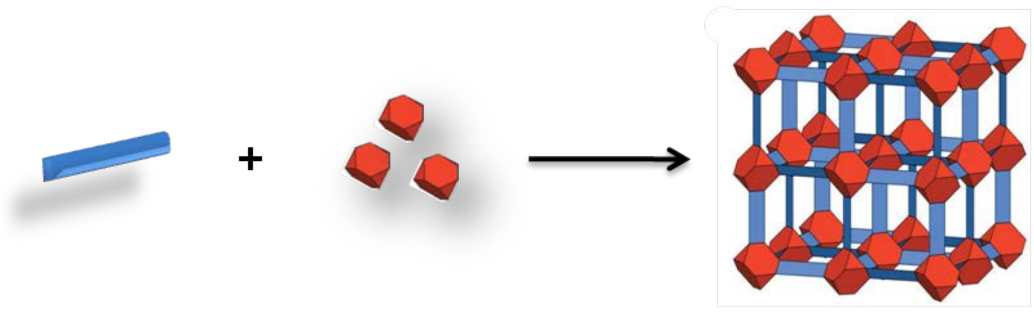

Scheme 1. General MOF assembly scheme (Red: metal ion or cluster; Blue: organic linker)

One of the most interesting properties of MOFs is their permanent porosity. MOFs can have high surface area and large pore volumes. The surface areas of permanently porous MOFs range from 100 m^2/g to greater than 7000 m^2/g[6-8] and pore sizes span the micro- to mesoporous range.[7, 9, 10] MOFs have been designed and their porosity has been exploited for various applications including guest recognition,[11-13] gas storage and separation,[14-16] catalysis,[17, 18] ion-exchange,[19] and drug delivery.[20, 21] For certain applications, MOFs ideally should be both biologically and environmentally compatible. Therefore, some recent efforts have been made to prepare MOFs from biologically and environmentally compatible components. In particular, researchers have begun to investigate the use of biological molecules as linkers, and to date, these efforts have been only modestly successful.

1.1.1 Biomolecule-based MOFs

Most simple biomolecules, including amino acids, sugars, and nucleobases, have multiple Lewis-basic sites, which render them potential linkers for constructing MOFs. Amino acids are readily available in enantiopure forms and thus can be easily used as homochiral ligands to build homochrial MOFs. Several amino-acid based MOFs have been prepared and reported. [22-25] These structures have potential applications for enantioselective separation and asymmetric catalysis. For example, Rosseinsky and co-workers synthesized a microporous Ni-based MOF, $[Ni_2(L\text{-}asp)_2(bipy)]\cdot$guest, using aspartic acid as a building block.[22] The pores of this material were decorated with the homochiral aspartates, an aspect that rendered it useful for enantioselective adsorption of small chiral diols. In some cases, short peptides have been used as linkers to generate new MOFs. Peptides are short oligomers of amino acids; they have versatile binding modes and are longer and more flexible linkers than single amino acids. Peptides also have intrinsic chirality that could be useful for asymmetric catalysis and enantioselective separations. Taubert and co-workers reported the first synthesis of a MOF based on peptides.[26] The material was made from oligovaline peptides such as Z-L-Val-L-Val-L-Glu(OtBu)OtBu and Z-L-Val-L-Val-L-Glu(OH)OH and Cu(II) and Ca(II). However, they were unable to produce the materials in single crystalline form, and the structure had to be solved using powder diffraction. Marsh and co-workers also reported the synthesis and the structure of chiral 1-D and 2-D frameworks using chiral di- and tripeptides with Cd(II) ions.[27] $[Cd(Gly_3)_2]\cdot 2H_2O$, $[Cd(Ala_3)_2]$, $[Cd(Ala_2)_2]$, and $[Cd(Ala, Thy)_2]\cdot 4H_2O$ were synthesized. The structures formed units in which, either two peptides linked with two Cd(II) metal ions into a ring, or four peptides linked with four Cd(II) into a square unit. These units extended into either 1-D chains or 2-D networks. These preliminary successful experiments have demonstrated that peptides may indeed be viable linkers for generating new and interesting MOF materials.

Unfortunately, the construction of permanently porous biomolecule-based MOFs has been largely unsuccessful because most biomolecules are either too small to afford an open framework with accessible pores or too flexible to build a rigid porous structure. Nevertheless, the synthesis of porous materials constructed with biological molecules is significant because they may have potential bio-medical and environmental impact. For instance, such materials could be used as capsules to store and deliver drug molecules or biologically-relevant gas molecules such as nitric oxide (NO).[28, 29] They can also be used as containers for confining and protecting large biomolecules such as enzymes or DNA. They may also be useful for environmental applications, including heavy metal ion sequestration and or carbon capture. The overarching goal of my doctoral research was to develop synthetic methods for organizing biological molecules into structurally well-defined porous materials and then to explore the biomedical and environmental applications of these materials. In particular, my research focused on the exploration of adenine as a MOF biomolecular building block. I studied various potential applications of adenine-based MOF materials, including CO_2 capture and drug storage and release.

1.2 Adenine

Many biological molecules could potentially be used as linking ligands for MOF construction, as the only prerequisite is that they must have multiple sites for coordinating metal ions or clusters. Nucleobases have been chosen for this study. Nucleobases are one of the simplest biological molecules, and various groups have studied the simple coordination chemistry of nucleobases in the context of understanding metal ion-nucleic acid interactions. In addition, other groups have begun exploring the use of adenine as a building block for supramolecular materials.[30-32] Prior to our work in this area, only one MOF was reported in which adenine served as a building block. My studies have concentrated on adenine as a linker for MOFs because 1) it is rigid, 2) it has multiple possible metal binding modes, and 3) its molecular coordination chemistry is well-developed.[33, 34] I began by investigating and studying the coordination chemistry of adenine in the context of constructing discrete and extended coordination assemblies.

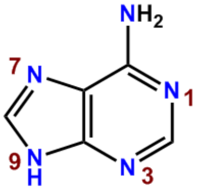

Figure 1. Adenine.

1.2.1 Properties of Adenine

Adenine contains five Lewis base donors sites (N1, N3, N7, N9, and N10) which allow for a diverse coordination chemistry (Figure 1). In the context of preparing MOF materials, adenine's diverse coordination chemistry is particularly appealing because each different coordination mode would be expected to yield a completely new MOF structure and each new MOF structure could potentially exhibit new properties. As shown Figure 2, there are three possible adenine-metal binding modes that have been observed to date. In Mode 1, imidazolate nitrogens (N7, N9) of the adenine coordinate the metal ions. In this case, N1 and amine (N10-H_2)

can potentially participate in hydrogen bonding, which could be important for structure formation.[35] In Mode 2, the imidazolate nitrogens (N7, N9) coordinate the metal ions as well as one of the pyrimidyl nitrogens (N3), leaving N1 and the amino group uncoordinated. Unlike Mode 1, the free N1 and amine groups in Mode 2 do not form hydrogen bonds very easily. This may be due to the fact that the adenine is fixed in one position by three coordination sites which limits its range of motion. Finally, in Mode 3, all of the heterocyclic nitrogens coordinate metal ions, while the amino group remains uncoordinated. However, only a few structures have been synthesized using Mode 3, perhaps because approach to N1 is sterically encumbered by the neighboring amino group.

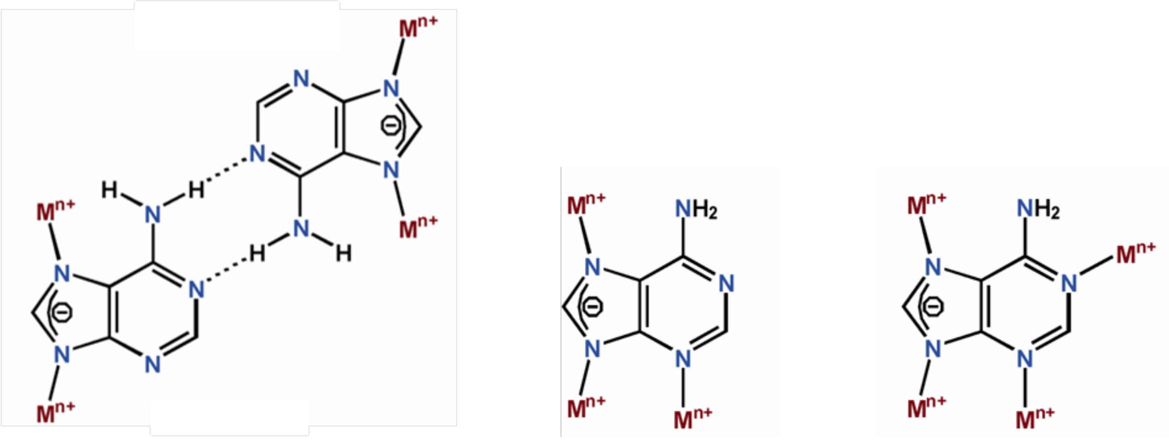

Mode 1 Mode 2 Mode 3

Figure 2. Adenine binding modes.

In carboxylate MOF chemistry, metal-carboxylate ($M(CO_2)_n$) clusters are common structural motifs, serving as vertices in the framework.[36] These metal-carboxylate cluster building blocks have been extensively used for constructing structurally rigid and permanently porous MOFs. Within the Cambridge structural database, there are more than 30 structures exhibiting a nitrogen-carbon-nitrogen bridged paddle-wheel cluster ($M(CN_2)_n$) which is similar to the metal-carboxylate paddle-wheel cluster. Thus, the ($M(CN_2)_n$) cluster might potentially serve as a rigid building block to generate permanently porous MOF structures. Interestingly, there are similar M-N-C-N-M bridges found in adenine coordination Mode 2 and Mode 3, indicating that adenine might be a potential ligand for forming such clusters and thus for constructing permanently porous biomolecular MOFs.

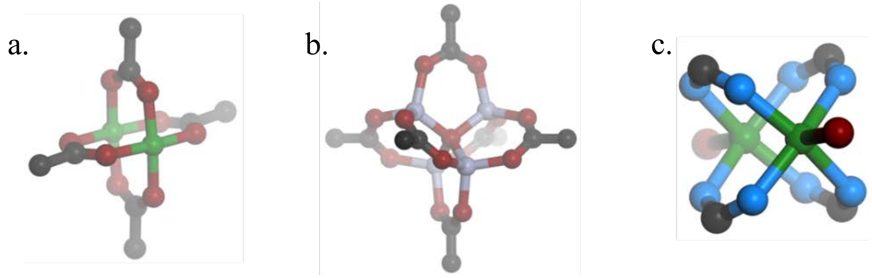

Figure 3. $M(CO_2)_n$ clusters (a, b) and $M(CN_2)_n$ cluster (c).

In addition, the multiple Lewis-basic sites of adenine make it a particularly intriguing ligand for making MOFs with high affinities and capacities for CO_2. Recently, Froudakis and coworkers reported a computational study which investigated the interaction energy between CO_2 and various N-heterocyclic molecules which could potentially be used as MOF linkers.[37] They found that Lewis basic sites of the heterocycles interact with the Lewis acidic site of carbon dioxide and that there are very weak interactions between negatively charged oxygens of CO_2 and hydrogens attached to the α-carbon of the heterocycles (Figure 4). Of all the potential MOF ligands studied, adenine showed one of the highest binding energies with CO_2. Therefore, one could reason that a metal-adenine MOF might have a particularly high affinity for CO_2.

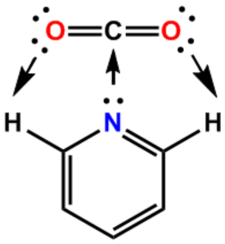

Figure 4. A example view of interaction between Lewis basic sites of the heterocycle (pyridine) and Lewis acidic sites of carbon dioxide.

1.2.2 General Reaction Strategy

In order to design and synthesize the potential target structures, a variety of synthetic conditions have been investigated. The general reaction strategy is shown in Scheme 2.

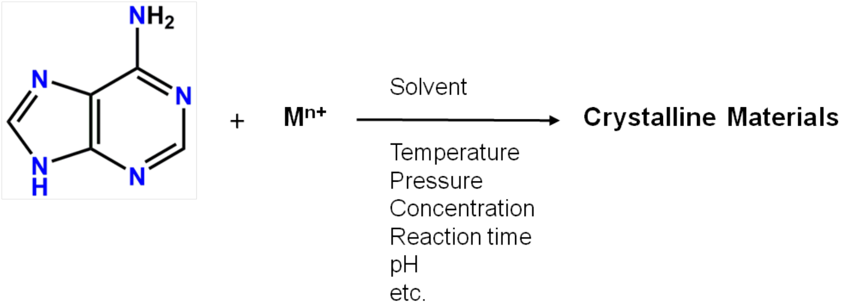

Scheme 2. General reaction conditions for metal-adeninate crystalline material.

In general, adenine and metal salts are reacted under solvothermal conditions using different reactant concentrations, solvents, pH, pressures, temperatures, and reaction times. During initial studies, serendipity played an important role in the syntheses of the metal-adeninate crystalline materials. As a result of these studies, general reaction conditions and strategies for constructing materials exhibiting each coordination mode have been established and developed. By exploiting adenine's diverse coordination modes, various materials including discrete macrocyclic structures, polymeric chains, 2-D sheets, and 3-D extended frameworks have been synthesized. Interestingly, some of adenine's coordination modes can be explained by pK_a. It is known that the pK_a of N9 is 9.80 and N1 is 4.15. For example, coordination mode 1 can be observed when pyridine is added to the syntheses. In our reaction conditions, the N9 is deprotonated to coordinate to the metal ion. When this happens, the anionic charge is distributed through N9, N7 and N3 by resonance. However, only N7 and N9 are coordinate metal ions in coordination mode 1. Moreover, pyridine coordinates to the metal ion instead of N3, because pyridine is more basic than N3 of adenine. On the other hand, in coordination mode 2, N3 binds to the metal ions in addition to N7 and N9 because, in this case, no pyridine is added to the synthesis. In coordination modes 1 and 2, N1 does not bind to the metal ion due to steric hindrance by the adjacent amine group. Coordination Mode 3 is observed rarely in which N9, N7, N3 and N1 coordinate to the metal ions. While we can rationalize the different coordination modes in terms or pK_a and synthetic conditions to some extent, we note that MOF syntheses must yield crystalline materials. In some cases, we may employ perfectly rational synthetic conditions derived from careful consideration of the relative pK_a values of adenine's coordination sites, but these conditions may not yield crystalline material. In this sense, the crystallization method or condition essentially adds another parameter to the reaction. One cannot always easily target specific coordination modes based on preconceived conditions because those conditions may not yield crystals.

Overall, some of the adeninate crystalline materials have interesting features which could potentially be useful for gas storage and gas separations. In addition, one of the structures is stable in aqueous solutions and biological buffers, indicating that it may be a candidate material for some biomedical applications, such as a drug storage/delivery.

1.3 CO_2 CAPTURE AND STORAGE

Worldwide CO_2 emissions from human activity have increased from an insignificant level two centuries ago to annual emissions of more than 33 billion tons today.[38] Global warming is one of the most serious challenges facing us now. It is a significant problem to solve, and many efforts have been made to reduce CO_2 emissions. Coal-fired power plants are a major source of CO_2 emissions. Emissions from the world's 2100 coal-fired power plants are responsible for roughly a third of the CO_2 generated by human activity. In The United States, roughly 600 plants produce about 30% of the 7 billion metric tons of greenhouse gases emitted by all US human made sources. Recently, China became the world's biggest CO_2 emitter, surpassing the United States. Additionally, the total emissions of CO_2 from coal will keep increasing even until 2030 according to studies released by the National Energy Technology Laboratory (NETL). Therefore, it is critical to make coal power plants cleaner by removing as much of CO_2 generated from fuel gases as possible before they are vented into the atmosphere.[38] In general, power plants produce flue gas as a mixture of various gases and a typical untreated flue gas composition is N_2 (~70%), H_2O (~7%), CO_2 (~15%), and traces of other gases.[39] [40]Selective CO_2 removal from flue gas needs to be accomplished in an efficient and economical manner.

The most common method employed in industry to capture and separate CO_2 uses a liquid amine such as monoethanolamine (MEA). MEA has been used for decades as a solvent to bind with CO_2 and separate it from neutral gases. The CO_2 capture and storage process is as follows: 1) Most coal plants burn coal to generate steam, running a turbine that produces electricity. The flue gases are generated at this time and move to an absorber where a solvent like MEA binds with the CO_2 molecules; 2) CO_2-solvent complexes are then separated in the stripper by heat; and 3) MEA is recovered to be reused and purified CO_2 is isolated for ground storage. (Scheme 3).

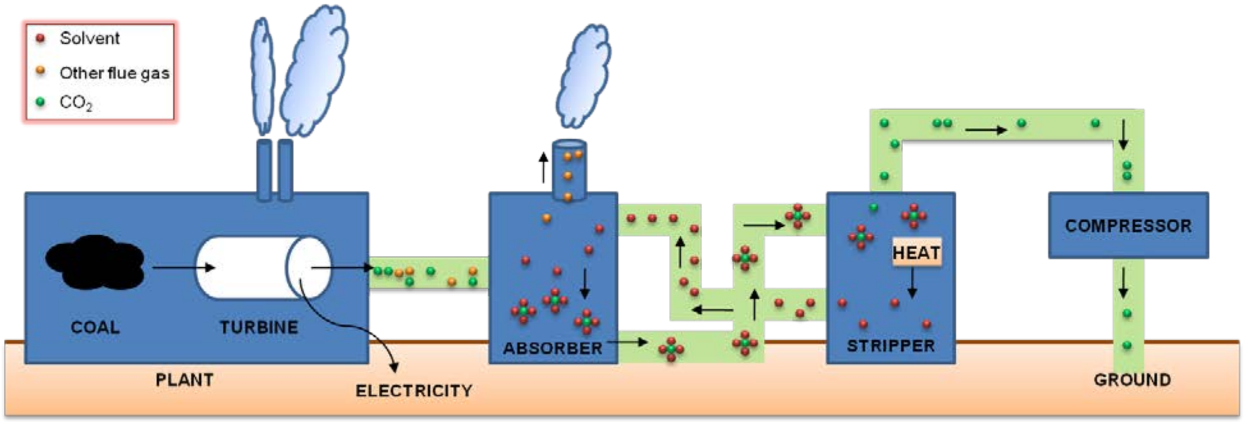

Scheme 3. CO_2 sequestration process.

However, using MEA as a CO_2 adsorber has some limitations.[41] First, the regeneration of the liquid amine after separation from CO_2 is very expensive because heat input is needed to regenerate the MEA due to its chemisorptive mechanism of CO_2 capture; thus, this results in reduced net output and a more expensive electricity bill. In addition, MEA is very volatile, requiring a chiller plant on site to remove the evaporated solvent from the concentrated CO_2. Therefore, new materials for CO_2 capture need to be developed. Porous materials with physisorption properties might be ideal candidates because of energy efficient and economical regeneration. Various materials have been studied for CO_2 capture applications[40], among which MOFs have emerged as potential selective CO_2 adsorbers.[2, 4, 42-50]

1.4 METAL-ORGANIC FRAMEWORKS FOR DRUG DELIVERY

Drug-delivery with porous materials such as mesoporous silica has been intensively studied,[51, 52] but only recently have MOFs emerged as potential materials for drug-delivery due to their unique properties. Férey and co-workers reported a seminal drug-release study with MOFs.[53] MIL-100 and MIL-101 are mesoporous MOFs, synthesized from chromium and carboxylic acids (BTC or BDC). Ibuprofen was loaded into the materials, and the kinetics of Ibuprofen delivery to simulated body fluid was measured. The MOFs exhibited high drug storage capacities, up to 1.4 g of Ibuprofen per gram of material, and complete drug controlled release under physiological conditions from 3 to 6 days. However, the fact that MIL-100 and MIL-101 contain chromium, which is a known toxin, is a limitation for biological applications.

Férey and co-workers then reported a second report of controlled drug-release.[54] Instead of employing rigid mesoporous MOFs (MIL-100, MIL-101), MIL-53, a flexible nanoporous framework, was used. MIL-53 was synthesized from either Cr or Fe and terephtalates (BDC). While MIL-53(Cr) is toxic material, MIL-53(Fe) consists of more bio-compatible, less toxic metal ions. These MOFs adsorbed ~0.2 g of Ibuprofen per gram of material, and the release process took 3 weeks to complete which is longer than other mesoporous materials such as MIL-100, MIL-101, and MCM-41. The unusually lengthy drug release of MIL-53 is attributed to the adaptability of the flexible framework.

Efforts to utilize MOFs as efficient delivery vehicles for drug delivery also have been attempted by controlling the size of the materials and synthesizing them with biocompatible components. Lin and co-workers utilized nanoscale metal-organic frameworks (NMOFs) in their drug delivery study,[21, 55] succeeding in synthesizing a highly porous nanoscale Fe(III) analogue of MIL-101 by using $FeCl_3$ and terephthalic aicd (BDC). To allow for post-synthetic modification of MIL-101(Fe), amino-functionalized nano-particles with the same structure of MIL-101(Fe) were synthesized by incorporating NH_2-BDC as a ligand. These amino groups were reacted with the ethoxysuccinato-cisplatin (ESCP) prodrug to load drugs into the particles. ESCP-loaded particles were soaked in PBS buffer, and the amount of drug released by degradation of particles was studied. Instability of the materials led to a disappointing half life of 1.2 h in PBS buffer. An alternative procedure to improve the release-time used Na_2SiO_3 to coat the nano-sized MIL-53(Fe) particles. When the silica-coated particle was soaked in PBS buffer, drug release was retarded with a $t_{1/2}$ of ~14h. Lin and co-workers also evaluated the effectiveness of the system in vitro by treating HT-29 cells with silica coated drug-loaded nanoparticles. The particles were considerably cytotoxic.

In conclusion, MOFs studied for drug delivery described above consist of metal ions and organic ligands which are not biological molecules. If MOFs were constructed from biological molecules and biologically benign metal cations, they would be a powerful potential drug delivery material. Depending on how the ligands are functionalized, delivering the drug molecules to specific host cells might be possible. Moreover, the pore size and functionality of MOFs could be tuned to carefully modulate the release profile of the drug molecule. Ultimately, adenine may be an ideal ligand for constructing porous materials for biological applications including drug-delivery.

2.0 COORDINATION MODE 1: 1-D ZINC-ADENINATE POLYMERS AND ZINC-ADENINATE MACROCYCLES AND THEIR GAS ADSORPTION PROPERTIES

In studying the coordination chemistry between adenine and metal ions, several interesting coordination patterns have been discovered. Adeninate (deprotonation at N9) can coordinate metal ions through any of its five nitrogens, thus versatile coordination modes are possible. Efforts to discover and understand general reaction conditions of each coordination mode have been made with the aim of controlling the metal-adeninate coordination mode to ultimately precisely control the architecture of the resulting metal-adeninate material. Various complexes, in which adenine is bound to metal ions principally through a combination of the N1, N3, N7, and N9 coordination sites have been isolated.[31-33, 56-59] However, exclusive coordination at the N7 and N9 sites is rare for crystalline materials.[60-62] This chapter focuses on studies aimed at controlling the coordination so that it occurs exclusively between the metal cation and the imidazolate nitrogens (N7, N9) of adenine (Mode 1) (Figure 5). By restricting the metal coordination to the imidazole ring while leaving the pyrimidal nitrogens uncoordinated to participate in hydrogen bonding, one can potentially build hierarchically assembled structures which rely on both metal coordination and hydrogen bonding for assembly and structural rigidity. Thus far, several compounds have been discovered that exhibit this coordination mode (Mode 1): 1 -D zinc-adeninate coordination polymers and zinc-adeninate hexameric macrocycles. The structures and physical properties of these new materials have been examined.

Remarkably, the zinc-adeninate macrocycles pack into a porous 3-D structure with intriguing gas adsorption properties.

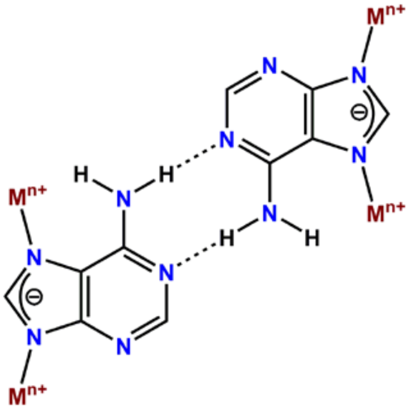

Figure 5. Metal-adeninate coordination Mode 1.

2.1 ZINC-ADENINATE 1-D COORDINATION POLYMERS

A simple chain structure was synthesized which displays coordination Mode 1. A synthesis was performed in which a mixture of adenine and zinc nitrate hexahydrate was dissolved in dimethylformamide (DMF) and pyridine. Heating this solution resulted in a single crystalline material formulated as $[Zn(ad)(py)(NO_3) \cdot 3.8DMF]$. (ad = adenine; py = pyridine) The crystal structure of the material reveals that Zn(II) tetrahedra are bridged together by the imidazolate nitrogens of the adeninate (N7, N9), forming a one-dimensional helical coordination polymer. A nitrate group and a pyridine complete the tetrahedral coordination around the Zn(II). Each infinite chain is aligned along the *b*-crystallographic axis and the overall crystal structure is composed of both right-handed and left-handed zinc-adeninate helices (Figure 6). Neighboring helices within the structure hydrogen bond to each other through the amino hydrogens and the N1 nitrogens of adjacent adeninates (Figure 7). Complete characterization of this 1-D coordination polymer (X-ray powder diffraction (XRPD), elemental analysis (EA) and thermogravimetric analysis (TGA)) was performed. (See Supporting Information)

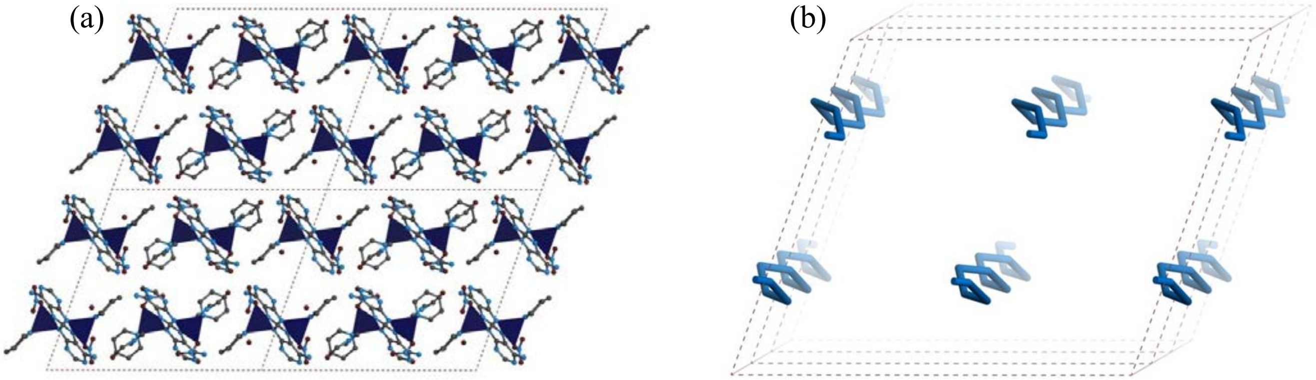

Figure 6. Zn(ad)(py)(NO_3) · (3.8DMF). View of crystal structure along the *b* crystallographic axis (Zn(II), dark blue tetrahedra; C, dark grey spheres; O, dark red spheres; N, light blue spheres; H, omitted for clarity) (a). Connecting the Zn(II) reveals that each polymeric chain is either a left-handed (top row) or right-handed (bottom row) 1-D helix (b).

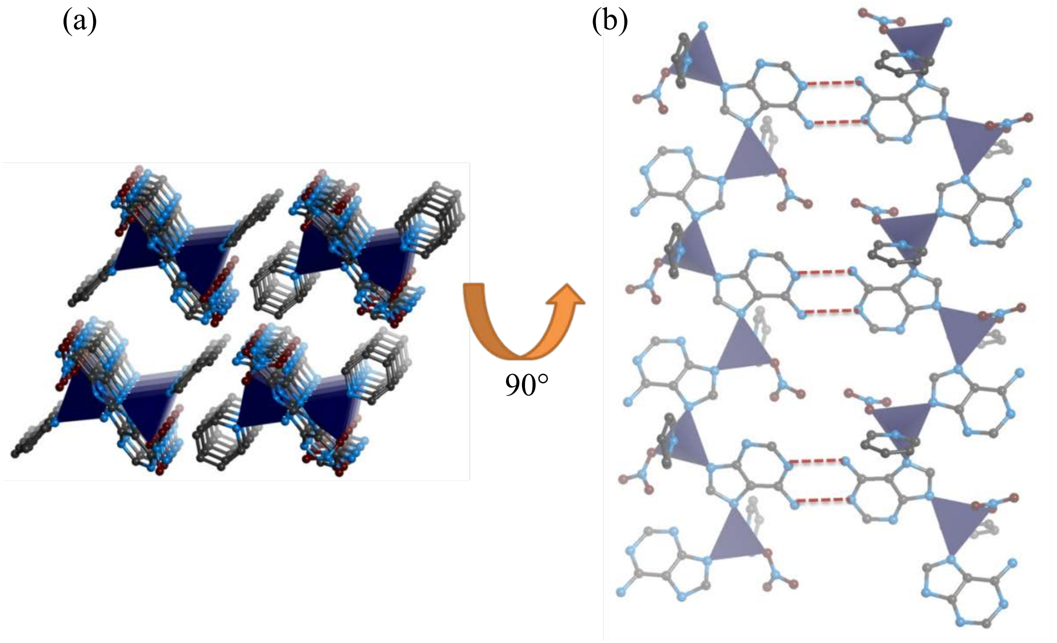

Figure 7. Zn(ad)(py)(NO$_3$) · (3.8DMF), view of crystal structure of 1-D helices directing to *b*- crystallographic direction (a) Neighboring helices hydrogen bond to each other, as illustrated by the red dash lines (b) (Zn(II), dark blue tetrahedra; C, dark grey spheres; O, dark red spheres; N, light blue spheres; H, omitted for clarity).

2.2 2-D ZINC–ADENINATE SHEETS

A 2-D sheet structure was also synthesized by connecting 1-D zinc-adeninate polymer chains into a layered structure. Originally, pyridine was used in the coordination polymer synthesis as a base to facilitate adenine deprotonation at N9 and also to compete with N1 and N3 for coordination to Zn(II) by favorably coordinating to the metal ions and completing the tetrahedral coordination of Zn(II). Since pyridine contains a nitrogen-donating group which can coordinate to the metals, we reasoned that bipyridine would serve as a ditopic ligand to link the 1-D chains into a 2-D structure. We found that introducing 1,2-bis(4-pyridyl)ethane into reactions between adenine and zinc trifluoacetate in DMF yielded a single crystalline material formulated as [Zn(ad)(bipy)(tfa) · 5DMF, $0.75H_2O$] (bipy = 1,2-bis(4-pyridyl)ethane; tfa = trifluoroacetate). The 1-D chains were linked together and formed a 2-D sheet in which the coordinated pyridine is replaced with 1,2-bis(4-pyridyl)ethane. An infinite 1-D polymer chain is formed using coordination Mode 1, in which Zn(II) was bridged by imidazolate nitrogens, leaving the amino group and N1 available for further hydrogen bonds. The tetrahedral coordination environment around Zn(II) is completed by trifluoroacetate anion and 1,2-bis(4-pyridyl)ethane (Figure 8). As a result, a layered structure is formed through the coordination of the bipyridine linker, and the layers are assembled together via hydrogen bonds. Complete characterization of this 2-D coordination polymer (XRPD, EA and TGA) has been performed (see Supporting Information).

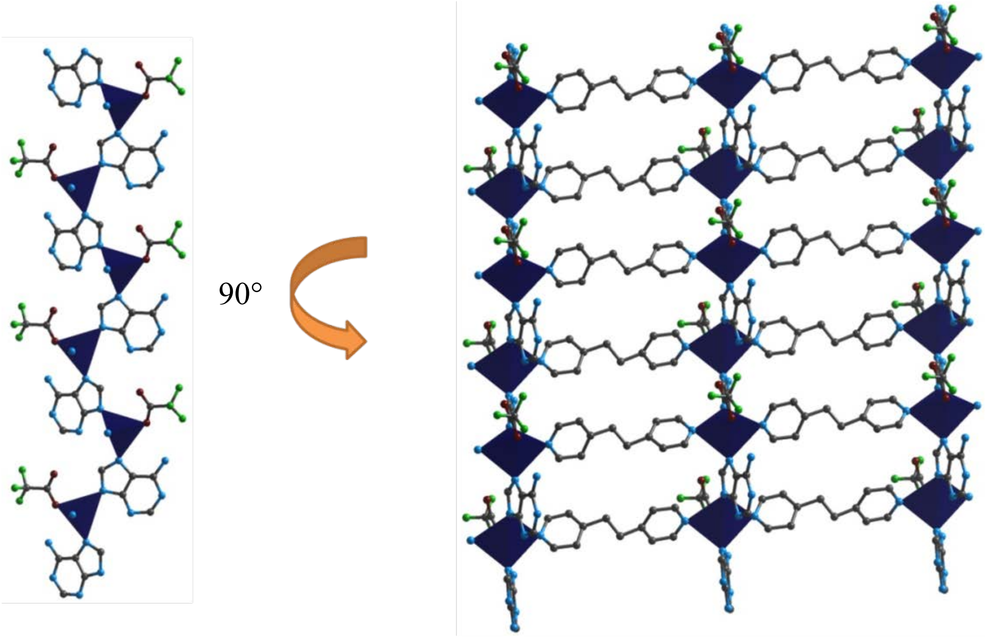

Figure 8. Zn(ad)(py)(tfa)(bipy) · 5DMF, $0.75H_2O$. View of crystal structure of 2-D polymeric sheet. 1-D helix (a) is connected by 1,2-bis(4-pyridyl)ethane into a 2-D layered structure (b) (Zn(II), dark blue tetrahedra; C, dark grey spheres; O, dark red spheres; N, light blue spheres; H, omitted for clarity).

2.3 ZINC-ADENINATE MACROCYCLES

The zinc-adeninate 1-D polymeric chains and 2-D layered structures described in the previous sections are infinite polymeric materials. Unlike these structures, a discrete macrocycle (0-D) was also synthesized. In this structure, adeninate is also coordinated to Zn(II) via coordination Mode 1. To access structures that exploit this coordination mode, we performed a synthesis in which a mixture of adenine and zinc salts was dissolved in dimethylformamide (DMF) and pyridine. Heating this solution resulted in formation of a zinc-adeninate hexameric macrocycle, $Zn_6(ad)_6(py)_6(X)_6$ (X=acetate, dimethylcarbamate, or trifluoroacetate). Three different zinc-adeninate hexameric macrocycles were synthesized from various zinc salts such as zinc acetate, zinc nitrate, and zinc trifluoroacetate, respectively. Their structures and packing modes are all identical apart from the coordinated anion components. However, each hexameric macrocycle has unique properties as illustrated by their TGA data (Figure 9). In this section, we will focus on $Zn_6(ad)_6(py)_6(\text{dimethylcarbamate})_6$ and its structural and physical property studies will be described.

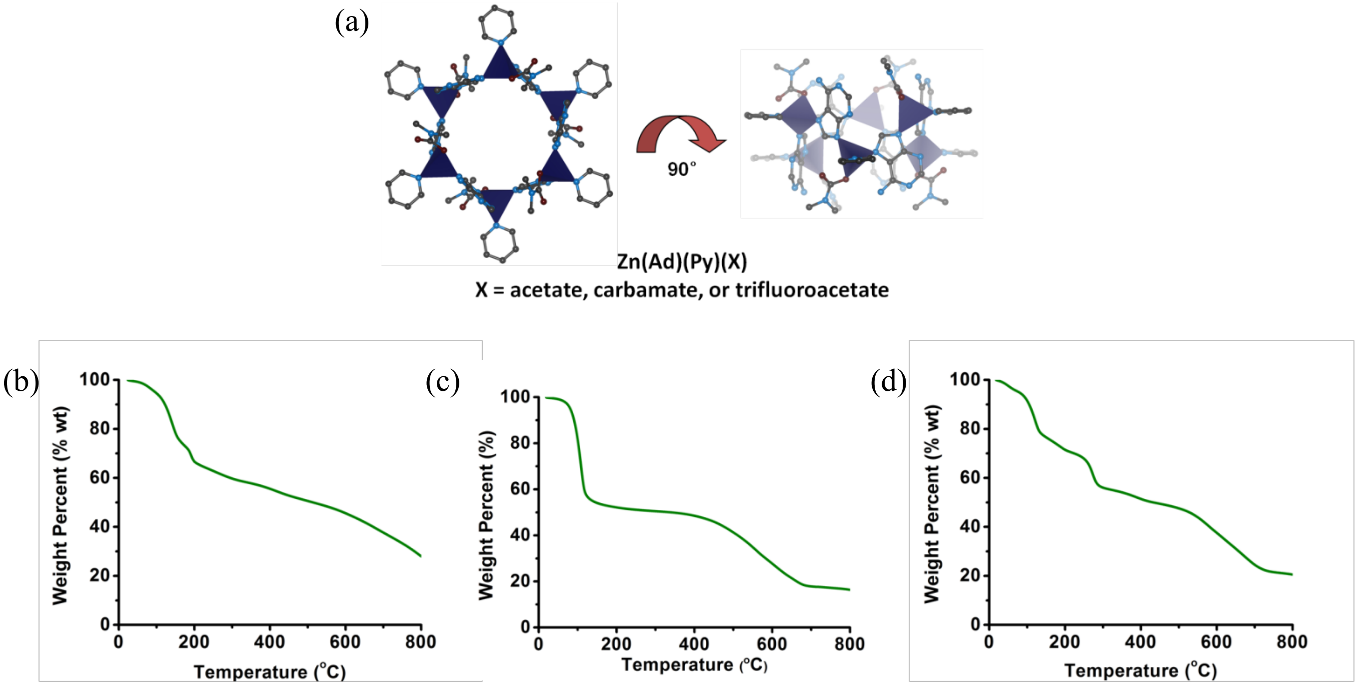

Figure 9. Zn(ad)(py)(X), view of crystal structure of Zinc-adeninate hexameric macrocycles (a) (Zn(II), dark blue tetrahedra; C, dark grey spheres; O, dark red spheres; N, light blue spheres; H, omitted for clarity), Thermogravimetric analysis data for Zn(ad)(py)(acetate) (b), Zn(ad)(py)(carbamate) (c), and Zn(ad)(py)(trifluoroacetate) (d).

2.3.1 Structure

A crystalline material, $Zn_6(ad)_6(py)_6(dimethylcarbamate)_6 \cdot 10.5$ DMF, was prepared via a solvothermal reaction between adenine and zinc nitrate hexahydrate in DMF and pyridine. Single crystal X-ray diffraction data revealed that the macrocycle is composed of six adeninates and six Zn(II) cations. Each Zn(II) is bound to either the N7 or N9 position of two different adeninates. The imidazole rings of the adeninates bridge the Zn(II) centers. In addition, each Zn(II) is coordinated to a single carbamate anion and a single pyridine, which complete the tetrahedral coordination sphere (Figure 10). The carbamate anion is formed in situ from the thermal decomposition of DMF.[63] Since only the imidazolate nitrogens of the adeninate coordinate the Zn^{2+}, N1 and the amino group remain available for hydrogen bonding. The macrocycles self-assemble into an extended structure via cooperative adeninate-adeninate hydrogen bonding interactions. This structure consists of alternating layers of macrocycles that stack in an a-b-c fashion (Figure 11). Each macrocycle forms a total of 12 hydrogen bonds (two per adeninate) with its six nearest-neighbor macrocycles within the structure. This packing motif results in the formation of cylindrical cavities (~ 5 × 20 Å) arranged periodically throughout the 3-D structure (Figure 12a). The confines of each cavity are defined by one central macrocycle and fragments of the six nearest-neighbor macrocycles. (Figure 12b, 13).

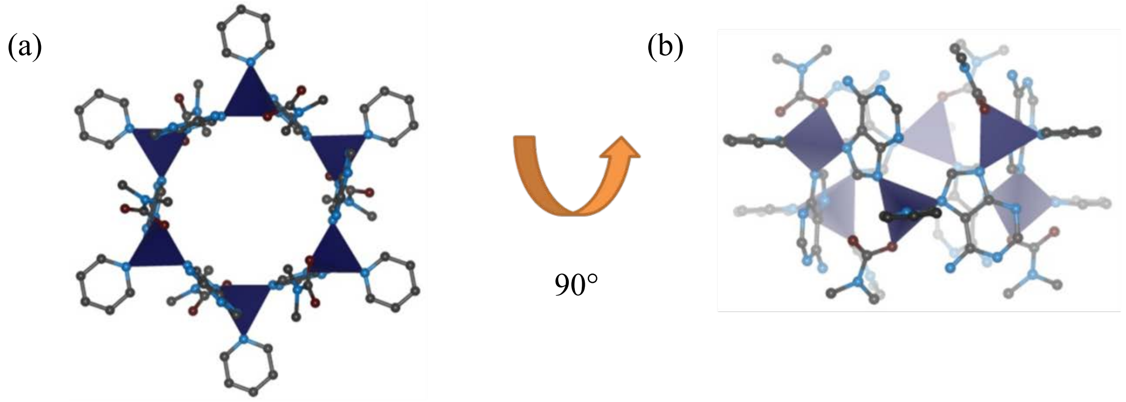

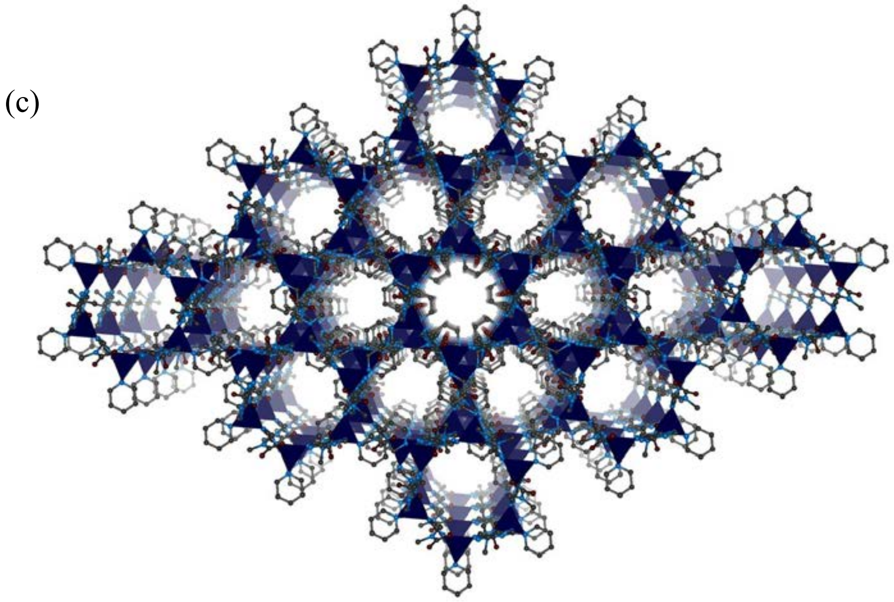

Figure 10. Top view (a) and side view (b) of a single $Zn_6(adeninate)_6(pyridine)_6(carbamate)_6$ macrocycle (c) perspective view of the macrocycles packing along *c*-crystallographical axis (Zn^{2+}, dark blue; C, dark grey; N, light blue; O, red; H omitted for clarity).

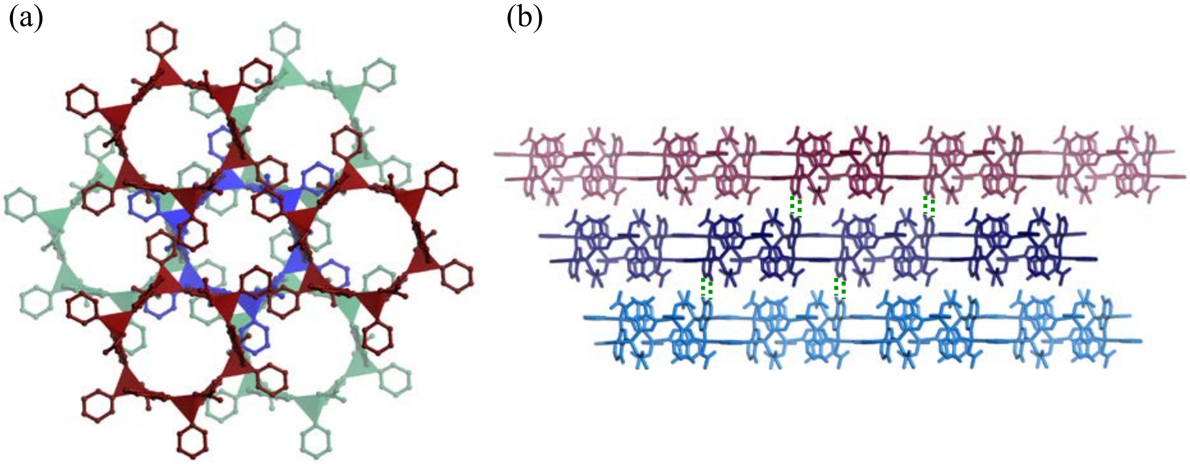

Figure 11. (a) The macrocycles pack into layers which are held together by hydrogen bonds between macrocycles in adjacent layers (A-B-C fashion) (b) side view of packing via hydrogen bonding (hydrogen bonding was illustrated as green dash lines).

Although free solvent molecules could not be resolved from the X-ray data, Platon analysis[64] revealed significant residual electron density within the cavities, which we attribute to DMF guest molecules. Elemental analysis (EA) and thermal gravimetric analysis (TGA) data both suggest that approximately 10.5 DMF molecules per macrocycle reside within the structure.

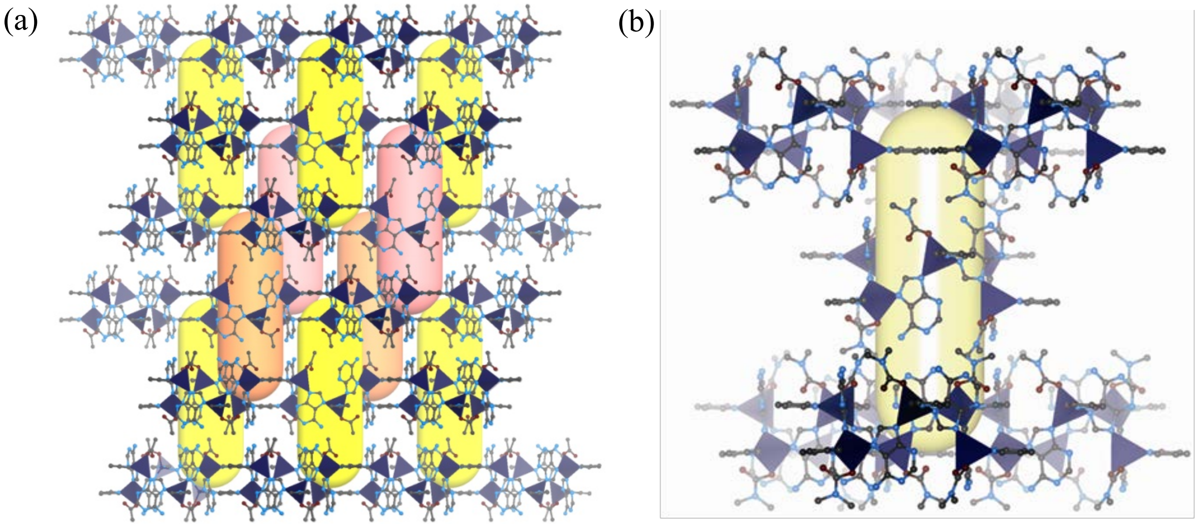

Figure 12. The macrocycles pack into layers which are held together by hydrogen bonds between macrocycles in adjacent layers. The 3-D packing of the macrocycles within the crystal structure results in the formation of large tubular cavities ((a), (b)). ((Zn^{2+}, dark blue; C, dark grey; N, light blue; O, red; H omitted for clarity; the yellow and orange cylinders represent the space in the channel).

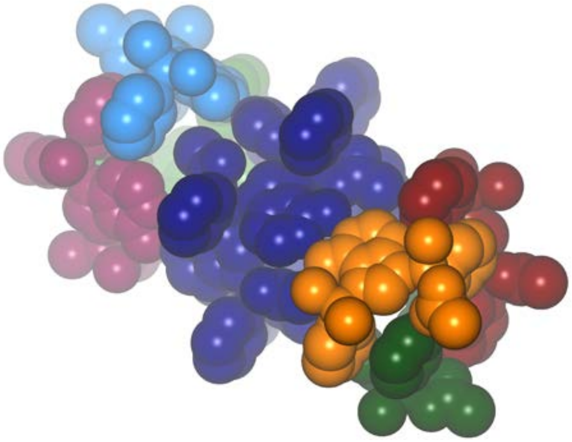

Figure 13. 1-D Channel composition space filling model (purple; a hexameric ring, yellow, red, green, violet, blue, light green; parts of different hexameric macrocycles).

2.3.2 Characterization

Given that the assembled 3-D macrocycle structure exhibits large cavities, we were naturally interested in evaluating its porosity. Although many crystal structures of macrocyclic compounds exhibit 1-D channels in the solid state, few exhibit permanent porosity upon removal of guest molecules.[65-68] This collapse is likely due to weak interactions between the neighboring macrocycles within the structure, which may lead to structural shear and obstruction of the channels upon guest removal. In our case, though, we reasoned that the strong adenine-adenine hydrogen bonding interactions between adjacent macrocycles might serve to lock the macrocycles in place and stabilize the crystal structure upon removal of guest molecules.

Inspection of the structure reveals that three pyridine rings occlude the entrance to each cavity, resulting in an aperture measuring only ~1.2 Å (Figure 14). In order to access the cavities, we needed to first remove a portion of the pyridine molecules to increase the pore aperture and allow diffusion of guest molecules within the structure.

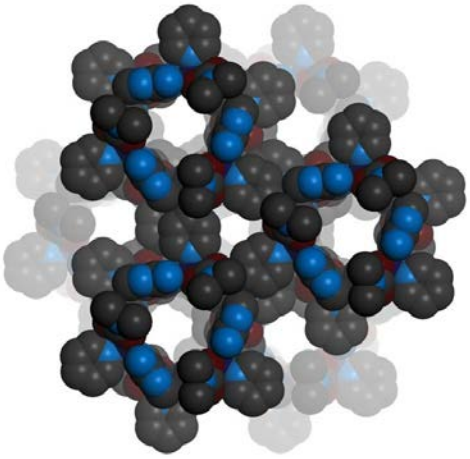

Figure 14. A top view of the packed macrocycles. The entrance of the pore which located at the center is blocked by three pyridine molecules from the neighboring macrocycles (C, dark grey; N, light blue; O, wine; H omitted for clarity).

TGA studies were performed to assess the stability of the assembled structure and the mobility of the free DMF and coordinated pyridine molecules (Figure 15). We observed a 43 % weight loss upon heating to 125 °C, which corresponds roughly to the loss of the free DMF molecules and a fraction of the coordinated pyridines, based on EA data collected for the heated sample.

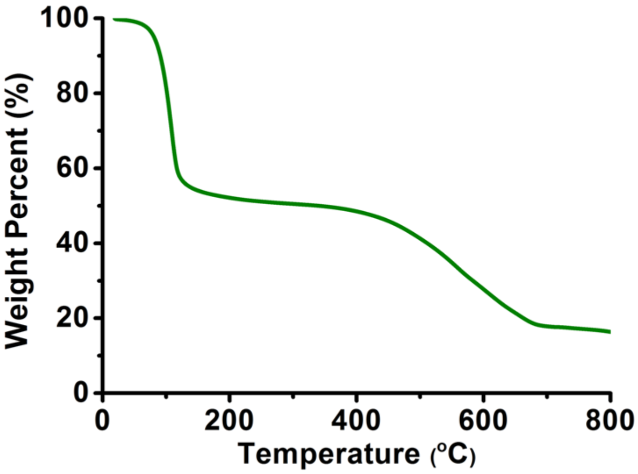

Figure 15. Thermogravimetric analysis data for the as-synthesized $Zn_6(ad)_6(py)_6(carbamate)_6 \cdot (10.5\ DMF)$.

Remarkably, the powder X-ray diffraction pattern of the heated sample matches that of the as-synthesized material (Figure 16), indicating that the material maintains its structural integrity despite loss of DMF and coordinated pyridine, an aspect that points towards the utility of the multiple hydrogen bond interactions for generating a structurally robust material.

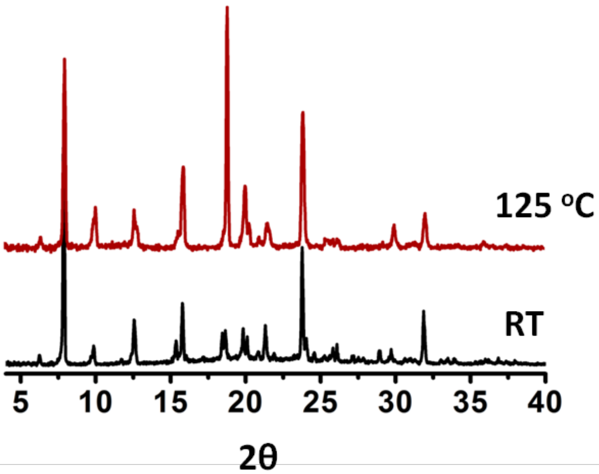

Figure 16. Powder X-ray diffraction patterns for the as-synthesized material (black) and the material after heating to 125 °C (red).

2.3.3 Gas sorption properties

Encouraged by characterization studies from EA, TGA and PXRD, we surmised that activating the material at 125 °C would effectively widen the cavity aperture (via loss of coordinated pyridine), allowing evacuation of guest molecules from the material. Indeed, sorption studies performed on the material after 125 °C activation revealed a small uptake of nitrogen (N_2; 77 K) (Figure 17a) and a comparatively large uptake of both hydrogen (H_2; 77 K) (Figure 17b) and carbon dioxide (CO_2; 273 K) (Figure 18), which is likely due to the different kinetic radii for the three gases (N_2, 3.64 Å; CO_2, 3.3 Å; H_2, 2.89 Å).[69] The maximum H_2 uptake is 0.9 weight percent at 77 K and 1 atm which is similar to the uptake of many microporous metal-organic framework (MOF) materials.[15, 70] Significantly, the H_2 isotherm was steep in the low pressure region, indicating a high affinity of the adsorbed H_2 to the material, which may be due to vacant coordination sites on the Zn(II) that result from removal of some of the coordinated pyridine molecules.[15, 70]

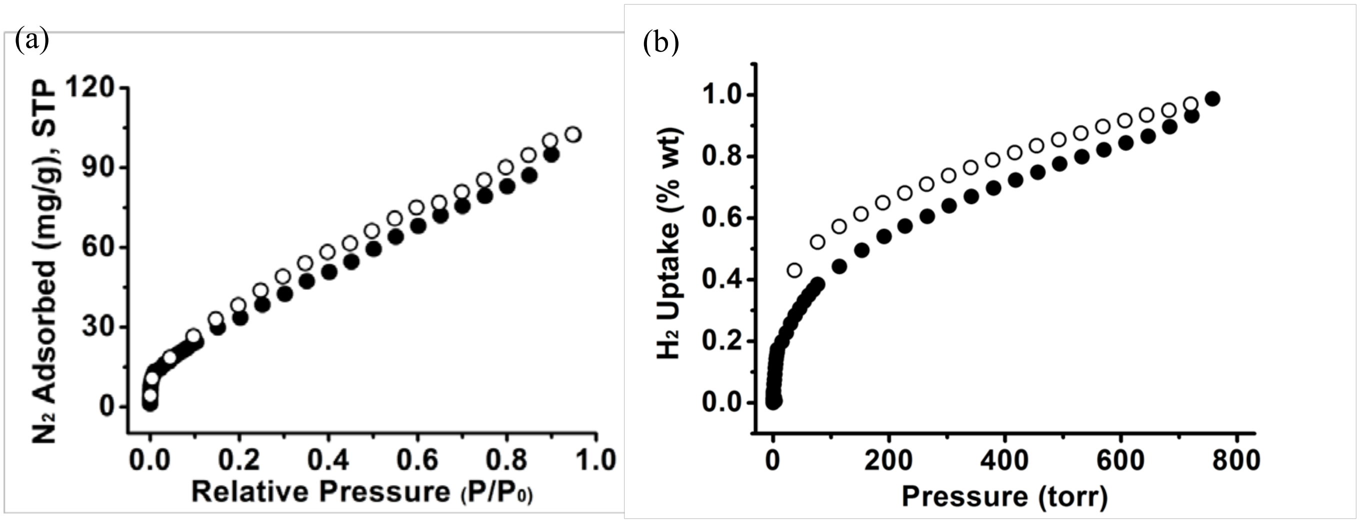

Figure 17. (a) N_2 sorption isotherm (77 K), (b) H_2 sorption isotherm (77 K) for material activated at 125 °C ((●) adsorption; (○) desorption).

Interestingly, the isotherms for both H_2 and CO_2 exhibited significant hysteresis upon desorption.[71, 72] We hypothesized this could be due to hindered diffusion through the narrow pore apertures.[73, 74] To understand the origin of the hysteresis, we compared the CO_2 sorption isotherm of the material activated at 125 °C (**1**) (Figure 18a) to the CO_2 isotherm of the material activated at 100 °C (**2**) (Figure 18b). The hysteresis was more dramatic for **2**. Upon desorption, **1** retained approximately 38 % of its sorbed CO_2 at 40 torr while **2** retained nearly 45 % of its sorbed CO_2 at the same desorption pressure. This observation suggests that the hysteresis is indeed likely due to a gating effect caused by the narrow pore apertures. Activation at 125 °C resulted in a greater loss of coordinated pyridine compared to activation at 100 °C; therefore, we expect that the pore aperture for **2** is smaller than for **1**, consequently resulting in a more dramatic hysteresis. The decrease in the pore aperture is supported by N_2 sorption experiments: like typical microporous materials, **1** exhibits some N_2 uptake at low pressures, although it does not reach saturation, whereas **2** is essentially nonporous to N_2 (see Supporting Information). Collectively, these sorption data suggest that the size of the pore aperture can be tailored to tune the material's ability to selectively trap CO_2 within its structure.

It is important to note that small sorbent-induced structural rearrangements[75] may also contribute to the hysteresis. However, if this were the case, we would expect to see more dramatic hysteresis for **1** rather than **2**, because more structural components have been removed for **1**. We also considered that strong sorbate open-metal site interactions might contribute to the observed hysteresis. However, using the Dubinin-Radushkevitch (DR) equation, the isosteric heat of adsorption was calculated to be approximately 21 kJ/mol at 273 K. This value is much smaller than those usually observed for chemisorption[76] and also smaller than those observed for

MOF materials with open-metal sites.[45] Therefore, we reason that sorbate open-metal site interactions do not contribute significantly to the hysteresis.

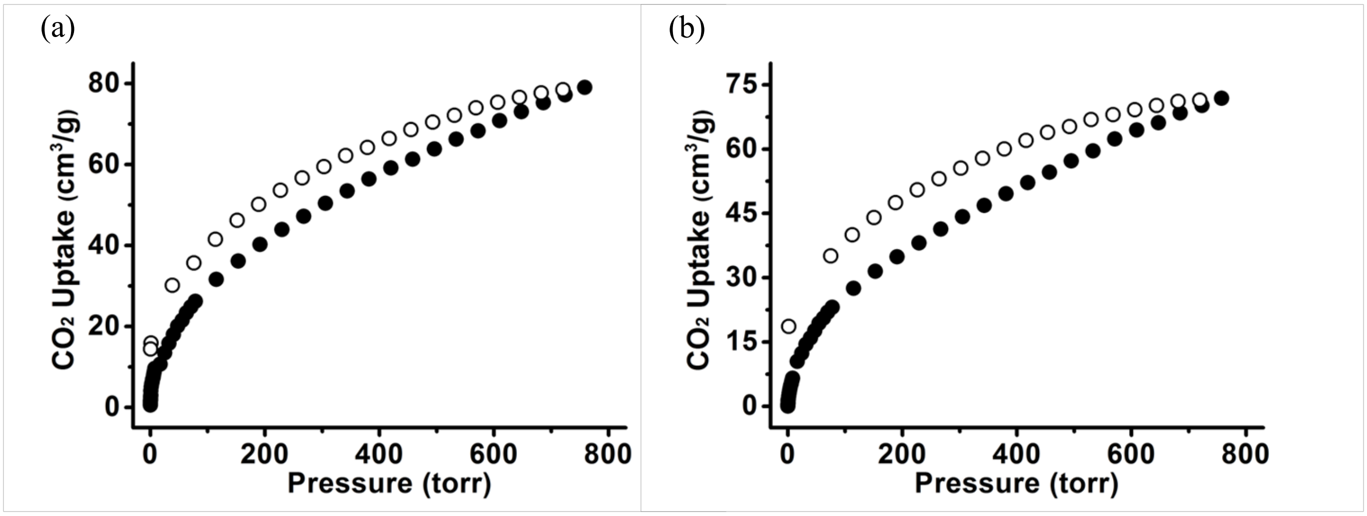

Figure 18. CO_2 sorption isotherms (273 K) for material activated at 125 °C (a) and 100 °C (b) ((●) adsorption; (○) desorption).

In summary, we have demonstrated that strong biomolecular hydrogen bonding interactions can be used to assemble zinc-adeninate macrocycles into robust materials that exhibit large cavities within their structures. Careful removal of the coordinated pyridine molecules that "gate" the cavity entrances allows for modulation of the cavity aperture dimensions and therefore discrimination of adsorbate molecules based on their kinetic diameter. In addition, by tuning the aperture size, we can adjust the amount of CO_2 that can be trapped within the structure. Together, these results point toward the potential utility of this material in gas separation and sequestration applications.[77-79] We note that the specific strategy we present for modulating pore aperture dimensions to impart specific gas sorption properties is unique. We believe that this strategy can be extended to the design of new porous materials that have controllable pore “gates” that can be opened or closed to affect the capture and release of specific gas molecules.

3.0 COORDINATION MODE 2: BIO-MOF-11 AND PORES EXHIBITING EXPOSED LEWIS BASIC SITES FOR OPTIMAL CO_2 ADSORPTION

Adenine's multiple Lewis-basic sites, including an amino group and pyrimidine nitrogens, can interact with CO_2, potentially resulting in materials with high CO_2 adsorption energies. Indeed, a recent computational study revealed that the interaction energy between CO_2 and adenine is higher than that between CO_2 and other nitrogen-containing MOF linker molecules, indicating that adenine-based MOFs would be ideal for selective CO_2 adsorption.[37]

The previous chapter described the adsorption properties of porous zinc-adeninate macrocyclic structures which selectively adsorbed CO_2 and exhibited rapid CO_2 uptake at low pressures. We attributed the selectivity to the presence of narrow pore apertures that exclude gases with larger kinetic diameters and the rapid uptake at low pressures to favorable interactions between CO_2 and the pore walls. In this structure, the zinc adeninate macrocycles assemble via hydrogen bonding between the amino group and one pyrimidal nitrogen from each adeninate. These hydrogen-bonding interactions may limit the accessibility of the Lewis basic sites and may therefore decrease the material's affinity for CO_2. Therefore, we reasoned that exposing these sites within the pores of a MOF should lead to materials with enhanced CO_2 adsorption properties, including high uptake and high selectivity. By constructing a structure exploiting binding Mode 2 (Figure 19), the imidazolate nitrogens (N7, N9) and one of the nitrogens (N3) from the hexameric ring will coordinate to the metal ions. This leaves N1 and the amino group free and exposed within the structure for potential CO_2 interactions.

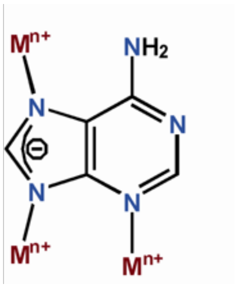

Figure 19. Metal-adeninate coordination Mode 2.

3.1 BIO-MOF-11 STRUCTURE AND CHARACTERIZATION

To expose the Lewis basic sites, we prepared $Co_2(ad)_2(CO_2CH_3)_2 \cdot 2DMF \cdot 0.5H_2O$ (bio-MOF-11) via a solvothermal reaction between cobalt acetate tetrahydrate and adenine in DMF. Single-crystal X-ray studies revealed that the structure consists of cobalt-adeninate-acetate "paddle-wheel" clusters (Figure 20a) in which two Co(II) are bridged by two adeninates (via the N3 and N9 positions) and two acetates; each cobalt adeninate cluster can be represented as a square secondary building unit (SBU). These SBUs are linked together through apical coordination of the adeninate N7 atoms to Co ions on neighboring clusters to generate a three-dimensional (3D) framework structure (Figure 20b) exhibiting the augmented **lvt** network topology (Figure 20c, 20d), one of the default topologies for connecting square building units with equivalent linkers.[80, 81] This underlying topology results in cavities that are periodically distributed throughout the structure. Each cavity (Figure 20c) is defined by 16 interconnected square building units and can accommodate a 5.8 Å diameter sphere. The aperture to each cavity measures 5.2Å. The cavities align into channels that run along the *a* and *b* crystallographic directions (Figure 20b).

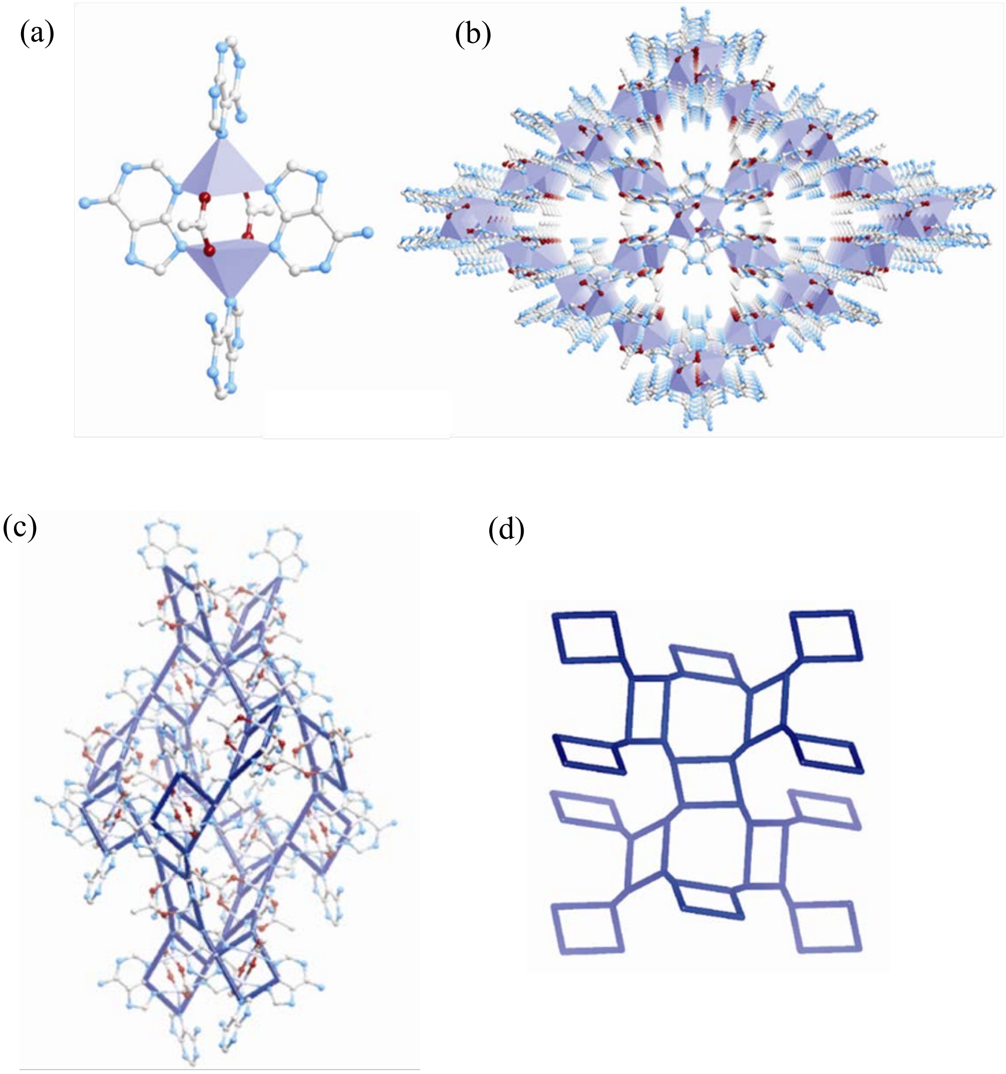

Figure 20. Crystal structure of bio-MOF-11. Co^{2+}-adeninate-acetate clusters (A) are bridged by adeninate to generate a 3-D extended porous structure with channels (B) along the *a* and *b* crystallographic directions. Each cluster can be represented as a square (dark blue) building block and internal cavities within the framework consist of 16 interconnected square clusters (C). The framework adopts the augmented lvt topology (D). (Co^{2+}, light purple; C, grey; O, red; N, light blue; H's omitted for clarity)

Carboxylate cluster building blocks (e.g., paddle-wheel clusters) have been used extensively for constructing structurally rigid and permanently porous MOFs. We hypothesized that MOFs constructed from structurally similar adeninate-based clusters should also be stable and permanently porous. Indeed, bio-MOF-11 remains stable upon heating to 200 °C. In this framework, metal-adeninate binding Mode 2 was observed, thus amino and pyrimidine groups are free and exposed inside the pores for further CO_2 interactions. As shown in the Figure 21, the inside of the pore of bio-MOF-11 is decorated by the amine and pyramidyl nitrogen of the adeninate in a high density.

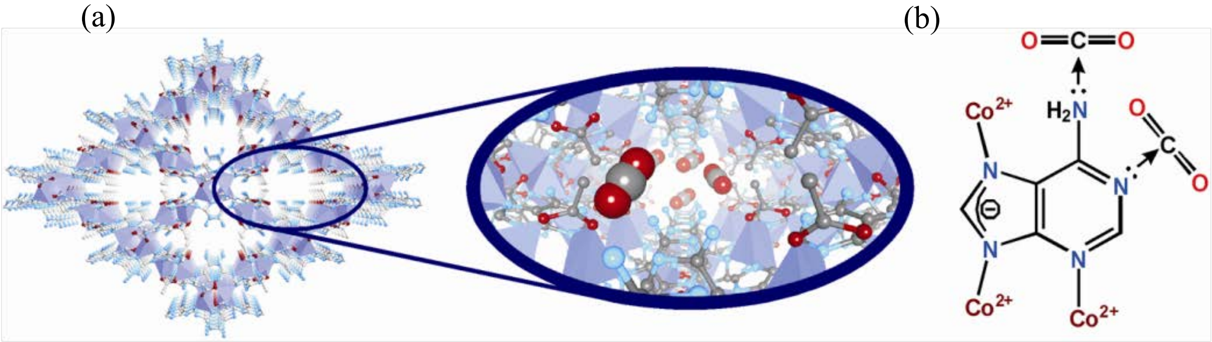

Figure 21. (a) Amino-, pyrimidine group decorated pore of bio-MOF-11 (Co^{2+}, light purple; C, grey; O, red; N, light blue; H's omitted for clarity.), (b) Co-adeninate coordination mode with potential interaction between adeninate and CO_2.

EA data confirmed that there are 2 DMF molecules and 0.5 water molecules per unit cell. The TGA data shows a weight loss of 22.0 % from room temperature to 200 °C which corresponds to a removal of solvent guest molecules, which is 22.5 % (2 DMF and 0.5 H_2O molecules). (Figure 22a) The powder X-ray diffraction pattern of the as-synthesized material confirms the phase purity of the material. PXRD pattern of the chloroform exchanged sample and heated sample at 200 °C matches that of the as-synthesized material (Figure 22b), indicating that the material maintains its structural integrity. Furthermore, PXRD pattern of the sample after gas sorption studies showed that the crystallinity of the material was still kept even after multiple cycles of gas adsorption experiments.

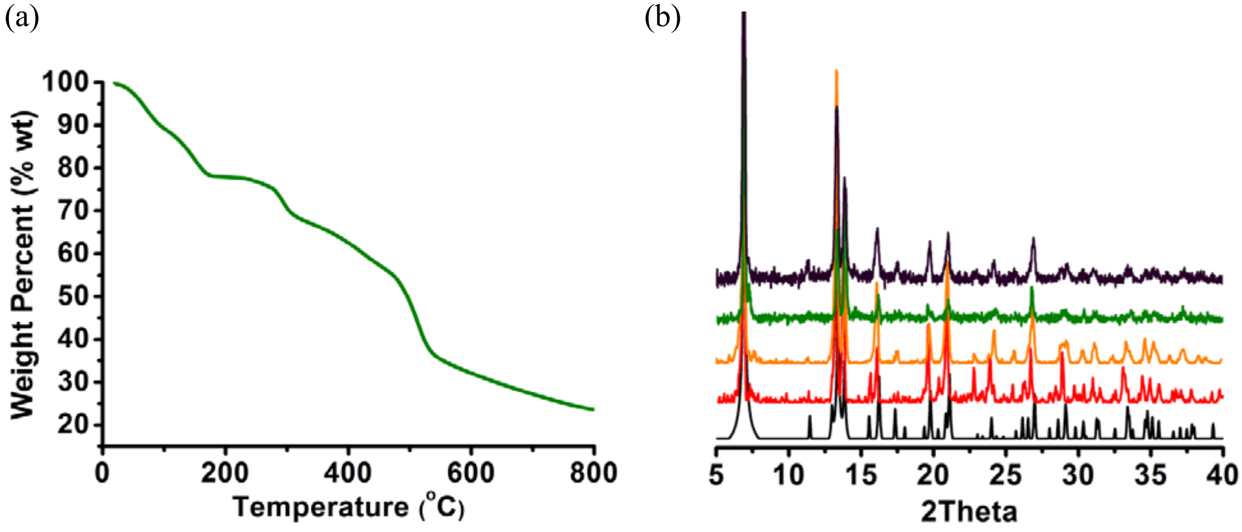

Figure 22. Thermogravimetic analysis for bio-MOF-11 (a), X-ray Powder diffraction pattern for bio-MOF-11 (b) (as synthesized (red); chloroform exchanged (orange); heated to 200 °C (green); and after sorption study (navy)).

3.2 GAS ADSORPTION STUDY

We conducted N_2 adsorption experiments at 77 K to evaluate its permanent porosity. The material was activated at 100 °C under reduced pressure after soaking in chloroform for 24 h. The resulting type-I isotherm (Figure 23) reveals rapid gas adsorption at low pressures and is consistent with permanent microporosity. The estimated Brunauer-Emmett-Teller (BET) surface area is 1040 m^2/g, and the pore volume is 0.45 cm^3/g.

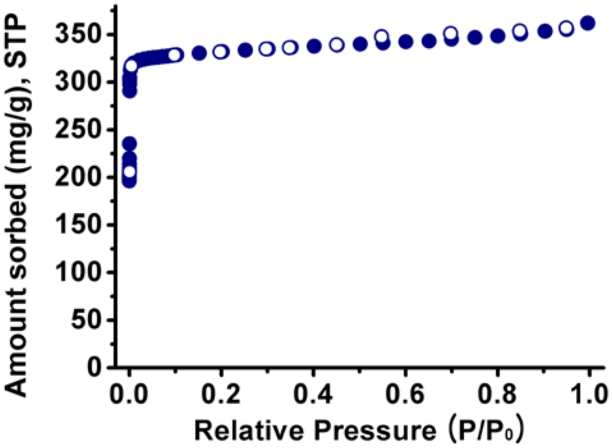

Figure 23. N_2 sorption isotherm (77 K) for bio-MOF-11 ((●) adsorption; (○) desorption).

The pores of bio-MOF-11 are densely lined with Lewis basic amino and pyrimidine groups (Figure 20b, 21a). A total of four amino groups and four pyrimidine groups are directly exposed to each individual cavity. This feature prompted us to examine the material's CO_2 adsorption properties. We first collected the CO_2 isotherm at 273 K. It is completely reversible, exhibits a steep rise at low pressures, and reaches a maximum of 6.0 mmol/g at 1 bar (Figure 24a). Comparatively, the N_2 uptake at 273 K is only 0.43 mmol/g at 1 bar. At 298 K, the maximum CO_2 uptake is 4.1 mmol/g, compared with only 0.13 mmol/g for N_2 (Figure 24a).

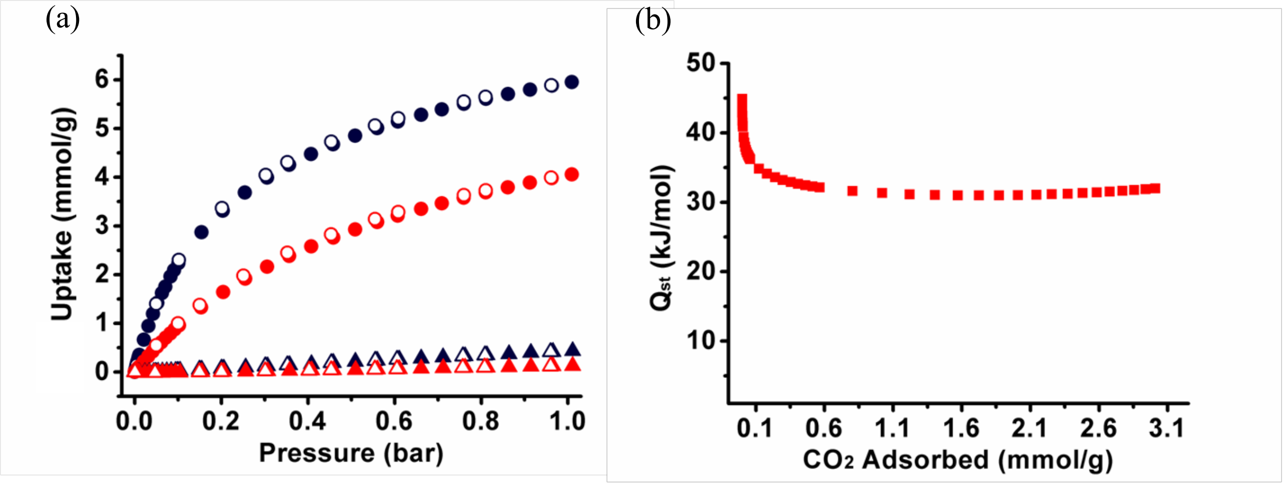

Figure 24. (a) CO_2 adsorption isotherms (circles) and N_2 adsorption isotherms (triangles) at 273 K (navy) and 298 K (red). (filled, adsorption; empty, desorption) (b) Isosteric heat of adsorption for CO_2 at different CO_2 loadings.

The initial slopes of the CO_2 and N_2 adsorption isotherms were calculated, and the ratios of these slopes were used to estimate the adsorption selectivity for CO_2 over N_2 (Figure 25a, 25b). From these data, the calculated CO_2/ N_2 selectivity is 81:1 at 273 K and 75:1 at 298 K. To our knowledge, these selectivity values are the best reported to date for MOF materials. We also calculated the isosteric heat of adsorption (Q_{st}) for CO_2 using adsorption data collected at 298, 303, 308, and 313 K. At the onset of adsorption, Q_{st} is ~45 kJ/mol, which is similar to values for some other amine-functionalized MOF materials. Q_{st} decreases to 30-35 kJ/mol at higher CO_2 pressures and remains steady at this value throughout the adsorption process (Figure 24b). We believe that this high Q_{st} is due to favorable interactions between adsorbed CO_2 molecules and the Lewis basic amine and pyrimidine functionalities decorating the pores.[37, 82, 83]

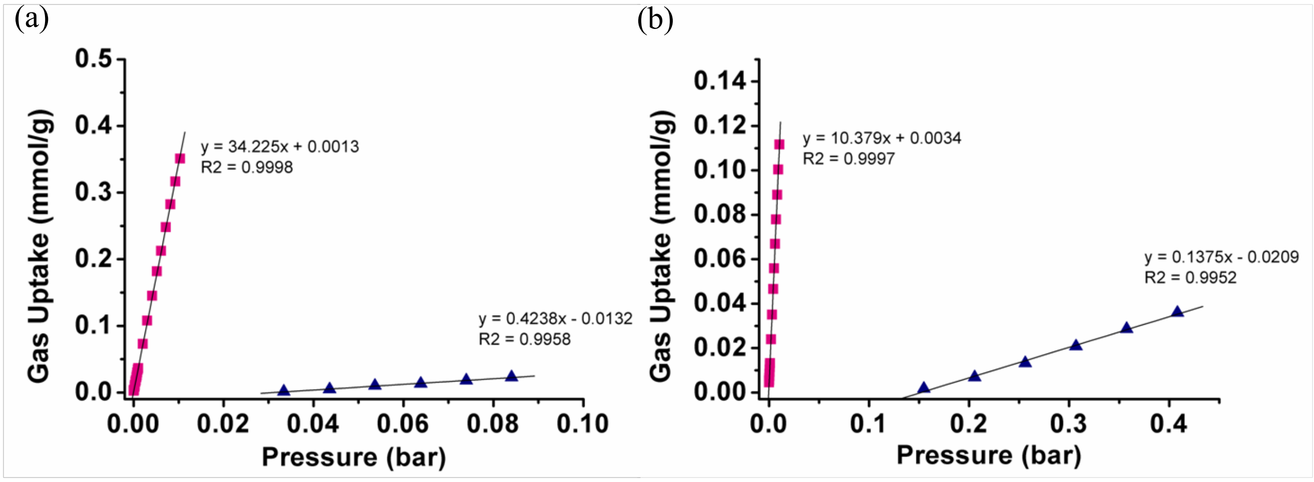

Figure 25. Initial slope calculation for CO_2 and N_2 isotherms collected at 273K (a) and 298K (b) (CO_2: pink squares; N_2: blue triangles).

Given the rapid uptake of N_2 at 77 K and CO_2 at 273 K, we decided to study the H_2 adsorption properties to determine whether the relatively small pores of bio-MOF-11 may be intrinsically well suited for condensing gases at low pressures. The hydrogen isotherms collected at 77 K and 87 K were also both steep in the low-pressure regime and completely reversible. At 77 K, the material adsorbs a maximum of ~1.5 wt % H_2. The maximum Q_{st} for H_2 is ~13 kJ/mol at low pressure. As the H_2 loading increases to ~0.7 wt %, Q_{st} decreases to ~7 kJ/mol, and from 0.7 to 1.1 wt%, Q_{st} increases slightly. The increase in Q_{st} at higher loadings may be due to intersorbate interactions that are promoted in the restricted pore space. [84]

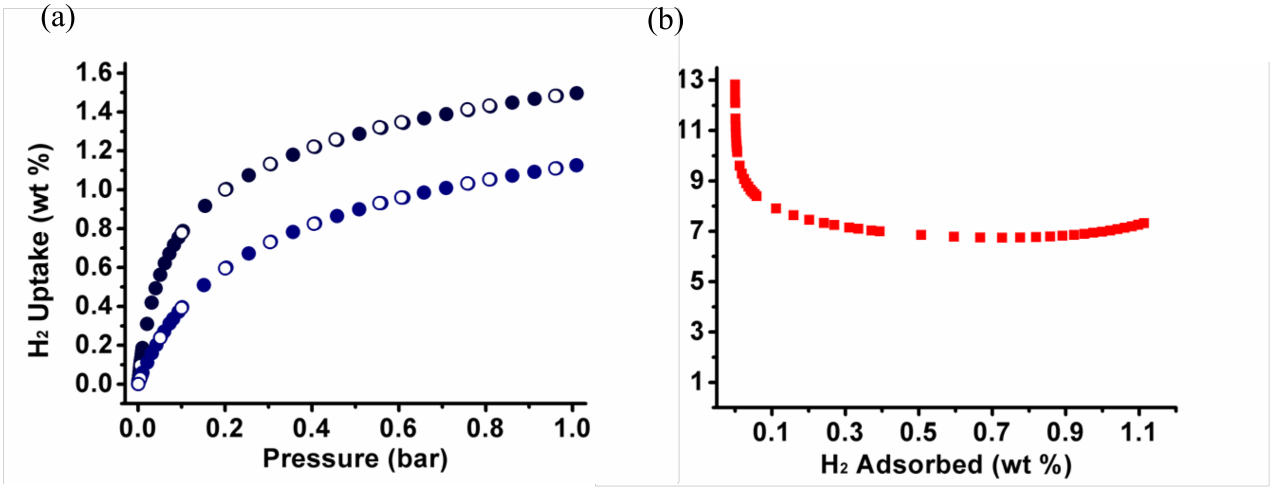

Figure 26. (a) H_2 sorption isotherm for bio-MOF-11 at 77 K (navy) and 87 K (blue). ((●) adsorption; (○) desorption) (b) Isosteric heat of adsorption for H_2 at different H_2 loadings.

In conclusion, bio-MOF-11 has a high heat of adsorption for CO_2, high CO_2 capacity, and impressive selectivity for CO_2 over N_2. We attribute these favorable CO_2 adsorption properties to the presence of the Lewis basic amino and pyrimidine groups of adenine and the narrow pore dimensions of bio-MOF-11. In terms of several important CO_2 capture and separation performance criteria, this material outperforms other amine-functionalized MOFs and imidazole-based frameworks. Specifically, it exhibits higher CO_2 capacities and higher selectivities for CO_2 over N_2. Collectively, these results point toward the value of utilizing adenine as a building block for constructing MOFs for CO_2 capture applications.

4.0 COORDINATION MODE 3: BIO-MOF-1

Metal-adeninate crystalline materials constructed based on Mode 1 and Mode 2 have been synthesized, and their interesting structural or physical properties are described in Chapters 2 and 3. Some crystalline materials exhibiting binding Mode 3 (Figure 27) have also been synthesized, and they exhibit a host of unique properties.

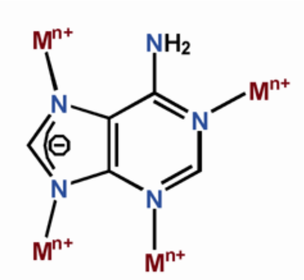

Figure 27. Metal-adeninate coordination Mode 3.

In carboxylate MOF chemistry, the oxo-centered metal-carboxylate cluster is commonly observed. We synthesized a framework that has similar oxo-centered clusters by using adenine instead of a carboxylic acid. The oxo-centered metal-carboxylate cluster contains six carboxylate groups coordinated to the M_4O cluster. However, there are only four adenines coordinated to the M_4O cluster in the oxo-centered metal-adeninate cluster, as adenine is bulkier than the carboxylates. This oxo-centered metal-adeninate cluster is observed in bio-MOF-1 where zinc-adeninate octahedral cages, used as a secondary building unit, are fused together by sharing an oxo group (Figure 28). Further structural description of bio-MOF-1 will be presented in the next section.

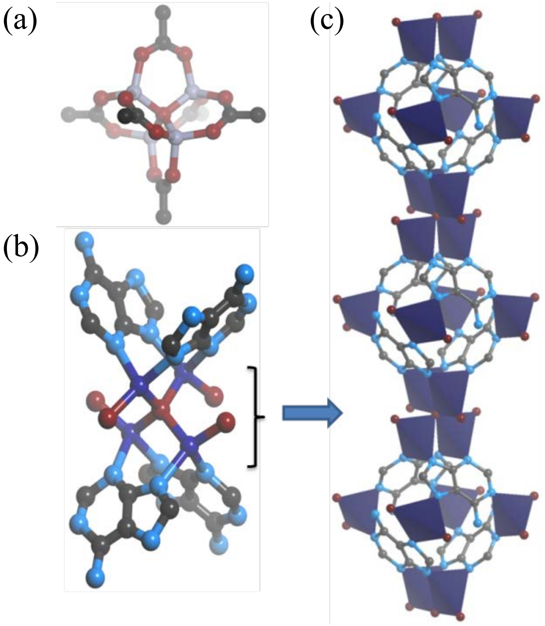

Figure 28. (a) Oxo-centered metal-carboxylate cluster, (b) oxo-centered metal-adeninate cluster which is part of zinc-adeninate columnar secondary building units of bio-MOF-1 (c) (Zn^{2+}, dark blue; C, dark grey; N, light blue; O, red; H omitted for clarity).

4.1 STRUCTURE AND CHARACTERIZATION

From the previous work, initial reactions between adenine and zinc salts resulted principally in the formation of condensed materials with small, inaccessible pores. These results prompted us to include auxiliary linking molecules into our syntheses to promote the formation of larger pores which would potentially accommodate larger molecules. Specifically, we found that introducing biphenyldicarboxylic acid to reactions between adenine and zinc acetate dihydrate in DMF yielded a single crystalline material formulated as $Zn_8(ad)_4(BPDC)_6O$ ·

$2Me_2NH_2$, 8DMF, $11H_2O$, heretofore referred to as bio-MOF-1 (ad = adeninate; BPDC = biphenyldicarboxylate). Single crystal X-ray analysis revealed that bio-MOF-1 consists of infinite zinc-adeninate columnar secondary building units (SBUs) composed of apex-sharing zinc-adeninate octahedral cages (Figure 29a). Each cage consists of four adeninates which occupy alternating faces of the octahedron and eight Zn(II) tetrahedra, four at the corners of the equatorial plane of each cage and two at each apical position. The Zn(II) comprising the apexes constitute half of a Zn_4O cluster that links adjacent octahedral cages together. Pairs of Zn(II) within each Zn_4O cluster are bridged by two adeninates through the N3 and N9 positions. N1 and N7 of each adeninate coordinate to the Zn(II) in the equatorial plane. The zinc-adeninate columns are interconnected via multiple BPDC linkers. One carboxylate from each linker coordinates in a monodentate fashion to a Zn(II) in the Zn_4O cluster, while the other carboxylate binds in a monodentate fashion to one of the equatorial Zn(II) on an adjacent column. This connectivity pattern results in channels that run along the *c*- crystallographic direction (Figure 29d). The zinc-adeninate columns pack in parallel according to the **pcu** network topology.[85]

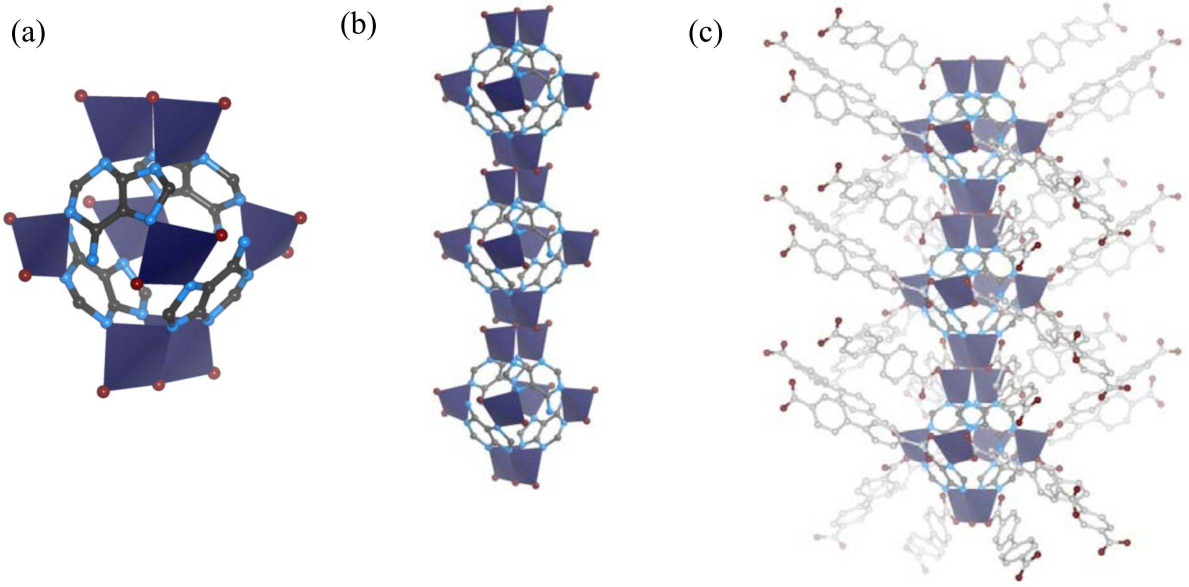

(d)

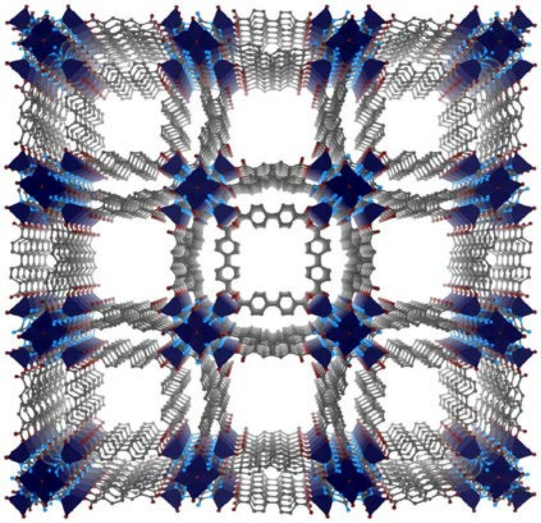

Figure 29. The crystal structure of bio-MOF-1. Zinc-adeninate columns (b) are composed of zinc-adeninate octahedral cages (a). They are linked together into a 3-D framework by biphenyldicarboxylate linkers (c) to generate a material with 1-D channels along the *c*-crystallographic direction (d) (Zn^{2+}, dark blue; C, dark grey; N, light blue; O, red; H omitted for clarity).

Overall, the framework structure is anionic, and dimethylammonium cations (the product of DMF decomposition) as well as DMF and water guests reside in the channels, as determined by EA and TGA. The TGA data reveal a weight loss of 26 % from room temperature to 125 °C, which can be attributed to the loss of solvent guest molecules (Figure 30). Thereafter, we observe a small weight loss (2.8 % at 180 °C) prior to decomposition, which corresponds to the loss of dimethylammonium cations.

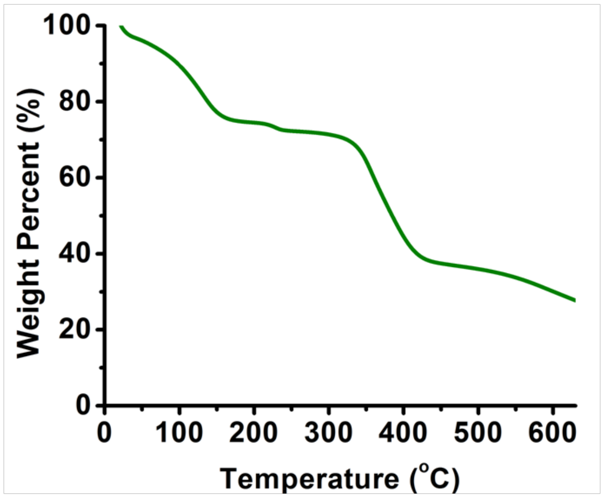

Figure 30. Thermogravimetric analysis for bio-MOF-1.

Solvent exchange experiments performed on the as-synthesized material reveal that the DMF and water guest molecules can be completely exchanged from the pores without loss of framework crystallinity. Indeed, bio-MOF-1 maintains its crystallinity after soaking for several weeks in various organic solvents, water, and, importantly, biological buffers such as phosphate-buffered saline (PBS buffer), as evidenced by powder X-ray diffraction (PXRD) experiments (Figure 31).

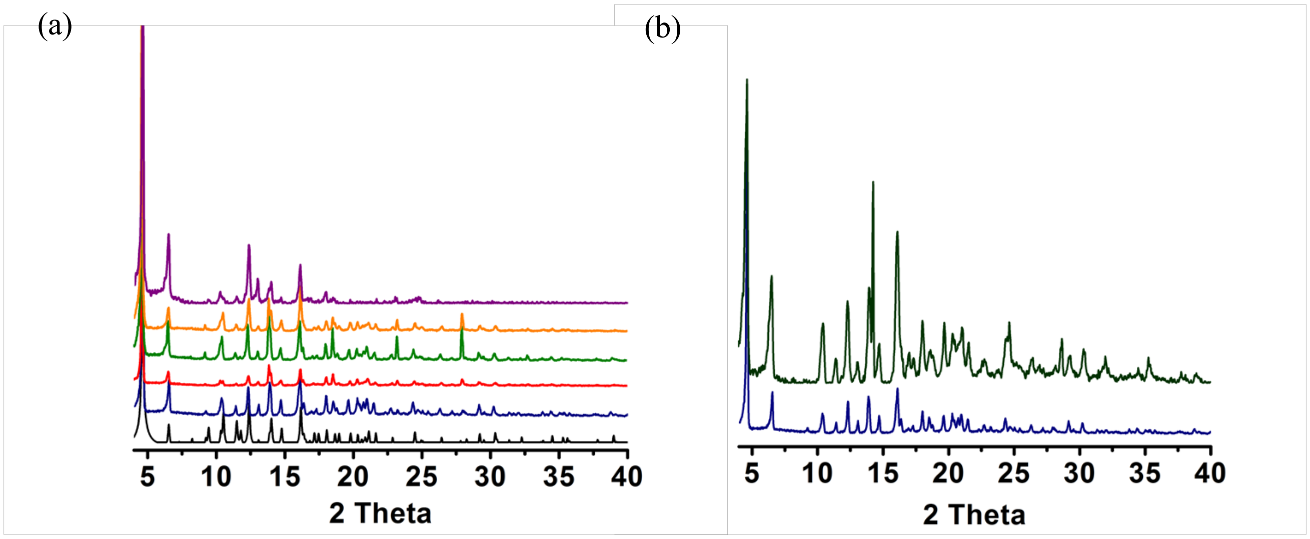

Figure 31. Powder X-ray diffraction patterns for bio-MOF-1. (a) As synthesized (navy), and solvent exchanged with chloroform(red), ethanol(green), acetonitrile (orange) and water (purple) (b) as synthesized (navy) and soaked in PBS buffer for 14 days (dark green).

TGA data for chloroform-exchanged samples revealed a region of thermal stability following the initial loss of solvent guest molecules. Collectively, these results prompted us to evaluate the permanent porosity of bio-MOF-1. Nitrogen adsorption studies yielded a type-I isotherm characteristic of a microporous material (Figure 32). The BET surface area is ~1700 m^2/g and the pore volume is 0.75 cm^3/g.

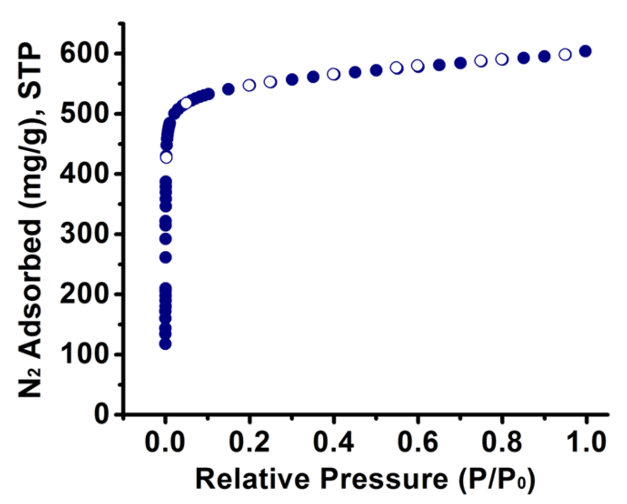

Figure 32. N_2 sorption isotherm for bio-MOF-1. ((●) adsorption; (○) desorption)

4.2 CATION EXCHANGE STUDY

Bio-MOF-1 is an anionic framework, and contains 2 dimethylammonium cations. These cation molecules are not part of the framework structure, and they reside within the pores outside of the framework. This means that the dimethylammonium cations can potentially be easily replaced with other cationic molecules via cation exchange. Cationic exchanged frameworks can be useful for various applications by exploiting the unique properties of the exchanged cationic molecules. For example, gas sorption capacities can be tuned depending on the interaction between cations and gas molecules. Therefore, the impact of the cations in the framework for gas sorption can be studied. In addition, cationic bio-MOFs can potentially be used for biomedical applications. Cationic drug molecules can be loaded into the framework readily via cation exchange, and the release profile of these drug molecules in biological buffers can be studied as the sodium or potassium ions in the buffers slowly replace the drug molecules within the framework via additional cation exchange processes. Luminescent MOFs can also be synthesized by introducing lanthanide cations into the framework via cation exchange and studying their photophysical properties can potentially lead to the use of these MOFs for biological imaging applications.

The cation exchange procedure is similar to the solvent exchange experiments. The crystals are soaked in a concentrated solution of cationic molecules until it is fully exchanged. The results of the cation exchange experiments are shown in Table 1. Complete cation exchange is confirmed by elemental analysis (EA), inductively coupled plasma (ICP), and energy dispersive X-ray spectroscopy (EDS). Initial studies were performed using colorful metal solutions such as Ni^{2+} and Co^{2+}. The color change of the material was observed within a few days, indicating a successful cation exchange (Figure 33).

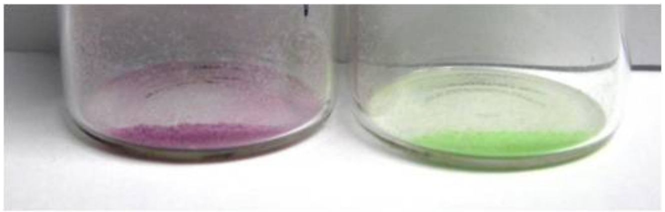

Figure 33. A photograph of bio-MOF-1 after cation exchange with Co^{2+} (pink) and Ni^{2+} (green).

Encouraged by the success of the cobalt and nickel cation exchange experiments, further systematic cation exchange studies were performed. A variety of metal ions have been used in the cation exchange experiments. Furthermore, organic cationic molecules also have been used and chosen depending on their size and functional groups (Figure 34). XRPD was used to confirm that bio-MOF-1 retains its crystalline integrity throughout the cation exchange process. Hence, any cations can be introduced into the framework via cation exchange as long as the cations are small enough to fit into the framework. Cation exchange, therefore, is an effective way to tune the functionality and the pore metrics of the material because new materials can be easily synthesized by adding any desired cations into one framework for desired property studies.

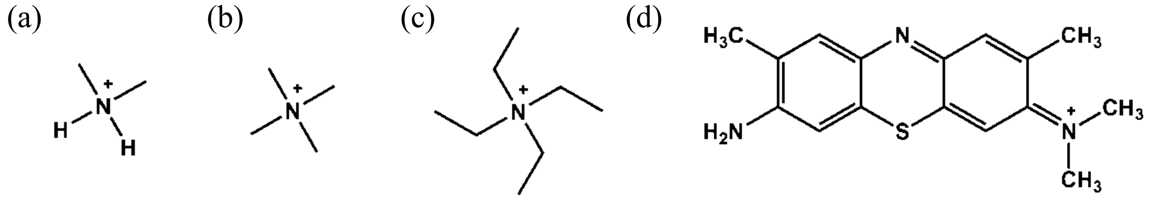

Figure 34. Cationic organic molecule examples (a) dimethylammonium (as-synthesized), (b) tetramethylammonium, (c) tetraethylammonium, and (d) toluidine blue O.

Table 1. List of formula of bio-MOF-1 after metal or organic cation exchange.

Cation	***Formula***
Li^+	$Zn_8 (BPDC)_6(Ad)_4O \bullet 2 (Li)^+$, 7 H_2O, 7 $CHCl_3$
Na^+	$Zn_8(BPDC)_6(Ad)_4O \bullet 2 (Na)^+$, 8 H_2O, 3 $CHCl_3$
Co^{2+}	$Zn_8 (BPDC)_6(Ad)_4O \bullet 1 (Co)^{2+}$, 13 H_2O, 4 $CHCl_3$
Ni^{2+}	$Zn_8 (BPDC)_6(Ad)_4O \bullet 1 (Ni)^{2+}$, 9 H_2O, 6 $CHCl_3$
TMA	$Zn_8 (BPDC)_6(Ad)_4O \bullet 2 (TMA)^+$, 3 H_2O, 9 $CHCl_3$
TEA	$Zn_8 (BPDC)_6(Ad)_4O \bullet 2 (TEA)^+$, 1 H_2O, 8 $CHCl_3$
TBO	$Zn_8 (BPDC)_6(Ad)_4O \bullet 2 (TBO)^+$, 3 H_2O, 9 $CHCl_3$

4.3 GAS ADSORPTION STUDIES

Developing new materials for CO_2 capture and separation is critically important. Metal-organic frameworks (MOFs) are emerging as promising materials for selectively adsorbing CO_2. In general, most research efforts in this area have focused on either 1) increasing the MOF pore volume and surface area to increase CO_2 capacity[48, 86] or 2) modifying the pore chemistry by incorporating functional moieties having high affinities for CO_2.[43-46, 49, 50, 87] Little experimental effort has focused on determining the optimal pore size for effectively condensing and adsorbing CO_2 at temperatures relevant to real-world application.

We have recently shown that metal-adeninate porous materials selectively adsorb large quantities of CO_2. We attribute their favorable CO_2 adsorption properties to both the presence of adeninate amino and pyrimidine Lewis-basic sites that decorate the pores and their relatively narrow pore dimensions. Given that these materials have exceptional capacities for CO_2 despite their relatively small and constricted pores, we decided to systematically evaluate the impact that pore volume has on a MOF's capacity for CO_2 adsorption.

In order to optimize a MOF for a particular application, it is important to be able to tailor its pore metrics and functionality in a straightforward fashion.[88] Post-synthetic MOF modification[89] has emerged as a facile means of introducing new functional moieties into MOF pores. In this section, we demonstrate that post-synthetic exchange of extra-framework cations within anionic bio-MOF-1 can be used as a means to systematically modify its pore dimensions and metrics. We effectively utilize this strategy to optimize its CO_2 adsorption properties.

bio-MOF-1 is anionic and dimethylammonium (DMA) cations reside in its pores. We have shown that the DMA cations are mobile and that they can be easily replaced with other organic cations. To tailor the pore dimensions and pore volume of bio-MOF-1, we selected a series of organic cations which are structurally and chemically similar to DMA but each different in size (Scheme 4). We expected that as the organic cation size increased, the pore volume and surface area of the cation-exchanged bio-MOF-1 would decrease. Accordingly, we introduced tetramethylammonium (TMA), tetraethylammonium (TEA), and tetrabutylammonium (TBA) via cation exchange into the pores in order to systematically decrease the pore volume and surface area of the material.

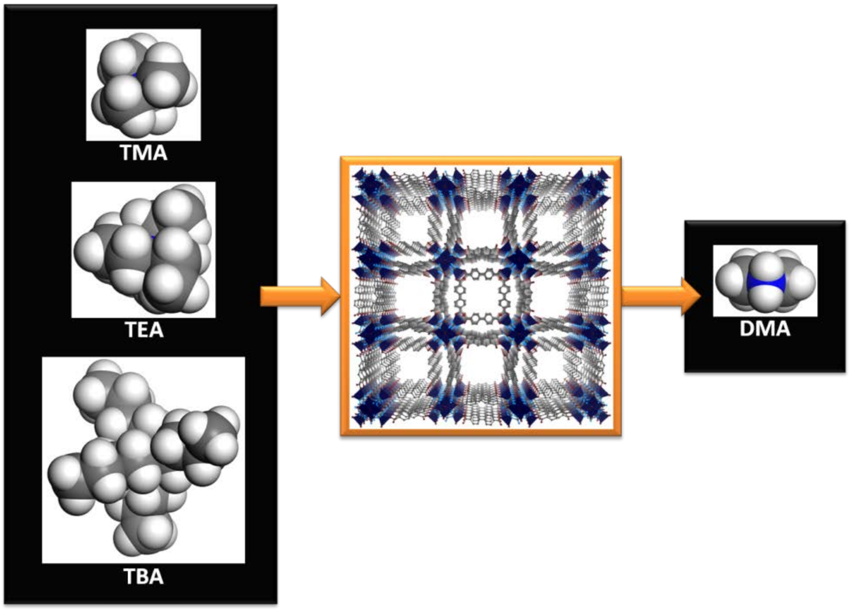

Scheme 4. DMA of bio-MOF-1 can be replaced with other organic cations (TMA, TEA and TBA) via cation exchange.

Cation-exchange was performed by soaking samples of as-synthesized bio-MOF-1 (**a**) in a DMF solution of either TMA, TEA, or TBA to generate TMA@bio-MOF-1 (**b**), TEA@bio-MOF-1 (**c**), and TBA@bio-MOF-1 (**d**), respectively. In each case, retention of bio-MOF-1 crystallinity was confirmed using powder X-Ray diffraction (Figure 35a) and complete exchange of the DMA cations to yield [$Zn_8(Ad)_4(BPDC)_6O\cdot 2$ cation] was determined using ^{1}H NMR and by correlating data from elemental and thermogravimetric analyses (Figure 35b and Supporting Information).

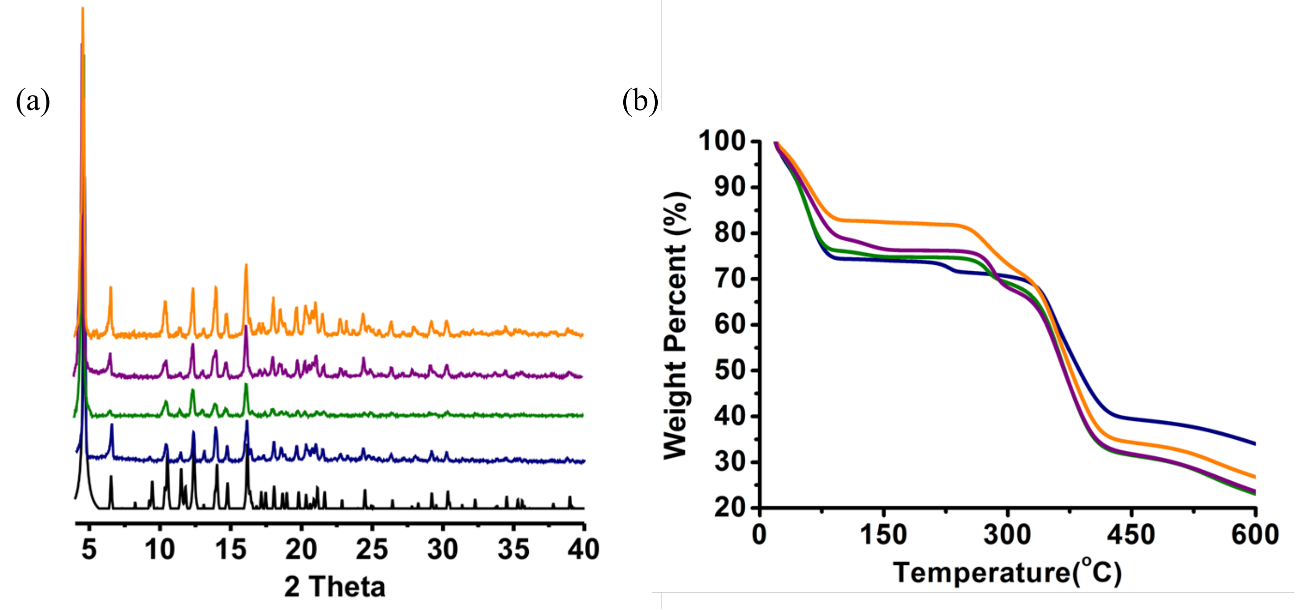

Figure 35. Powder X-ray diffraction patterns for a-d (a) and thermogravimetric analyses (b) for a-d. (a, navy; b, green; c, purple; d, orange).

To determine how the cation size impacts the pore volume and BET surface area, we collected N_2 adsorption isotherms for **a-d** (Figure 36). Each material was activated at 100 ºC under reduced pressure after soaking in chloroform for 24 h. The isotherms exhibited type-I behavior, were completely reversible, and showed no hysteresis upon desorption, which is consistent with permanent microporosity. Using this post-synthetic pore modification strategy, we were able to systematically decrease the pore volume and BET surface area from 0.75 cm^3/g and 1680 m^2/g for **a** to 0.37 cm^3/g and 830 m^2/g for **d** (Table 2).

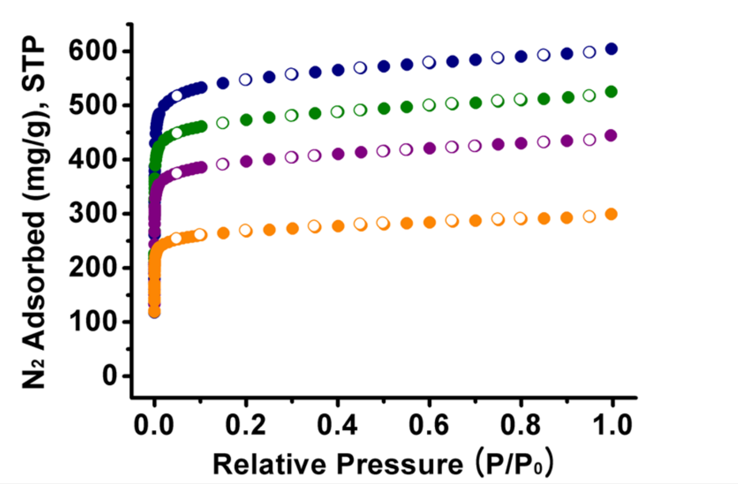

Figure 36. N_2 sorption isotherms for a-d. ((●) adsorption; (○) desorption; a, navy; b, green; c, purple; d, orange)

In order to determine how these pore modifications would impact the CO_2 capacity of bio-MOF-1, we first studied the CO_2 adsorption of **a-d** at 273 K (Figure 37a). Interestingly, the CO_2 capacity of **a-d** did not scale with pore volume and BET surface area.[90] **b** adsorbed the largest amount of CO_2 (4.5 mmol/g at 1 bar), followed by **c** (4.2 mmol/g at 1 bar). The as-synthesized material, **a**, which has the largest BET surface area and pore volume, and **d**, which has the smallest BET surface area and pore volume adsorbed 3.41 mmol/g and 3.44 mmol/g CO_2, respectively, at 1 bar. We also calculated the number of CO_2 molecules adsorbed per formula unit ($Zn_8(Ad)_4(BPDC)_6O{\cdot}2$ cation) for **a-d**. At 273 K, **b** and **c** adsorb 11.9 and 11.6 molecules of CO_2 per formula unit, respectively, while **a** and **d** adsorb 8.9 and 10.3 molecules of CO_2 per formula unit, respectively (Figure 37b; Table 2). From these data, we can conclude that pores with smaller volumes may be better suited for adsorbing CO_2, because **b-d** all adsorb more CO_2 per formula unit than **a**, even though they have smaller pore volumes.

We also collected CO_2 isotherms at higher temperatures (298 K, 303 K, 308 K, and 313 K; see Supporting Information) (Figure 37b; Table 2). In general, at these higher temperatures, the trend was similar to what was observed at 273 K. At all temperatures, **a** exhibited the lowest CO_2 capacity compared to **c-d**. **c** and **d** were comparatively more effective sorbents as the temperature increased. Specifically, we found that **c** had the largest CO_2 capacity at each of the elevated temperatures and **d** was nearly as effective as **b** at each of these temperatures. It is notable that **d** is a more effective CO_2 sorbent than **a** even though its pore volume and surface area are approximately half as large.

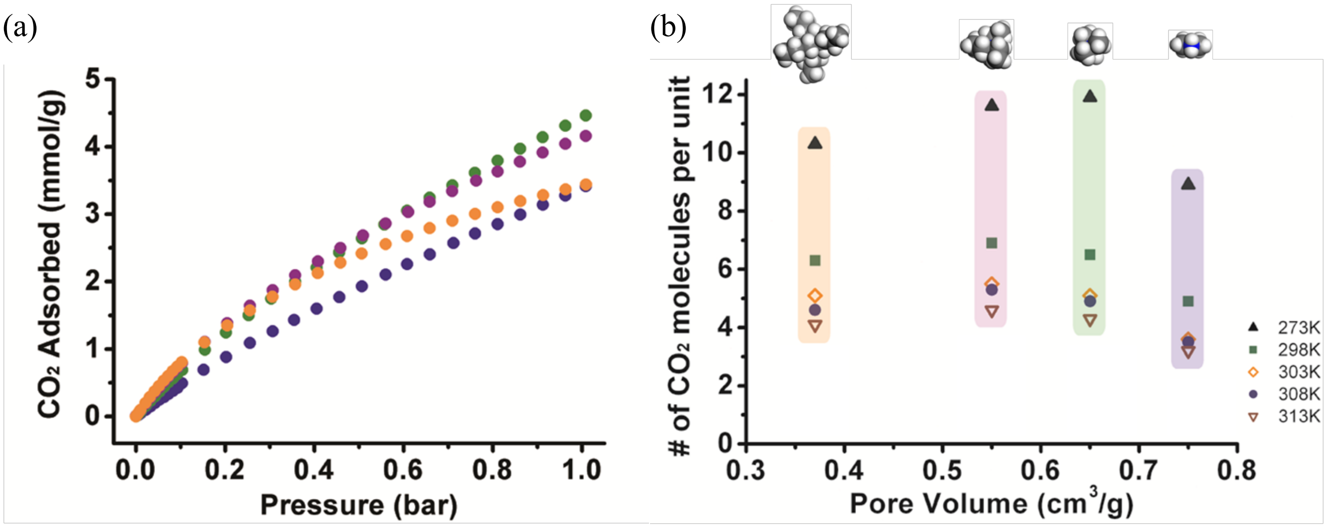

Figure 37. (a) CO_2 adsorption isotherms (273K) for a-d, (b) number of CO_2 molecules adsorbed per formula ($Zn_8(Ad)_4(BPDC)_6O\cdot2$ cation) versus pore volume of a-d at different adsorption temperatures (a, navy; b, green; c, purple; d, orange).

To better understand these observations, we calculated the isosteric heats of adsorption (Q_{st}) for **a-d** using the adsorption data collected at 298 K, 303 K, 308 K and 313 K (see

Supporting Information). The results of these experiments are consistent with the CO_2 uptake data. At zero loading, Q_{st} for **a-c** are each approximately 35 kJ/mol, while the initial Q_{st} for **d** is significantly larger, ~55 kJ/mol. Q_{st} for **a-d** then decrease to constant values at higher CO_2 pressures (**a**, ~22 kJ/mol; **b**, ~24 kJ/mol; **c**, ~26 kJ/mol; **d**, ~31 kJ/mol) (Table 2). While **d** has the largest Q_{st}, its smaller pore volume may ultimately limit its CO_2 capacity. These data suggest that smaller pores lead to stronger adsorbate/sorbent interactions.

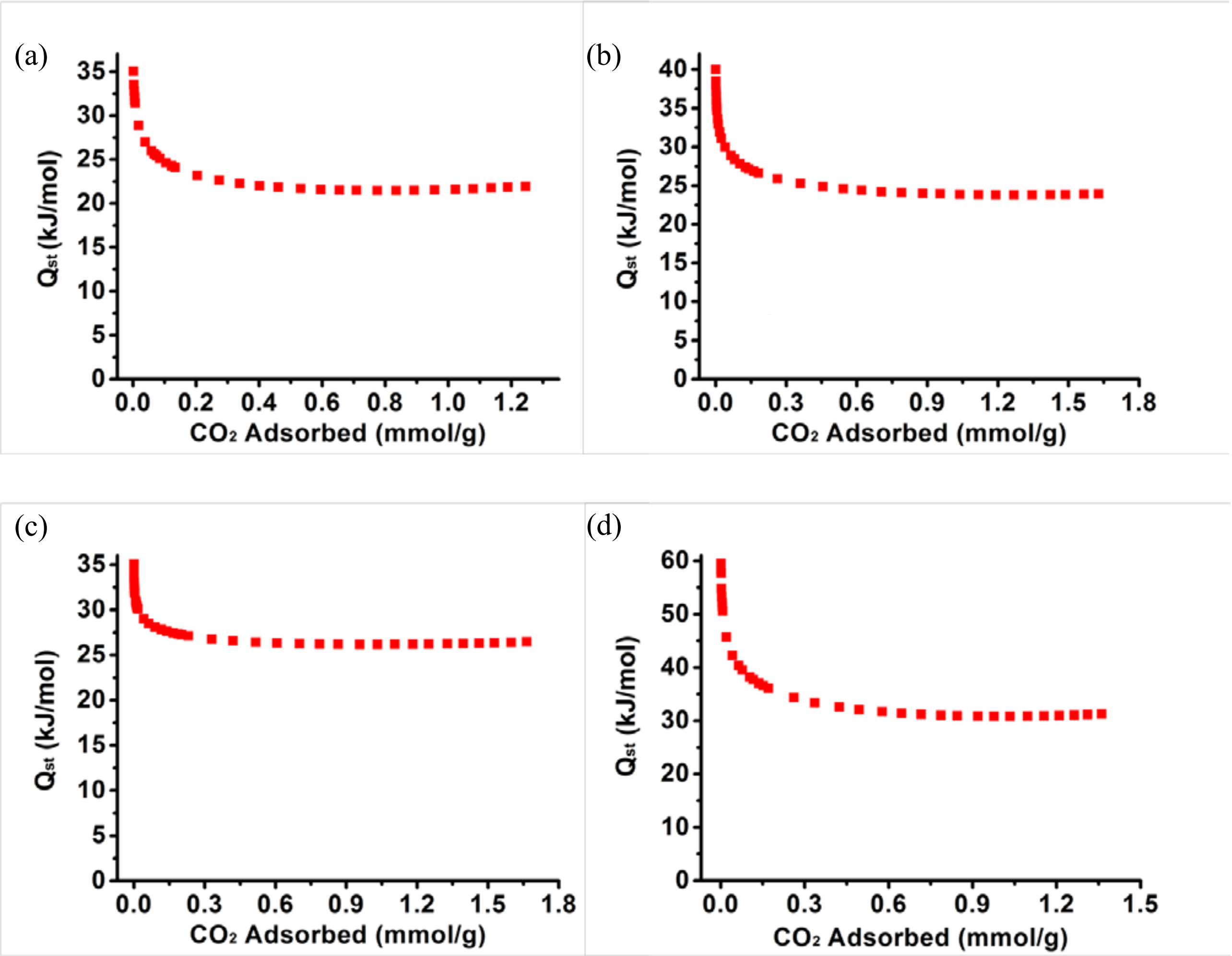

Figure 38. CO_2 Isosteric heats of adsorption (Q_{st}) for DMA (a), TMA (b), TEA (c), and TBA (d).

Table 2. N_2 and CO_2 adsorption data and Isosteric heat of adsorption data for a-d.

	BET SA[a]	V_p[b]	*CO_2 at 273K*[c]	*CO_2 at 298K*[c]	Q_{st}[d]
a	1680	0.75 (1951)	3.41 (8.91)	1.25 (3.25)	21.9
b	1460	0.65 (1732)	4.46 (11.9)	1.63 (4.34)	23.9
c	1220	0.55 (1528)	4.16 (11.6)	1.66 (4.62)	26.5
d	830	0.37 (1112)	3.44 (4.09)	1.36 (4.09)	31.2

([a] surface area, m^2/g, [b] pore volume, cm^3/g (cm^3/mol); [c] mmol/g (molecules CO_2/formula unit); [d] Isosteric heat of adsorption, kJ/mol at 1 bar)

In summary, we showed that the pore size of bio-MOF-1 can be modified post-synthetically via straightforward cation-exchange experiments and that such modifications can be used to systematically tune the CO_2 adsorption capacity of this material. In our data, although **d** has the largest Q_{st}, **b** or **c** showed the highest CO_2 uptake. This might because **b** or **c** has more room to accommodate more CO_2 than **d** with a considerably high Q_{st}. Therefore, we can conclude that in order to determine the optimal pore size for high CO_2 uptake at temperatures relevant to real-world application, both Q_{st} and capacity should be considered and determining the appropriate balance of these two factors is important.

5.0 BIO-MOF-1: EXPLORATION OF POTENTIAL BIOLOGICAL APPLICATIONS

Porous materials are attractive for drug delivery applications.[51, 91, 92] So far, most drug delivery approaches rely upon biocompatible dendrimers or polymer materials.[93-95] Recently, metal organic frameworks (MOFs) have been investigated and shown to have potential properties as materials for drug delivery.[20, 53, 54, 96] MOFs have many characteristics which make them attractive candidates for drug delivery: 1) MOFs have very rigid structures with high surface areas and pore volumes that can potentially accommodate large amounts of drug molecules; 2) MOFs can be rationally designed and synthesized by using different organic building blocks or biological molecules; and 3) MOF pore metrics and functionality can be tuned for specific purposes such as delivering different kinds of drugs, targeting specific substrates, and controlling drug release at desired rates. By making MOFs with biological building block molecules and nontoxic metal ions,[22, 27, 31, 97] the biocompatibility of the framework can potentially be improved and ultimately these materials could be used to deliver drug molecules to a specific target. One of the interesting aspects of the adeninate framework is that is assembled from biological molecules which represents a first step toward potential biocompatibility. Investigations into the drug storage and release capacity of metal-adeninate MOFs is important for determining whether such MOFs may be useful for drug delivery applications.

Luminescent MOFs have also been studied for biological applications.[13, 98-101] Luminescent lanthanide cations, in particular those emitting in the near-infrared (NIR) domain, have several emissive properties that are highly desirable for biomedical analysis.[102-104] However, their luminescent intensities are often limited in aqueous media. This is typically due to the low quantum yields and therefore the relatively low number of photons emitted by their molecular complexes. Furthermore, the stability in water and hence biocompatibility of lanthanide molecular complexes often limit their use in biological applications. For such applications, it is critical that these complexes do not dissociate at low concentration. This would result in the loss of lanthanide sensitization and/or the release of free lanthanide cations.

Metal-organic frameworks (MOFs) have several advantages that render them useful for sensitizing lanthanide cations.[98, 105, 106] First, MOFs have well-defined structures in which a large number of chromophoric sensitizers and lanthanide cations can be incorporated. This fundamental aspect of MOFs results in a large number of photons emitted per unit volume, an important advantage that enhances detection sensitivity.[107] Second, MOF structures can be tailored to modulate and optimize the photoluminescence properties of lanthanide cations. Third, MOFs provide a rigid scaffold that can serve to protect lanthanide cations from solvent quenching. To date, most lanthanide MOFs consist of a lanthanide cation and an organic linker/sensitizer, and therefore the lanthanide cation is an important structural component of the MOF. Ideally, one would be able to use a single MOF as a sensitizer for multiple different lanthanide cations. Anionic bio-MOF-1 is an ideal candidate MOF sensitizer, because various lanthanide cations can be incorporated into its pores via cation exchange. Further bio-MOF-1 is composed in part of biological constituents and it is relatively stable in biological media, aspects which make it ideal for biological applications.

5.1 DRUG RELEASE STUDY

The anionic nature of bio-MOF-1 pointed toward its potential utility as a material for the storage and release of cationic drug molecules. We reasoned that cationic drugs could be loaded into the pores via cation exchange with the dimethylammonium cations. Cations in biological fluids could then affect the controlled release of the cationic drug molecules from the pores. For our initial studies, we chose to study storage and release of procainamide HCl, an antiarrythmia drug. Procainamide HCl has a short half-life *in vivo* and must be dosed every 3-4 h. [108, 109] It is therefore an ideal candidate for controlled release administration, and several controlled release formulations are currently available. [110, 111] Procainamide HCl was introduced into the pores of bio-MOF-1 through a cation exchange process which does not affect the crystalline integrity of the material (Figure 39b). Complete loading (0.22 g/g material) was achieved after 15 days, as determined by elemental analysis, TGA, and gas adsorption studies (Figure 39 and Supporting Information).

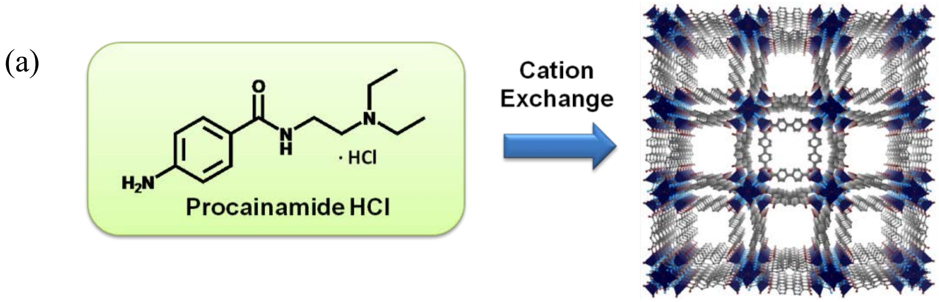

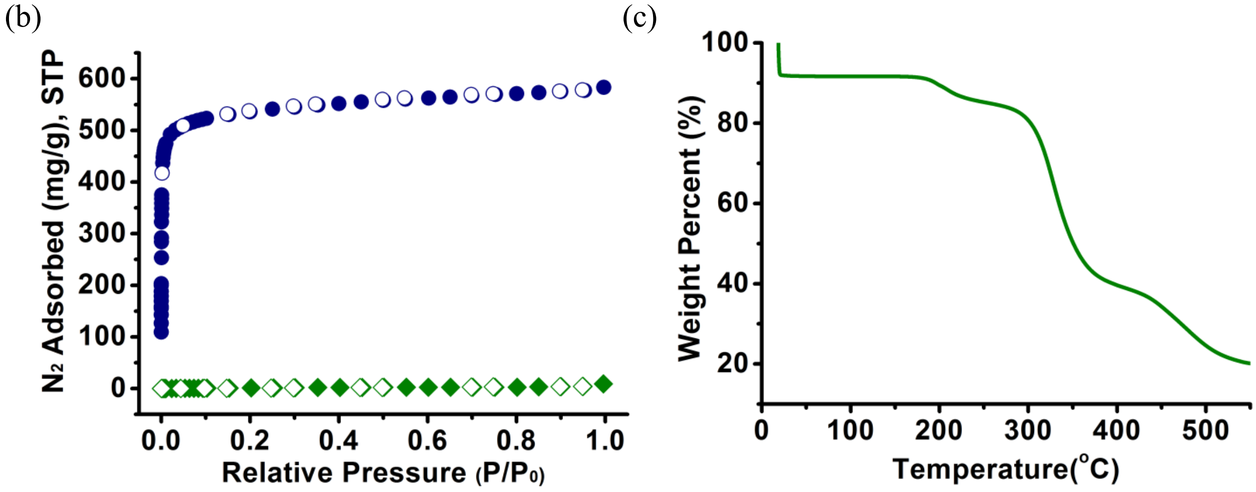

Figure 39. (a) A scheme of procainamide loading to bio-MOF-1 via cation exchange, (b) N_2 sorption isotherms for as synthesized (blue) and procainamide loaded (green), (filled, adsorption; empty, desorption) (c) thermogravimetric analysis for procainamide loaded bio-MOF-1.

The procainamide loaded material was formulated as $Zn_8(ad)_4(BPDC)_6O \cdot 3.5(\text{procainamide-H}^+)$, $1.5Cl^-$, $16.5H_2O$ (see Supporting Information). We estimated that ~2.5 procainamide molecules per formula unit reside in the pores, while the remaining procainamide molecules likely adhere to the exterior surfaces of the material. Because of the ionic interactions between procainamide and bio-MOF-1, cations can be used to trigger procainamide release from the framework (Scheme 5).

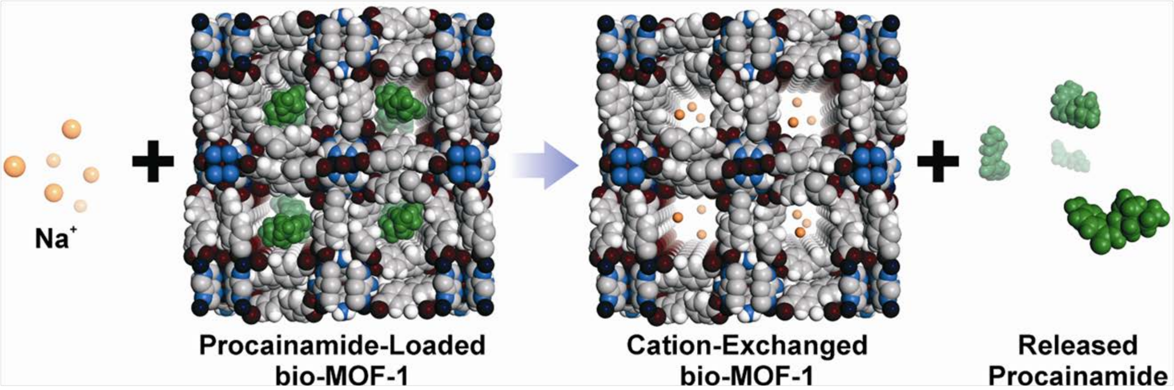

Scheme 5. A demonstration of caion-triggered procainamide release from bio-MOF-1 in PBS buffer.

To determine the release profile, we placed a sample of the procainamide-exchanged material in 0.1 M PBS buffer (pH = 7.4) and monitored the release of procainamide via HPLC. At each time point, aliquots of buffer were removed from the buffer/bio-MOF-1 suspension and replaced with fresh buffer. The aliquot was then analyzed for procainamide. Steady procainamide release was observed over the course of 20 h, and complete release was realized after 72 h (Figure 40a). The crystalline integrity of the framework is maintained throughout the release process, as evidenced by PXRD studies (Figure 40b). To verify that procainamide release was mediated by the buffer cations, we performed a control experiment in which drug-loaded bio-MOF-1 was placed in nanopure water (18.2 mΩ), and the solution was assayed for procainamide content in the same fashion as described above. In this case, only 20% of the procainamide was released, which likely corresponds to the molecules which are associated to the exterior surfaces of bio-MOF-1.

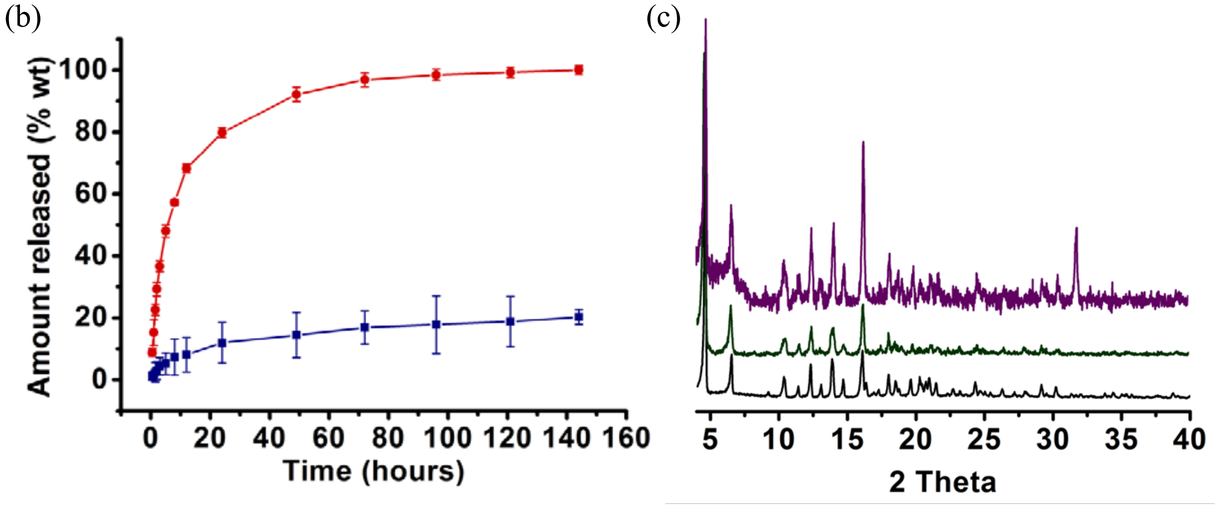

Figure 40. (a) Procainamide release profiles from bio-MOF-1 (red, PBS buffer; blue, deionized nanopure water), (b) Powder X-ray diffraction patterns for bio-MOf-1, as synthesized (black); procainamide loaded (green); after procainamide released for 5 days (purple).

In conclusion, we have shown that a permanently porous bio- MOF can be constructed using biomolecular building blocks. Further, we have exploited the anionic nature of this bio-MOF for the storage and release of an important cationic drug molecule. To our knowledge, this is the first example of cation-triggered drug release from a metal-organic framework and also the first demonstration of a potential biomedical application for an MOF constructed with biomolecule building blocks. We expect that construction and study of bio-MOFs will become increasingly important as more biomedical applications of MOFs are uncovered.

5.2 LUMINESCENCE STUDIES

In this section, we present a new versatile strategy for generating luminescent MOFs. Specifically, we show that a MOF can serve as both a host and an antenna for protecting and sensitizing extra-framework lanthanide cations encapsulated within the MOF pores. In this study, we use bio-MOF-1 [$Zn_8(ad)_4(BPDC)_6O\bullet 2Me_2NH_2$,8DMF,$11H_2O$], a rigid, permanently porous (BET Surface area; ~1700 m^2/g) structure as a scaffold for hosting and sensitizing several visible and NIR-emitting lanthanide cations. Bio-MOF-1 is anionic and dimethylammonium (DMA) cations reside in its 1-D pores. We have shown that the DMA cations can be exchanged with other organic cations or cationic drug molecules via straightforward cation exchange experiments. We therefore reasoned that we could replace the DMA cations with specific lanthanide cations in a similar fashion. Thus, we could load lanthanide cations into the pores of bio-MOF-1 and then study the luminescence properties of the resulting host-guest material (Scheme 6). Ideally, the MOF would serve as a 'lantern' for protecting the lanthanide cations and enhancing their luminescence.

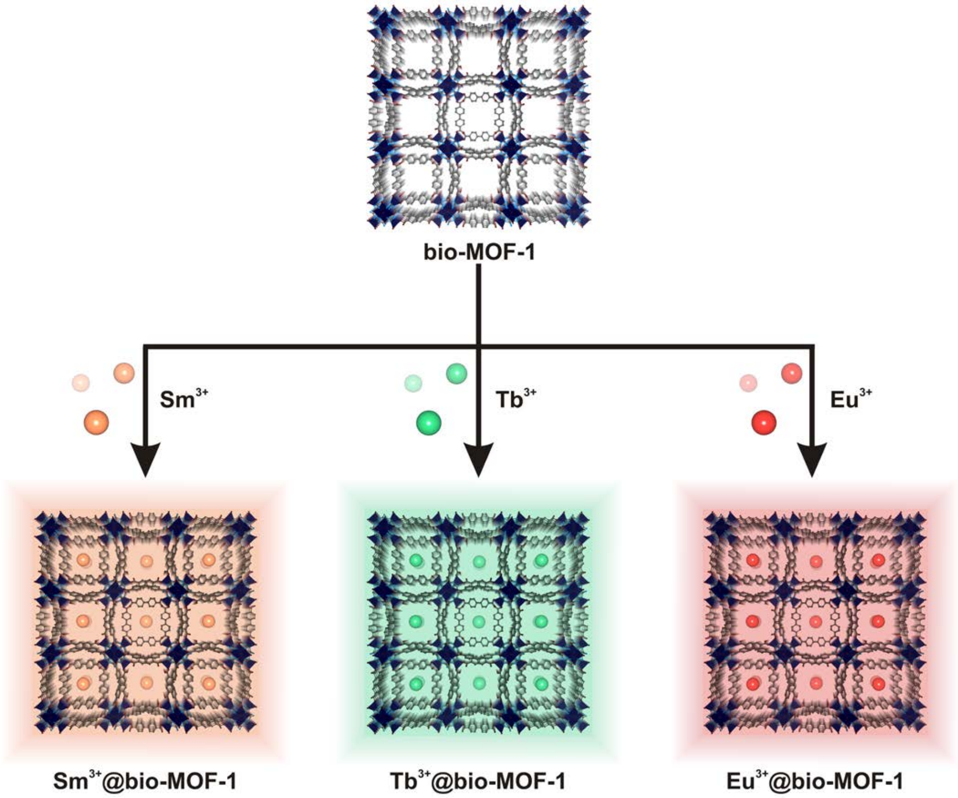

Scheme 6. Luminescent Sm@bio-MOF-1, Tb@bio-MOF-1 and Eu@bio-MOF-1 are synthesized via lanthanide cation exchange of bio-MOF-1.

To introduce lanthanide ions into the pores of bio-MOF-1, samples of the material were soaked in DMF solutions of nitrate salts of either Tb^{3+}, Sm^{3+}, Eu^{3+}, or Yb^{3+} (see Supporting Information). Examination of energy-dispersive X-Ray spectroscopy (EDS) and elemental analysis (EA) data of the Ln^{3+}-exchanged materials revealed, for each material, approximately one lanthanide cation per $[Zn_8(ad)_4(BPDC)_6O]_{1.5}$ units: Tb@bio-MOF-1= $[Zn_8(ad)_4(BPDC)_6O]_{1.5}$•$Tb^{3+}$; Sm@bio-MOF-1= $[Zn_8(ad)_4(BPDC)_6O]_{1.5}$•$Sm^{3+}$; Eu@bio-MOF-1= $[Zn_8(ad)_4(BPDC)_6O]_{1.5}$•$Eu^{3+}$; Yb@bio-MOF-1= $[Zn_8(ad)_4(BPDC)_6O]_{1.5}$•$Yb^{3+}$. The crystalline integrity of the Ln^{3+}-loaded samples of bio-MOF-1 was confirmed using PXRD (Figure 43). It still retained the permanent porosity after incorporating Ln^{3+} into the pore. (Figure 44a)

Prior to evaluating the lanthanide cation luminescence, we measured, in direct collaboration with Prof. Petoud's research group, the photophysical properties of bio-MOF-1 to determine the location of its donating energy levels and therefore the lanthanide cations it may be able to sensitize. The emission spectrum of bio-MOF-1 displays two fluorescence bands with an apparent maximum centered at 415 nm, as well as a less intense band centered around 340 nm. Each of the two fluorescence bands has a unique excitation spectrum, with apparent maxima located at 385 and 280 nm, respectively. To determine the origin of these bands, the absorbance spectra of the two MOF components, adenine and biphenyldicarboxylic acid (H_2-BPDC), were measured (see Supporting information). Adenine has two absorbance bands with maxima at 205 and 260 nm and H_2-BPDC displays an absorbance band centered at 285 nm. Since the H_2-BPDC band at 285 nm and the adenine band at 260 nm are overlapping, it is difficult to specifically assign the bio-MOF-1 excitation band at 280 nm to either component. Surprisingly, neither component exhibits a band at 385 nm, the principle excitation band of bio-MOF-1, which suggests that the MOF structure introduces new electronic states to the system.

Spectroscopic studies of Tb@bio-MOF-1, Sm@bio-MOF-1, Eu@bio-MOF-1 and Yb@bio-MOF-1 in DMF indicated that bio-MOF-1 sensitizes visible and near-infrared emitting lanthanide cations in an organic solvent (see Supporting Information). Encouraged by these results, we proceeded to study the luminescence properties of these materials in aqueous environments. Each Ln@bio-MOF-1 sample was soaked in nanopure (18 MΩ) water to completely remove the DMF solvent molecules, and PXRD of the water-exchanged samples confirmed retention of crystalline integrity (Figure 43). When excited with a standard laboratory

UV lamp (365 nm), the samarium, europium, and terbium samples emitted their distinctive colors (Eu^{3+}, red; Tb^{3+}, green; Sm^{3+}, orange-pink), which were readily observed with the naked eye (Figure 41). Excitation spectra recorded for Tb@bio-MOF-1, Sm@bio-MOF-1, Eu@bio-MOF-1 and Yb@bio-MOF-1 all demonstrate a main band with an apparent maximum located at 340 nm, an indication that energy migrates through the same electronic levels located in the MOF structure for all four compounds. The individual samples were then each irradiated with 340 nm light and the characteristically sharp emission bands corresponding to the respective encapsulated lanthanide cations were detected (Figure 42).

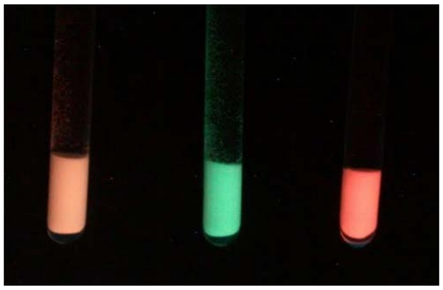

Figure 41. Photograph of Eu@bioMOF-1, Tb@bioMOF-1, and Sm@bioMOF-1 (from left to right) under H_2O, illuminated by an Entela Mineralight lamp (model UVGL-55) with 365 nm excitation (115 V, 0.16 amp); a 460 nm glass cut-on filter was placed in front of the camera lens to remove the UV light.

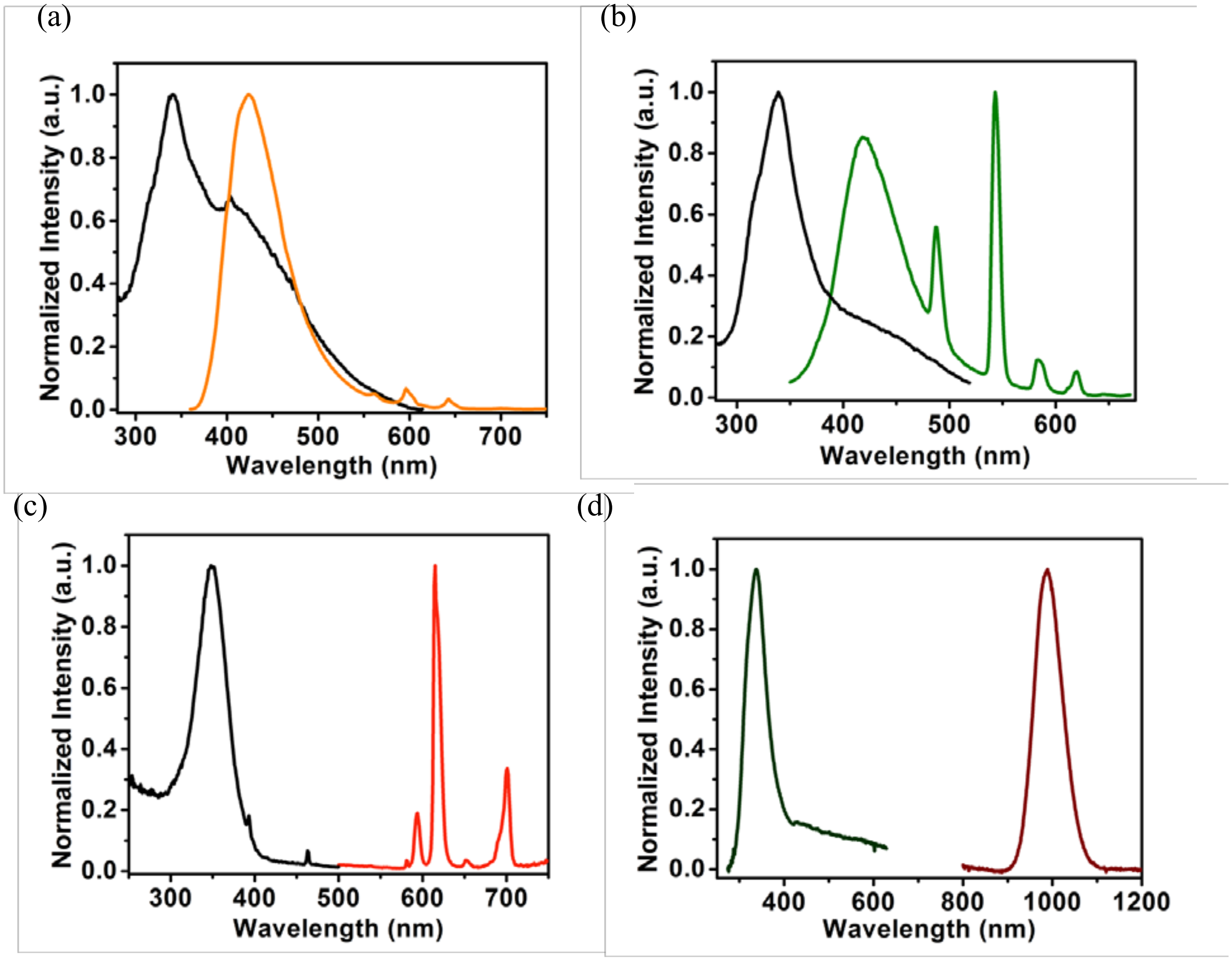

Figure 42. (a) Steady-state excitation, λ_{em}: 596 nm (black) and emission, λ_{ex}: 340 nm (orange) spectra for Sm@bio-MOF-1. (b) Steady-state excitation, λ_{em}: 545 nm, (black) and emission, λ_{ex}: 340 nm (green) spectra for Tb@bio-MOF-1. (c) Steady-state excitation spectrum, λ_{ex}: 615 nm (black) and emission λ_{ex}: 340 (red) specta for Eu@bio-MOF-1. (d) Excitation, λ_{em}: 980 nm spectrum (dark green) and emission, λ_{ex}: 340 nm (wine) for Yb@bio-MOF-1 in water.

Despite the strong ability of water to quench NIR emitting lanthanides, the Yb^{3+} signal is easily detected. These data demonstrate that the MOF scaffold, can effectively serve as an antenna for sensitizing three different visible-emitting lanthanide cations and a NIR-emitting lanthanide cation in an aqueous environment. Importantly, after all the measurements in water, the materials still retained their crystallinity as evidenced by their PXRD patterns (see Supporting Information). These results indicate that these luminescent materials are therefore fully compatible with aqueous conditions and are photo-stable. Our ability to easily detect lanthanide luminescence in the presence of water provided an indication that the MOF was able to not only sensitize but also provide sufficient protection to the lanthanide.

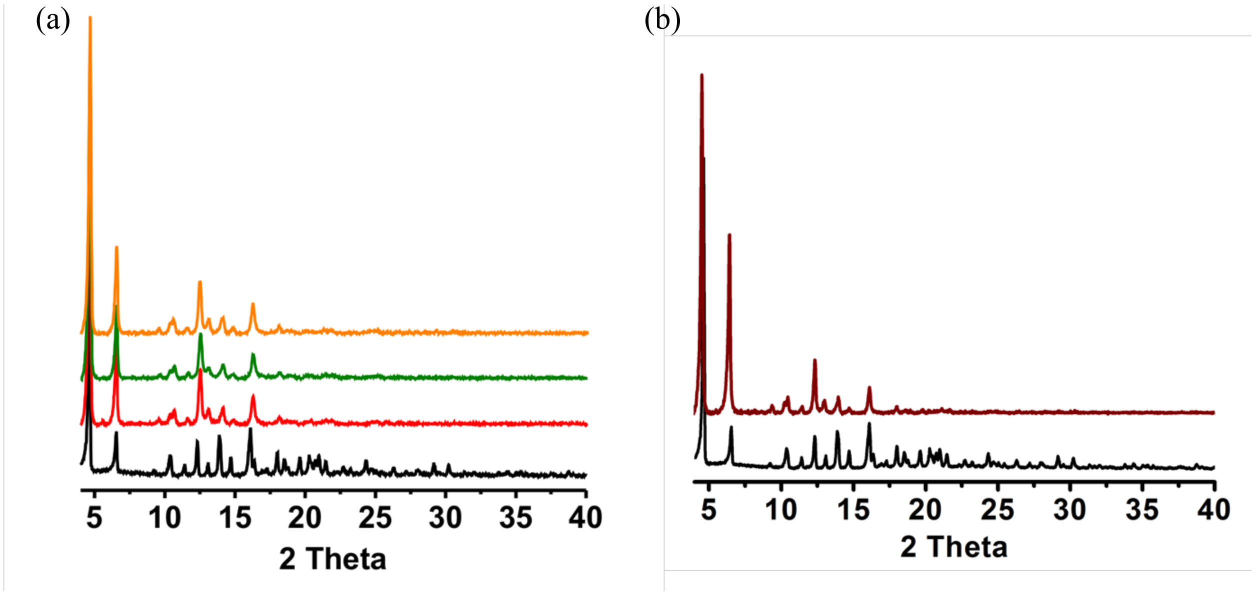

Figure 43. Powder X-ray diffraction patterns for Ln@bio-MOF-1 (black, as-synthesized; red, Eu@bio-MOF-1; green, Tb@bio-MOF-1; orange, Sm@bio-MOF-1; wine, Yb@bio-MOF-1).

To quantify the level of protection provided by bio-MOF-1 and to better understand the environment of the encapsulated lanthanide cations, lanthanide-centered luminescence quantum yields and lifetimes in water were explored directly by the Petoud lab (see Supporting Information). The quantum yields are all reasonably high considering the aqueous environment, providing an indication that the lanthanide cations are protected to a significant extent within the pores, and the energy transfer from the sensitizer embedded in the MOF to the lanthanide cations is efficient. Since bio-MOF-1 encapsulates a large number of lanthanide cations within a defined space, the luminescence intensity of Ln@bio-MOF-1 is quite high. The luminescence lifetimes of the lanthanide cations in Ln@bio-MOF-1 were measured in water, as well as deuterated water, to gain information on the environment of the lanthanide cations in the MOFs and their levels of protection. The q values (the calculated number of water molecules coordinating to each lanthanide cation) were obtained. There were two different lifetimes for Ln@bio-MOF-1 samples, suggesting the presence of two distinct lanthanide environments within the MOF architecture. The q-values calculated from the luminescence lifetime data confirm that some water molecules bind to the lanthanide cations in the MOF pores, and it is also consistent with TGA data, which reveals two different types of water loss in the graph. (see Supporting Information). From both the quantum yields and lifetimes, coworkers in Petoud lab found that bio-MOF-1 did indeed provide protection from water to the encapsulated lanthanide cations.

Effectively, bio-MOF-1 serves as a high surface area scaffold for sensitizing lanthanide cations and arranging and exposing them in 3-D space. We therefore reasoned that Ln@bio-MOF-1 materials could potentially serve as sensors for small molecules. To evaluate this possibility, we, in collaboration with the Petoud lab, performed preliminary O_2 detection experiments using Yb@bio-MOF-1 in solid-state conditions. Samples of Yb@bio-MOF-1 were dried for 15 hours at 200 ^{o}C and mounted on quartz slides in a gas chamber housed within a fluorimeter. Yb@bio-MOF-1 responds to the presence of O_2 gas, as evidenced by monitoring the Yb^{3+} luminescence signal upon excitation with 340 nm light. An approximate 40% signal decrease was observed within the first five minutes of introducing O_2 gas to a purged chamber under ambient pressure. After five minutes, the system had reached equilibrium and the signal maintained its intensity for the duration of the experiment, approximately one hour. Although purging the chamber once more with N_2 gas restored the Yb^{3+} signal to its original intensity, we noted a much longer period of time required to reach equilibrium. Qualitatively reproducible results were observed through collecting saturated signals cycled between flowing N_2 and O_2 (Figure 44).

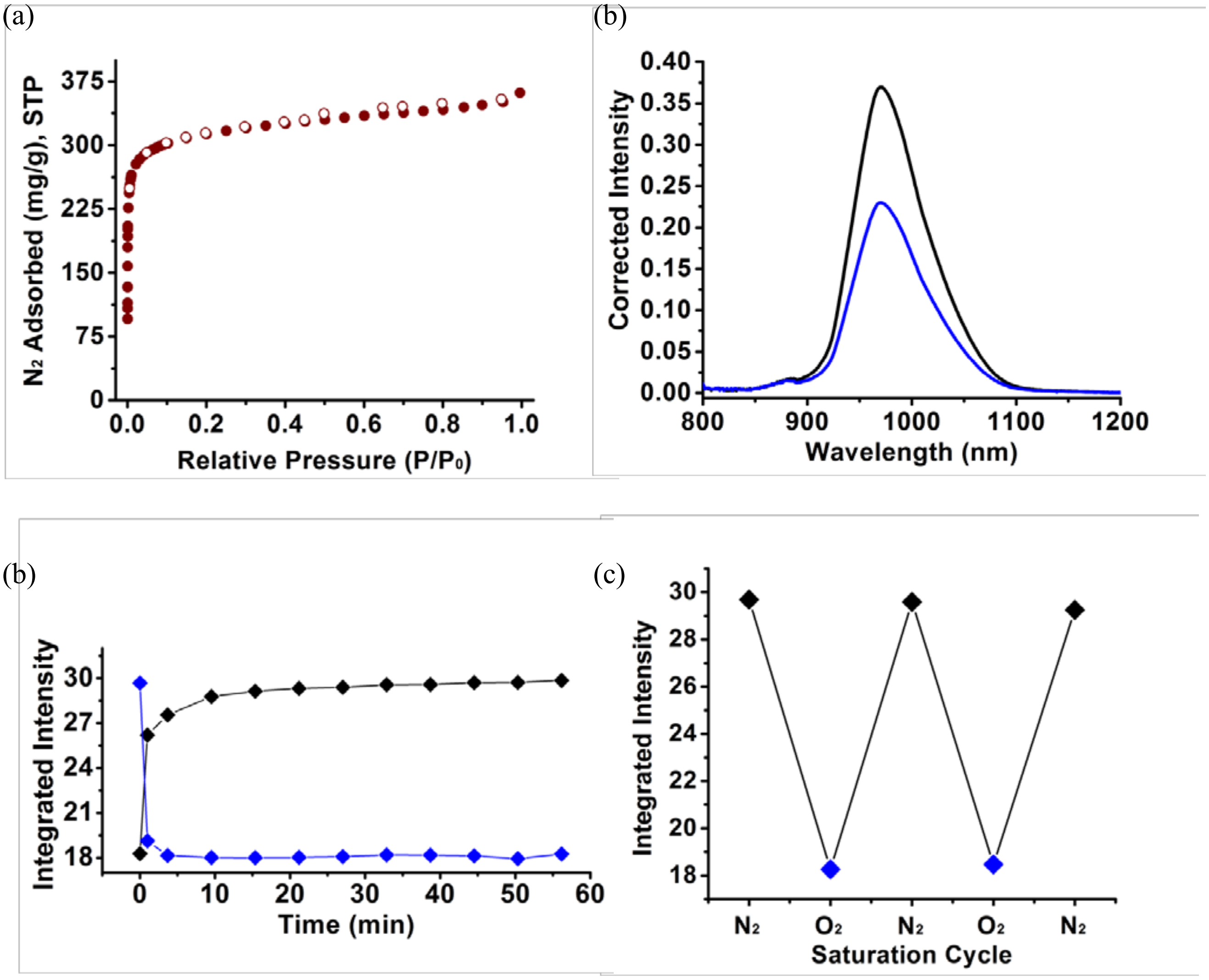

Figure 44. (a) N_2 sorption isotherm for Yb@bio-MOF-1, (b) Characteristic Yb^{3+} emission band observed upon saturation with O_2 (blue) or N_2 (black) (c), time versus integrated intensity plot, demonstrating the level of reversibility and rapid equilibration of Yb@bio-MOF-1 upon exposure to O_2 (blue) and N_2 (black). (d), integrated intensity of the Yb^{3+} emission band cycled between O_2 (blue) and N_2 (black) saturation.

In conclusion, we have shown that porous anionic bio-MOF-1 can incorporate lanthanide cations via a simple cation exchange process and sensitize multiple lanthanide cations, thus allowing for the facile preparation of multiple different luminescent materials. Further, we showed that bio-MOF-1 protects and sensitizes visible and NIR-emitting lanthanides in water. These results are particularly exciting as water is a highly quenching solvent, and materials which protect lanthanides from water are necessary for enabling the use of NIR-emitting lanthanides in biological environments. Finally, we have demonstrated that Ln@bio-MOF-1 materials can potentially be used as versatile high surface area sensors for small molecules, including dioxygen. We believe this versatile strategy for generating new luminescent lanthanide materials will be useful for preparing new sensors and reporters for biological systems.

6.0 METAL-ADENINATE CLUSTERS FOR THE PREPARATION OF MESOPOROUS BIO-MOFS

MOFs have been particularly attractive to researchers due to their high surface areas and pore volumes. Potential applications exploiting their porosity have been investigated such as catalysis, gas storage, and drug storage/delivery. Design and synthesis of porous metal-organic frameworks (MOFs) with increasingly large pores has been extremely difficult due to the possibility of interpenetration/catenation challenges inherent in solving a structure with large cell dimensions. Nevertheless, the effort to build MOFs with higher surface area or pore volume is still important. Typically, incorporating longer and expanded ligands into the synthesis in order to build materials with larger pores has been a popular method in MOF chemistry.[6, 8, 10, 112] Recently, strategies utilizing bigger molecular secondary building units (SBUs) to build MOFs with larger pores have also been developed.[7, 113-115]

Constructing well-structured porous MOFs from biological molecules has been a challenge because of the limited size, length and flexibility of biological molecules as ligands. Sometimes incorporating a secondary ligand such as a carboxylic acid is necessary to promote the construction of frameworks with accessible pores.[116-118] Despite these efforts, few microporous MOF synthesized from biomolecules has been reported. Furthermore, no mesoporous MOFs constructed from biomolecules have been reported. We have shown that adenine can be a good potential ligand for constructing crystalline porous materials because it is a rigid biomolecule and it has versatile metal-adeninate binding modes. In this chapter, we illustrate a strategy of to prepare a mesoporous bio-MOF using discrete zinc-adeninate cages secondary building units (SBUs). We also describe the structure and the interesting adsorption properties of the material.

6.1 STRUCTURE AND CARACTERIZATION

Previously, we have described a synthesis and structure of microporous bio-MOF-1 constructed from columns of fused zinc-adeninate cages. These columns are connected by biphenyldicarboxylate linkers to yield a 3-D structure. Bio-MOF-1 exhibits 1-D channels and a BET surface area of ~1700 m^2/g. We reasoned that since zinc-adeninate cages serve as a SBU and they are relatively bigger than simple metal-oxide cluster SBUs, exploitation of the zinc-adeninate cages (SBUs) in synthesis would potentially lead to materials with large pores. With this strategy in mind, we were able to synthesize a mesoporous bio-MOF using the same zinc-adeninate cages as SBUs and biphenyldicarboxylic acids as auxiliary ligands which are used in synthesis of microporous bio-MOF-1. We prepared a single crystalline material formulated as $Zn_8(ad)_4(BPDC)_6,O_2$• $4Me_2NH_2$, 49DMF, $31H_2O$ (bio-MOF-100) via a solvothermal reaction between adenine (ad), zinc acetate dehydrate, and biphenyldicarboxylic acid (BPDC) in *N*,*N’*-dimethylformamide (DMF). We note that these reaction conditions are similar to those used for bio-MOF-1, which helps account for the formation of the zinc-adeninate octahedral cage as an SBU.

Single crystal X-ray studies, in collaboration with Prof. Joanne Yeh, reveal that the structure of mesoporous bio-MOF is composed of discrete zinc-adeninate octahedral cages. In this case, each octahedral cage is connected to other octahedral cages by three biphenyldicarboxylates which coordinate to the Zn^{2+} on each open face of the octahedral cage. It generates a diamond-like building unit, where each zinc-adeninate octahedral cage effectively serves as a tetrahedral four-connected SBU (Figure 45). By virtue of the length of the dicarboxylate linker and the size of the zinc-adeninate cage unit, the resulting framework exhibits large mesoporous cavities. The structure contains 3-D pores and the pore diameter is ~2.6 nm which is in the range of mesoporous materials. The zinc-adeninate cage in bio-MOF-1 has oxo groups which are shared by neighboring zinc-adeninate cages to form columns. Interestingly, the oxo group of the zinc-adeninate cage in mesoporous bio-MOF is not shared by any other components.

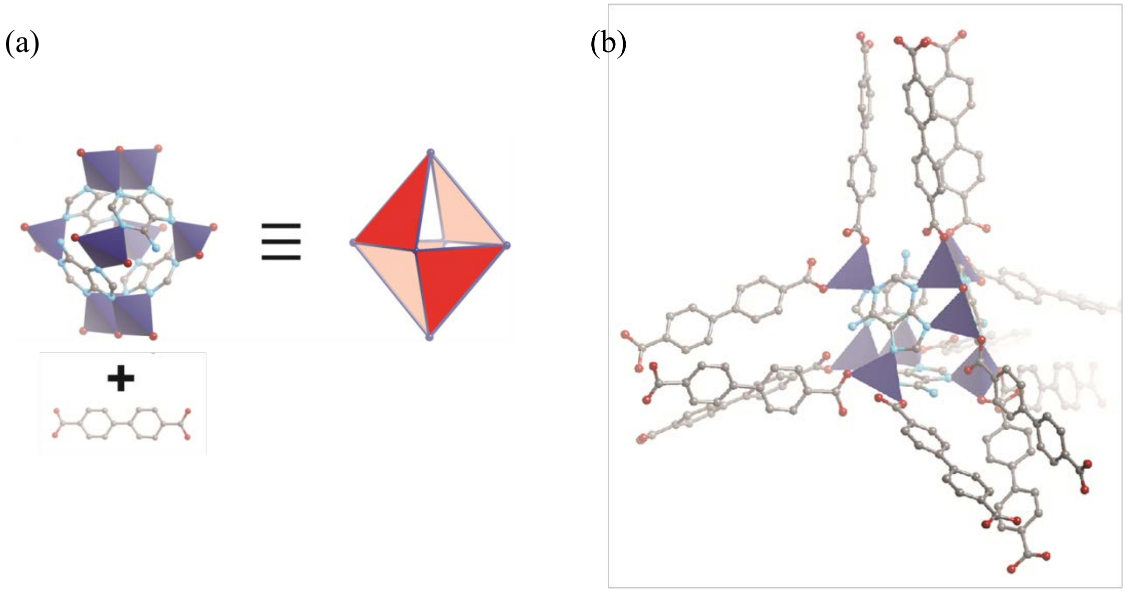

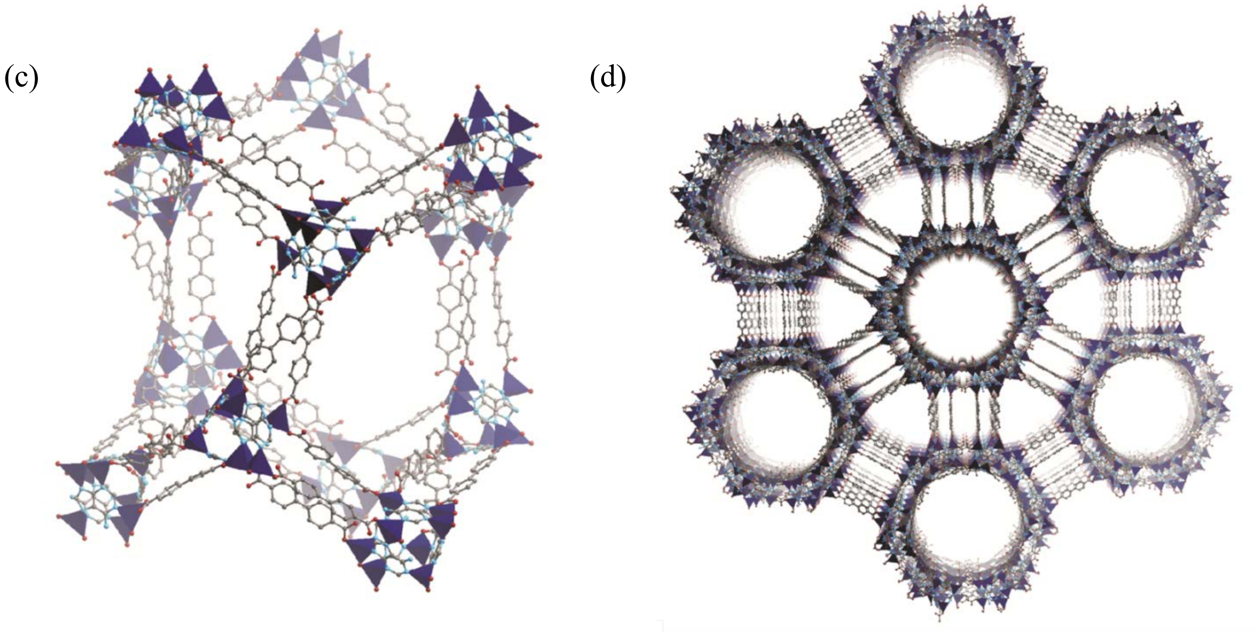

Figure 45. View of crystal structure of bio-MOF-100 (a) zinc-adeninate octahedral cage (SBUs) was represented as octahedral building block. (red) each open side of the cage (red triangle) links with three biphenyldicarboxylic acids to forms a terahedra unit (b) which extends to a diamond unit (c), the diamond units further packed into a 3-D structure (d). (Zn^{2+}, dark blue; C, dark grey; N, light blue; O, red; H omitted for clarity).

The framework is anionic, and dimethylammonium cations (the product of DMF decomposition) as well as DMF and water guests reside in the channels, as determined by elemental analysis (EA) and thermogravimetric analysis (TGA). The TGA data reveal a weight loss of ~60 (56-68) % from room temperature to 200 °C, which can be attributed to the loss of solvent guest molecules (200 °C; 55-67%). This large weight loss from the removal of the guest molecules indicates large cavities within the framework. The powder X-ray diffraction pattern of the as-synthesized material confirms the phase purity of the material. The stability of the material in various solvents could not be confirmed by PXRD. PXRD patterns of the solvent exchanged samples could not be collected because the structure loses periodic order quickly as soon as the guest molecules evaporate.

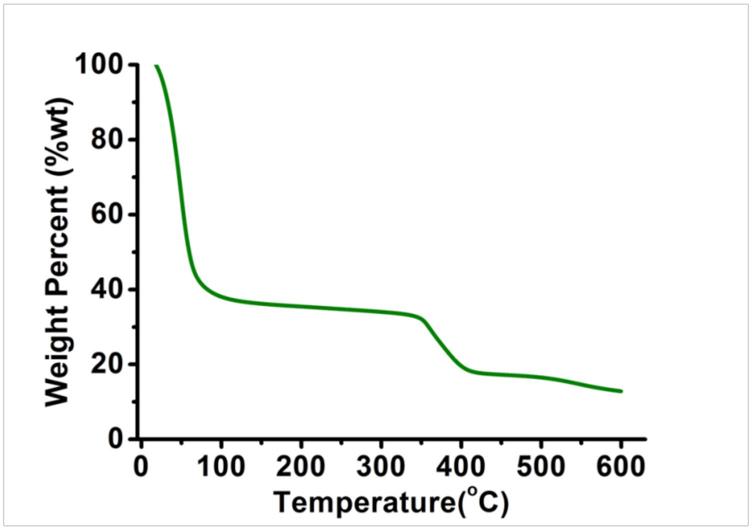

Figure 46. Thermogravimetric analysis for bio-MOF-100.

6.2 GAS ADSORPTION STUDY

An N_2 adsorption experiment at 77K was conducted to evaluate the permanent porosity of bio-MOF-100. Initially, an N_2 isotherm was collected using a conventional activation method ($CHCl_3$ exchange followed by solvent evaporation). However, this experiment resulted in a BET surface area of ~20 m^2/g (Figure 47a). It is known that the structure of porous materials with large mesopores can collapse easily or rearrange upon removal of guest molecules. We therefore decided to use an alternative activation strategy which has proven useful for mesoporous materials: supercritical CO_2 activation.[119, 120] The material was mainly evacuated by supercritical CO_2 drying process in collaboration with Prof. Joe Hupp's research group, followed by further evacuation at rt under reduced pressure for 24 h to remove residual ethanol. (see Supporting

Information) Surprisingly, the N_2 adsorption experiment resulted in a type-IV isotherm characteristic of a mesoporous material. The BET surface area was estimated as ~3440 m^2/g and the pore volume was calculated to be ~4.2 cm^3/g, the largest known for any MOF material (Figure 47b). PXRD confirmed the material's integrity after multiple cycles of sorption studies (Figure 48).

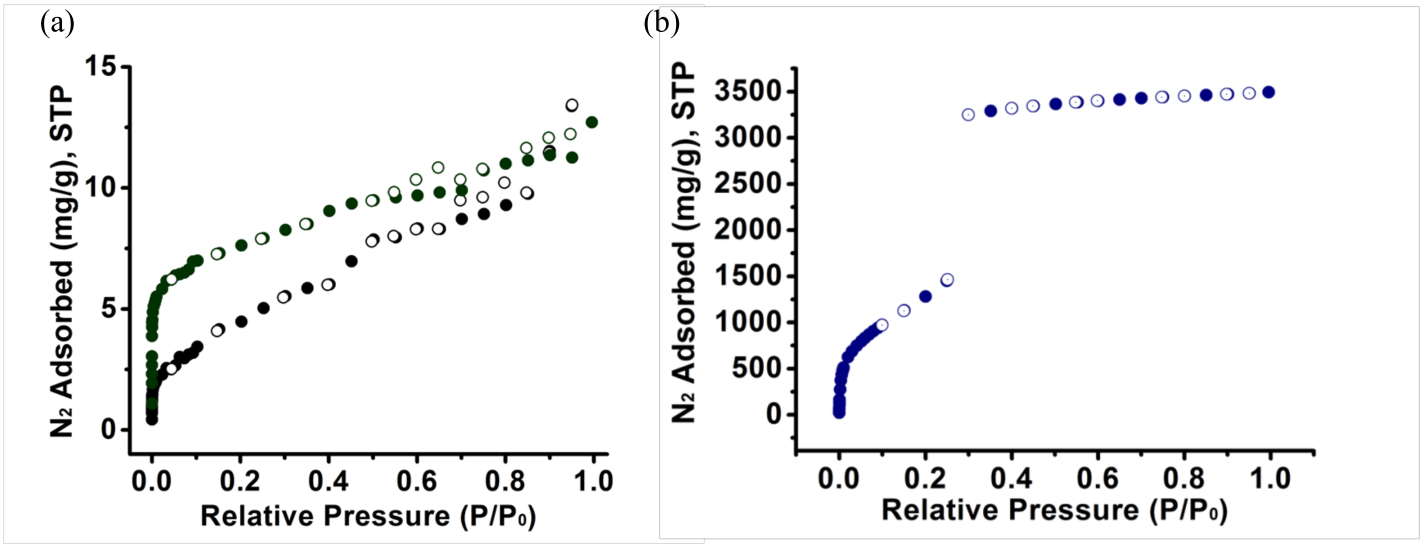

Figure 47. N_2 sorption isotherm for bio-MOF-100 with (a) conventional activation at room temperature (green) and at 100 °C (black), (b) supercritical CO_2 activation (navy) ((●) adsorption; (○) desorption).

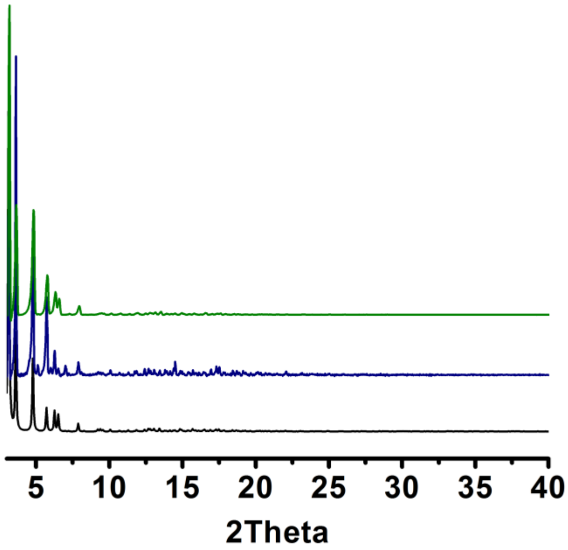

Figure 48. Powder X-ray diffraction patterns for bio-MOF-100. (blue, as synthesized; green, after sorption studies)

We also performed CO_2 and H_2 adsorption experiments. 44.8 cc/g of CO_2 was adsorbed at 273 K (1 bar) and ~1.1 wt % of H_2 was adsorbed at 77 K (1 bar) (Figure 49). Considering the total pore volume of this material, the amount of the H_2 and CO_2 adsorbed is small; however, this is not an unusual phenomenon for mesoporous materials.[121]

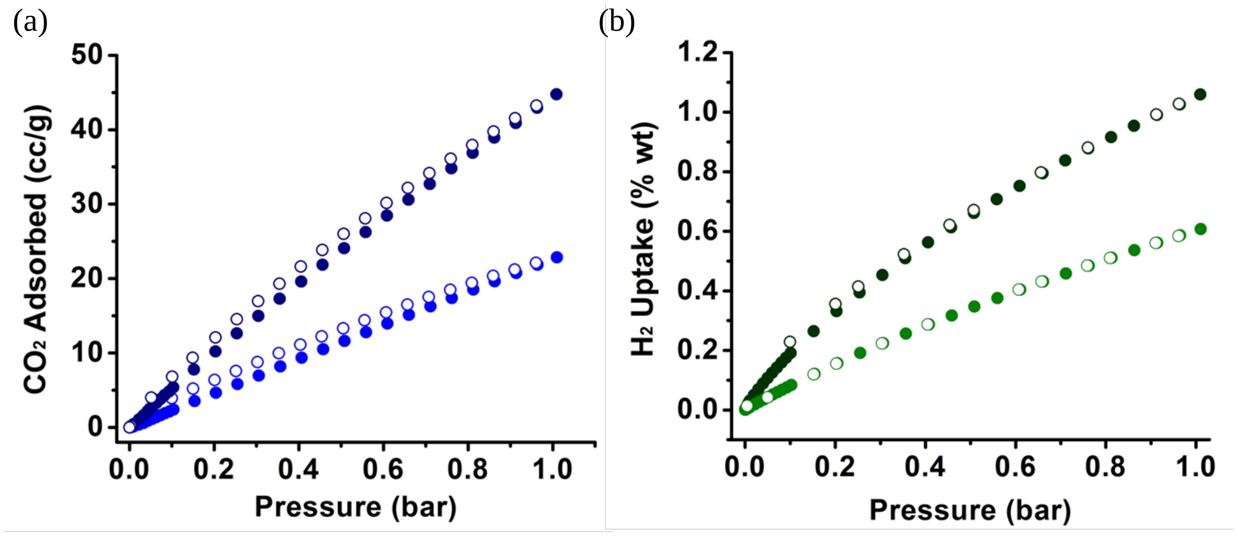

Figure 49. (a) CO_2 sorption isotherms at 273 K (navy), 298 K (blue), (b) H_2 sorption isotherms at 77 K (dark green), 87 K (light green) for MOF-100. ((●) adsorption; (○) desorption)

In conclusion, a unique zinc-adeninate mesoporous bio-MOF was synthesized. We described a strategy for preparing mesoporous bio-MOFs by using discrete zinc-adeninate octahedral cage as SBUs. Using the discrete zinc-adeninate octahedral cage as an SBU allows for building not only microporous MOFs but also mesoporous MOFs. The new mesoporous material shows a high surface area and extraordinary large pore volume for a mesoporous material. We expect that the utility of the large porosity of this material will open new avenues for potential applications.

7.0 CONCLUSION

This research is aimed at designing and synthesizing porous biomolecule-based materials for environmental and biological applications, such as gas storage/separation, or drug delivery. As a first step in this direction, we developed methods to control the coordination chemistry between adenine and metal ions with the aim of producing porous metal-adeninate frameworks. As a result, the several interesting frameworks that have been synthesized have shown that adenine is a versatile biomolecular ligand for the construction of crystalline supramolecular and extended porous solid-state materials.

Zn/Adenine hexamers/polymers were synthesized based on metal-adeninate Mode 1, exhibiting an interesting relationship between synthetic methods and structures. In particular, a discrete zinc-adeninate hexameric macrocycle assembled into a 3-D structure and selectively adsorbed CO_2 and H_2 over N_2. Its CO_2 adsorption properties were modulated by tuning the pore aperture size.

Metal-adeninate materials can be permanently porous and can store various gas molecules. Bio-MOF-11, based metal-adeninate Mode 2, exhibited remarkable high CO_2 uptake. Bio-MOF-1 exhibited interesting physical properties and structure. It was synthesized based on metal-adeninate coordination Mode 3, and it was a permanently porous and anionic framework. The pore functionality and pore metrics of anionic-MOFs can be easily tuned via cation exchange, and anionic-MOFs can be used as materials for drug storage and release study and the sensitization of lanthanides**.** For example, various gas sorption studies, controlled drug release studies, and lanthanide sensitization studies were enabled utilizing cation exchange. Finally, a mesoporous bio-MOF was synthesized using the octahedral zinc-adeninate SBUs revealing a new strategy for preparing mesoporous MOFs. The material had high surface areas and extraordinarily large pore volumes. It is expected that research that exploits the porosity of this material will be lead to a variety of potential applications.

APPENDIX: SUPPORTING INFORMATION

Experimental Section

General Procedures and experimental protocols.

Unless otherwise mentioned, all chemicals were purchased from Aldrich Chemical Co. Pyridine and N, N'-dimethylformamide (DMF) were purchased from Fisher Scientific. All purchased starting materials were used without further purification. The elemental microanalyses were performed by Galbraith Laboratories. INC. using the PerkinElmer 240 Elemental Analyzer and by the University of Illinois, Department of Chemistry Microanalytical Laboratory using an Exeter Analytical CE440. Thermogravimetric analysis (TGA) was performed using TGA Q500 thermal analysis system. All TGA experiments were performed under a N_2 atmosphere from 25-600 °C at a rate of 0.1 °C /min. Data were analyzed using TA Universal Analysis software package. Fourier transform infrared (FT-IR) spectra were measured using a Nicolet Avatar 360 FTIR E.S.D. and KBr pellet samples. Absorptions are described as follows: very strong (vs), strong(s), medium (m), weak (w), shoulder (sh), and broad (br). Data were analyzed using Omnic Software package. X-ray powder diffraction patterns were taken using a Phillips X'pert diffractometer at 40 kV, 30 mA for Cu Kα, (λ = 1.5406 Å) with scan speed of 0.50 sec/step and a step size of 0.02°. The data were analyzed for d-spacing measurements using X'pert Software program from the Phillips Powder Analysis Software package. The simulated powder patterns were calculated using Mercury 2.0. The purity and homogeneity of the bulk products were determined by comparison of the simulated and experimental X-ray powder diffraction patterns. Nanopure water (18.5 mΩ) was produced using a water purification system from Barnstead Nanopure. Proton nuclear magnetic resonance spectra (^{1}H NMR) were obtained using Bruker Avance 300 MHz spectrometers. Chemical shifts are in parts per million using the residual solvent peak as the reference value. The values used for proton spectra, respectively, are 2.5 ppm for d-DMSO.

Single X-ray Diffraction Studies

Crystals were mounted on a Bruker SMART APEX CCD diffractometer equipped with a normal focus Mo–target X–ray tube (λ = 0.71073 Å) operated at 2000 W power (45 kV, 35 mA). Unless otherwise noted, the X–ray intensities were measured at 173 K; the detector was placed at a distance of 5.002 cm from the crystal. Frames were collected with a scan width of 0.3° in ω and phi with an exposure time of 30 s/frame. The frames were integrated with the SAINT software package with a narrow frame algorithm. The structure was solved by direct methods and the subsequent difference Fourier syntheses and refined with the SHELXTL (version 6.14) software package.

Chapter 2

Synthesis of Zn(Ad)(Py)(NO_3)·3.8DMF

54 mg of adenine (0.4 mmol) and 238 mg of zinc nitrate hexahydrate (0.8 mmol) were added to a 20 mL vial. 10 mL of N,N'-dimethylformamide (DMF) and 2.5 mL of pyridine was added to the vial. The vial was sealed with the cap, and heated at 100 °C for 24 hours. After cooling to room temperature, crystals started to grow (about after 3 hours). Crystals were pale yellow, rod shape. They were washed with DMF (3 mL X 3) and dried under Ar gas. (yield: 0.0928 g; 37.5 % based on adenine) ***Elemental analysis*** $C_{21.4}H_{35.6}N_{10.8}O_{6.8}Zn$ = Zn(adeninate)(pyridine)(NO_3) · 3.8 DMF : Calcd. C, 41.57; H, 5.8; N, 10.8. Found C, 41.68; H, 4.29; N, 24.6. ***FT-IR*** **:** (KBr 4000-400 cm^{-1}) : 3338.39(br), 3193.21(br), 2930.69(w), 2859.81(w), 1659.17(s), 1603.03(s), 1469.36(m), 1409.55(m), 1384.32(s), 1296.92(m), 1153.96(m), 1098.43(w), 796.59(w), 743.57(w)

Thermogravimetric analysis

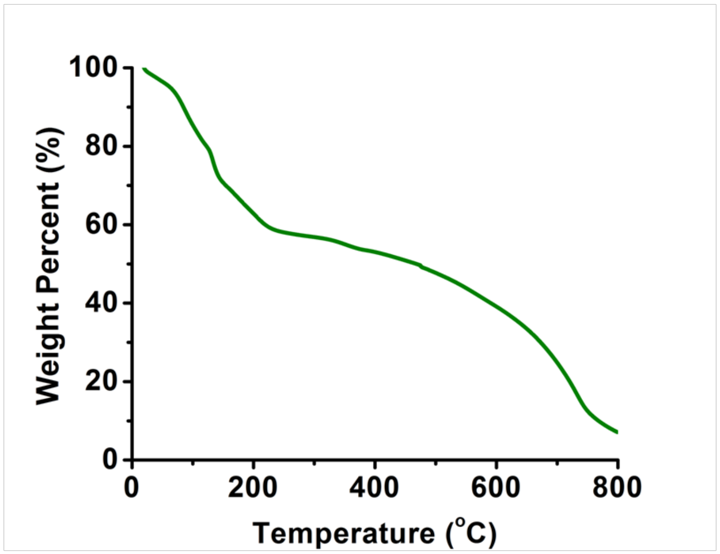

Figure S1. Thermogravimetric analysis for Zn(Ad)(Py)(NO_3)·3.8DMF

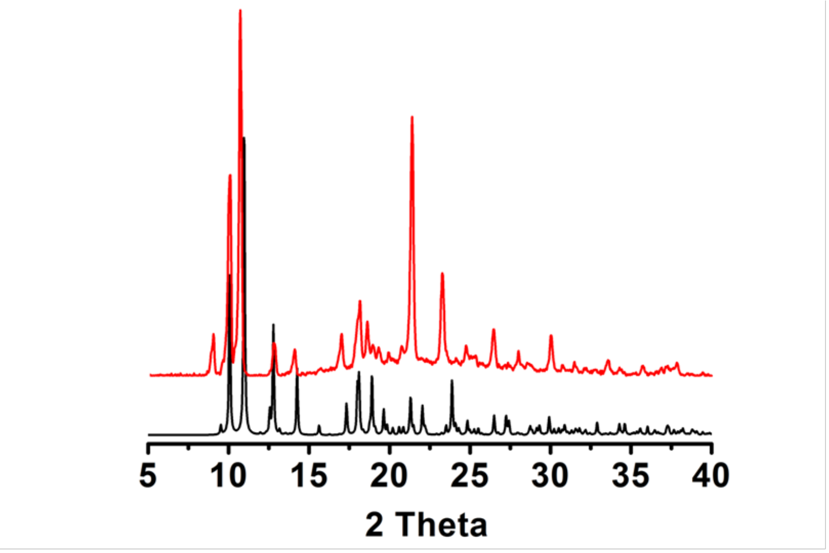

Figure S2. Powder X-ray diffraction pattern for Zn(Ad)(Py)(NO_3)·3.8DMF (black, simulated; red, as synthesized)

Synthesis of Zn(Ad)(bipyridine)(trifluoroacetate) · 5DMF, 0.75H_2O

A stock solution of adenine (0.05 M) in DMF was prepared. Ultra-sonification and heating was employed to completely dissolve adenine in DMF. A stock solution of zinc trifluoroacetate hexahydrate (0.05 M) and 1,2-bis(4-pyridyl)ethane (0.25 M) in DMF was prepared. Adenine stock solution (0.5 mL, 0.025 mmol), zinc trifluoroacetate hexahydrate stock solution (0.5 mL, 0.025 mmol) and 1,2-bis(4-pyridyl)ethane stock solution (0.25 mL, 0.0625 mmol) were added to a glass tube (0.8 cm diameter). The tube was frozen in liquid nitrogen and evacuated to 200 mTorr. The tube was then sealed, heated at 100 °C (24 h), and then cooled to rt. The resultant colorless crystals were washed with DMF (3 mL x 3) and dried under Ar gas (15 min) (yield: 0.00927 g; 43.7 % based on adenine) ***Elemental analysis*** $C_{32}H_{48.5}N_{812}O_{7.75}Zn$ = Zn(adeninate)(bipyridine)(CF_3CO_2) · 5 DMF, 0.75H_2O : Calcd. C, 36.21; H, 4.82; N, 18.93. Found C, 36.19; H, 3.13; N, 18.71. ***FT-IR*** **:** (KBr 4000-400 cm^{-1}) : 3392.37(br), 3332.92(s), 3134.22(br), 1705.75(s), 1673.15(vs), 1597.40(s), 1560.36(w), 1472.36(w), 1417.93(m), 1399.77(m), 1197.76(s), 1140.92(s), 725.13(w) cm^{-1}

Thermogravimetric analysis

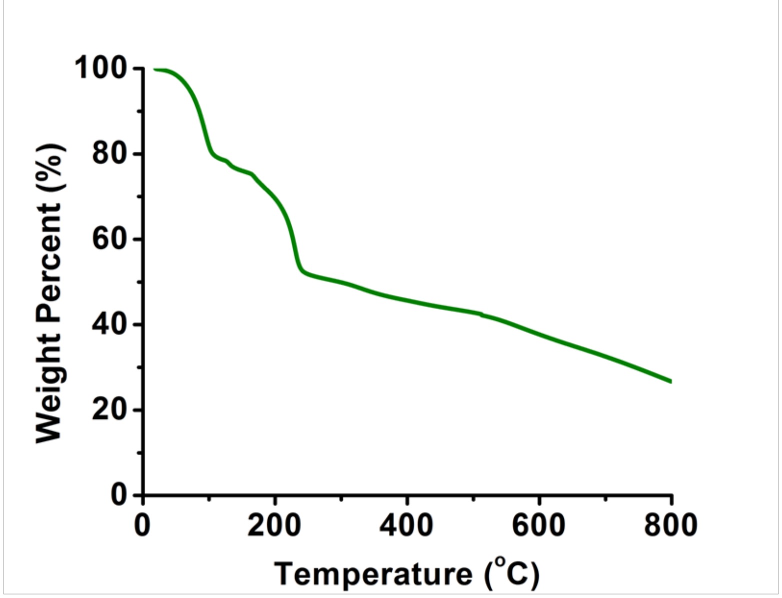

Figure S3. Thermogravimetric analysis for Zn(Ad)(bipyridine)(trifluoroacetate)·5DMF, 0.75H_2O

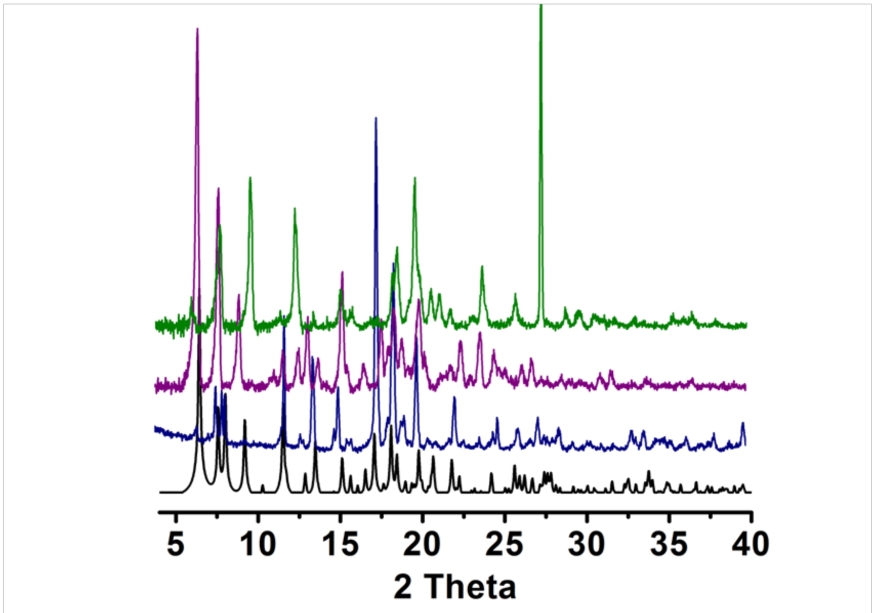

Figure S4. Powder X-ray diffraction patterns for Zn(Ad)(bipyridine)(trifluoroacetate)·5DMF, 0.75H_2O. (black, simulated; navy, as synthesized; purple, after soaking in toluene; green, after soaking in pyridine)

Synthesis of $Zn_6(Ad)_6(Py)_6(CH_3CO_2)_6 \cdot 9DMF$

A stock solution of adenine (0.05 M) in N,N-dimethylformamide (DMF) was prepared. Ultra-sonification and heating were carried out in order to dissolve the adenine completely in DMF. A stock solution of Zinc acetate dihydrate (0.05 M) in DMF was prepared. 2.5 mL of the adenine solution, 5 mL of the zinc nitrate solution and 2.5 mL of pyridine were added to a 20 mL vial. The vial was capped and remained at room temperature. After 8 hours, the colorless crystal were produced, washed with DMF (3 mL x 3) and dried under Ar gas (15 min) (yield: 0.039 g, 70 % based on adenine) ***Elemental analysis*** $C_{99}H_{135}N_{45}O_{21}Zn_6$ = $Zn_6(adeninate)_6(pyridine)_6(CH_3CO_2)_6 \cdot 9DMF$: Calcd. C, 44.31; H, 5.07; N, 23.49. Found C, 44.50; H, 4.98; N, 23.62. ***FT-IR*** **:** (KBr 4000-400 cm-1): 3324.99(br), 3184.27(br), 2926.97(w), 1662.44(s), 1600.80(s), 1470.30(m), 1395.40(s), 1326.02(m), 1219.67(s), 1149.59(m), 1046.02(w), 801.65(m), 744.20(w)

Thermogravimetric analysis

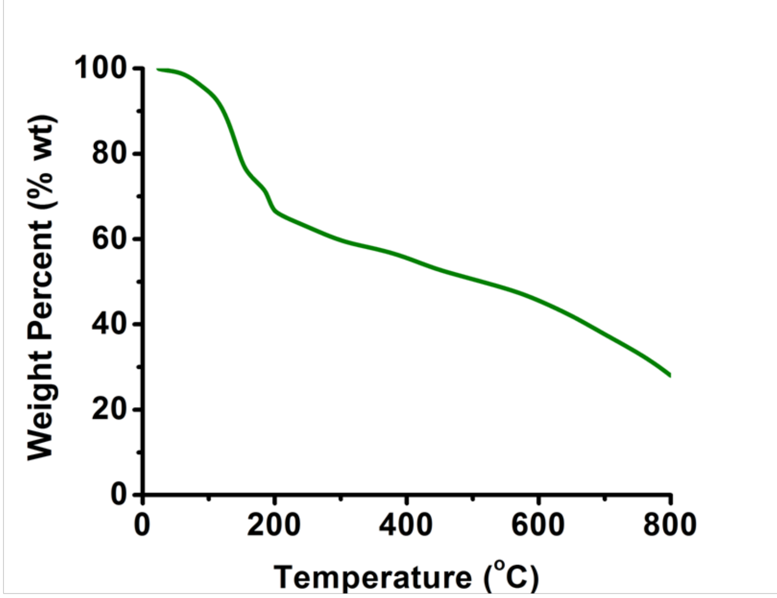

Figure S5. Thermogravimetric analysis for $Zn_6(Ad)_6(Py)_6(CH_3CO_2)_6 \cdot 9DMF$

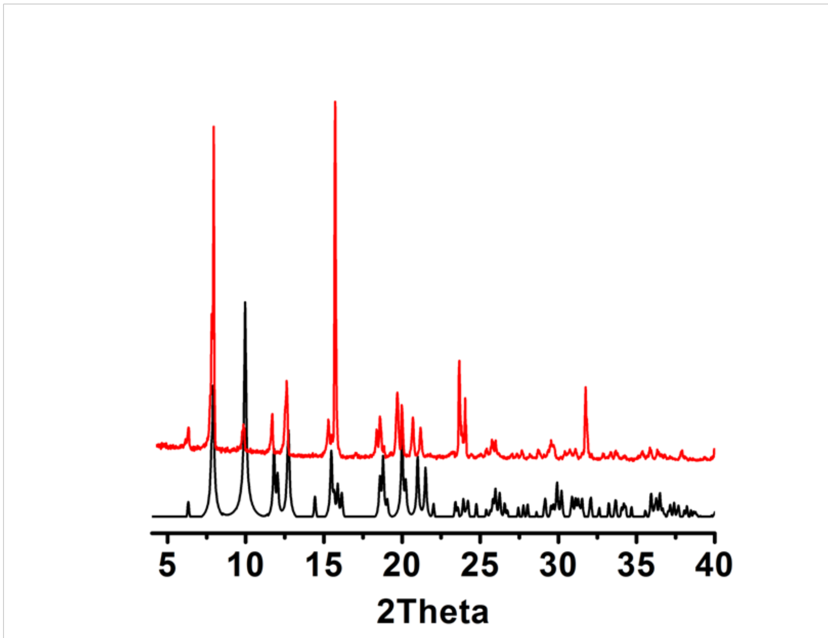

Figure S6. Power X-ray diffraction pattern for $Zn_6(Ad)_6(Py)_6(CH_3CO_2)_6 \cdot 9DMF$ (black, simulated; red, as synthesized)

Synthesis of $Zn_6(Ad)_6(Py)_6(CF_3CO_2)_6 \cdot 10.8DMF, 18H_2O$

A stock solution of adenine (0.05 M) in DMF was prepared. Ultra-sonification and heating were carried out in order to dissolve the adenine completely in DMF. A stock solution of trifluoroacetate hexahydrate (0.05 M) in DMF was prepared. Adenine stock solution (0.5 mL, 0.025 mmol), zinc trifluoroacetate hexahydrate stock solution (0.5 mL, 0.025 m mol) and pyridine (0.25 mL) were added to a glass tube (0.8 cm diameter). The tube was frozen in liquid nitrogen and evacuated to 200 mTorr. The tube was then sealed, heated at 100 °C (72 h), and then cooled to rt. The resultant colorless crystals were washed with DMF (3 mL x 3) and dried under Ar gas (15 min). ***Elemental analysis*** $C_{104.4}H_{165.6.6}N_{46.8}O_{40.8}F_{18}Zn_6$ = $Zn_6(Ad)_6(Py)_6(CF_3CO_2)_6 \cdot 10.8DMF, 18H_2O$: Calcd. C, 44.32; H, 5.55; N, 24.78. Found C, 44.39; H, 4.72; N, 24.88. ***FT-IR*** **:** (KBr 4000-400 cm^{-1}) : 3391.32(br), 3333.93(m), 3114.99(w), 1709.35(s), 1676.34(vs), 1599.75(s), 1405.89(m), 1200.41(s), 1146.32(s) cm^{-1}

Thermogravimetric analysis

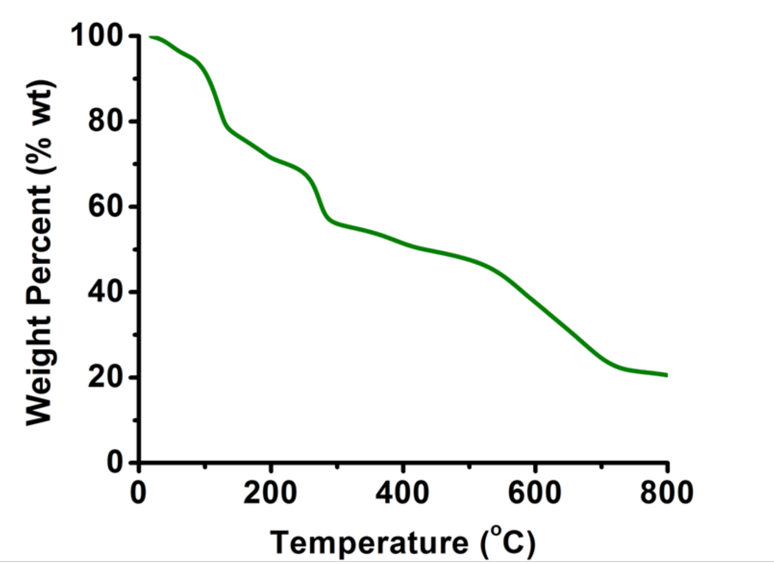

Figure S7. Thermogravimetric analysis for $Zn_6(Ad)_6(Py)_6(CF_3CO_2)_6 \cdot 10.8DMF, 18H_2O$

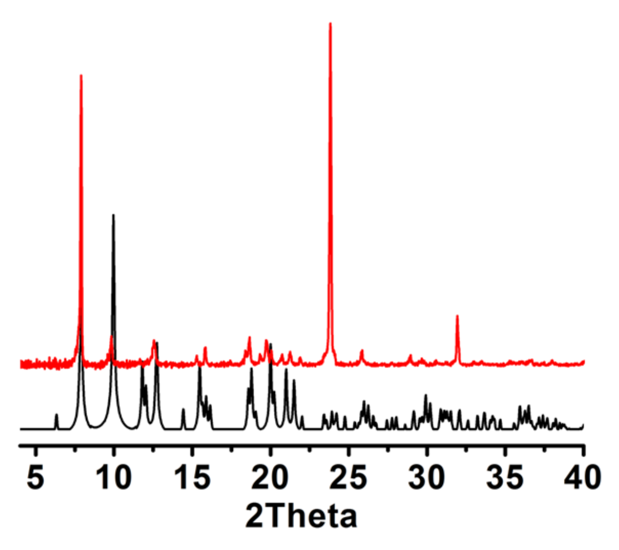

Figure S8. Power X-ray diffraction pattern for $Zn_6(Ad)_6(Py)_6(CF_3CO_2)_6 \cdot 10.8DMF, 18H_2O$ (black, simulated; red, as synthesized)

Synthesis of Zn_6(adeninate)$_6$(pyridine)$_6$(carbamate)$_6$ • 10.5DMF

A stock solution of adenine (0.05 M) in N, N-dimethylformamide (DMF) was prepared. Ultra-sonification and heating were carried out in order to dissolve the adenine completely in DMF. A stock solution of zinc nitrate hexahydrate (0.05 M) in DMF was prepared. 3 mL of the adenine solution, 6 mL of the zinc nitrate solution and 3mL of pyridine were added to a 23 mL Teflon reaction vessel. The reaction vessel was placed in a steel autoclave and heated at 140 °C for 24 hours. After the reaction cooled to room temperature, the reaction solution was transferred to a 20 mL vial. After 3 days, colorless crystals grow in the vial. The crystals were washed with DMF (3 mL x 3) and dried under Ar gas (15 min) (yield: 0.0171 g; 23 % based on adenine) ***Elemental analysis*** $C_{109.5}H_{163.5}N_{52.5}O_{22.5}Zn_6$ = Zn_6(adeninate)$_6$(pyridine)$_6$(carbamate)$_6$ · 10.5DMF. Calcd.: C, 44.32; H, 5.55; N, 24.78. Found: C, 44.39; H, 4.72; N, 24.88. ***FT-IR* :** (KBr 4000-400 cm^{-1}) : 3306.41(br), 3114.13(br), 2923.04(w), 1668.24(s), 1652.79(m), 1601.52(s), 1475.03(s), 1402.75(m), 1387.33(m), 1223.63(w) cm^{-1}.

Gas adsorption Measurements

Gas sorption experiments for Zn_6(adeninate)$_6$(pyridine)$_6$(carbamate)$_6$ • 10.5DMF were collected by measuring the increase in volume at equilibrium as a function of relative pressure by using Autosorb 1 by Quantachrome. Measurements of the sample were performed using an AB54-S/FACT (Mettler Toledo) electrogravimetric balance (sensitivity 0.1 mg). 9 mm large bulb cells (from Quantachrome) of a known weight were loaded with 45 mg of sample for N_2 and CO_2 sorption experiments and 100 mg sample for H_2 sorption experiments. Samples were degassed at 100 °C or 125 °C for 20-22 hours on degassing station until the outgas rate was no more than 3.5 mTorr/min. The degassed sample and sample cell were weighed precisely and then transferred back to the analyzer. Adsorption isotherms were measured at 77 K in a liquid nitrogen bath and at 87 K in a liquid argon bath. The temperature at 273 K for N_2 and CO_2 isotherms were maintained with water bath controlled by refrigerated circulating bath (endocal RET 98, NESLAB)

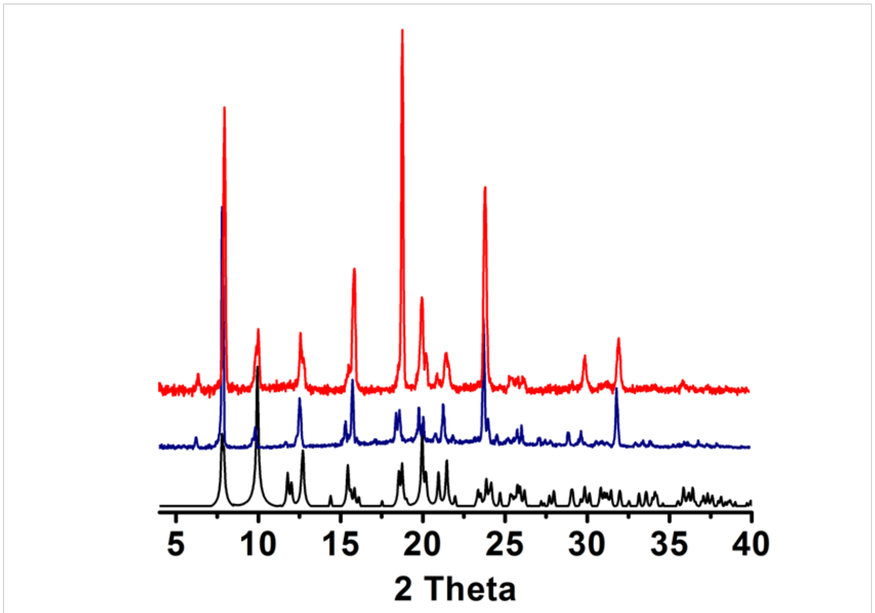

Figure S9. Powder X-ray Patterns for of Zn_6(adeninate)$_6$(pyridine)$_6$(carbamate)$_6$ • 10.5DMF. (black, simulated; navy, experimental at RT; red, experimental at 125 ºC)

Additional gas sorption isotherms

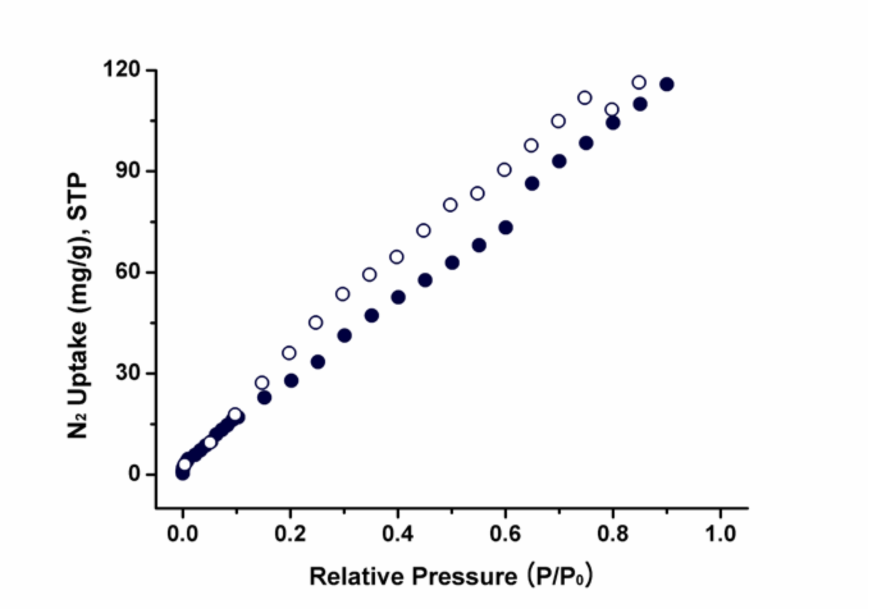

Figure S10. N_2 isotherm (77 K) for Zn_6(adeninate)$_6$(pyridine)$_6$(carbamate)$_6$ • 10.5DMF collected after activation at 100 ºC (filled circles: adsorption; empty circles: desorption).

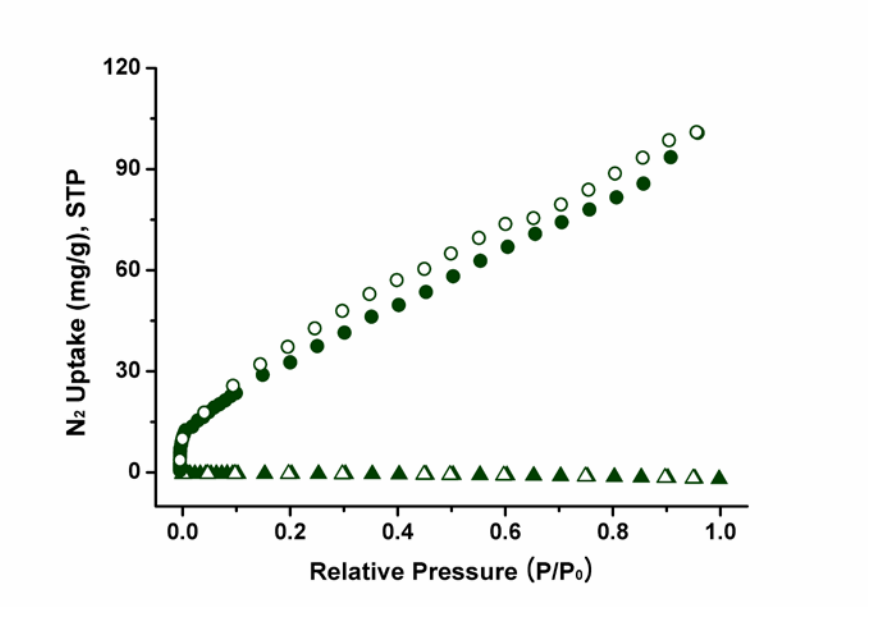

Figure S11. N_2 isotherm (77 K; circle, 273K; triangle) for Zn_6(adeninate)$_6$(pyridine)$_6$(carbamate)$_6$ • 10.5DMF collected after activation at 125 ºC (filled circles/triangles: adsorption; empty circles/triangles: desorption).

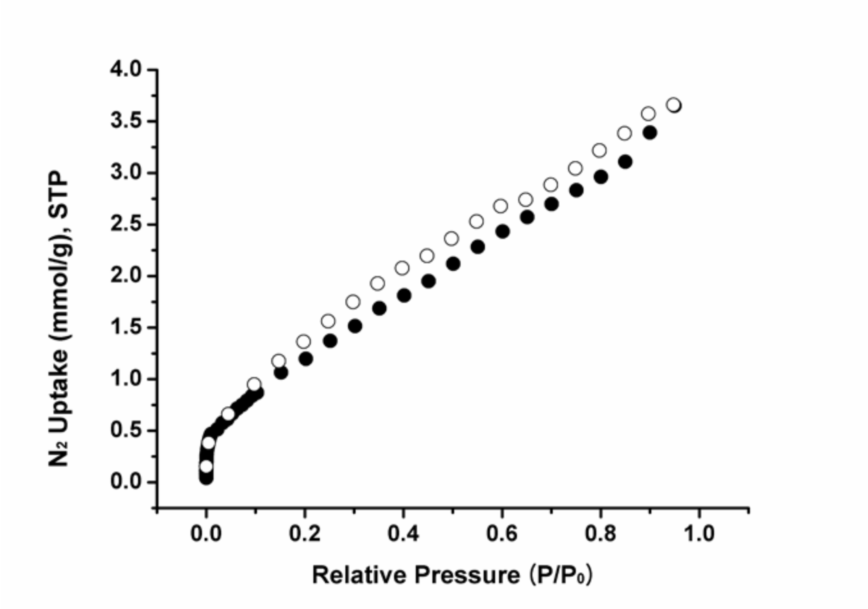

Figure S12. N_2 isotherm (77 K) for $Zn_6(adeninate)_6(pyridine)_6(carbamate)_6$ • 10.5DMF collected after activation at 125 °C (filled circles: adsorption; empty circles: desorption).

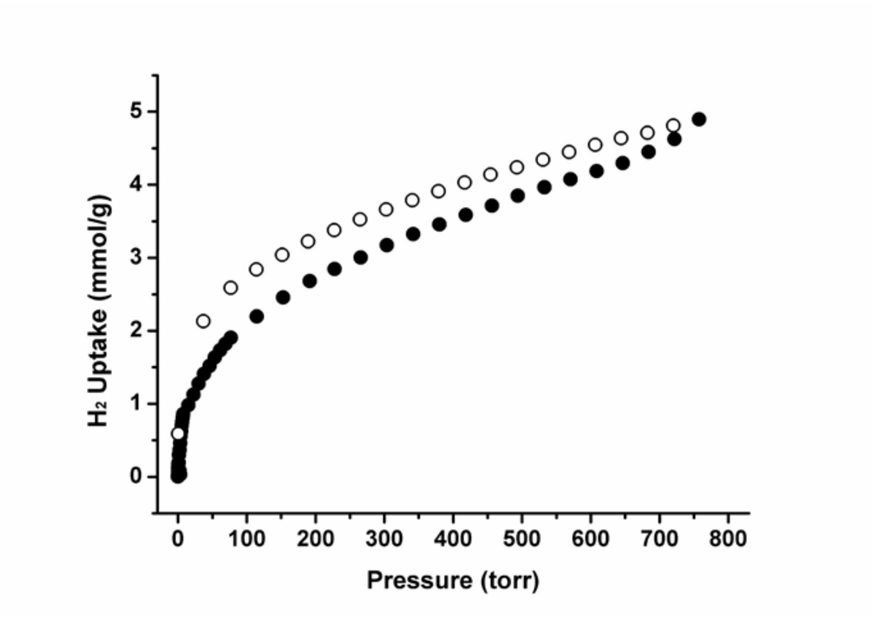

Figure S13. H_2 isotherm (77 K) for $Zn_6(adeninate)_6(pyridine)_6(carbamate)_6$ • 10.5DMF collected after activation at 125 °C (filled circles: adsorption; empty circles: desorption).

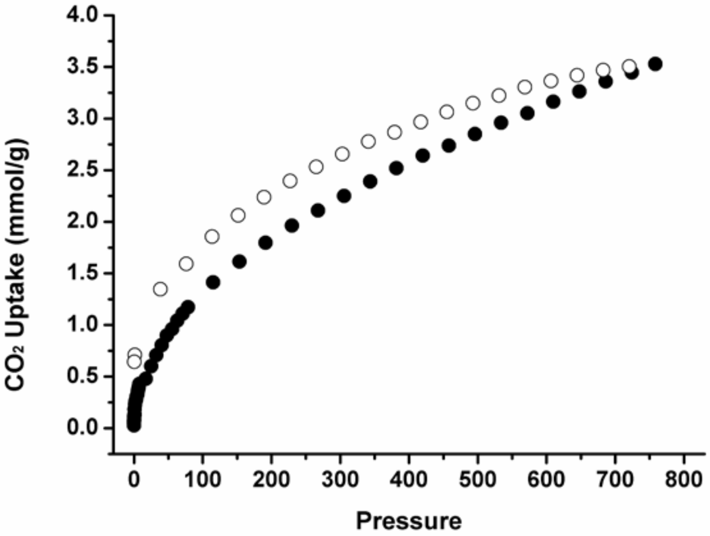

Figure S14. CO_2 isotherm (273K) for $Zn_6(adeninate)_6(pyridine)_6(carbamate)_6$ • 10.5DMF collected after activation at 125 ºC (filled circles: adsorption; empty circles: desorption).

Chapter 3

Synthesis of $Co_2(Ad)_2(CH_3CO_2)_2 \cdot 2DMF, 0.5H_2O$ (bio-MOF-11)

A stock solution of adenine (0.05 M) in N,N-dimethylformamide (DMF) was prepared. Ultra-sonification and heating was employed to completely dissolve adenine in DMF. A stock solution of cobalt acetate tetrahydrate (0.05 M) in DMF was prepared. Adenine stock solution (0.75 mL, 0.0375 mmol) and cobalt acetate tetrahydrate stock solution (0.25 mL, 0.0125 mmol) were added to a glass tube (0.8 cm diameter). The tube was frozen in liquid nitrogen and evacuated to 200 mTorr. The tube was then sealed, heated at 130 °C (24 h), and then cooled to rt. The resultant purple octahedral crystals were washed with DMF (3 mL x 3) and dried in air (15 min) (yield: 0.0037 g, 30 % based on adenine). ***Elemental analysis*** $C_{10}H_{14.5}N_6O_{3.25}Co_1$ = Co(Ad)(OAc) · DMF, 0.25 H_2O; Calcd. C, 36.43; H, 4.43; N, 25.49. Found C, 36.19; H, 4.02; N, 25.44. ***FT-IR :*** (KBr 4000-400 cm^{-1}) : 3341(br), 3208(br), 1655(s), 1600(s), 1583(s), 1496(w), 1445(m), 1396(m), 1344(w), 1309(w), 1270(w), 1209 (m), 1146 (m).

Chloroform-Exchange Experiment for bio-MOF-11

In a typical chloroform exchange experiment, a sample of as-synthesized bio-MOF-11 was rinsed with DMF (3X). Thereafter, the sample was soaked in chloroform (2X; 10 min). Then, fresh chloroform was added and the material was allowed to soak for 24 h. Prior to adsorption experiments, the chloroform-exchanged material was dried with Ar gas. The material remains stable after chloroform exchange, as evidenced by X-Ray powder diffraction (see Figure S1).

Low-Pressure Gas Adsorption Measurements

Sorption isotherm studies for $Co_2(Ad)_2(CH_3CO_2)_2 \cdot 2DMF, 0.5H_2O$ (bio-MOF-11) were performed volumetrically as a function of relative pressure by using the Autosorb 1 by Quantachrome. Samples of chloroform-exchanged bio-MOF-11 were weighed using an AB54-S/FACT (Mettler Toledo) electrogravimetric balance (sensitivity 0.1 mg). 9 mm large bulb cells (from Quantachrome) of a known weight were loaded with ~60 mg of sample for gas sorption experiments. The samples were degassed at 100 °C for 22-24 hours on degassing station until the outgas rate was no more than 3.5 mTorr/min. The degassed sample and sample cell were weighed precisely and then transferred back to the analyzer. The temperature of each sample for N_2 and H_2 adsorption experiments was controlled by a refrigerated bath of either liquid nitrogen (77 K) or liquid argon (87 K). CO_2 isotherms (273 K, 298 K, 303 K, 308 K, and 313 K) were measured in a temperature-controlled water bath. The N_2, CO_2, and H_2 adsorbates were of UHP grade.

Additional Supporting Gas sorption Experiments for bio-MOF-11

a) CO$_2$ Isotherms

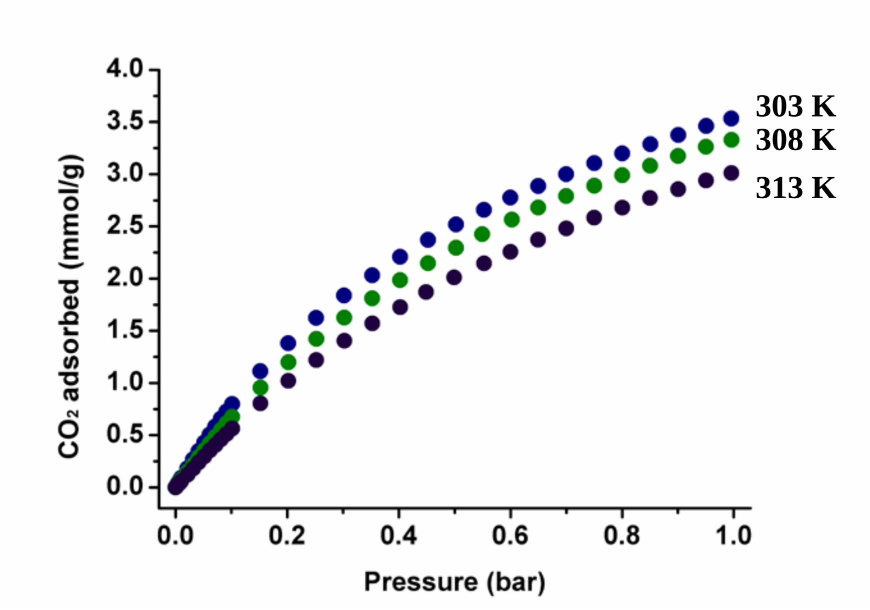

Figure S15. CO$_2$ adsorption isotherms measured at 303K (blue), 308K (green) and 313K (purple).

Table S1. Adsorption and desorption data for CO$_2$ uptake at 298K, 303K, 308K and 313K.

CO$_2$ at 298 K		CO$_2$ at 303 K		CO$_2$ at 308 K		CO$_2$ at 313 K	
P (bar)	Q(mmol/g)	P (bar)	Q(mmol/g)	P (bar)	Q(mmol/g)	P (bar)	Q(mmol/g)
2.26E-4	0.00553	6.33E-4	0.00565	8.32E-4	0.00555	0.00102	0.00512
3.28E-4	0.00646	7.28E-4	0.00645	9.38E-4	0.00626	0.00204	0.01104
4.25E-4	0.00739	8.33E-4	0.00735	0.00102	0.00665	0.00305	0.01689
5.27E-4	0.00839	9.28E-4	0.00817	0.00211	0.01436	0.00411	0.02315
6.19E-4	0.00928	0.00102	0.00877	0.00305	0.02118	0.00519	0.02923
7.27E-4	0.01035	0.00209	0.01802	0.0041	0.0287	0.00625	0.03522
8.27E-4	0.01137	0.00313	0.02703	0.00517	0.03605	0.0073	0.04116
9.2E-4	0.01231	0.00422	0.03662	0.00621	0.04338	0.00835	0.04694
0.00102	0.01317	0.00513	0.04446	0.00731	0.05097	0.00941	0.0528

0.00207	0.02395	0.00621	0.05366	0.00837	0.0582	0.0104	0.05867
0.00311	0.03501	0.00724	0.06259	0.0094	0.06529	0.0218	0.12227
0.00419	0.0466	0.00827	0.07145	0.0105	0.07243	0.0321	0.18037
0.00509	0.05588	0.00936	0.08089	0.0215	0.14844	0.0422	0.23972
0.00612	0.06684	0.0104	0.08943	0.0318	0.21909	0.0524	0.29606
0.00717	0.07785	0.0212	0.18055	0.0419	0.28857	0.0623	0.35502
0.00822	0.08895	0.0314	0.26648	0.0521	0.35529	0.0727	0.40732
0.00931	0.10032	0.0417	0.34844	0.0623	0.42149	0.0827	0.46072
0.0104	0.1116	0.0518	0.42957	0.0725	0.48566	0.0929	0.51276
0.0209	0.21748	0.062	0.50673	0.0827	0.55046	0.103	0.56467
0.031	0.32249	0.0722	0.58248	0.0927	0.61474	0.154	0.80409
0.0412	0.42112	0.0823	0.65687	0.103	0.67588	0.205	1.01996
0.0513	0.5189	0.0925	0.72696	0.154	0.95519	0.255	1.22062
0.0616	0.61151	0.103	0.79772	0.205	1.19856	0.306	1.40425
0.0717	0.70403	0.154	1.11185	0.255	1.42235	0.357	1.57183
0.0819	0.79245	0.205	1.38132	0.306	1.62641	0.408	1.72512
0.0921	0.87689	0.255	1.62396	0.357	1.81142	0.455	1.87143
0.102	0.95751	0.306	1.8362	0.408	1.98393	0.506	2.00983
0.153	1.32659	0.357	2.03151	0.458	2.14634	0.56	2.1446
0.204	1.64124	0.408	2.20916	0.509	2.29394	0.608	2.25612
0.255	1.91847	0.458	2.3712	0.557	2.42557	0.658	2.37247
0.306	2.16215	0.509	2.51889	0.61	2.56493	0.709	2.48084
0.356	2.3835	0.56	2.65684	0.658	2.67988	0.76	2.58384
0.407	2.58036	0.608	2.77536	0.709	2.78968	0.811	2.67824
0.458	2.76154	0.658	2.8873	0.76	2.8894	0.861	2.77169
0.509	2.927	0.709	2.99899	0.811	2.98943	0.912	2.85658
0.56	3.07918	0.76	3.10392	0.862	3.0811	0.963	2.9395
0.607	3.21113	0.811	3.19893	0.912	3.17411	1.01	3.01067
0.661	3.35164	0.862	3.28636	0.963	3.26309		
0.709	3.46553	0.913	3.37475	1.01	3.32932		
0.76	3.58131	0.963	3.46155				
0.81	3.68968	1.01	3.53301				
0.861	3.79192						
0.912	3.88922						
0.963	3.98253						
1.01	4.06033						

Table S2. Adsorption and desorption data for H_2 uptake at 77K, and 87K.

H_2 at 77K				H_2 at 87K			
P (bar)	Q(mmol/g)	P (bar)	Q(mmol/g)	P (bar)	Q(mmol/g)	P (bar)	Q(mmol/g)
1.82E-5	0.001546	0.0204	1.537775	2.84E-5	0.001013	0.0212	0.553288
2.75E-5	0.00232	0.0312	2.079956	4.49E-5	0.001334	0.0316	0.790565
3.51E-5	0.00298	0.0402	2.446397	5.65E-5	0.001562	0.042	1.004176
4.3E-5	0.003535	0.0508	2.789819	6.66E-5	0.001751	0.0523	1.204224
5.85E-5	0.004933	0.0615	3.08312	7.31E-5	0.001877	0.06	1.343104
6.42E-5	0.005395	0.072	3.330718	7.92E-5	0.001997	0.0724	1.547577
7.76E-5	0.006535	0.0825	3.550933	8.33E-5	0.002037	0.0807	1.670445
9.0E-5	0.007567	0.093	3.741109	8.69E-5	0.00212	0.0932	1.84868
9.24E-5	0.007825	0.103	3.910198	1.06E-4	0.002548	0.101	1.960571
1.05E-4	0.00887	0.154	4.545632	1.08E-4	0.0026	0.151	2.526735
2.12E-4	0.019643	0.203	4.979157	2.3E-4	0.005717	0.203	2.974596
3.16E-4	0.030826	0.255	5.328713	3.35E-4	0.008758	0.254	3.33278
4.14E-4	0.041676	0.306	5.610667	4.39E-4	0.011913	0.305	3.632067
5.22E-4	0.053747	0.356	5.85122	5.29E-4	0.014704	0.356	3.880213
6.12E-4	0.063899	0.407	6.050726	6.37E-4	0.017979	0.407	4.099269
7.13E-4	0.075123	0.458	6.227408	7.19E-4	0.020578	0.458	4.291121
8.58E-4	0.091425	0.509	6.386973	8.17E-4	0.023744	0.509	4.460535
9.45E-4	0.101097	0.56	6.537254	9.62E-4	0.028329	0.56	4.620332
0.00104	0.111037	0.611	6.667044	0.00107	0.031451	0.611	4.763213
0.00203	0.215725	0.658	6.782503	0.00205	0.061938	0.658	4.886768
0.00305	0.317025	0.709	6.88851	0.0031	0.093342	0.709	5.005287
0.00407	0.413739	0.76	6.991619	0.00407	0.122087	0.76	5.117473
0.00508	0.505937	0.811	7.086904	0.00508	0.151366	0.811	5.221231
0.00613	0.59803	0.861	7.185688	0.00609	0.180434	0.861	5.317373
0.00711	0.68022	0.912	7.278972	0.0072	0.211586	0.912	5.416374
0.00817	0.765306	0.963	7.358291	0.00814	0.235131	0.963	5.506267
0.00916	0.843066	1.01	7.422416	0.00919	0.26286	1.01	5.58347
0.0102	0.921528			0.0102	0.291953		

b) Heat of Sorption Calculation for CO_2 Uptake

Adsorption data listed at Table S1 were used to calculate the heat of sorption. The isotherms were fit to the Langmuir-Freundlich model (Figure S16).

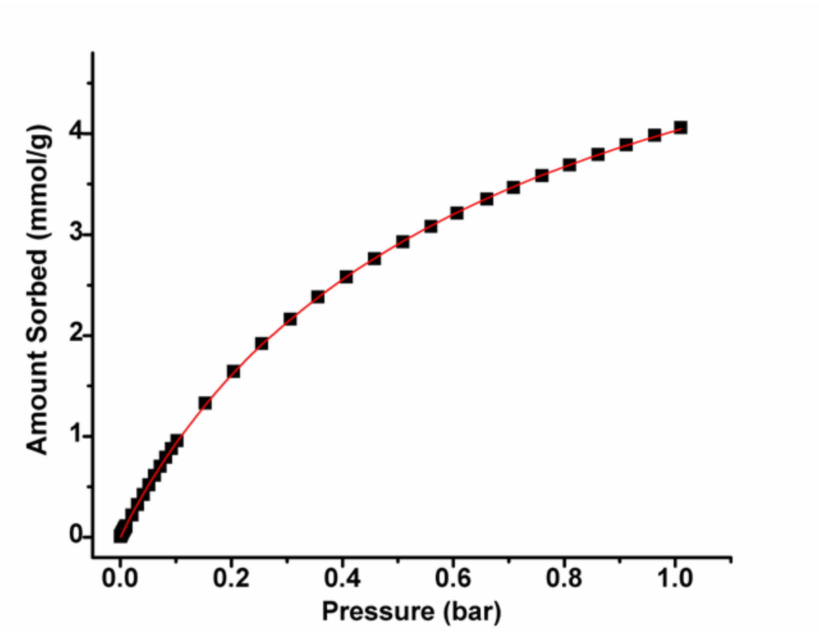

Figure S16. CO_2 isotherm at 298K (black squares) and Langmuir-Freundlich fit to the experimental data (red solid line).

The isosteric heat of adsorption values were calculated using the Clausius-Clapeyron equation:

$$\ln(P_i) = -\Delta H_{ads} \times \frac{1}{R \times T_i} + cons\tan t$$

Pi = pressure for isotherm i

Ti = temperature for isotherm i

R = 8.315 J / K· mol

We plotted $\ln(P_i)$ vs. $1/T_i$ (for T_i = 298K, 303K,308K and 313K). The slope of these lines was used to determine the isosteric heat of adsorption at each pressure point.

Pressure as a function of the amount of CO_2 adsorbed was determined using the Langmuir-Freundlich fit for the isotherms:

$$\frac{Q}{Q_m} = \frac{B \times P^{(1/t)}}{1 + B \times P^{(1/t)}}$$

Q is moles adsorbed

Q_m is moles adsorbed at saturation

P = Pressure
B and t = constants

It can be rearranged to

$$P = \left(\frac{Q/Q_m}{B - B \times Q/Q_m} \right)^t$$

The isosteric heat of adsorption of H_2 is calculated in the same way.

Reference: Dinca, M,; Long, J.R. *J. Am. Chem. Soc.* **2005,** *127*, 9376-9377.[122]

Chapter 4

Synthesis of $Zn_8(Ad)_4(BPDC)_6O \cdot 2(NH_2(CH_3)_2)^+$, 8DMF, $11H_2O$ (bio-MOF-1)

Adenine (0.125 mmol), 4, 4'-biphenyl dicarboxylic acid (BPDC) (0.25 mmol), zinc acetate dihydrate (0.375 mmol), nitric acid (1 mmol), DMF (13.5 mL), and water (1 mL) were added to a 20.0 mL vial. The vial was capped and the resulting solution was heated (130 °C; 24 h). Rod-shaped colorless crystals were produced. The crystals were collected, washed with DMF (3 mL x 3), and dried under Ar gas (30 min) (yield 0.914 g, 86 % based on adenine) ***Elemental analysis*** $C_{132}H_{158}N_{30}O_{44}Zn_8$= $Zn_8(Ad)_4(BPDC)_6O \cdot 2(NH_2(CH_3)_2)^+$, 8DMF, $11H_2O$ Calcd. C, 46.74; H, 4.70; N, 12.39. Found C, 46.58; H, 4.55; N, 12.49. ***FT-IR*** **:** (KBr 4000-400 cm^{-1}) : 3341.39(br), 3188.47(br), 2930.38(w), 1663.76(s), 1606.79(s), 1544.77(m), 1472.12(m), 1382.97(s), 1280.50(w), 1213.98(m), 1176.56(m), 1153.11(m), 1100.61(m), 845.33(m), 772.43(s), 702.00(m)

Gas sorption Measurements for bio-MOF-1

Sorption isotherm studies for the as-synthesized material, $Zn_8(Ad)_4(BPDC)_6O \cdot 2(NH_2(CH_3)_2)^+$, 8DMF, $11H_2O$, and procainamide loaded sample, $Zn_8(Ad)_4(BPDC)_6O \cdot 3.5(\text{procainamide-}H^+)$, $1.5Cl^-$, $16.5H_2O$, were performed volumetrically as a function of relative pressure by using the Autosorb 1 by Quantachrome. The samples were weighed using an AB54-S/FACT (Mettler Toledo) electrogravimetric balance (sensitivity 0.1 mg). 9 mm large bulb cells (from Quantachrome) of a known weight were loaded with 55 mg of sample for N_2 sorption experiments. Samples were degassed at 100 °C for 22-24 hours on degassing station until the outgas rate was no more than 3.5 mTorr/min. The degassed sample and sample cell were weighed precisely and then transferred back to the analyzer. Adsorption isotherms were measured at 77 K in a liquid nitrogen bath.

Preparation of materials (a-d)

a was synthesized according to the previously described procedure. Dimethylammonium cations (DMA^+) in **a** were replaced with either tetramethylammonium (TMA^+), tetraethylammonium (TEA^+) or tetrabutylammonium (TBA^+) cations via cation exchange to yield **b**-**d**, respectively. For example, a solution of TMA^+ tetrafluoroborate (BF_4^-) in D.I. water (0.02 M) was prepared. Cation exchange was performed as follows: a) the as-synthesized material was rinsed with DMF (3x); b) the material was then soaked in the $TMA^+BF_4^-$ solution (10 min) followed by solution removal; c) the material was again soaked in the $TMA^+BF_4^-$ solution (10 min) followed by solution removal; d) the material was again soaked in the $TMA^+BF_4^-$ solution (24 h) followed by solution removal. Step d) was repeated every 24 hours for 8 days. The exchange of TEA^+ and TBA^+ was performed using the same procedure, but in these cases 0.1 M solution of TEA^+ or TBA^+ was used and the exchange was completed after 7 d and 21 d, respectively. The material maintains its crystallinity during and after cation exchange, as evidenced by X-Ray powder diffraction (see Figure 1 in manuscript). After cation exchange was completed, the materials were thoroughly washed with dry chloroform ($CHCl_3$)

Composition of cation-exchanged materials b-d

We calculated the number of cations in **b-d** by analyzing data collected from EA, TGA and ^{1}H NMR. From these data, we determined that after cation exchange, there were 2 cations per unit material ($Zn_8(Ad)_4(BPDC)_6O$).

Elemental Analysis:

b:

$C_{121}H_{103}N_{22}O_{28}Zn_8 = Zn_8(Ad)_4(BPDC)_6O \bullet 2(N(CH_3)_4^+, 3H_2O, 9CHCl_3$

Calcd.: C, 38.31; H, 2.74; N, 8.12. Found: C, 38.26; H, 2.64; N, 8.10.

c:

$C_{128}H_{114}N_{22}O_{26}Zn_8 = Zn_8(Ad)_4(BPDC)_6O \bullet 2(N(C_2H_5)_4)^+, H_2O, 8CHCl_3$

Calcd.: C, 40.99; H, 3.06; N, 8.22. Found: C, 40.96; H, 2.92; N, 8.16.

d:

$C_{141}H_{151}N_{22}O_{30}Zn_8 = Zn_8(Ad)_4(BPDC)_6O \bullet 2(N(C_4H_9)_4)^+, 5H_2O, 5CHCl_3$

Calcd.: C, 45.91; H, 4.13; N, 8.35. Found: C, 45.95; H, 3.67; N, 8.40.

Thermogravimetric analysis:

We correlated the EA data with the TGA data. There are two major weight loss steps in the TGA plots of **b-d** (Figure S1): **b**, 26.0 % weight loss (rt to 240 °C) corresponds to loss of 3 H_2O and 9 $CHCl_3$ (calcd. 29.7 %) and 4.2 % weight loss (240 to 285 °C) corresponds to loss of

TMA^+ (calcd. 3.9 %). **c**: 24.0 % weight loss (rt to 250 °C) corresponds to loss of 1 H_2O and 8 $CHCl_3$ (calcd. 25.9 %) and 7.3 % weight loss (250 to 295 °C) corresponds to loss of TEA^+ (calcd. 6.9 %). **d**: 16.5 % weight loss (rt to 230 °C) corresponds to loss of 5 H_2O and 5 $CHCl_3$ (calcd. 18.6 %) and 13.1 % weight loss (230 to 325 °C) corresponds to loss of TBA^+ (calcd. 13.1 %).

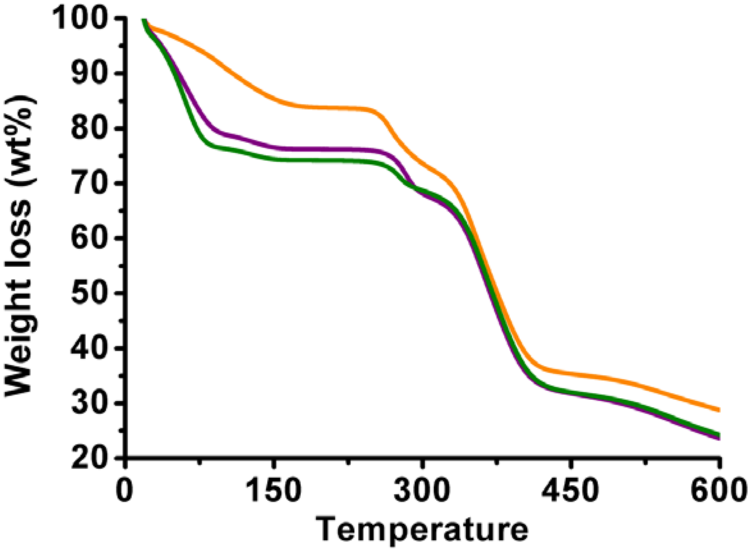

Figure S17. Thermogravimetric analyses of b (green), c (purple), and d (orange).

^1H NMR:

Proton NMR study was performed to determine the number of cations per unit material. 23 µL of DCl (35 wt% in D_2O) was diluted in 1 mL of d-DMSO. 5 mg of each sample of **a-d** was completely dissolved in the solution of 150 µL of diluted DCl and 500 µL of d-DMSO. ^1H NMR (300 MHz) spectra of **a-d** was obtained at room temperature.

Aromatic four hydrogens of biphenyldicarboxylic acid were integrated as 4H which is set as a standard and number of CH_3 hydrogen of each cation was evaluated. NMR spectra supports there are 2 cations per unit material. When four hydrogens of biphenyldicarboxylic acid is integrated as 4H, number of CH_3 hydrogens of cations was integrated as 2H for **a**, and 4H for **b-d**.

a. $NH_2(C\underline{\mathbf{H_3}})_2^+$, δ 2.54 (singlet, 1.77H)
b. $N(C\underline{\mathbf{H_3}})_4^+$, δ 3.09 (singlet, 3.92H)
c. $N(CH_2C\underline{\mathbf{H_3}})_4^+$, δ 1.12-1.18(triplet, 3.82H)
d. $N(CH_2CH_2CH_2C\underline{\mathbf{H_3}})_4^+$, δ 0.91-0.95 (triplet, 3.63H)

3. Gas Adsorption Experiments

Low-Pressure Gas Adsorption Measurements for a-d

Sorption isotherm studies **a-d** were performed volumetrically as a function of relative pressure by using the Autosorb 1 by Quantachrome. Samples of $CHCl_3$-exchanged materials were weighed using an AB54-S/FACT (Mettler Toledo) electrogravimetric balance (sensitivity 0.1 mg). 9 mm large bulb cells (from Quantachrome) of a known weight were loaded with ~60 mg of sample for gas sorption experiments. The samples were degassed at 100 °C for 22-24 hours on degassing station until the outgas rate was no more than 3.5 mTorr/min. The degassed sample and sample cell were weighed precisely and then transferred back to the analyzer. The temperature of each sample for N_2 adsorption experiments was controlled by a refrigerated bath of liquid nitrogen (77 K). CO_2 isotherms (273 K, 298 K, 303 K, 308 K, and 313 K) were measured in a temperature-controlled water bath. The N_2 and CO_2 adsorbates were of UHP grade.

All materials maintain their crystallinity throughout the adsorption experiment, as evidenced by XRPD patterns.

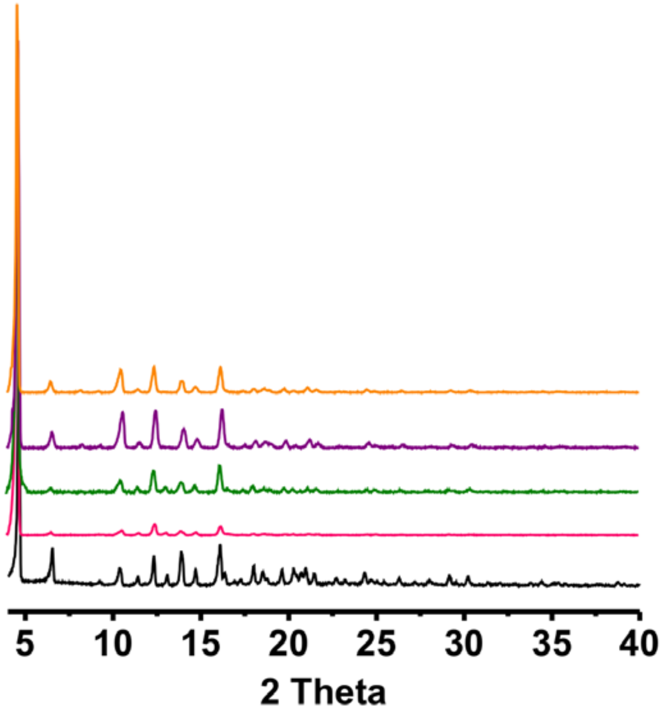

Figure S18. Powder X-ray diffraction patterns of a-d after sorption experiments. (black, as-synthesized material (no adsorption experiment performed); pink, a ; green, b; purple; c, orange, d)

Supplementary Adsorption Data

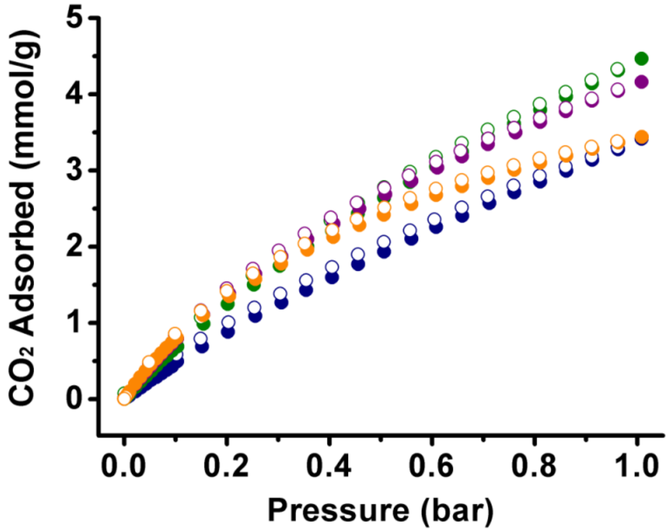

Figure S19. CO_2 isotherms at 273 K with adsorption (filled circle) and desorption (empty circle) points. a (navy), b (green), c (purple) and d (orange). (y coordinate: mmol/g)

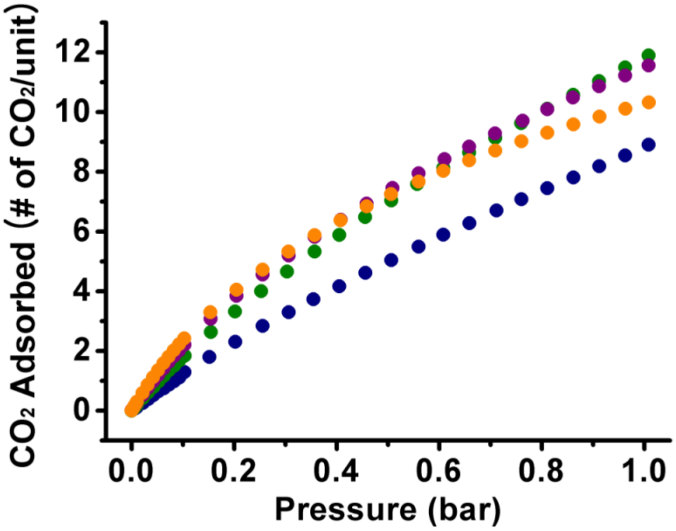

Figure S20. CO_2 isotherms at 273 K. a (navy), b (green), c (purple) and d (orange). Here, the data is reported as #CO_2 per formula unit to account for the different molar mass of each material.

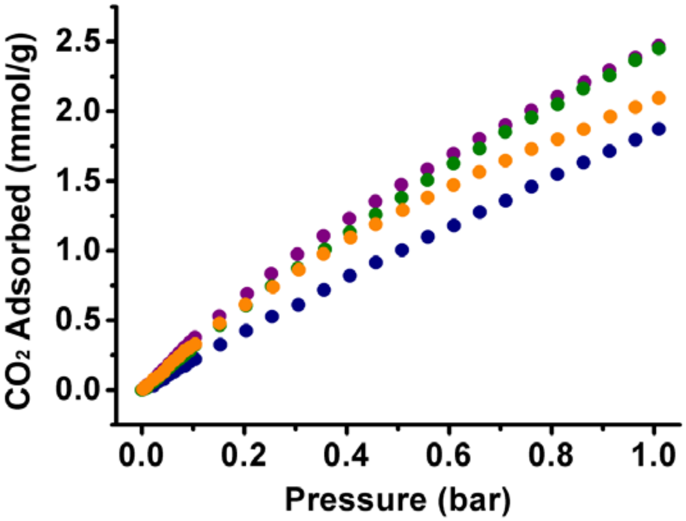

Figure S21. CO_2 isotherms at 298 K. a (navy), b (green), c (purple) and d (orange). (y coordinate: mmol/g)

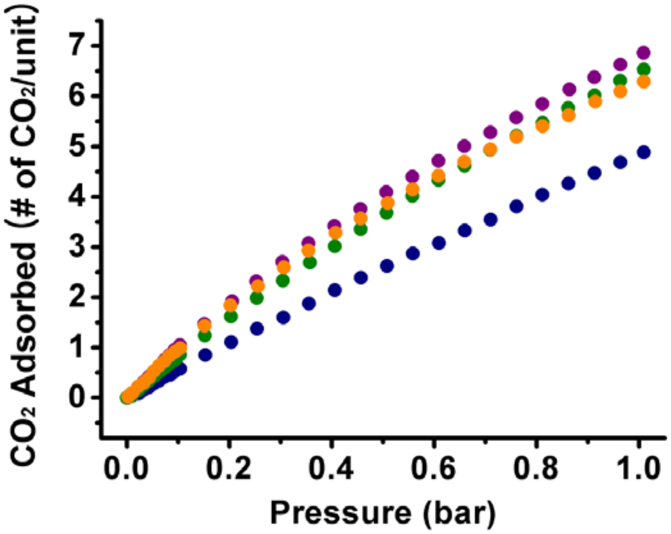

Figure S22. CO_2 isotherms at 298 K. a (navy), b (green), c (purple) and d (orange). Here, the data is reported as #CO_2 per formula unit to account for the different molar mass of each material.

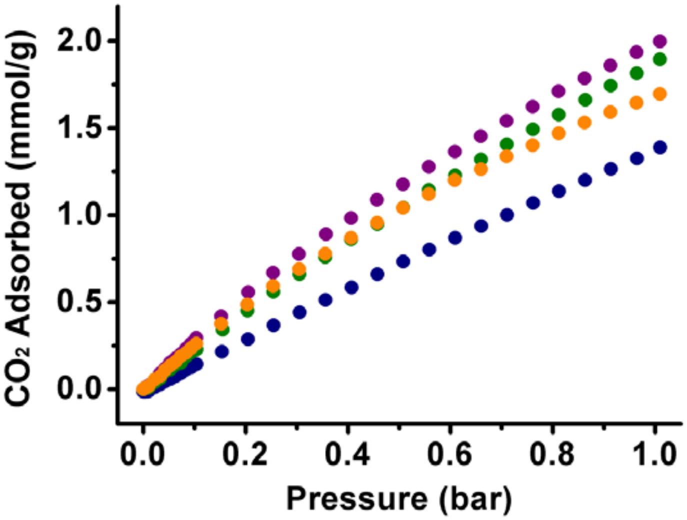

Figure S23. CO_2 isotherms at 303 K. a (navy), b (green), c (purple) and d (orange). (y coordinate: mmol/g)

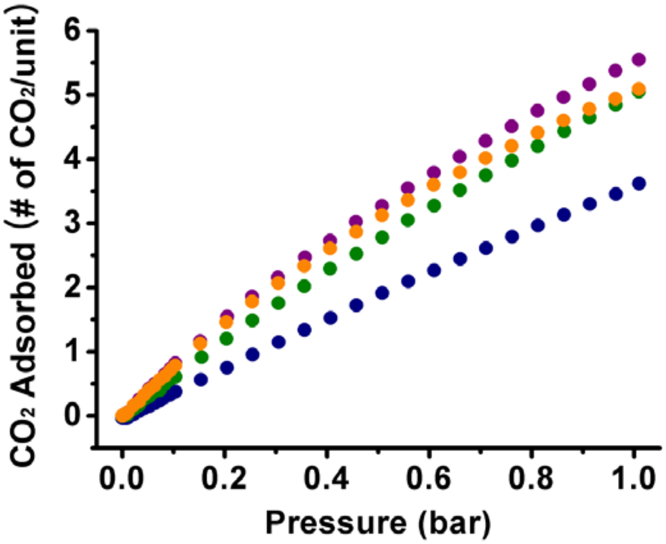

Figure S24. CO_2 isotherms at 303 K. a (navy), b (green), c (purple) and d (orange). Here, the data is reported as #CO_2 per formula unit to account for the different molar mass of each material.

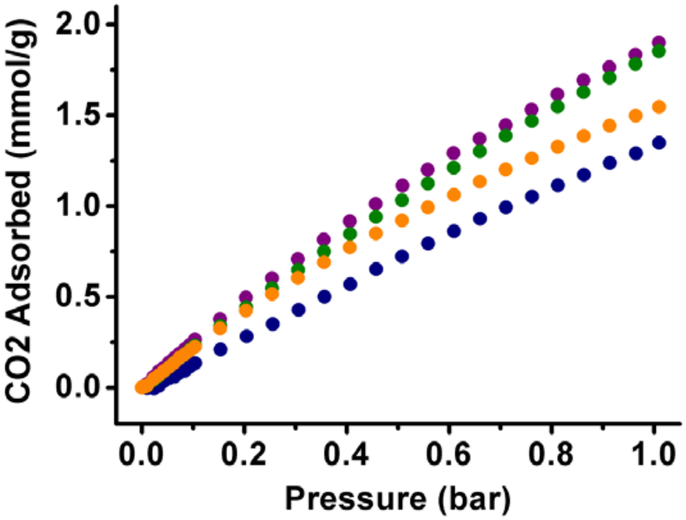

Figure S25. CO_2 **isotherms at 308 K. a (navy), b (green), c (purple) and d (orange). (y coordinate: mmol/g)**

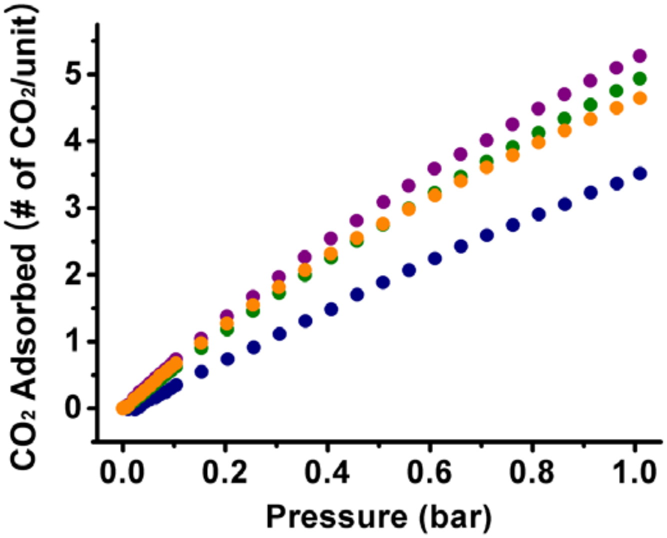

Figure S26. CO_2 **isotherms at 308 K. a (navy), b (green), c (purple) and d (orange). Here, the data is reported as #**CO_2 **per formula unit to account for the different molar mass of each material.**

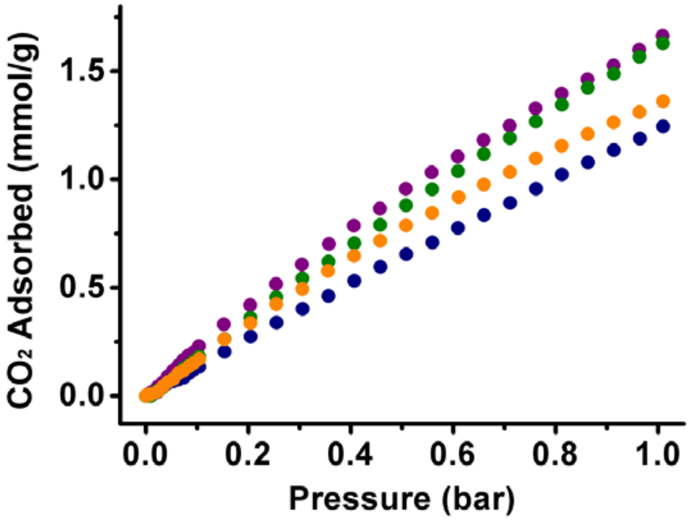

Figure S27. CO_2 isotherms at 313 K. a (navy), b (green), c (purple) and d (orange). (y coordinate: mmol/g)

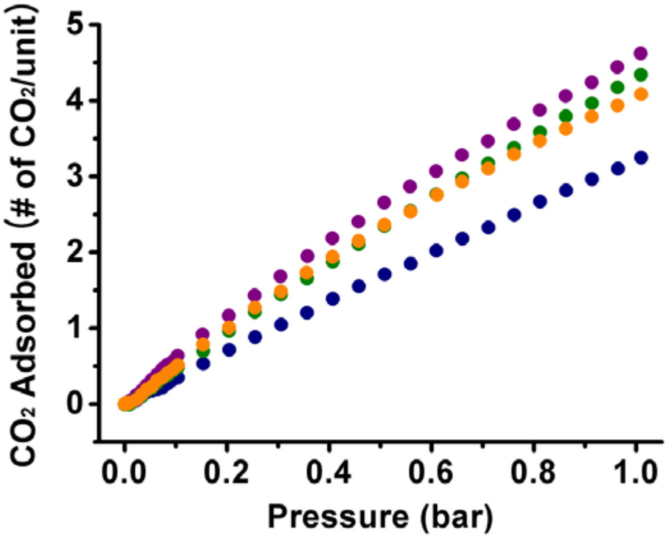

Figure S28. CO_2 isotherms at 313 K. a (navy), b (green), c (purple) and d (orange). Here, the data is reported as #CO_2 per formula unit to account for the different molar mass of each material.

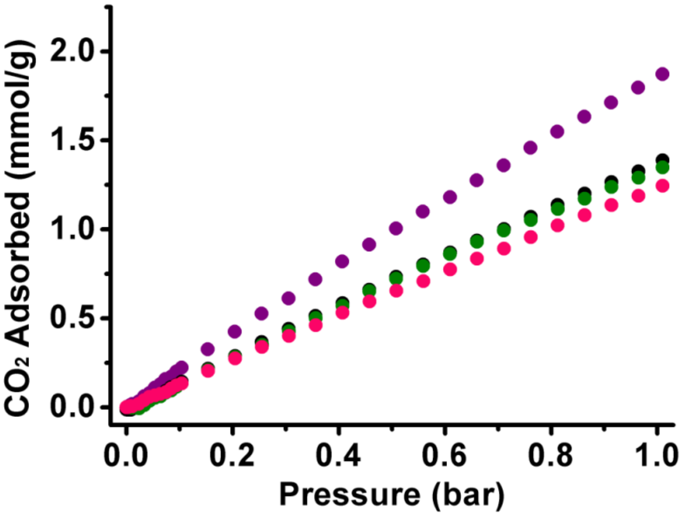

Figure S29. CO_2 isotherms for a measured at 298 K (purple), 303 K (black), 308 K (green) and 313 K (pink).

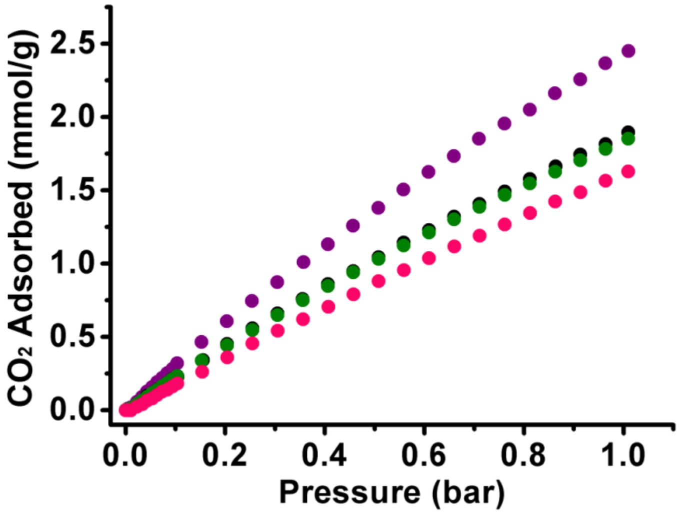

Figure S30. CO_2 isotherms for b measured at 298 K (purple), 303 K (black), 308 K (green) and 313 K (pink).

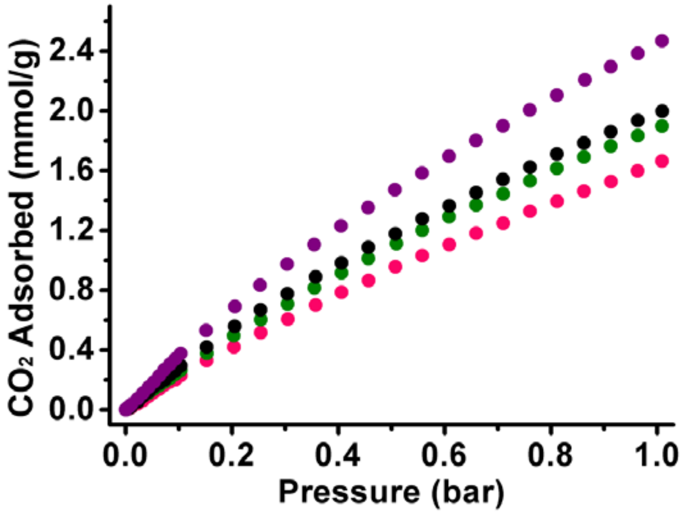

Figure S31. **CO_2 isotherms for c measured at 298 K (purple), 303 K (black), 308 K (green) and 313 K (pink).**

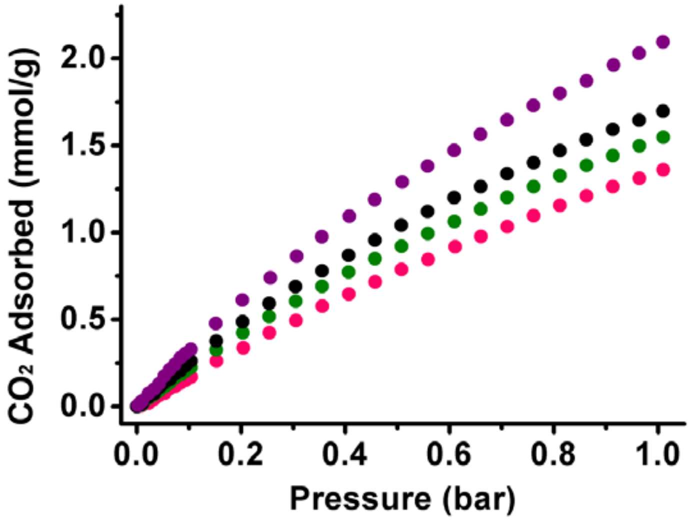

Figure S32. **CO_2 isotherms for d measured at 298 K (purple), 303 K (black), 308 K (green) and 313 K (pink).**

Table S3. Adsorption and desorption data for CO_2 uptake at 298 K, 303 K, 308 K and 313K.

As-synthesized (DMA)							
CO_2 at 298 K		CO_2 at 303 K		CO_2 at 308 K		CO_2 at 313 K	
P (bar)	Q (mmol/g)	P (bar)	Q (mmol/g)	P (bar)	Q (mmol/g)	P (bar)	Q (mmol/g)
0.00215	0.00287	0.02286	0.01096	0.03355	0.01138	0.00312	0.00156
0.00312	0.00476	0.03310	0.02771	0.04337	0.03641	0.00421	0.00286
0.00416	0.00680	0.04318	0.04527	0.05362	0.05269	0.00529	0.00383
0.00530	0.00851	0.05346	0.05916	0.06405	0.06109	0.00634	0.00484
0.00645	0.01041	0.06354	0.07524	0.07389	0.08160	0.00736	0.00582
0.00753	0.01220	0.07369	0.09172	0.08430	0.09363	0.00842	0.00656
0.00856	0.01385	0.08368	0.11257	0.09415	0.11521	0.00963	0.00531
0.00962	0.01563	0.09384	0.12522	0.10429	0.13411	0.01058	0.00546
0.01069	0.01745	0.10398	0.14408	0.15382	0.20963	0.02300	0.01789
0.02326	0.03244	0.15368	0.21584	0.20450	0.28256	0.03312	0.03860
0.03309	0.06213	0.20443	0.28744	0.25541	0.34997	0.04313	0.05817
0.04343	0.07987	0.25481	0.36678	0.30591	0.42739	0.05349	0.06730
0.05320	0.10935	0.30558	0.44078	0.35644	0.50125	0.06390	0.07479
0.06340	0.12955	0.35623	0.51316	0.40718	0.56939	0.07396	0.08477
0.07333	0.15747	0.40688	0.58512	0.45746	0.65274	0.08398	0.10456
0.08394	0.17225	0.45745	0.66074	0.50807	0.72237	0.09399	0.12241
0.09382	0.20131	0.50812	0.73310	0.55878	0.79370	0.10432	0.13354
0.10398	0.22208	0.55882	0.80273	0.60948	0.86057	0.15376	0.20364
0.15302	0.32515	0.60959	0.86897	0.66016	0.93002	0.20443	0.27377
0.20378	0.42454	0.66016	0.93722	0.71076	0.99322	0.25520	0.33822
0.25433	0.52635	0.71099	1.00185	0.76177	1.05223	0.30590	0.40134
0.30551	0.61136	0.76162	1.07042	0.81245	1.11354	0.35648	0.46102
0.35558	0.71879	0.81220	1.13723	0.86319	1.17198	0.40715	0.53174
0.40617	0.82000	0.86301	1.20114	0.91367	1.23814	0.45779	0.59520
0.45698	0.91472	0.91372	1.26482	0.96466	1.28990	0.50854	0.65464
0.50776	1.00457	0.96443	1.32552	1.00997	1.34845	0.55917	0.70887
0.55826	1.09953	1.00991	1.38826			0.60958	0.77473
0.60935	1.18057					0.66045	0.83492
0.65977	1.27555					0.71114	0.89173
0.71045	1.35889					0.76182	0.95669
0.76091	1.45855					0.81231	1.02230
0.81150	1.54891					0.86305	1.07918
0.86230	1.63305					0.91359	1.13563
0.91309	1.71326					0.96457	1.18884

0.96377	1.79612					1.00976	1.24520
1.00951	1.87232						

Table S4. **Adsorption and desorption data for CO_2 uptake at 298 K, 303 K, 308 K and 313 K.**

TMA exchanged							
CO_2 at 298 K		CO_2 at 303 K		CO_2 at 308 K		CO_2 at 313 K	
P (bar)	Q (mmol/g)	P (bar)	Q (mmol/g)	P (bar)	Q (mmol/g)	P (bar)	Q (mmol/g)
0.00213	0.00484	0.00857	0.00534	0.00424	0.00531	0.02276	0.02401
0.00317	0.00769	0.00962	0.00696	0.00533	0.00589	0.03324	0.03963
0.00417	0.01050	0.01073	0.00877	0.00643	0.00557	0.04314	0.06507
0.00529	0.01124	0.02272	0.03947	0.00747	0.00710	0.05353	0.08016
0.00637	0.01179	0.03295	0.06106	0.00847	0.00863	0.06338	0.10313
0.00745	0.01234	0.04260	0.09944	0.00956	0.01107	0.07357	0.12659
0.00833	0.01354	0.05342	0.11380	0.01064	0.01258	0.08394	0.14052
0.00954	0.01679	0.06341	0.14107	0.02275	0.04128	0.09394	0.16245
0.01054	0.01897	0.07388	0.15080	0.03301	0.06538	0.10413	0.18128
0.02262	0.05732	0.08356	0.18680	0.04311	0.09062	0.15386	0.26233
0.03274	0.09045	0.09374	0.21160	0.05324	0.11460	0.20413	0.36087
0.04299	0.12656	0.10418	0.22807	0.06338	0.13846	0.25465	0.45611
0.05328	0.15761	0.15510	0.34225	0.07346	0.16374	0.30542	0.54272
0.06326	0.19217	0.20387	0.45157	0.08368	0.18628	0.35633	0.62040
0.07345	0.22114	0.25436	0.55858	0.09377	0.21028	0.40706	0.70462
0.08361	0.25231	0.30512	0.66005	0.10384	0.23341	0.45744	0.79028
0.09390	0.28133	0.35559	0.75850	0.15304	0.33873	0.50789	0.87987
0.10355	0.32082	0.40630	0.86116	0.20372	0.44289	0.55891	0.95499
0.15235	0.46483	0.45731	0.94798	0.25438	0.54775	0.60926	1.03789
0.20302	0.60668	0.50794	1.04356	0.30506	0.64832	0.65995	1.11744
0.25369	0.74544	0.55820	1.14411	0.35566	0.74960	0.71093	1.19102
0.30457	0.87350	0.60924	1.22845	0.40635	0.84654	0.76151	1.26783
0.35744	1.00974	0.65984	1.31980	0.45706	0.94048	0.81204	1.34535
0.40606	1.13160	0.71050	1.40646	0.50776	1.03209	0.86254	1.42345
0.45652	1.25832	0.76112	1.49232	0.55838	1.12374	0.91358	1.48705
0.50725	1.38056	0.81173	1.57702	0.60908	1.21163	0.96388	1.56621
0.55767	1.50613	0.86371	1.66332	0.65966	1.30128	1.00960	1.62845
0.60847	1.62536	0.91319	1.74370	0.71040	1.38688		
0.65932	1.73315	0.96407	1.81589	0.76113	1.46798		

0.70961	1.85169	1.00932	1.89545	0.81181	1.54697		
0.76070	1.95461			0.86241	1.62703		
0.81178	2.05086			0.91318	1.70547		
0.86200	2.16291			0.96380	1.78273		
0.91312	2.25687			1.00942	1.85216		
0.96331	2.36668						
1.00963	2.44996						

Table S5. **Adsorption and desorption data for CO_2 uptake at 298 K, 303 K, 308 K and 313 K.**

TEA exchanged							
CO_2 at 298 K		CO_2 at 303 K		CO_2 at 308 K		CO_2 at 313 K	
P (bar)	Q (mmol/g)	P (bar)	Q(mmol/g)	P (bar)	Q(mmol/g)	P (bar)	Q(mmol/g)
0.00209	0.00706	0.00316	0.00753	0.00317	0.00622	0.00430	0.00753
0.00319	0.01107	0.00422	0.01049	0.00422	0.00884	0.00535	0.00752
0.00411	0.01452	0.00524	0.01107	0.00519	0.00890	0.00647	0.00933
0.00522	0.01656	0.00635	0.01202	0.00636	0.01155	0.00748	0.01097
0.00626	0.02019	0.00733	0.01259	0.00736	0.01352	0.00856	0.01283
0.00731	0.02385	0.00839	0.01534	0.00853	0.01618	0.00967	0.01458
0.00835	0.02746	0.00959	0.01841	0.00953	0.01841	0.01079	0.01656
0.00941	0.03122	0.01064	0.02094	0.01064	0.02089	0.02270	0.04174
0.01046	0.03494	0.02273	0.05264	0.02227	0.05801	0.03318	0.06326
0.02241	0.07427	0.03257	0.09016	0.03254	0.08887	0.04292	0.09004
0.03273	0.11229	0.04282	0.11838	0.04294	0.11091	0.05302	0.11617
0.04291	0.15024	0.05285	0.15406	0.05299	0.13875	0.06306	0.13984
0.05305	0.18766	0.06316	0.17780	0.06321	0.16321	0.07309	0.16625
0.06311	0.22735	0.07344	0.20057	0.07327	0.18771	0.08321	0.18724
0.07304	0.26906	0.08346	0.23401	0.08350	0.21196	0.09375	0.20240
0.08331	0.30556	0.09368	0.26315	0.09358	0.23733	0.10364	0.23034
0.09340	0.34172	0.10368	0.29587	0.10378	0.26584	0.15239	0.33006
0.10353	0.37736	0.15211	0.41940	0.15258	0.37631	0.20350	0.41997
0.15147	0.53036	0.20517	0.55808	0.20304	0.49612	0.25394	0.51640
0.20547	0.69228	0.25353	0.66916	0.25396	0.60233	0.30486	0.60649
0.25293	0.83411	0.30425	0.77690	0.30477	0.70804	0.35731	0.70184
0.30362	0.97445	0.35724	0.88997	0.35509	0.81592	0.40611	0.78641
0.35449	1.10597	0.40606	0.98384	0.40583	0.91623	0.45699	0.86516
0.40531	1.23051	0.45638	1.08809	0.45660	1.01177	0.50728	0.95642

0.45597	1.35359	0.50738	1.17728	0.50917	1.11251	0.55805	1.03208
0.50672	1.47343	0.55786	1.27826	0.55803	1.20018	0.60888	1.10588
0.55758	1.58417	0.60878	1.36529	0.60841	1.29213	0.65943	1.18176
0.60824	1.69662	0.65954	1.45371	0.65954	1.36970	0.71051	1.24852
0.65904	1.80258	0.70992	1.54159	0.71050	1.44492	0.76061	1.32808
0.71004	1.90030	0.76070	1.62344	0.76072	1.53137	0.81162	1.39565
0.76043	2.00663	0.81111	1.71142	0.81135	1.61497	0.86239	1.46270
0.81117	2.10473	0.86210	1.78627	0.86208	1.69249	0.91312	1.52699
0.86398	2.20828	0.91286	1.86060	0.91272	1.76499	0.96330	1.59901
0.91275	2.29602	0.96349	1.93590	0.96348	1.83447	1.00911	1.66381
0.96347	2.38560	1.00927	1.99794	1.00919	1.89930		
1.00906	2.46943						

Table S6. Adsorption and desorption data for CO_2 uptake at 298 K, 303 K, 308 K and 313 K.

TBA exchanged							
CO_2 at 298 K		CO_2 at 303 K		CO_2 at 308 K		CO_2 at 313 K	
P (bar)	Q (mmol/g)	P (bar)	Q (mmol/g)	P (bar)	Q (mmol/g)	P (bar)	Q (mmol/g)
0.00321	0.01005	0.00212	0.00379	0.00214	0.00284	0.00734	0.00407
0.00425	0.01349	0.00326	0.00675	0.00329	0.00527	0.00848	0.00507
0.00553	0.01685	0.00423	0.00923	0.00426	0.00714	0.00947	0.00590
0.00655	0.02079	0.00540	0.00999	0.00550	0.00753	0.01052	0.00702
0.00742	0.02327	0.00634	0.01007	0.00656	0.00768	0.02313	0.02015
0.00850	0.02644	0.00755	0.01124	0.00759	0.00762	0.03319	0.04230
0.00957	0.02956	0.00851	0.01332	0.00863	0.00930	0.04320	0.06409
0.01073	0.03244	0.00953	0.01542	0.00969	0.01100	0.05359	0.07749
0.02228	0.07461	0.01068	0.01813	0.01079	0.01292	0.06345	0.10362
0.03310	0.09974	0.02246	0.05481	0.02253	0.04730	0.07388	0.11641
0.04306	0.13267	0.03306	0.07502	0.03297	0.06674	0.08397	0.13612
0.05289	0.17564	0.04286	0.10972	0.04297	0.09053	0.09416	0.15175
0.06296	0.21174	0.05301	0.13687	0.05316	0.11315	0.10433	0.17043
0.07314	0.24205	0.06339	0.15777	0.06324	0.13643	0.15301	0.26153
0.08326	0.27874	0.07322	0.18785	0.07314	0.16409	0.20418	0.33636
0.09358	0.30469	0.08362	0.20827	0.08358	0.18274	0.25445	0.42423
0.10399	0.32788	0.09370	0.23592	0.09363	0.20499	0.30555	0.49440
0.15168	0.47697	0.10377	0.26107	0.10390	0.22481	0.35568	0.57660
0.20245	0.61277	0.15233	0.37574	0.15260	0.32611	0.40663	0.64633

0.25629	0.73926	0.20303	0.48654	0.20331	0.42356	0.45732	0.71610
0.30672	0.86302	0.25372	0.59255	0.25403	0.51607	0.50788	0.78712
0.35485	0.97602	0.30447	0.68970	0.30481	0.60470	0.55889	0.84537
0.40761	1.09330	0.35555	0.77865	0.35547	0.69067	0.61073	0.91840
0.45647	1.18892	0.40609	0.86934	0.40620	0.77215	0.66008	0.97647
0.50932	1.29039	0.45688	0.95585	0.45697	0.84952	0.71090	1.03326
0.55787	1.38164	0.50749	1.04172	0.50784	0.92050	0.76133	1.09648
0.60864	1.47115	0.55804	1.12061	0.55846	0.99341	0.81170	1.15541
0.65916	1.56452	0.60859	1.20011	0.60922	1.06221	0.86256	1.20983
0.71007	1.64728	0.65981	1.26382	0.65974	1.13430	0.91324	1.26346
0.76088	1.72927	0.71011	1.33779	0.71045	1.20187	0.96391	1.31101
0.81176	1.79959	0.76101	1.40090	0.76132	1.26319	1.00978	1.36086
0.86263	1.87204	0.81166	1.46965	0.81178	1.32683		
0.91448	1.96249	0.86229	1.53245	0.86257	1.38572		
0.96385	2.02940	0.91295	1.59216	0.91326	1.44179		
1.00952	2.09459	0.96380	1.64547	0.96396	1.49814		
		1.00930	1.69673	1.00969	1.54647		

Heat of adsorption calculation for CO_2 Uptake

Adsorption data listed in Table S3-S6 were used to calculate the heat of sorption. The isotherms were fit to the Langmuir-Freundlich model (Figure S33). [122]

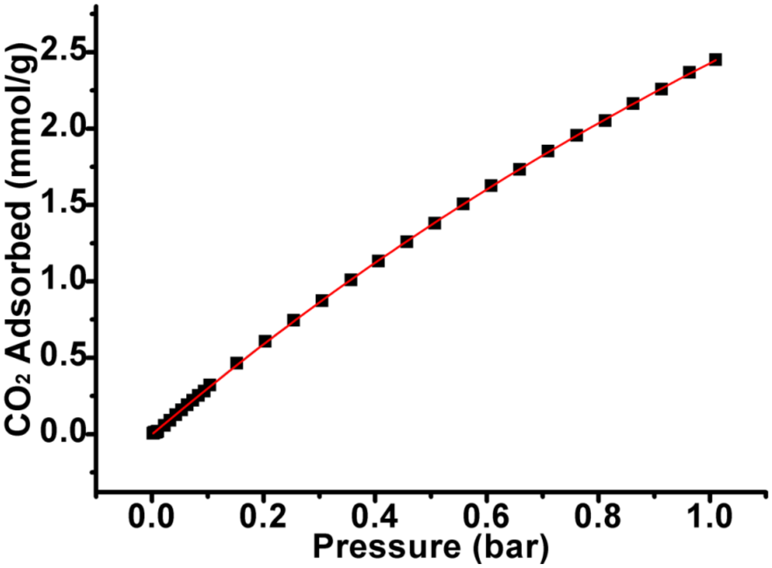

Figure S33. CO_2 isotherm of b at 298 K (black squares) and Langmuir-Freundlich fit to the experimental data (red solid line).

The isosteric heat of adsorption values were calculated using the Clausius-Clapeyron equation:

$$\ln(P_i) = -\Delta H_{ads} \times \frac{1}{R \times T_i} + constant$$

P*i* = pressure for isotherm *i*

T*i* = temperature for isotherm *i*

R = 8.315 J / K· mol

We plotted ln(P_i) vs. 1/T_i (for T_i = 298 K, 303 K,308 K and 313 K). The slope of these lines was used to determine the isosteric heat of adsorption at each pressure point. Pressure as a function of the amount of CO_2 adsorbed was determined using the Langmuir-Freundlich fit for the isotherms:

$$\frac{Q}{Q_m} = \frac{B \times P^{(1/t)}}{1 + B \times P^{(1/t)}}$$

Q is moles adsorbed

Q_m is moles adsorbed at saturation

P = Pressure
B and t = constants

It can be rearranged to

$$P = \left(\frac{Q / Q_m}{B - B \times Q / Q_m} \right)^t$$

Chapter 5

5.1 Procainamide controlled release experiment

Procainamide loading into bio-MOF-1

The procainamide loading was performed by cation exchange. Procainamide hydrochloride was purchased from Aldrich Chemical Co. Its purity was confirmed by ^{1}H NMR, and it was used without further purification. A solution of procainamide hydrochloride in D.I. water (0.1M) was prepared. Procainamide cation exchange was performed as follows: a) the as-synthesized material was rinsed with DMF (2x); b) material was soaked in procainamide HCl solution (10 min) followed by solution removal; c) material was soaked in procainamide HCl solution (10 min) followed by solution removal; d) material was soaked in procainamide HCl solution (24 h) followed by solution. Step d) was repeated every 24 hours for 15 days.

Gas sorption Measurements

Sorption isotherm studies for the as-synthesized material, $Zn_8(Ad)_4(BPDC)_6O \cdot 2(NH_2(CH_3)_2)^+$, 8DMF, $11H_2O$, and procainamide loaded sample, $Zn_8(Ad)_4(BPDC)_6O \cdot 3.5(\text{procainamide-H}^+)$, $1.5Cl^-$, $16.5H_2O$, were performed volumetrically as a function of relative pressure by using the Autosorb 1 by Quantachrome. The samples were weighed using an AB54-S/FACT (Mettler Toledo) electrogravimetric balance (sensitivity 0.1 mg). 9 mm large bulb cells (from Quantachrome) of a known weight were loaded with 55 mg of sample for N_2 sorption experiments. Samples were degassed at 100 °C for 22-24 hours on degassing station until the outgas rate was no more than 3.5 mTorr/min. The degassed sample and sample cell were weighed precisely and then transferred back to the analyzer. Adsorption isotherms were measured at 77 K in a liquid nitrogen bath.

Determination of the procainamide content in procainamide-loaded bio-MOF-1

Thermogravimetric analysis

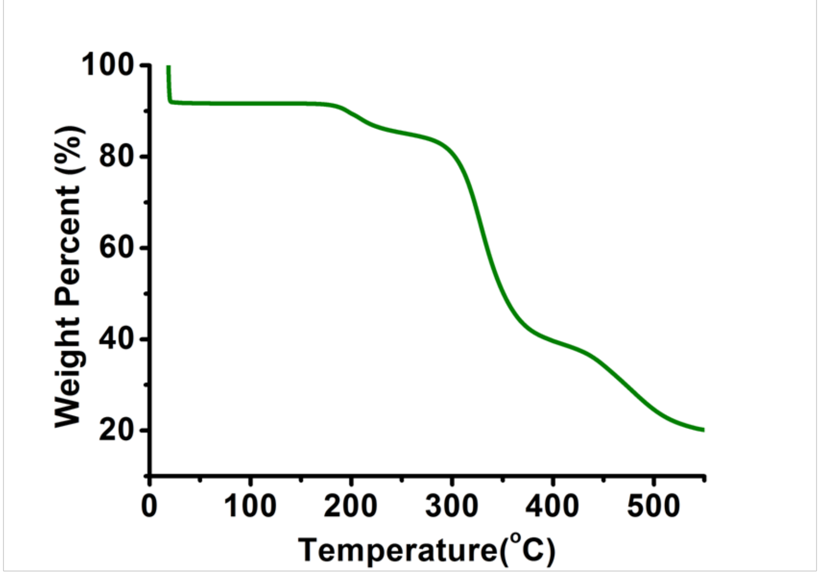

Figure S34. **Thermogravimetric analysis for the procainamide loaded bio-MOF-1.**

Elemental analysis

$C_{149.5}H_{174}N_{30.5}O_{45}Zn_8$= $Zn_8(Ad)_4(BPDC)_6O$ · 3.5(procainamide)$^+$, 1.5Cl^-, 16.5H_2O

Calcd. C, 48.60; H, 4.75; N, 11.56. Found C, 48.79; H, 4.02; N, 11.15.

Estimation of procainamide contents in bio-MOF-1

We calculated the amount of procainamide that was loaded into bio-MOF-1 by analyzing data collected from EA, TGA, and the procainamide-release experiments. From these data, we determined that after procainamide loading, there was 0.22 g procainamide/g material. There are two major weight loss steps in the TGA plot of procainamide loaded bio-MOF-1 (Figure S2):
8.0 % weight loss (rt to 165°C) corresponds to 16.5H_2O molecules (calcd 8.0%) and a
6.9 % weight loss (165 to 245°C) corresponds to loss of 1 procainamide · HCl (calcd 7.3%) (the decomposition temperature for procainamide HCl is between 200 °C and 250 ° C). The remainder of the procainamide likely decomposes during the framework decomposition step in the TGA from 300 °C to 400 °C. We note that the initial loss of procainamide · HCl likely corresponds to the procainamide HCl molecules bound to the external surfaces of the material. The remainder of the procainamide in the pores of the material decomposes with the framework. This is not surprising, as most of the procainamide within the pores (procainamide-H$^+$) is chemically associated with the framework via ionic interactions.

Cation-triggered procainamide release: HPLC determination

Reverse-phase high-pressure liquid chromatography (HPLC) was performed at ambient temperature with an Agilent 1200 liquid chromatographic system equipped with diode array and multiple wavelength detectors and a Grace Vydac protein C4 column (214TP1010, 1.0 cm × 25 cm). The mobile phase consisted of 0.1% formic acid (v/v) in acetonitrile. The flow rate was 0.52 mL/min^{-1}. The effluent was monitored at 278 nm and the injection volume of the sample was 100 μL.

A calibration plot was generated by using several procainamide solutions in PBS buffer (0.1 M, pH 7.4) with different concentrations.

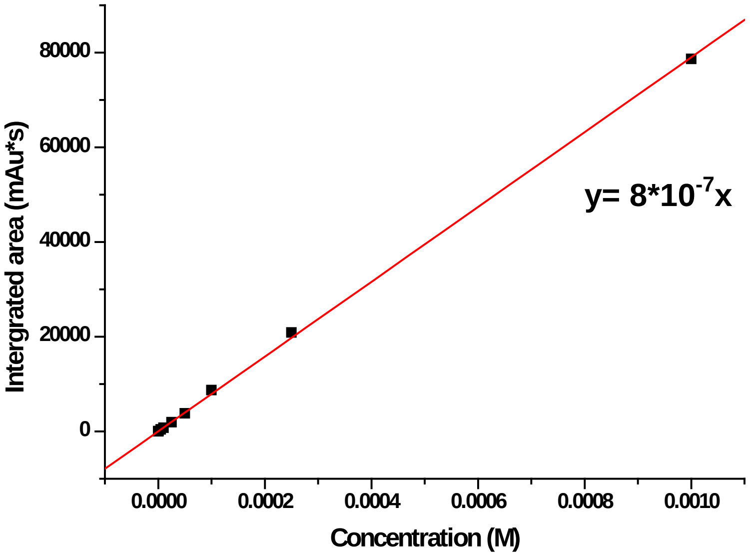

Figure S35. Calibration plot of procainamide by HPLC.

Procainamide identification by HPLC

For as-purchased procainamide HCl, there are two peaks in the HPLC plot, with retention times of 10.4 min and 12.5 min, respectively.

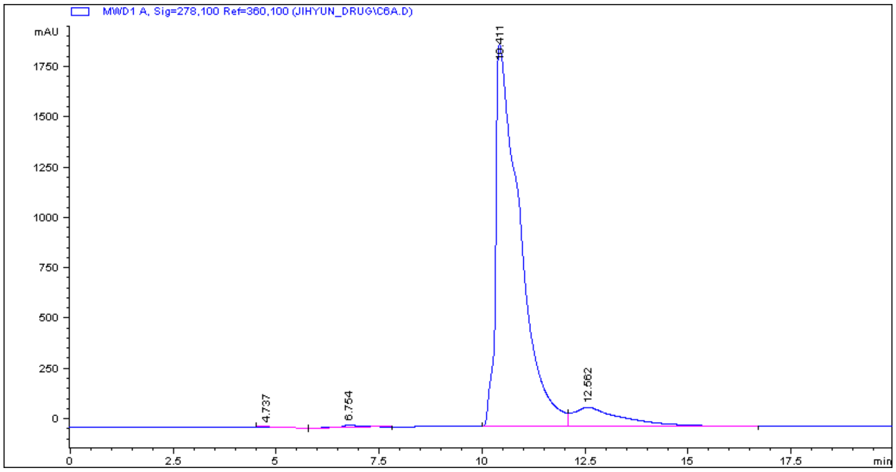

Figure S36. **HPLC plot of procainamide HCl.**

Experimental procedure for measuring procainamide release

15 mg of procainamide-loaded material was added to a 4 mL vial. 1mL of PBS buffer (0.1M, pH 7.4) was added to the vial. At different times, 150 μL of the solution from the vial was removed and 150 μL of fresh PBS buffer was added to the vial. The procainamide concentrations in the samples that were removed from the vial were measured for procainamide content.

Procainamide release: control experiment procedure

15 mg of procainamide-loaded material was added to a 4 mL vial. 1 mL of nanopure water (18.2 mΩ) was added. At different times, 150 μL of the solution from the vial was

removed and 150 μL of the fresh water was added to the vial. The procainamide concentrations in the samples that were removed from the vial were measured for procainamide content.

5.2 Luminescent Properties of Ln@bio-MOF-1

Preparation of Ln@bio-MOF-1

bio-MOF-1 was synthesized according to previously described procedure. The lanthanide cation loading was performed by cation exchange. Ln nitrate (yitterbium nitrate, samarium nitrate, terbium nitrate, and europium nitrate) was purchased and used without further purification. A solution of Ln nitrate in DMF (0.1 M) was prepared. Ln^{3+} cation exchange was performed as follows: a) the as-synthesized material was rinsed with DMF (3 x); b) the material was soaked in Ln nitrate solution (10 min) followed by solution removal; c) the material was again soaked in Ln nitrate solution (10 min) followed by solution removal; d) the material was soaked in Ln nitrate solution (24 h) followed by solution removal. Step d) was repeated every 24 h for 21 days. After cation exchange was completed, the materials were thoroughly washed with NP water. The material maintains its crystallinity during and after cation exchange, as evidenced by Powder X-ray diffraction patterns.

Composition of Ln^{3+} exchanged materials

We calculated the number of cations in Ln@bio-MOF-1 by analyzing data collected from EA, TGA and EDX. From these data, we determined that after cation exchange, there were 0.06669 -0.908 cations per unit material ($Zn_8(Ad)_4(BPDC)_6O$).

EDX

	Yb:BioMOF-1	Eu:BioMOF-1	Tb-BioMOF-1	Sm-BioMOF-1
Ln^{3+} %	10.2 (± 0.2) %	7 (± 1.0) %	5.1 (± 0.7) %	7 (± 1.0) %
Zn^{2+} %	98.2 (± 0.2) %	93 (± 1.0) %	94.9 (± 0.7) %	93 (± 1.0) %

Elemental analysis

Yb@bio-MOF-1

$C_{121}H_{103}N_{22}O_{28}Zn_8Yb_{0.908}$ = $Zn_8(Ad)_4(BPDC)_6O$ • $0.908Yb^{3+}$, $0.72NO_3^-$,$11H_2O$

Calcd.: C, 38.31; H, 2.74; N, 8.12. Found: C, 38.26; H, 2.64; N, 8.10

Eu@bio-MOF-1

$C_{104}H_{106}N_{20}O_{46}Zn_8Eu_{0.6668}$ = $Zn_8(Ad)_4(BPDC)_6O \cdot 0.6668Eu^{3+}$, $21H_2O$

Calcd.: C, 41.69; H, 3.57; N, 9.35. Found: C, 41.84; H, 2.64; N, 9.33

Sm@bio-MOF-1

$C_{104}H_{146}N_{20}O_{66}Zn_8Sm_{0.6668}$ = $Zn_8(Ad)_4(BPDC)_6O \cdot 0.6668Sm^{3+}$,$41H_2O$

Calcd.: C, 37.22; H, 4.39; N, 8.35. Found: C, 37.09; H, 3.22; N, 8.65

Tb@bio-MOF-1

$C_{104}H_{132}N_{20}O_{59}Zn_8Tb_{0.6668}$ = $Zn_8(Ad)_4(BPDC)_6O \cdot 0.6668Tb^{3+}$, $34H_2O$

Calcd.: C, 38.61; H, 4.11; N, 8.66. Found: C, 38.38; H, 3.09; N, 8.98

Thermogravimetric Analysis:

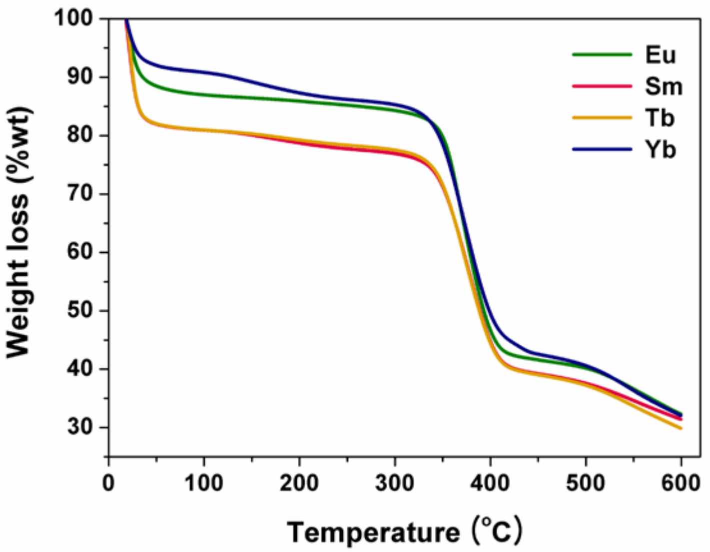

Figure S37. Thermogravemetric analyses for Ln@bio-MOF-1.

Luminescence Measurement

Absorption spectra were recorded on a Perkin-Elmer Lambda 9 Spectrometer coupled with a personal computer using software supplied by Perkin-Elmer. Spectra were collected after instrumental zeroing with two quartz cuvettes of solvent.

Luminescence spectra in the visible and near infrared range (NIR) were measured using a Jobin Yvon–Horiba Fluorolog-322 spectrofluorimeter equipped with an Electro-Optical Systems, Inc. DSS-IGA020L detector for the NIR domain fitted with an integrating sphere developed by Frédéric Gumy and Jean-Claude G. Bünzli (Laboratory of Lanthanide Supramolecular Chemistry, École Polytechnique Féderale de Lausanne (EPFL), BCH 1402, CH- 1015 Lausanne, Switzerland) as an accessory to the Fluorolog FL3-22 spectrometer (Patent pending) using quartz tube sample holders.[123] Quantum yield measurements of the solid state samples were measured using the integration sphere, using ytterbium tropolonate, $[Yb(trop)_4]^-$ [124] as the reference for the NIR range and TbH_2IAM [125] as the reference for the visible range.

Lanthanide luminescence lifetimes in the NIR were measured using a Nd:YAG Continuum Powerlite 8010 laser (354 nm, third harmonic) as the excitation source. Emission was collected at a right angle to the excitation beam, and wavelengths were selected by a Spectral Products CM 110 1/8 meter monochromator. The signal was monitored by a Hamamatsu R316-02 photomultiplier tube for the NIR range, and was collected on a 500 MHz band pass digital oscilloscope (Tektronix TDS 754D). Luminescence lifetimes in the visible range were measured using the flash lamp and detector of a Jobin Yvon–Horiba Fluorolog-322 spectrofluorimeter. The signal was monitored with the Tektronix TDS 754D oscilloscope. Signals from >1000 flashes were collected and averaged. Luminescence decay curves were treated with Origin 7.0 software using exponential fitting models. Three decay curves were collected on each sample, and reported lifetimes are an average of at least two independent measurements.

Oxygen Sensing Experiments

A custom-built gas-delivery chamber, housed within a modified JY Horiba Fluorolog-322 spectrofluorimeter coupled to an Electro-Optical Systems, Inc. DSS-IGA020L detector, was used to collect steady-state emission spectra for the gas-sensitivity measurements. A 715 nm long-pass filter was used, and spectra were corrected for non-linearities in the lamp and detector.

Additional Supporting Luminescence Measurement Data

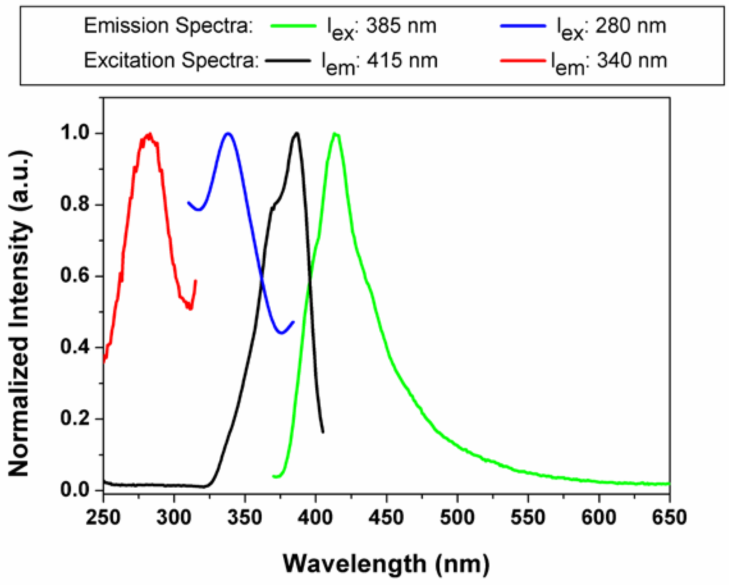

Figure S38. Fluorescence spectra, λ_{ex}: 280 nm (blue) and λ_{ex}: 385 nm (green) of bio-MOF-1 in DMF and corresponding excitation spectra, λ_{em}: 340 nm (red) and λ_{em}: 415 nm (black) of the band maxima.

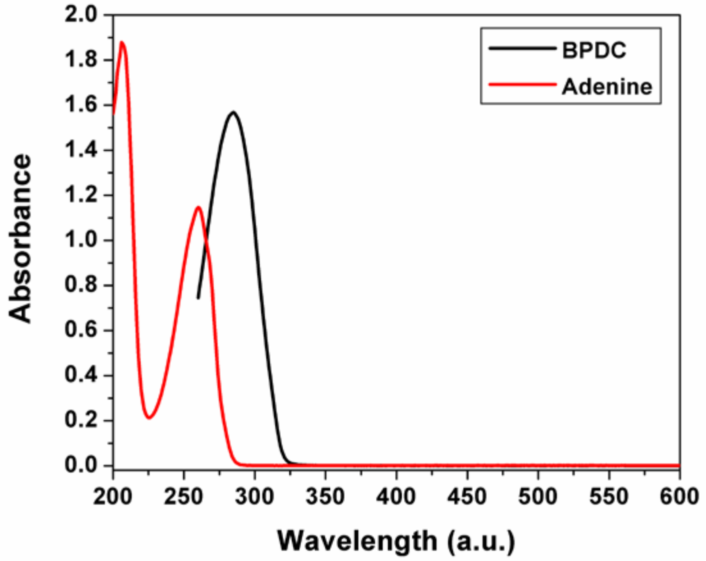

Figure S39. Absorbance spectra of BPDC in DMSO (black) and adenine in water (red).

Time-gated spectra for Tb@bio-MOF-1 and Sm@bio-MOF-1

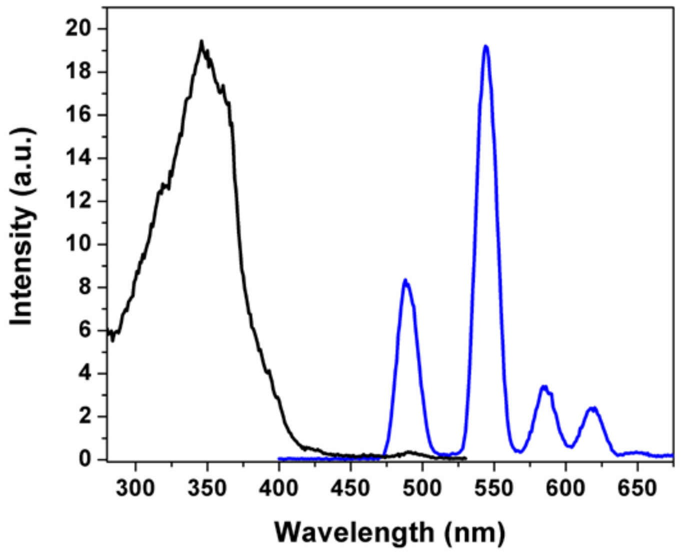

Figure S40. Time-gated (right) excitation, λ_{em}: 545 nm, (black) and emission, λ_{ex}: 340 nm, (blue) spectra for Tb@bio-MOF-1 in water.

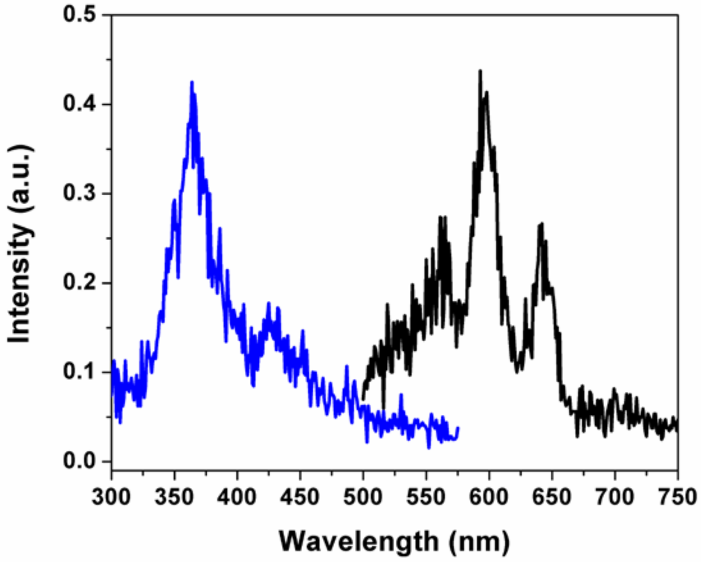

Figure S41. Time-gated (right) excitation, λ_{em}: 596 nm, (black) and emission, λ_{ex}: 340 nm (blue), λ_{ex}: 425 nm (red), spectra for Sm@bio-MOF-1 under water.

Luminescent Measurement of Ln@bio-MOF-1 in DMF

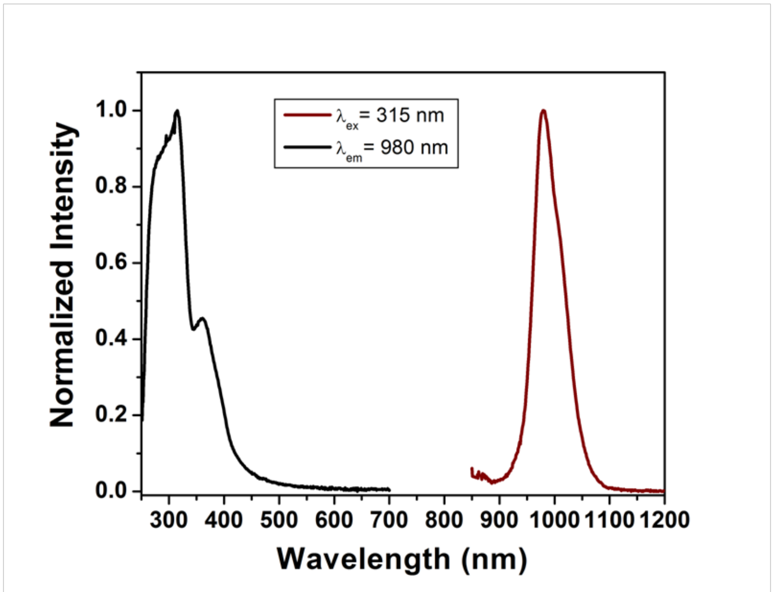

Figure S42. Excitation spectrum (black) of ytterbium luminescence at 980 nm and the NIR emission spectrum (wine) with λ_{ex}: 315 nm.

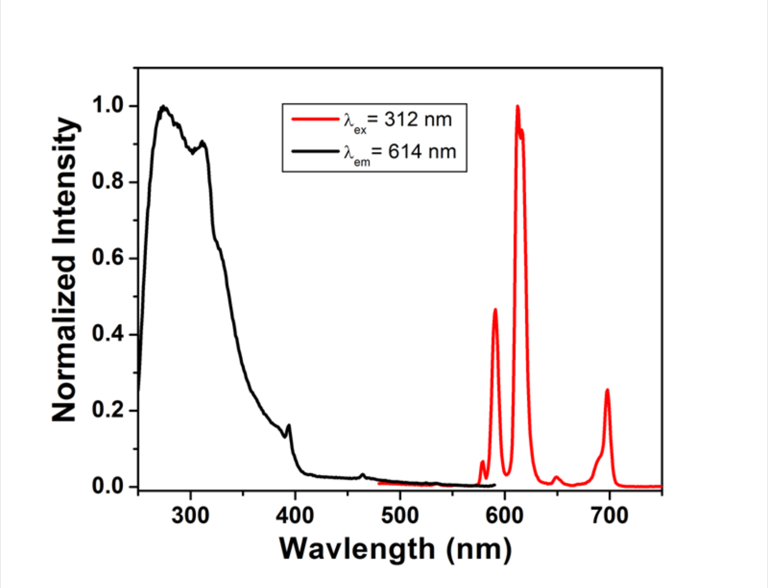

Figure S43. Excitation spectrum (black) of europium luminescence at 614 nm and the emission spectrum (red) with λ_{ex}: 312 nm.

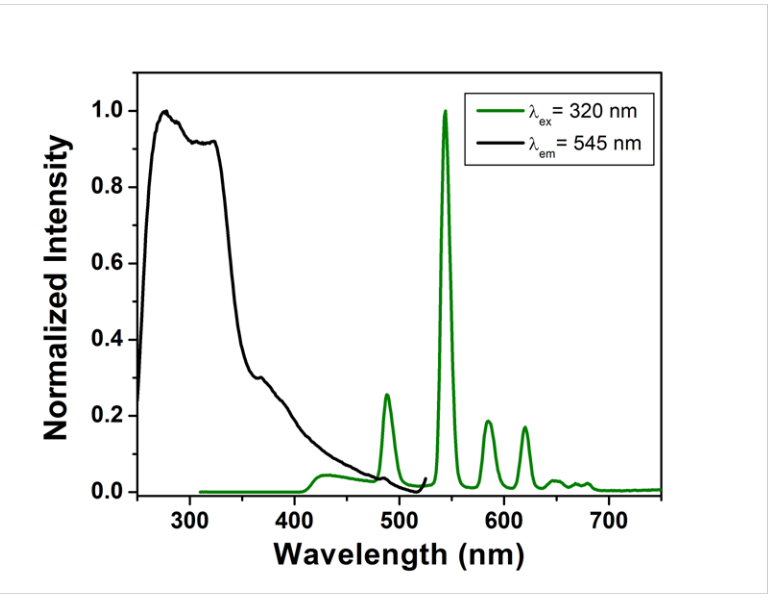

Figure S44. Excitation spectrum (black) of turbium luminescence at 545 nm and the emission spectrum (green) with λ_{ex}: 320 nm.

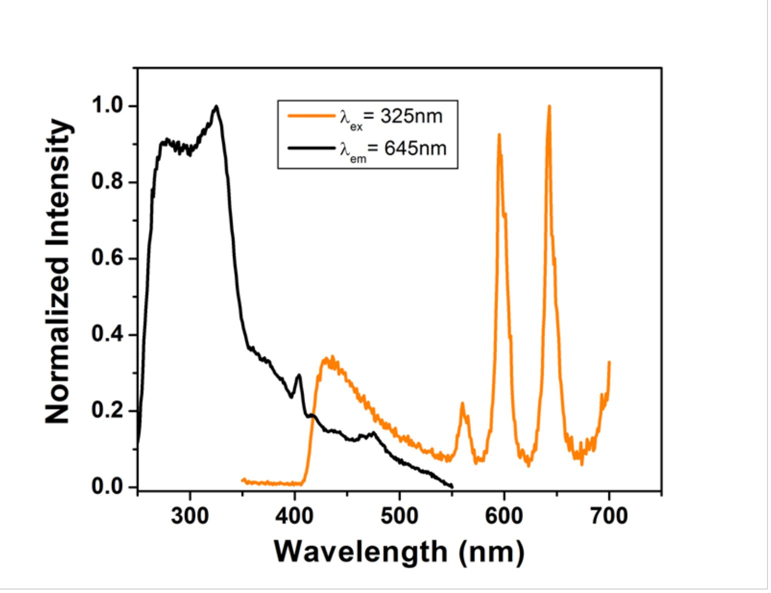

Figure S45. Excitation spectrum (black) of samarium luminescence at 645 nm and the emission spectrum (orange) with λ_{ex}: 325 nm.

Table S7. Luminescence lifetimes for Ln@bio-MOF-1 in H_2O and D_2O, the calculated quenching values (q-values) that result from the lifetime measurements, and lanthanide-centered quantum yield values measured in H_2O.

Ln@bio-MOF-1	$\tau_{H2O}(\mu s)$	$\tau_{D2O}(\mu s)$	*Q*	Φ_{Ln}
Tb	62(1)	54(1)	†	1.7 (±0.1) x 10^{-2}
	224(14)	142(5)		
	1900(200)*			
Sm	7.4(1)	131.1(3)	-	2.8 (±0.2) x 10^{-3}
	35(1)	539(33)		
Eu	300(1)	1163(32)	2.6	8.4 (±0.1) x 10^{-2}
	986(75)	1886(60)	0.5	
Yb	1.1(1)	12.05(4)	0.7	2.5 (±0.2) x 10^{-4}
	5.5(4)	56(1)	0.1	

(* the lifetime of Tb was measured at 77 K; †, the q values could not be calculated for Tb due to the highly quenched values; Sm lifetimes in water could not be measured due to sample and instrumental limitations)

Power X-ray diffraction patterns

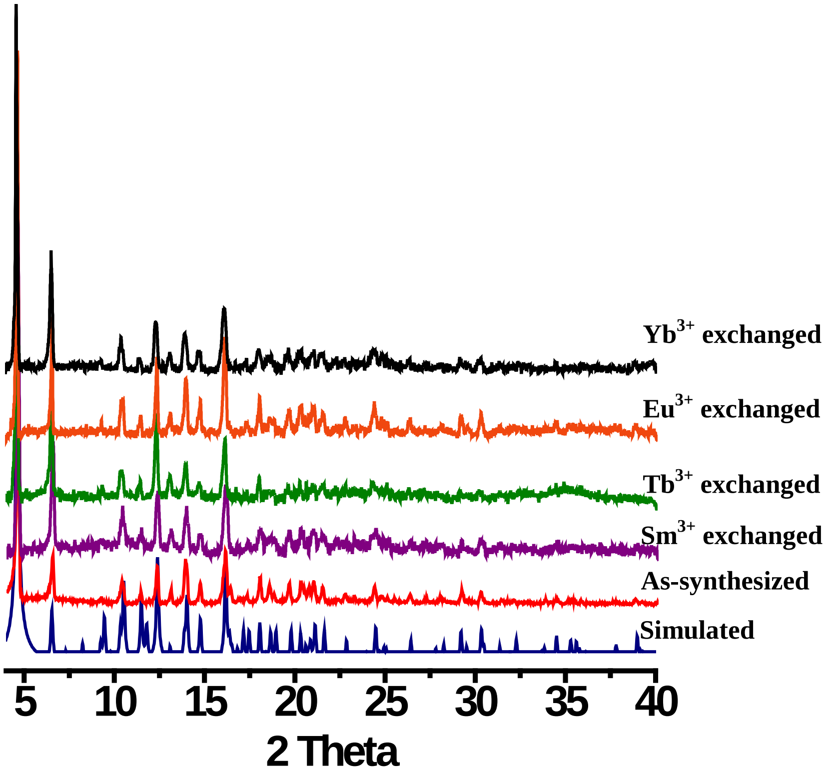

Figure S46. Powder X-Ray Diffraction of Ln@bio-MOF-1 after luminescence experiments. (navy, simulated; red, as synthesized; purple, Sm@bio-MOF-1; green, Tb@bio-MOF-1; orange, Eu@bio-MOF-1; black, Yb@bio-MOF-1)

Chapter 6

Synthesis of $Zn_8(ad)_4(BPDC)_6,O_2 \cdot 4Me_2NH_2$, 49DMF, $31H_2O$ (bio-MOF-100)

A stock solution of adenine (0.05 M) in N,N-dimethylformamide (DMF) was prepared. Ultra-sonification and heating was employed to completely dissolve adenine in DMF. A stock solution of zinc acetate dihydrate (0.05 M) and 4, 4'-biphenyldicarboxylic acid (0.1 M) in DMF was prepared. Adenine stock solution (2.5 mL, 0.125 mmol), zinc acetate dihydrate stock solution (5 mL, 0.25 mmol) and 4, 4'-biphenyldicarboxylic acid stock solution (2.5 mL, 0.25 mmol) were added to a 20 mL vial. 2.5 mL of DMF, 1 mL of methanol and 0.25 mL of nanopure water was followed. The vial was sealed with the cap, and heated at 85 °C for 24 hours, and then cooled to rt. The resultant colorless cubic crystals were washed with DMF (3 mL x 3) and dried under Ar gas (30 min) (yield: 0.218 g, 25.4 % based on a denine). ***Elemental analysis*** $C_{259}H_{501}N_{73}O_{106}Zn_8$=$Zn_8(ad)_4(BPDC)_6,O_2 \cdot 4Me_2NH_2$, 49DMF, $31H_2O$ Calcd. C, 45.37; H, 7.36; N, 14.91. Found C, 45.43; H, 7.51; N, 14.84. ***FT-IR*** **:** (KBr 4000-400 cm^{-1}) : 3341.18(br), 3185.33(br), 2929.70(w), 1669.40(s), 1607.51(s), 1547.96(w), 1467.74(w) 1386.25(s), 1255.31(w), 1212.29(m), 1176.27(w), 1152.77(m), 1097.54(m), 855.89 (m) 843.48(m), 773.25(s).

Figure S47. Photographs of $Zn_8(ad)_4(BPDC)_6,O_2 \cdot 4Me_2NH_2$, 49DMF, $31H_2O$ (bio-MOF-100).

Low-Pressure Gas Adsorption Measurements

Conventional activation

Sorption isotherm studies of $Zn_8(ad)_4(BPDC)_6,O_2 \cdot 4Me_2NH_2$, 49DMF, $31H_2O$ (bio-MOF-100) were performed volumetrically as a function of relative pressure by using the Autosorb 1 by Quantachrome. Samples of either DMF washed materials or $CHCl_3$-exchanged materials were weighed using an AB54-S/FACT (Mettler Toledo) electrogravimetric balance (sensitivity 0.1 mg). 9 mm large bulb cells (from Quantachrome) of a known weight were loaded with ~100 mg of sample for gas sorption experiments. The samples were degassed at rt or 100 °C for 22-24 hours on degassing station until the outgas rate was no more than 3.5 mTorr/min. The degassed sample and sample cell were weighed precisely and then transferred back to the analyzer. The temperature of each sample for N_2 adsorption experiments was controlled by a refrigerated bath of liquid nitrogen (77 K).

Supercritical Drying

The samples were activated in supercritical drying method with collaboration with Professor Joe Hupp at Northwestern University. The general supercritical drying method is performed according to the published procedures.[119] The samples were evacuated with supercritical CO_2 in a Tousimis ™ Samdri® PVT-30 critical point dryer. Prior to dying the DMF solvated samples were soaked in absolute ethanol (EtOH), replacing the soaking solution for 24 hrs for 48 hrs, to exchange the occluded solvent for EtOH. After the EtOH exchange process was complete the samples were placed inside the dryer and the ethanol was exchanged with $CO_{2(L)}$ over a period of 6hrs. During this time the liquid CO_2 was vented under positive pressure for five minutes each hour. The rate of venting of $CO_{2(L)}$ was always kept below the rate of filling so as to maintain a full drying chamber. After 6 hrs of venting and soaking with $CO_{2(L)}$ the chamber was sealed and the temperature was raised to 40 °C. This brought the chamber pressure to around 1300 psi above the critical point of CO_2. The chamber was over the course of 12-18 hrs. The dried samples were placed in sealed containers and stored in a desiccator.

Samples of the supercritical CO_2 dried materials were weighed using an AB54-S/FACT (Mettler Toledo) electrogravimetric balance (sensitivity 0.1 mg). 9 mm large bulb cells (from Quantachrome) of a known weight were loaded with ~50 mg of sample for gas sorption experiments. The samples were degassed at rt for 24 hours on degassing station until the outgas rate was no more than 3.5 mTorr/min. The degassed sample and sample cell were weighed precisely and then transferred back to the analyzer. The temperature of each sample for N_2 and H_2 adsorption experiments was controlled by a refrigerated bath of either liquid nitrogen (77 K) or liquid argon (87 K). CO_2 isotherms (273 K, 298 K) were measured in a temperature-controlled water bath. The N_2, CO_2, and H_2 adsorbates were of UHP grade.

Single Crystal X-ray Diffraction Studies

Crystallographic data and structure refinements for Zn(adeninate)(pyridine)(NO_3) · 3.8DMF

An X-ray crystal structure was determined for Zn(adeninate)(pyridine)(NO_3) · 3.8DMF (**1**), using a single crystal on a Bruker Smart Apex CCD diffractometer with graphite-monochromated MoKα (λ= 0.71073 A) radiation. The parameters used during the collection of diffraction data are summarized in Table S7. The crystal was mounted in fluorolube on a glass loop and collected at 203K under nitrogen.

Zn(adeninate)(pyridine)(NO_3) · 3.8DMF (**1**) was assigned to centrosymmetric $P\ 2_1/n$ based on unit-cell parameters and systematic absences. Unit-cell dimensions were derived from the least-squares fit of the angular settings of 1329 reflections. Data were corrected for absorption using the Bruker program Sadabs. The structure was solved via direct methods which located the positions of all non-hydrogen atoms, which were refined anisotropically except for the pyridine carbon atoms. Idealized atom positions were calculated for all hydrogen atoms (*d*-(C-H) = 0.96A, $U = 1.2U_{iso}$ of attached carbon).

The structure forms a 1-dimensionl polymer with Zn atoms linked by adenines. Each zinc is also coordinated to a pyridine (N-bound) and a disordered anion. Despite multiple crystal growing attempts and several X-ray data collections we consistently obtain structures where the bound anion is disordered and difficult to identify absolutely. We have tentatively assigned it as a disordered nitrate with O2 and O2’ at half-occupancy each, but acetate is also a possibility.

After refinement no chemically identifiable peaks remained. However, Platon Squeeze found large void areas in the packing which could accommodate solvent molecules (2 voids of 307 e^- $/A^3$ per unit-cell, with about 101 electrons each). We did not use Squeeze to modify the reflection data. Attempts at modeling the disordered solvent were unsuccessful. All computer programs used in the data collection and refinements are contained in the Bruker program packages SMART (vers. 5.625), SAINT (vers. 6.22), and SHELXTL (vers. 6.10) and Platon (Spek, A.L. (1990) **Acta Cryst. A46**, C34).

Table S8. Crystal data and structure refinement for Zn(adeninate)(pyridine)(NO_3) · 3.8DMF.

Identification code		
Empirical formula	C10 H9 N7 O3 Zn	
Formula weight	340.61	
Temperature	173(2) K	
Wavelength	0.71073 Å	
Crystal system	Monoclinic	
Space group	P2(1)/n	
Unit cell dimensions	a = 10.5724(14) Å	α= 90°.
	b = 9.7181(13) Å	β= 102.840(3)°.
	c = 18.074(2) Å	γ = 90°.
Volume	1810.6(4) Å^3	
Z	4	
Density (calculated)	1.250 Mg/m^3	
Absorption coefficient	1.373 mm^{-1}	
F(000)	688	
Crystal size	0.14 x 0.15 x 0.31 mm^3	
Theta range for data collection	2.31 to 25.00°.	
Index ranges	-12<=h<=12, -11<=k<=11, -21<=l<=21	
Reflections collected	14039	
Independent reflections	3190 [R(int) = 0.0437]	
Completeness to theta = 25.00°	99.8 %	
Absorption correction	multi-scan	
Refinement method	Full-matrix least-squares on F^2	
Data / restraints / parameters	3190 / 4 / 163	
Goodness-of-fit on F^2	1.503	
Final R indices [I>2sigma(I)]	R1 = 0.1427, wR2 = 0.3858	
R indices (all data)	R1 = 0.1746, wR2 = 0.4079	
Largest diff. peak and hole	1.530 and -0.959 e.Å^{-3}	

Table S9. Atomic coordinates (x 10^4) and equivalent isotropic displacement parameters ($Å^2$x10^3) for Zn(adeninate)(pyridine)(NO_3) · 3.8DMF. U(eq) is defined as one third of the trace of the orthogonalized U_{ij} tensor.

	x	y	z	U(eq)
Zn	8998(1)	3208(1)	2300(1)	77(1)
O(1)	9580(15)	3926(14)	1448(6)	141(5)
O(2)	9470(40)	5000(40)	520(20)	260(20)
O(2')	8340(40)	4250(30)	970(11)	230(20)
O(3)	9900(30)	5970(40)	1828(16)	331(16)
N(1)	6712(8)	6302(8)	2923(4)	67(2)
N(2)	7918(8)	4474(8)	2762(4)	72(2)
N(3)	7569(11)	3061(9)	3808(5)	85(3)
N(4)	6121(9)	4115(8)	4497(4)	84(3)
N(5)	5141(9)	6249(9)	4198(5)	88(3)
N(7)	9510(30)	5000(20)	1222(17)	246(18)
C(1)	7487(10)	5673(10)	2534(5)	73(3)
C(2)	7385(11)	4232(10)	3370(5)	77(3)
C(3)	6897(13)	3116(11)	4336(6)	85(3)
C(4)	5913(10)	5270(11)	4052(6)	78(3)
C(5)	6617(10)	5349(10)	3461(5)	72(3)
N(6)	10718(9)	2981(11)	3019(6)	108(3)
C(6)	11844(13)	3111(13)	2748(7)	191(10)
C(7)	13049(9)	3019(16)	3246(12)	282(18)
C(8)	13128(13)	2797(19)	4015(11)	195(9)
C(9)	12002(19)	2670(20)	4285(6)	307(17)
C(10)	10797(14)	2758(16)	3788(6)	222(11)

Table S10. Bond lengths [Å] and angles [°] for Zn(adeninate)(pyridine)(NO_3) · 3.8DMF.

Zn-O(1)	1.912(9)
Zn-N(6)	1.998(9)
Zn-N(2)	1.985(7)
Zn-N(1)#1	2.006(8)
O(1)-N(7)	1.12(2)
O(1)-O(2')	1.44(4)
O(2)-N(7)	1.25(3)
O(2')-N(7)	1.43(3)
O(3)-N(7)	1.44(3)
N(1)-C(1)	1.340(10)
N(1)-C(5)	1.363(11)
N(1)-Zn#2	2.006(8)
N(2)-C(1)	1.285(11)
N(2)-C(2)	1.362(10)
N(3)-C(3)	1.310(13)
N(3)-C(2)	1.375(13)
N(4)-C(4)	1.371(14)
N(4)-C(3)	1.344(13)
N(5)-C(4)	1.317(13)
N(5)-H(5A)	0.8800
N(5)-H(5B)	0.8800
C(1)-H(1A)	0.9500
C(2)-C(5)	1.388(13)
C(3)-H(3A)	0.9500
C(4)-C(5)	1.433(11)
N(6)-C(6)	1.3900
N(6)-C(10)	1.3900
C(6)-C(7)	1.3900
C(6)-H(6A)	0.9500
C(7)-C(8)	1.3900
C(7)-H(7A)	0.9500
C(8)-C(9)	1.3900
C(8)-H(8A)	0.9500

C(9)-C(10)	1.3900
C(9)-H(9A)	0.9500
C(10)-H(10A)	0.9500
O(1)-Zn-N(6)	98.9(6)
O(1)-Zn-N(2)	115.5(4)
N(6)-Zn-N(2)	108.7(4)
O(1)-Zn-N(1)#1	110.4(5)
N(6)-Zn-N(1)#1	105.9(4)
N(2)-Zn-N(1)#1	115.6(3)
N(7)-O(1)-O(2')	66.5(16)
N(7)-O(1)-Zn	129.0(13)
O(2')-O(1)-Zn	98.5(15)
O(1)-O(2')-N(7)	46.0(15)
C(1)-N(1)-C(5)	102.4(8)
C(1)-N(1)-Zn#2	124.1(6)
C(5)-N(1)-Zn#2	133.4(6)
C(1)-N(2)-C(2)	103.6(7)
C(1)-N(2)-Zn	128.6(5)
C(2)-N(2)-Zn	127.7(7)
C(3)-N(3)-C(2)	110.8(8)
C(4)-N(4)-C(3)	119.4(8)
C(4)-N(5)-H(5A)	120.0
C(4)-N(5)-H(5B)	120.0
H(5A)-N(5)-H(5B)	120.0
O(3)-N(7)-O(1)	111(3)
O(3)-N(7)-O(2)	135(3)
O(1)-N(7)-O(2)	111(3)
O(3)-N(7)-O(2')	132(2)
O(1)-N(7)-O(2')	68(2)
O(2)-N(7)-O(2')	81(3)
N(2)-C(1)-N(1)	117.4(7)
N(2)-C(1)-H(1A)	121.3
N(1)-C(1)-H(1A)	121.3
N(3)-C(2)-N(2)	125.3(9)
N(3)-C(2)-C(5)	126.1(8)
N(2)-C(2)-C(5)	108.6(8)

N(3)-C(3)-N(4)	130.0(9)
N(3)-C(3)-H(3A)	115.0
N(4)-C(3)-H(3A)	115.0
N(5)-C(4)-N(4)	120.0(8)
N(5)-C(4)-C(5)	123.9(10)
N(4)-C(4)-C(5)	116.0(9)
N(1)-C(5)-C(2)	108.0(7)
N(1)-C(5)-C(4)	134.5(9)
C(2)-C(5)-C(4)	117.5(9)
C(6)-N(6)-C(10)	120.0
C(6)-N(6)-Zn	119.2(7)
C(10)-N(6)-Zn	120.8(7)
C(7)-C(6)-N(6)	120.0
C(7)-C(6)-H(6A)	120.0
N(6)-C(6)-H(6A)	120.0
C(6)-C(7)-C(8)	120.0
C(6)-C(7)-H(7A)	120.0
C(8)-C(7)-H(7A)	120.0
C(9)-C(8)-C(7)	120.0
C(9)-C(8)-H(8A)	120.0
C(7)-C(8)-H(8A)	120.0
C(10)-C(9)-C(8)	120.0
C(10)-C(9)-H(9A)	120.0
C(8)-C(9)-H(9A)	120.0
C(9)-C(10)-N(6)	120.0
C(9)-C(10)-H(10A)	120.0
N(6)-C(10)-H(10A)	120.0

Symmetry transformations used to generate equivalent atoms:

#1 -x+3/2,y-1/2,-z+1/2   #2 -x+3/2,y+1/2,-z+1/2

Table S11. Anisotropic displacement parameters (Å^{2}x 10^3) for Zn(adeninate)(pyridine)(NO$_3$) · 3.8DMF. The anisotropic displacement factor exponent takes the form: -2p^2 [h^2 a^{*2}U^{11} + ... + 2 h k a* b* U^{12}]

	U^{11}	U^{22}	U^{33}	U^{23}	U^{13}	U^{12}
Zn	106(1)	81(1)	66(1)	-5(1)	66(1)	-2(1)
O(1)	241(14)	124(9)	101(8)	18(6)	126(9)	26(9)
O(2)	320(50)	260(40)	290(50)	140(30)	220(40)	50(30)
O(2')	520(60)	125(19)	33(9)	-44(10)	40(20)	-50(30)
O(3)	420(40)	360(40)	260(30)	10(30)	190(30)	120(30)
N(1)	95(6)	68(5)	54(4)	-2(4)	49(4)	-3(4)
N(2)	112(6)	64(5)	59(4)	1(4)	60(4)	-2(4)
N(3)	130(7)	85(6)	59(5)	3(4)	59(5)	10(5)
N(4)	141(8)	69(5)	69(5)	-10(4)	78(5)	-8(5)
N(5)	140(8)	75(5)	81(6)	-13(4)	90(6)	-10(5)
N(7)	340(40)	190(20)	300(40)	90(30)	270(40)	80(20)
C(1)	109(8)	75(7)	55(5)	-6(5)	61(5)	-7(5)
C(2)	125(8)	71(6)	57(5)	-11(4)	67(6)	-13(5)
C(3)	138(10)	86(7)	50(5)	1(4)	62(6)	-7(6)
C(4)	98(7)	90(7)	64(6)	-22(5)	59(5)	-27(5)
C(5)	105(7)	83(6)	45(5)	-5(4)	51(5)	-9(5)
N(6)	110(8)	156(10)	72(6)	2(6)	52(6)	13(6)

Table S12. Hydrogen coordinates (x 10^4) and isotropic displacement parameters (Å^{2}x 10^3) for Zn(adeninate)(pyridine)(NO_3) · 3.8DMF.

	x	y	z	U(eq)
H(5A)	4760	6160	4581	106
H(5B)	5008	6991	3912	106
H(1A)	7709	6097	2107	88
H(3A)	6970	2328	4653	102
H(6A)	11790	3263	2223	229
H(7A)	13819	3108	3061	339
H(8A)	13952	2734	4355	234
H(9A)	12056	2514	4811	369
H(10A)	10027	2669	3973	267

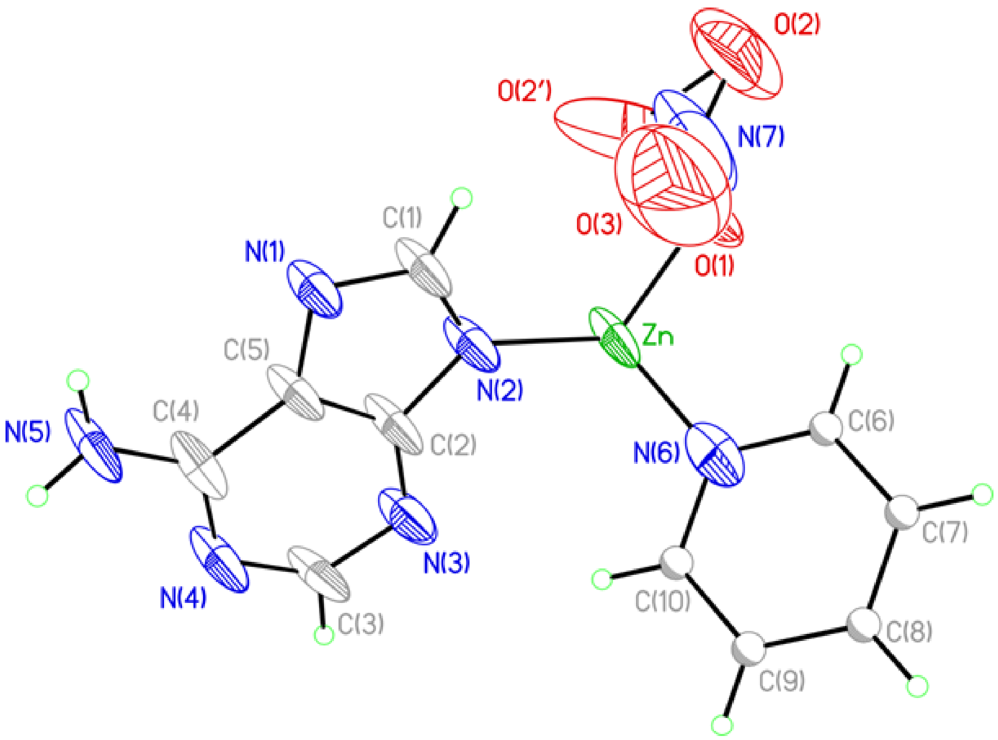

Figure S48. The building unit and asymmetric unit present in crystalline Zn(adeninate)(pyridine)(nitrate) · 3.8DMF with all atoms of the zinc-adeninate 1-D polymer represented by thermal ellipsoids drawn at the 35 % probability level.

Crystallographic data and structure refinements for Zn(adeninate)(bipy)(trifluoroacetate) · 5DMF, $0.75H_2O$

An X-ray crystal structure was determined for Zn(adeninate)(bipyridine)(trifluoroacetate) · 5DMF, $0.75H_2O$ (**2**) using a single crystal on a Bruker Smart Apex CCD diffractometer with graphite-monochromated MoKα (λ= 0.71073 A) radiation. The parameters used during the collection of diffraction data are summarized in Table S12. The crystal was mounted in a capillary and data collected at room tempereature.

Zn(adeninate)(bipyridine)(trifluoroacetate) · 5 DMF, $0.75H_2O$ (**2**) was assigned to centrosymmetric P $2_1/c$ based on unit-cell parameters and systematic absences. Unit-cell dimensions were derived from the least-squares fit of the angular settings of 2660. Data were corrected for absorption using the Bruker program Sadabs. The structure was solved via direct methods which located the positions of all non-hydrogen atoms, which were refined anisotropically. Idealized atom positions were calculated for all hydrogen atoms (*d*-(C-H) = 0.96A, $U = 1.2U_{iso}$ of attached carbon). The structure forms a two dimensional polymer with Zn bridged by adenines in one direction and bridged by 1,2-bis(4-pyridyl)ethane in an orthogonal direction. The environment about Zn is best described as distorted trigonal bipyramidal.

After refinement no large residual peaks remained. However, Platon Squeeze found large void areas in the packing which could accommodate solvent molecules (2 voids of 731 e/A3 per unit-cell, with about 75 electrons each). We did not use Squeeze to modify the reflection data. Attempts at modeling the disordered solvent were unsuccessful. All computer programs used in the data collection and refinements are contained in the Bruker program packages SMART (vers.

5.625), SAINT (vers. 6.22), and SHELXTL (vers. 6.10) and Platon (Spek, A.L. (1990) **Acta Cryst. A46**, C34).

Table S13. Crystal data and structure refinement for Zn(adeninate)(bipyridine)(trifluoroacetate) · 5DMF, $0.75H_2O$.

Identification code		
Empirical formula	C19 H16 F3 N7 O2 Zn	
Formula weight	496.76	
Temperature	298(2) K	
Wavelength	0.71073 Å	
Crystal system	Monoclinic	
Space group	P2(1)/c	
Unit cell dimensions	a = 13.829(3) Å	α= 90°.
	b = 22.070(5) Å	β= 95.983(5)°.
	c = 10.742(2) Å	γ = 90°.
Volume	3260.7(13) $Å^3$	
Z	4	
Density (calculated)	1.012 Mg/m^3	
Absorption coefficient	0.791 mm^{-1}	
F(000)	1008	
Crystal size	0.14 x 0.16 x 0.28 mm^3	
Theta range for data collection	1.74 to 25.00°.	
Index ranges	-16<=h<=16, -26<=k<=26, -12<=l<=12	
Reflections collected	25589	
Independent reflections	5715 [R(int) = 0.0682]	
Completeness to theta = 25.00°	99.7 %	
Absorption correction	Multi-scan (Sadabs)	
Refinement method	Full-matrix least-squares on F^2	
Data / restraints / parameters	5715 / 3 / 290	
Goodness-of-fit on F^2	1.611	
Final R indices [I>2sigma(I)]	R1 = 0.0842, wR2 = 0.2197	
R indices (all data)	R1 = 0.1253, wR2 = 0.2308	
Extinction coefficient	0.0053(10)	
Largest diff. peak and hole	1.059 and -0.466 e.$Å^{-3}$	

Table S14. Atomic coordinates (x 10^4) and equivalent isotropic displacement parameters (Å^{2}x10^3) for Zn(adeninate)(bipyridine)(trifluoroacetate) · 5DMF, 0.75H_2O. U(eq) is defined as one third of the trace of the orthogonalized U_{ij} tensor.

	x	y	z	U(eq)
Zn	6079(1)	8114(1)	8321(1)	41(1)
N(1)	6063(3)	7461(2)	9608(4)	41(1)
C(1)	6149(4)	7480(2)	10872(5)	40(1)
O(1)	6136(3)	8998(2)	8759(4)	61(1)
F(1)	6144(9)	10173(3)	9010(9)	236(6)
N(2)	5607(5)	6654(3)	8178(5)	76(2)
C(2)	5798(5)	6873(3)	9333(5)	48(2)
O(2)	6722(6)	8913(3)	10717(5)	127(3)
F(2)	6186(11)	10073(3)	10905(9)	269(7)
C(3)	5353(7)	6072(4)	8200(7)	99(3)
N(3)	5270(5)	5712(3)	9191(5)	88(2)
F(3)	7370(8)	10048(4)	9967(16)	284(8)
N(4)	5963(3)	6962(2)	11439(4)	38(1)
C(4)	5452(5)	5947(3)	10373(6)	60(2)
N(5)	5342(5)	5585(2)	11332(5)	80(2)
C(5)	5736(4)	6564(3)	10452(5)	44(1)
C(6)	8265(7)	7768(7)	9128(12)	176(7)
C(7)	9297(9)	7759(11)	9090(20)	323(16)
N(7)	14439(4)	8161(3)	8294(6)	61(2)
N(8)	7717(4)	8081(3)	8359(6)	65(2)
C(8)	9732(8)	8076(8)	8216(17)	182(7)
C(9)	9158(8)	8381(7)	7453(12)	165(6)
C(10)	8163(6)	8397(5)	7569(11)	134(5)
C(11)	10745(12)	8051(11)	7830(20)	317(17)
C(12)	11413(11)	7999(10)	8906(19)	256(11)
C(13)	12465(8)	8095(6)	8583(15)	151(5)
C(14)	13059(7)	8347(5)	9422(11)	115(4)
C(15)	14029(6)	8366(4)	9249(9)	100(3)
C(16)	13879(6)	7896(6)	7473(11)	141(5)

C(17)	12829(9)	7862(9)	7511(15)	242(10)
C(18)	6459(5)	9195(3)	9799(7)	62(2)
C(19)	6531(12)	9858(5)	9864(13)	128(4)

Table S15. Bond lengths [Å] and angles [°] for Zn(adeninate)(bipyridine)(trifluoroacetate) · 5DMF, 0.75H_2O.

Zn-N(1)	1.999(4)
Zn-O(1)	2.007(4)
Zn-N(4)#1	2.018(4)
Zn-N(8)	2.263(5)
Zn-N(7)#2	2.267(5)
N(1)-C(1)	1.352(6)
N(1)-C(2)	1.372(7)
C(1)-N(4)	1.334(6)
C(1)-H(1A)	0.9300
O(1)-C(18)	1.238(7)
F(1)-C(19)	1.229(13)
N(2)-C(3)	1.333(9)
N(2)-C(2)	1.331(7)
C(2)-C(5)	1.392(8)
O(2)-C(18)	1.190(8)
F(2)-C(19)	1.347(15)
C(3)-N(3)	1.342(9)
C(3)-H(3A)	0.9300
N(3)-C(4)	1.370(8)
F(3)-C(19)	1.227(14)
N(4)-C(5)	1.387(7)
N(4)-Zn#3	2.018(4)
C(4)-N(5)	1.326(7)
C(4)-C(5)	1.417(8)
N(5)-H(5A)	0.8600
N(5)-H(5B)	0.8600
C(6)-N(8)	1.266(11)
C(6)-C(7)	1.432(15)
C(6)-H(6A)	0.9300
C(7)-C(8)	1.358(18)
C(7)-H(7A)	0.9300
N(7)-C(16)	1.255(11)
N(7)-C(15)	1.304(9)

N(7)-Zn#4	2.267(5)
N(8)-C(10)	1.302(10)
C(8)-C(9)	1.273(15)
C(8)-C(11)	1.505(14)
C(9)-C(10)	1.395(13)
C(9)-H(9A)	0.9300
C(10)-H(10A)	0.9300
C(11)-C(12)	1.410(17)
C(11)-H(11A)	0.9700
C(11)-H(11B)	0.9700
C(12)-C(13)	1.546(14)
C(12)-H(12A)	0.9700
C(12)-H(12B)	0.9700
C(13)-C(14)	1.282(15)
C(13)-C(17)	1.400(17)
C(14)-C(15)	1.374(11)
C(14)-H(14A)	0.9300
C(15)-H(15A)	0.9300
C(16)-C(17)	1.459(14)
C(16)-H(16A)	0.9300
C(17)-H(17A)	0.9300
C(18)-C(19)	1.468(13)
N(1)-Zn-O(1)	122.85(19)
N(1)-Zn-N(4)#1	128.85(18)
O(1)-Zn-N(4)#1	108.21(18)
N(1)-Zn-N(8)	92.7(2)
O(1)-Zn-N(8)	90.7(2)
N(4)#1-Zn-N(8)	89.4(2)
N(1)-Zn-N(7)#2	87.64(19)
O(1)-Zn-N(7)#2	88.51(19)
N(4)#1-Zn-N(7)#2	90.9(2)
N(8)-Zn-N(7)#2	179.2(2)
C(1)-N(1)-C(2)	103.9(4)
C(1)-N(1)-Zn	131.7(4)
C(2)-N(1)-Zn	123.7(4)
N(4)-C(1)-N(1)	115.5(5)

N(4)-C(1)-H(1A)	122.3
N(1)-C(1)-H(1A)	122.3
C(18)-O(1)-Zn	123.7(5)
C(3)-N(2)-C(2)	111.1(6)
N(2)-C(2)-N(1)	124.5(5)
N(2)-C(2)-C(5)	127.1(6)
N(1)-C(2)-C(5)	108.4(5)
N(2)-C(3)-N(3)	129.0(7)
N(2)-C(3)-H(3A)	115.5
N(3)-C(3)-H(3A)	115.5
C(3)-N(3)-C(4)	119.2(6)
C(1)-N(4)-C(5)	103.5(4)
C(1)-N(4)-Zn#3	122.0(4)
C(5)-N(4)-Zn#3	134.6(4)
N(5)-C(4)-N(3)	117.8(5)
N(5)-C(4)-C(5)	125.9(6)
N(3)-C(4)-C(5)	116.2(6)
C(4)-N(5)-H(5A)	120.0
C(4)-N(5)-H(5B)	120.0
H(5A)-N(5)-H(5B)	120.0
N(4)-C(5)-C(2)	108.7(5)
N(4)-C(5)-C(4)	133.8(5)
C(2)-C(5)-C(4)	117.4(5)
N(8)-C(6)-C(7)	121.2(11)
N(8)-C(6)-H(6A)	119.4
C(7)-C(6)-H(6A)	119.4
C(8)-C(7)-C(6)	121.8(12)
C(8)-C(7)-H(7A)	119.1
C(6)-C(7)-H(7A)	119.1
C(16)-N(7)-C(15)	115.3(7)
C(16)-N(7)-Zn#4	122.1(6)
C(15)-N(7)-Zn#4	121.5(6)
C(6)-N(8)-C(10)	115.1(8)
C(6)-N(8)-Zn	124.0(6)
C(10)-N(8)-Zn	120.9(6)
C(9)-C(8)-C(7)	115.2(11)

C(9)-C(8)-C(11)	112.0(14)
C(7)-C(8)-C(11)	131.7(15)
C(8)-C(9)-C(10)	120.6(11)
C(8)-C(9)-H(9A)	119.7
C(10)-C(9)-H(9A)	119.7
N(8)-C(10)-C(9)	125.7(10)
N(8)-C(10)-H(10A)	117.1
C(9)-C(10)-H(10A)	117.1
C(12)-C(11)-C(8)	108.9(16)
C(12)-C(11)-H(11A)	109.9
C(8)-C(11)-H(11A)	109.9
C(12)-C(11)-H(11B)	109.9
C(8)-C(11)-H(11B)	109.9
H(11A)-C(11)-H(11B)	108.3
C(11)-C(12)-C(13)	110.8(16)
C(11)-C(12)-H(12A)	109.5
C(13)-C(12)-H(12A)	109.5
C(11)-C(12)-H(12B)	109.5
C(13)-C(12)-H(12B)	109.5
H(12A)-C(12)-H(12B)	108.1
C(14)-C(13)-C(17)	118.6(10)
C(14)-C(13)-C(12)	116.8(14)
C(17)-C(13)-C(12)	124.2(14)
C(13)-C(14)-C(15)	118.8(10)
C(13)-C(14)-H(14A)	120.6
C(15)-C(14)-H(14A)	120.6
N(7)-C(15)-C(14)	127.3(9)
N(7)-C(15)-H(15A)	116.4
C(14)-C(15)-H(15A)	116.4
N(7)-C(16)-C(17)	123.1(10)
N(7)-C(16)-H(16A)	118.4
C(17)-C(16)-H(16A)	118.4
C(16)-C(17)-C(13)	116.6(11)
C(16)-C(17)-H(17A)	121.7
C(13)-C(17)-H(17A)	121.7
O(2)-C(18)-O(1)	127.9(7)

O(2)-C(18)-C(19)	117.9(8)
O(1)-C(18)-C(19)	114.1(8)
F(3)-C(19)-F(1)	101.9(14)
F(3)-C(19)-F(2)	102.6(12)
F(1)-C(19)-F(2)	104.8(14)
F(3)-C(19)-C(18)	113.8(13)
F(1)-C(19)-C(18)	120.5(10)
F(2)-C(19)-C(18)	111.3(12)

Symmetry transformations used to generate equivalent atoms:

#1 x,-y+3/2,z-1/2 #2 x-1,y,z #3 x,-y+3/2,z+1/2

#4 x+1,y,z

Table S16. Anisotropic displacement parameters ($Å^2$x 10^3) for Zn(adeninate)(bipyridine)(trifluoroacetate) · 5DMF, 0.75H_2O. The anisotropic displacement factor exponent takes the form: $-2p^2$ [h^2 $a^{*2}U^{11}$ + ... + 2 h k a^* b^* U^{12}]

	U^{11}	U^{22}	U^{33}	U^{23}	U^{13}	U^{12}
Zn	46(1)	38(1)	40(1)	2(1)	8(1)	-2(1)
N(1)	43(3)	35(3)	46(3)	2(2)	8(2)	-4(2)
C(1)	43(3)	35(3)	41(3)	-5(2)	2(3)	-6(2)
O(1)	68(3)	45(3)	69(3)	-3(2)	-1(2)	1(2)
F(1)	430(18)	57(4)	190(8)	3(5)	-105(9)	10(6)
N(2)	142(6)	49(3)	40(3)	-4(3)	23(3)	-26(4)
C(2)	66(4)	36(3)	45(3)	-2(3)	15(3)	-8(3)
O(2)	242(9)	71(4)	63(4)	5(3)	-4(4)	-13(5)
F(2)	540(20)	101(6)	176(9)	-46(6)	94(10)	8(9)
C(3)	191(10)	62(5)	45(4)	-11(4)	25(5)	-47(6)
N(3)	170(7)	51(4)	45(3)	-7(3)	20(4)	-45(4)
F(3)	208(10)	111(6)	520(20)	27(9)	-11(12)	-68(7)
N(4)	44(3)	35(3)	38(2)	1(2)	9(2)	-6(2)
C(4)	96(5)	39(4)	45(4)	-2(3)	8(4)	-15(3)
N(5)	152(6)	44(3)	44(3)	-2(3)	12(4)	-32(4)
C(5)	51(4)	38(3)	45(3)	-4(3)	11(3)	-9(3)
C(6)	45(6)	309(18)	177(12)	129(12)	26(6)	38(8)
C(7)	51(8)	550(40)	360(30)	290(30)	12(11)	46(13)
N(7)	39(3)	73(4)	72(4)	-2(3)	9(3)	-3(3)
N(8)	38(3)	84(4)	72(4)	15(3)	8(3)	3(3)
C(8)	46(6)	277(19)	227(16)	112(14)	33(8)	14(9)
C(9)	54(6)	289(18)	153(11)	90(12)	11(7)	-36(9)
C(10)	51(5)	195(11)	160(10)	101(9)	24(6)	-9(6)
C(11)	107(13)	400(40)	460(40)	180(30)	90(20)	63(18)
C(12)	115(13)	310(30)	360(30)	-40(20)	100(16)	19(16)
C(13)	53(6)	195(14)	211(15)	-42(11)	47(8)	-1(7)
C(14)	67(6)	136(9)	148(10)	-41(7)	44(6)	-25(6)
C(15)	55(5)	114(7)	135(8)	-49(6)	35(5)	-5(5)
C(16)	43(5)	260(15)	120(9)	-47(9)	14(5)	0(7)

C(17)	61(8)	490(30)	177(14)	-120(17)	27(8)	-77(12)
C(18)	79(5)	48(4)	60(5)	-13(4)	8(4)	-8(4)
C(19)	165(12)	86(8)	125(10)	-13(8)	-22(9)	-28(8)

Table S17. Hydrogen coordinates (x 10^4) and isotropic displacement parameters (Å^{2}x 10^3) for Zn(adeninate)(bipyridine)(trifluoroacetate) · 5DMF, 0.75H_2O.

	x	y	z	U(eq)
H(1A)	6325	7831	11317	48
H(3A)	5215	5890	7422	118
H(5A)	5162	5215	11201	96
H(5B)	5451	5719	12085	96
H(6A)	7992	7540	9730	211
H(7A)	9680	7530	9675	387
H(9A)	9405	8597	6813	198
H(10A)	7785	8655	7034	161
H(11A)	10807	7707	7280	381
H(11B)	10877	8417	7372	381
H(12A)	11356	7600	9271	307
H(12B)	11262	8297	9519	307
H(14A)	12838	8513	10135	137
H(15A)	14439	8546	9884	120
H(16A)	14147	7712	6809	169
H(17A)	12422	7695	6857	290

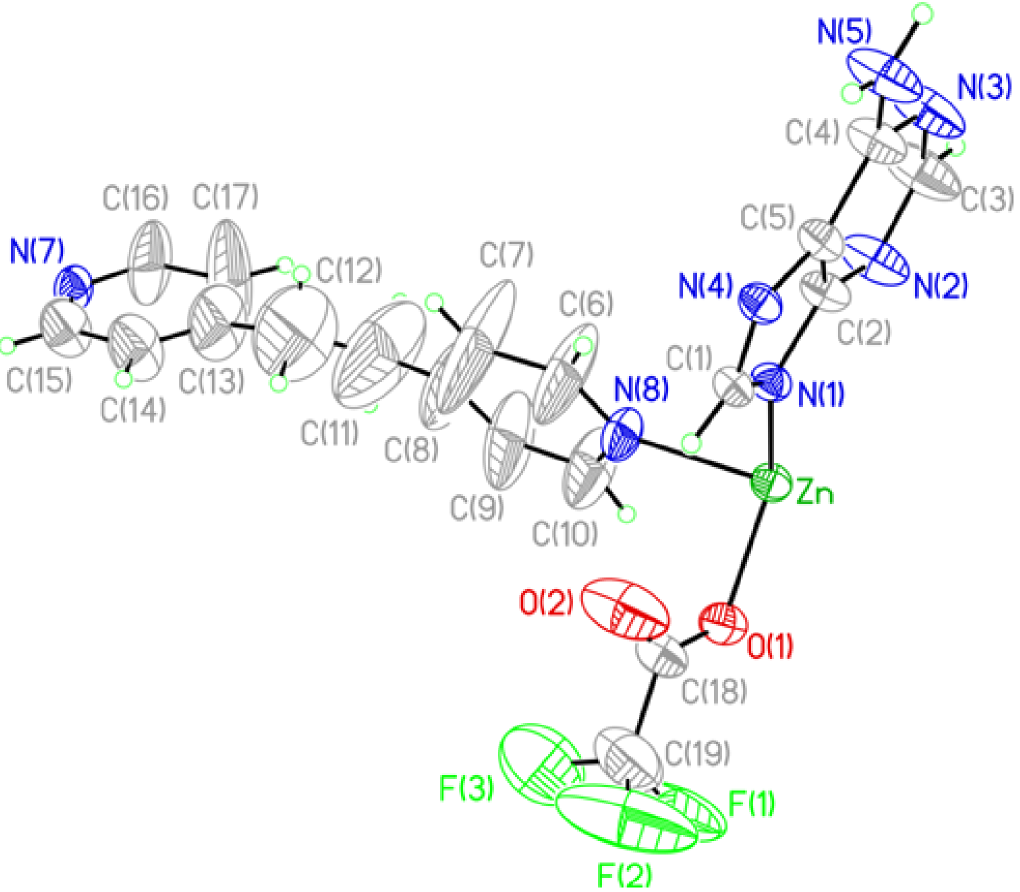

Figure S49. The building unit and asymmetric unit present in crystalline Zn(adeninate)(bipyridine) (trifluoroacetate) · 5DMF, 0.75H_2O with all atoms of the zinc-adeninate 2-D polymer represented by thermal ellipsoids drawn at the 35 % probability level.

Crystallographic data and structure refinements for $Zn_6(adeninate)_6(pyridine)_6(acetate)_6 \cdot 9DMF$

An X-ray crystal structure was determined for $Zn_6(adeninate)_6(pyridine)_6(acetate)_6 \cdot 9DMF$ (**3**), using a single crystal on a Bruker Smart Apex CCD diffractometer with graphite-monochromated MoKα (λ= 0.71073 A) radiation. The parameters used during the collection of diffraction data are summarized in Table S17. The crystal was adhered to a fine glass fiber with epoxy and placed in a cold N_2 stream (150 K) for data collection.

Unit-cell parameters and systematic absences indicated (**3)** crystallized in one of five rhombohedral space groups having equivalent systematic absences. Centrosymmetric R-3 was chosen based on *E*-values and the successful solution and refinement of the structure. Unit-cell dimensions were derived from the least-squares fit of the angular settings of 451 reflections obtained from 3 orthogonal sets of 20 frames. Data were corrected for absorption using the Bruker program Sadabs.

The structure was solved via direct methods which located the positions of all non-hydrogen atoms, which were refined anisotropically. Idealized atom positions were calculated for all hydrogen atoms (d-(C-H) = 0.96A, $U = 1.2U_{iso}$ of attached carbon). The structure consists of Zn-adenine units arranged in a cyclic hexamer, with Zn atoms coordinated to two adenines at the N1 and N2 positions. Each zinc is also *O*-bound to an acetate anion and *N*-bound to pyridine. The geometry about the Zn atoms may be described as a distorted tetrahedron.

After refinement some large residual peaks remained centered on or about a (0,0,0) 3-bar site. Additionally, Platon found large void areas in the packing which could accommodate solvent molecules. Elemental analysis indicated approximately 1.5 dimethyl formamides per Zn hexamer. Attempts at modeling the disordered solvent were unsuccessful. The Fobs component attributable to the disordered solvent was removed with the platon/Squeeze program. All computer programs used in the data collection and refinements are contained in the Bruker program packages SMART (vers. 5.625), SAINT (vers. 6.22), and SHELXTL (vers. 6.10) and Platon (Spek, A.L. (1990) **Acta Cryst. A46**, C34).

Table S18. Crystal data and structure refinement for $Zn_6(ad)_6(py)_6(acetate)_6 \cdot 9DMF$.

Identification code		
Empirical formula	C12 H12 N6 O2 Zn	
Formula weight	337.65	
Temperature	295(2) K	
Wavelength	0.71073 Å	
Crystal system	Rhombohedral	
Space group	R-3	
Unit cell dimensions	a = 17.7407(18) Å	α= 90°.
	b = 17.7407(18) Å	β= 90°.
	c = 33.450(3) Å	γ = 120°.
Volume	9117.3(16) $Å^3$	
Z	18	
Density (calculated)	1.107 Mg/m^3	
Absorption coefficient	1.222 mm^{-1}	
F(000)	3096	
Crystal size	0.18 x 0.22 x 0.26 mm^3	
Theta range for data collection	1.46 to 24.98°.	
Index ranges	-21<=h<=21, -21<=k<=21, -39<=l<=39	
Reflections collected	24288	
Independent reflections	3544 [R(int) = 0.0703]	
Completeness to theta = 24.98°	99.7 %	
Absorption correction	multi-scan (SADABS)	
Refinement method	Full-matrix least-squares on F^2	
Data / restraints / parameters	3544 / 0 / 190	
Goodness-of-fit on F^2	0.959	
Final R indices [I>2sigma(I)]	R1 = 0.0444, wR2 = 0.1111	
R indices (all data)	R1 = 0.0622, wR2 = 0.1187	
Largest diff. peak and hole	0.351 and -0.227 e.$Å^{-3}$	

Table S19. Atomic coordinates (x 10^4) and equivalent isotropic displacement parameters (Å^{2}x10^3) for $Zn_6(ad)_6(py)_6(acetate)_6\cdot 9DMF$. U(eq) is defined as one third of the trace of the orthogonalized U_{ij} tensor.

	x	y	z	U(eq)
Zn	6498(1)	7439(1)	1203(1)	57(1)
N(1)	5635(2)	6168(2)	1294(1)	54(1)
C(1)	5345(2)	5837(2)	1657(1)	54(1)
O(1)	6239(2)	7658(2)	671(1)	103(1)
C(2)	5190(2)	5452(2)	1048(1)	53(1)
O(2)	7193(3)	8990(2)	753(1)	153(2)
N(2)	4773(2)	4991(2)	1670(1)	52(1)
C(3)	5172(2)	5335(2)	631(1)	70(1)
N(3)	4149(2)	3923(2)	1145(1)	74(1)
N(4)	4654(2)	4523(2)	492(1)	87(1)
C(4)	4184(3)	3893(2)	755(1)	92(1)
N(5)	5627(2)	5956(2)	366(1)	101(1)
C(5)	4673(2)	4738(2)	1276(1)	53(1)
C(6)	6684(4)	8423(3)	543(1)	98(1)
N(6)	7666(2)	7500(2)	1180(1)	83(1)
C(7)	6543(5)	8606(4)	125(2)	188(3)
C(8)	7734(5)	6813(5)	1151(3)	183(4)
C(9)	8486(7)	6797(8)	1149(3)	222(4)
C(10)	9195(5)	7525(8)	1125(3)	179(3)
C(11)	9168(6)	8206(7)	1169(6)	349(11)
C(12)	8336(4)	8157(5)	1198(4)	298(8)

Table S20. Bond lengths [Å] and angles [°] for $Zn_6(ad)_6(py)_6(acetate)_6 \cdot 9DMF$.

Zn-O(1)	1.925(3)
Zn-N(2)#1	1.973(2)
Zn-N(1)	2.017(2)
Zn-N(6)	2.022(3)
N(1)-C(1)	1.336(3)
N(1)-C(2)	1.382(3)
C(1)-N(2)	1.328(4)
C(1)-H(1A)	0.9300
O(1)-C(6)	1.256(5)
C(2)-C(5)	1.367(4)
C(2)-C(3)	1.408(4)
O(2)-C(6)	1.190(5)
N(2)-C(5)	1.372(3)
N(2)-Zn#2	1.973(2)
C(3)-N(5)	1.327(4)
C(3)-N(4)	1.346(4)
N(3)-C(4)	1.308(4)
N(3)-C(5)	1.343(4)
N(4)-C(4)	1.338(4)
C(4)-H(4A)	0.9300
N(5)-H(5A)	0.8600
N(5)-H(5B)	0.8600
C(6)-C(7)	1.485(6)
N(6)-C(12)	1.179(7)
N(6)-C(8)	1.286(6)
C(7)-H(7A)	0.9600
C(7)-H(7B)	0.9600
C(7)-H(7C)	0.9600
C(8)-C(9)	1.348(10)
C(8)-H(8A)	0.9300
C(9)-C(10)	1.278(10)
C(9)-H(9A)	0.9300
C(10)-C(11)	1.242(10)

C(10)-H(10A)	0.9300
C(11)-C(12)	1.437(11)
C(11)-H(11A)	0.9300
C(12)-H(12A)	0.9300
O(1)-Zn-N(2)#1	121.00(12)
O(1)-Zn-N(1)	103.95(11)
N(2)#1-Zn-N(1)	108.39(10)
O(1)-Zn-N(6)	107.19(15)
N(2)#1-Zn-N(6)	110.46(13)
N(1)-Zn-N(6)	104.49(13)
C(1)-N(1)-C(2)	102.8(2)
C(1)-N(1)-Zn	122.64(19)
C(2)-N(1)-Zn	134.60(19)
N(2)-C(1)-N(1)	115.7(2)
N(2)-C(1)-H(1A)	122.1
N(1)-C(1)-H(1A)	122.1
C(6)-O(1)-Zn	116.6(3)
C(5)-C(2)-N(1)	109.2(2)
C(5)-C(2)-C(3)	117.5(3)
N(1)-C(2)-C(3)	133.3(3)
C(1)-N(2)-C(5)	103.9(2)
C(1)-N(2)-Zn#2	128.79(19)
C(5)-N(2)-Zn#2	127.0(2)
N(5)-C(3)-N(4)	117.7(3)
N(5)-C(3)-C(2)	125.3(3)
N(4)-C(3)-C(2)	117.0(3)
C(4)-N(3)-C(5)	110.4(3)
C(4)-N(4)-C(3)	118.2(3)
N(3)-C(4)-N(4)	130.2(3)
N(3)-C(4)-H(4A)	114.9
N(4)-C(4)-H(4A)	114.9
C(3)-N(5)-H(5A)	120.0
C(3)-N(5)-H(5B)	120.0
H(5A)-N(5)-H(5B)	120.0
N(3)-C(5)-C(2)	126.7(3)
N(3)-C(5)-N(2)	124.8(3)

C(2)-C(5)-N(2)	108.5(3)
O(2)-C(6)-O(1)	120.9(4)
O(2)-C(6)-C(7)	120.8(5)
O(1)-C(6)-C(7)	118.3(5)
C(12)-N(6)-C(8)	114.6(6)
C(12)-N(6)-Zn	123.3(4)
C(8)-N(6)-Zn	122.0(4)
C(6)-C(7)-H(7A)	109.5
C(6)-C(7)-H(7B)	109.5
H(7A)-C(7)-H(7B)	109.5
C(6)-C(7)-H(7C)	109.5
H(7A)-C(7)-H(7C)	109.5
H(7B)-C(7)-H(7C)	109.5
N(6)-C(8)-C(9)	125.6(8)
N(6)-C(8)-H(8A)	117.2
C(9)-C(8)-H(8A)	117.2
C(10)-C(9)-C(8)	117.6(9)
C(10)-C(9)-H(9A)	121.2
C(8)-C(9)-H(9A)	121.2
C(11)-C(10)-C(9)	118.6(8)
C(11)-C(10)-H(10A)	120.7
C(9)-C(10)-H(10A)	120.7
C(10)-C(11)-C(12)	119.1(9)
C(10)-C(11)-H(11A)	120.4
C(12)-C(11)-H(11A)	120.4
N(6)-C(12)-C(11)	123.6(8)
N(6)-C(12)-H(12A)	118.2
C(11)-C(12)-H(12A)	118.2

Symmetry transformations used to generate equivalent atoms:

#1 x-y+2/3,x+1/3,-z+1/3   #2 y-1/3,-x+y+1/3,-z+1/3

Table S21. Anisotropic displacement parameters ($Å^2$x 10^3) for $Zn_6(ad)_6(py)_6(acetate)_6{\cdot}9DMF$. The anisotropic displacement factor exponent takes the form: $-2p^2$ [h^2 $a^{*2}U^{11}$ + ... + 2 h k a^* b^* U^{12}]

	U^{11}	U^{22}	U^{33}	U^{23}	U^{13}	U^{12}
Zn	71(1)	51(1)	38(1)	-6(1)	7(1)	24(1)
N(1)	66(2)	52(2)	33(1)	-4(1)	8(1)	21(1)
C(1)	62(2)	58(2)	34(2)	-5(1)	2(1)	24(2)
O(1)	155(3)	62(2)	60(2)	-1(1)	-11(2)	30(2)
C(2)	66(2)	48(2)	33(2)	-2(1)	10(1)	20(2)
O(2)	203(4)	73(2)	117(3)	-7(2)	-14(3)	20(2)
N(2)	55(2)	55(2)	35(1)	4(1)	7(1)	19(1)
C(3)	92(3)	50(2)	40(2)	-6(1)	18(2)	15(2)
N(3)	92(2)	54(2)	44(2)	-1(1)	18(1)	12(2)
N(4)	120(3)	53(2)	43(2)	-8(1)	25(2)	10(2)
C(4)	123(3)	50(2)	58(2)	-9(2)	24(2)	11(2)
N(5)	151(3)	55(2)	36(2)	-4(1)	24(2)	7(2)
C(5)	66(2)	51(2)	37(2)	-2(1)	8(1)	24(2)
C(6)	145(4)	63(3)	67(3)	-2(2)	-2(3)	37(3)
N(6)	73(2)	78(2)	96(2)	4(2)	21(2)	35(2)
C(7)	308(10)	141(5)	76(4)	35(3)	-23(5)	84(6)
C(8)	145(6)	151(6)	299(11)	-24(6)	35(6)	108(5)
C(9)	189(9)	230(10)	316(13)	22(9)	82(9)	157(9)
C(10)	93(5)	197(9)	250(9)	22(7)	60(5)	73(6)
C(11)	102(6)	134(8)	790(40)	89(12)	74(10)	45(6)
C(12)	58(4)	116(5)	710(20)	48(9)	2(7)	33(4)

Table S22. Hydrogen coordinates (x 10^4) and isotropic displacement parameters ($Å^2$x 10^3) for $Zn_6(ad)_6(py)_6(acetate)_6$·9DMF.

	x	y	z	U(eq)
H(1A)	5532	6178	1887	65
H(4A)	3824	3348	644	110
H(5A)	5585	5833	116	121
H(5B)	5964	6482	445	121
H(7A)	6923	9211	67	282
H(7B)	5949	8466	92	282
H(7C)	6664	8258	-55	282
H(8A)	7220	6281	1129	220
H(9A)	8488	6275	1165	267
H(10A)	9720	7544	1075	215
H(11A)	9679	8741	1182	419
H(12A)	8326	8672	1233	358

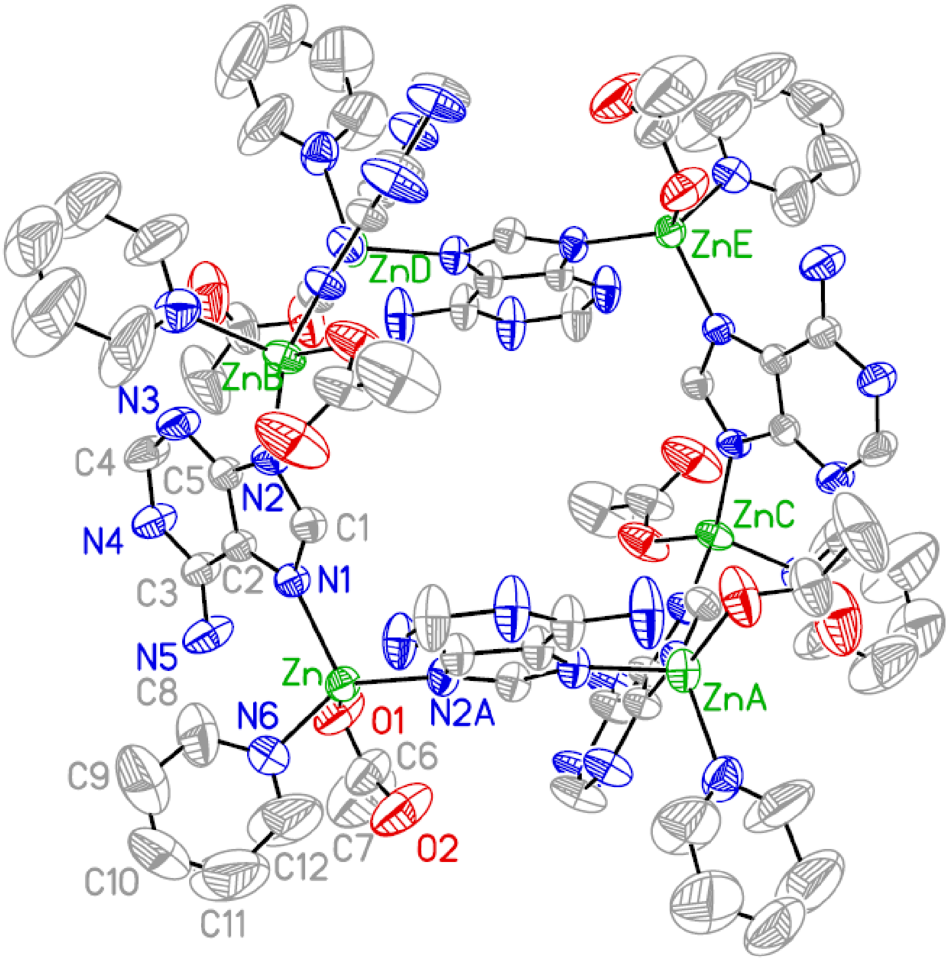

Figure S50. The building unit and asymmetric unit present in crystalline Zn_6(adeninate)$_6$ (pyridine)$_6$(acetate)$_6$ · 9DMF with all atoms of the zinc-adeninate hexameric macrocycle represented by thermal ellipsoids drawn at the 35 % probability level. All hydrogen atoms were omitted for clarity.

Crystallographic data and structure refinements for Zn_6 (adeninate)$_6$ (pyridine)$_6$ (trifluoroacetate)$_6$ · 10.8DMF, $18H_2O$

An X-ray crystal structure was determined for Zn_6(adeninate)$_6$(pyridine)$_6$ (trifluoroacetate)$_6$ · 10.8DMF, $18H_2$ (**4**), using a single crystal on a Bruker Smart Apex CCD diffractometer with graphite-monochromated MoKα (λ= 0.71073 A) radiation. The parameters used during the collection of diffraction data are summarized in Table S22. The crystal was adhered to a fine glass fiber with epoxy and placed in a cold N_2 stream (203 K) for data collection.

Unit-cell parameters and systematic absences indicated Zn_6(adeninate)$_6$(pyridine)$_6$ (trifluoroacetate)$_6$ · 10.8DMF, $18H_2$ (**4**) crystallized in one of five rhombohedral space groups having equivalent systematic absences. Centrosymmetric R-3 was chosen based on *E*-values and the successful solution and refinement of the structure. Unit-cell dimensions were derived from the least-squares fit of the angular settings of 9999 reflections. Data were corrected for absorption using the Bruker program Sadabs. The structure was solved via direct methods which located the positions of all non-hydrogen atoms, which were refined anisotropically. Idealized atom positions were calculated for all hydrogen atoms (d-(C-H) = 0.96A, $U = 1.2U_{iso}$ of attached carbon). The structure consists of Zn-adenine units arranged in a cyclic hexamer, with Zn atoms coordinated to two adenines at the N1 and N2 positions. Each zinc is also *O*-bound to an trifluoroacetate anion and *N*-bound to pyridine. The geometry about the Zn atoms may be described as a distorted tetrahedron. The crystal structure is isomorphous with the acetate anion containing hexameric macrocycle (Zn_6(ad)$_6$(py)$_6$(acetate)$_6$·9DMF) (**3**).

After refinement some large residual peaks remained centered on or about a (2/3,1/2,z) 3-bar site. Additionally, Platon found large void areas in the packing which could accommodate solvent molecules. Attempts at modeling the disordered solvent were unsuccessful. All computer programs used in the data collection and refinements are contained in the Bruker program packages SMART (vers. 5.625), SAINT (vers. 6.22), and SHELXTL (vers. 6.10) and Platon (Spek, A.L. (1990) **Acta Cryst. A46**, C34).

Table S23. Crystal data and structure refinement for Zn_6(adeninate)$_6$(pyridine)$_6$(trifluoroacetate)$_6$ · 10.8DMF,18H_2O.

Identification code		
Empirical formula	C7.20 H5.40 F1.80 N3.60 O1.20 Zn0.60	
Formula weight	234.97	
Temperature	203(2) K	
Wavelength	0.71073 Å	
Crystal system	Rhombohedral	
Space group	R-3	
Unit cell dimensions	a = 17.9994(8) Å	α= 90°.
	b = 17.9994(8) Å	β= 90°.
	c = 33.653(3) Å	γ = 120°.
Volume	9442.1(10) $Å^3$	
Z	30	
Density (calculated)	1.240 Mg/m^3	
Absorption coefficient	1.209 mm^{-1}	
F(000)	3528	
Crystal size	0.90 x 0.27 x 0.24 mm^3	
Theta range for data collection	1.78 to 32.38°.	
Index ranges	-26<=h<=26, -27<=k<=25, -50<=l<=50	
Reflections collected	39511	
Independent reflections	7210 [R(int) = 0.0533]	
Completeness to theta = 32.38°	95.8 %	
Absorption correction	None	
Max. and min. transmission	0.7602 and 0.4092	
Refinement method	Full-matrix least-squares on F^2	
Data / restraints / parameters	7210 / 0 / 217	
Goodness-of-fit on F^2	2.462	
Final R indices [I>2sigma(I)]	R1 = 0.0909, wR2 = 0.2827	
R indices (all data)	R1 = 0.1070, wR2 = 0.2901	
Largest diff. peak and hole	2.782 and -0.743 e.$Å^{-3}$	

Table S24. Atomic coordinates (x 10^4) and equivalent isotropic displacement parameters (Å^{2}x10^3) for $Zn_6(adeninate)_6(pyridine)_6(trifluoroacetate)_6 \cdot 10.8DMF,18H_2O$. U(eq) is defined as one third of the trace of the orthogonalized U_{ij} tensor.

	x	y	z	U(eq)
Zn	6004(1)	10182(1)	2899(1)	36(1)
N(1)	7243(2)	11070(2)	2969(1)	35(1)
C(1)	7578(2)	11364(2)	3329(1)	35(1)
O(1)	5708(2)	10369(3)	2364(1)	66(1)
F(1)	5438(4)	10148(7)	1582(1)	182(4)
O(2)	4346(3)	9417(4)	2435(1)	101(2)
F(2)	4118(4)	9683(8)	1671(2)	207(5)
N(2)	8406(2)	11979(2)	3328(1)	34(1)
C(2)	8634(2)	12086(2)	2935(1)	33(1)
N(3)	9418(2)	12643(2)	2791(1)	44(1)
C(3)	9436(3)	12603(3)	2398(1)	53(1)
F(3)	4912(10)	10846(10)	1777(4)	275(7)
N(4)	8819(2)	12083(3)	2150(1)	55(1)
C(4)	8031(2)	11538(3)	2299(1)	43(1)
C(5)	7928(2)	11530(2)	2714(1)	33(1)
N(5)	7402(2)	11058(3)	2037(1)	65(1)
N(6)	5941(3)	9035(3)	2872(1)	54(1)
C(6)	6656(5)	9002(4)	2833(3)	86(2)
C(7)	6696(6)	8251(6)	2803(3)	111(3)
C(8)	5962(6)	7506(5)	2804(3)	99(2)
C(9)	5243(6)	7518(5)	2804(5)	140(5)
C(10)	5256(5)	8354(4)	2875(5)	143(5)
C(11)	4939(3)	9906(4)	2244(1)	65(2)
C(12)	4792(6)	9964(11)	1809(2)	134(5)

Table S25. Bond lengths [Å] and angles [°] for Zn_6(adeninate)$_6$(pyridine)$_6$(trifluoroacetate)$_6$ · 10.8DMF,18H_2O.

Zn-O(1)	1.956(3)
Zn-N(2)#1	1.970(3)
Zn-N(1)	2.005(3)
Zn-N(6)	2.013(4)
N(1)-C(1)	1.339(4)
N(1)-C(5)	1.386(4)
C(1)-N(2)	1.339(5)
C(1)-H(1A)	0.9400
O(1)-C(11)	1.272(6)
F(1)-C(12)	1.286(10)
O(2)-C(11)	1.178(6)
F(2)-C(12)	1.153(9)
N(2)-C(2)	1.367(4)
N(2)-Zn#2	1.970(3)
C(2)-N(3)	1.349(5)
C(2)-C(5)	1.379(5)
N(3)-C(3)	1.323(5)
C(3)-N(4)	1.332(5)
C(3)-H(3A)	0.9400
F(3)-C(12)	1.49(2)
N(4)-C(4)	1.354(5)
C(4)-N(5)	1.351(5)
C(4)-C(5)	1.407(4)
N(5)-H(5A)	0.8700
N(5)-H(5B)	0.8700
N(6)-C(10)	1.229(8)
N(6)-C(6)	1.324(8)
C(6)-C(7)	1.393(11)
C(6)-H(6A)	0.9400
C(7)-C(8)	1.331(12)
C(7)-H(7A)	0.9400
C(8)-C(9)	1.305(13)

C(8)-H(8A)	0.9400
C(9)-C(10)	1.512(12)
C(9)-H(9A)	0.9400
C(10)-H(10A)	0.9400
C(11)-C(12)	1.503(9)
O(1)-Zn-N(2)#1	116.69(15)
O(1)-Zn-N(1)	105.06(13)
N(2)#1-Zn-N(1)	110.61(13)
O(1)-Zn-N(6)	104.65(19)
N(2)#1-Zn-N(6)	112.07(16)
N(1)-Zn-N(6)	107.08(16)
C(1)-N(1)-C(5)	103.5(3)
C(1)-N(1)-Zn	121.4(2)
C(5)-N(1)-Zn	135.0(2)
N(2)-C(1)-N(1)	114.8(3)
N(2)-C(1)-H(1A)	122.6
N(1)-C(1)-H(1A)	122.6
C(11)-O(1)-Zn	118.7(3)
C(1)-N(2)-C(2)	104.5(3)
C(1)-N(2)-Zn#2	130.4(2)
C(2)-N(2)-Zn#2	125.0(2)
N(3)-C(2)-C(5)	125.8(3)
N(3)-C(2)-N(2)	125.6(3)
C(5)-C(2)-N(2)	108.5(3)
C(3)-N(3)-C(2)	111.4(3)
N(3)-C(3)-N(4)	129.2(4)
N(3)-C(3)-H(3A)	115.4
N(4)-C(3)-H(3A)	115.4
C(3)-N(4)-C(4)	118.6(3)
N(5)-C(4)-N(4)	117.4(3)
N(5)-C(4)-C(5)	125.3(3)
N(4)-C(4)-C(5)	117.4(3)
C(2)-C(5)-N(1)	108.6(3)
C(2)-C(5)-C(4)	117.5(3)
N(1)-C(5)-C(4)	133.9(3)
C(4)-N(5)-H(5A)	120.0

C(4)-N(5)-H(5B)	120.0
H(5A)-N(5)-H(5B)	120.0
C(10)-N(6)-C(6)	118.0(6)
C(10)-N(6)-Zn	122.4(5)
C(6)-N(6)-Zn	119.5(4)
N(6)-C(6)-C(7)	125.0(7)
N(6)-C(6)-H(6A)	117.5
C(7)-C(6)-H(6A)	117.5
C(8)-C(7)-C(6)	118.0(8)
C(8)-C(7)-H(7A)	121.0
C(6)-C(7)-H(7A)	121.0
C(7)-C(8)-C(9)	118.5(8)
C(7)-C(8)-H(8A)	120.7
C(9)-C(8)-H(8A)	120.7
C(8)-C(9)-C(10)	119.6(7)
C(8)-C(9)-H(9A)	120.2
C(10)-C(9)-H(9A)	120.2
N(6)-C(10)-C(9)	119.9(8)
N(6)-C(10)-H(10A)	120.0
C(9)-C(10)-H(10A)	120.0
O(2)-C(11)-O(1)	126.9(5)
O(2)-C(11)-C(12)	117.3(6)
O(1)-C(11)-C(12)	115.7(5)
F(2)-C(12)-F(1)	119.4(8)
F(2)-C(12)-C(11)	123.1(8)
F(1)-C(12)-C(11)	115.4(7)
F(2)-C(12)-F(3)	90.0(12)
F(1)-C(12)-F(3)	93.0(11)
C(11)-C(12)-F(3)	101.9(10)

Symmetry transformations used to generate equivalent atoms:

#1 y-2/3,-x+y+2/3,-z+2/3 #2 x-y+4/3,x+2/3,-z+2/3

Table S26. Anisotropic displacement parameters (Å^{2}x 10^3) for Zn$_6$(adeninate)$_6$(pyridine)$_6$(trifluoroacetate)$_6$ · 10.8DMF, 18H$_2$O. The anisotropic displacement factor exponent takes the form: -2p^2 [h^2 a^{*2}U^{11} + ... + 2 h k a* b* U^{12}]

	U^{11}	U^{22}	U^{33}	U^{23}	U^{13}	U^{12}
Zn	31(1)	46(1)	23(1)	-4(1)	5(1)	14(1)
N(1)	36(2)	41(2)	20(1)	-3(1)	3(1)	12(1)
C(1)	39(2)	40(2)	19(1)	-3(1)	2(1)	15(2)
O(1)	40(2)	102(3)	30(1)	14(2)	-1(1)	15(2)
F(1)	134(5)	375(12)	42(2)	11(4)	12(3)	131(6)
O(2)	39(2)	148(5)	72(3)	7(3)	4(2)	14(2)
F(2)	117(5)	365(14)	88(4)	-5(6)	-48(4)	82(7)
N(2)	40(2)	37(2)	19(1)	-5(1)	-2(1)	16(1)
C(2)	34(2)	38(2)	21(1)	-6(1)	1(1)	14(1)
N(3)	35(2)	50(2)	28(2)	-10(1)	1(1)	7(1)
C(3)	35(2)	65(3)	29(2)	-11(2)	6(1)	2(2)
F(3)	351(17)	351(16)	192(10)	110(10)	-29(10)	228(16)
N(4)	33(2)	75(3)	27(2)	-16(2)	6(1)	4(2)
C(4)	33(2)	56(2)	23(2)	-12(2)	4(1)	9(2)
C(5)	30(2)	41(2)	20(1)	-5(1)	4(1)	12(1)
N(5)	37(2)	96(3)	20(1)	-13(2)	4(1)	1(2)
N(6)	57(2)	46(2)	58(2)	-12(2)	-5(2)	26(2)
C(6)	68(4)	64(4)	123(6)	-20(4)	4(4)	32(3)
C(7)	83(5)	91(5)	166(9)	-35(6)	4(5)	49(5)
C(8)	113(6)	84(5)	106(6)	-33(4)	-18(5)	54(5)
C(9)	82(5)	61(4)	263(15)	-29(6)	-50(7)	26(4)
C(10)	58(4)	52(4)	306(17)	6(6)	-32(6)	19(3)
C(11)	38(2)	109(4)	29(2)	2(2)	0(2)	22(3)
C(12)	84(5)	258(15)	49(4)	0(6)	-13(4)	76(7)

Table S27. Hydrogen coordinates (x 10^4) and isotropic displacement parameters (Å^{2}x 10^3) for $Zn_6(adeninate)_6(pyridine)_6(trifluoroacetate)_6 \cdot 10.8DMF, 18H_2O$.

	x	y	z	U(eq)
H(1A)	7258	11156	3564	42
H(3A)	9958	12997	2279	64
H(5A)	7512	11106	1783	78
H(5B)	6888	10701	2121	78
H(6A)	7177	9526	2825	103
H(7A)	7226	8269	2784	133
H(8A)	5961	6984	2803	119
H(9A)	4720	7010	2761	168
H(10A)	4741	8354	2921	171

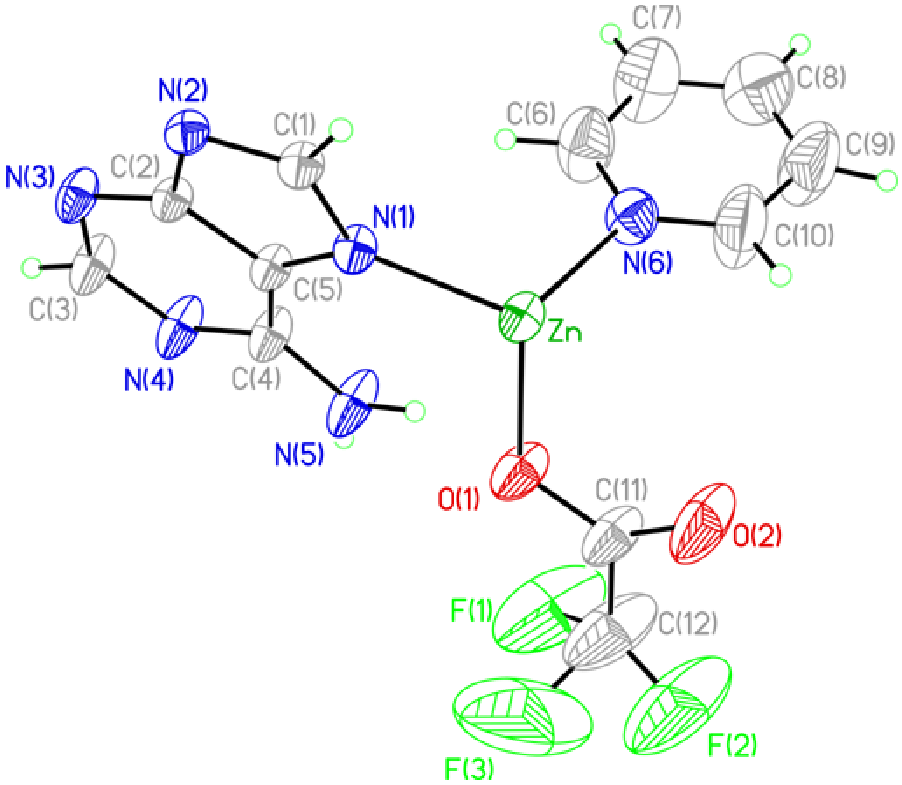

Figure S51. The building unit and asymmetric unit present in crystalline Zn_6(adeninate)$_6$ (pyridine)$_6$(trifluoroacetate)$_6$ · 10.8DMF, $18H_2O$ with all atoms represented by thermal ellipsoids drawn at the 35 % probability level.

Crystallographic data and structure refinements for Zn_6(adeninate)$_6$(pyridine)$_6$ (carbamate)$_6$ · 10.5DMF

An X-ray crystal structure was determined for Zn_6(adeninate)$_6$(pyridine)$_6$(carbamate)$_6$ ·10.5DMF (**5**), using a single crystal on a Bruker Smart Apex CCD diffractometer with graphite-monochromated MoKα (λ= 0.71073 A) radiation. The parameters used during the collection of diffraction data are summarized in Table S27. The crystal was adhered to a fine glass fiber with epoxy and placed in a cold N_2 stream (150 K) for data collection.

Unit-cell parameters and systematic absences indicated (**5**) crystallized in one of five rhombohedral space groups having equivalent systematic absences. Centrosymmetric R-3 was chosen based on *E*-values and the successful solution and refinement of the structure. Unit-cell dimensions were derived from the least-squares fit of the angular settings of 999 reflections obtained from 3 orthogonal sets of 30 frames. Data were corrected for absorption using the Bruker program Sadabs.

The structure was solved via direct methods. Remaining non-hydrogen atoms were located from subsequent difference Fourier syntheses. All non-hydrogen atoms were refined anisotropically. Idealized atom positions were calculated for all hydrogen atoms (*d*-(C-H) = 0.96A, $U = 1.2U_{iso}$ of attached carbon). The structure consists of Zn-adenine units arranged in a cyclic hexamer, with Zn atoms coordinated to two adenines at the N1 and N4 positions. Each zinc is also *O*-bound to carbamato anion and *N*-bound to pyridine. The geometry about the Zn atoms may be described as a distorted tetrahedron.

Three large residual peaks remain which are believed to be part of unresolvable disordered solvate molecules. Additionally, Platon found large void areas in the packing which could accommodate solvent molecules. These include three voids of 822 Å^3 with electron counts of 212 each and three voids of 128 Å^3 with electron counts of 44 each. Elemental analysis indicated approximately 10.5 dimethylformamides per Zn hexamer. Attempts at modeling the disordered solvent were unsuccessful. From the single crystal X-ray diffraction data, we can unambiguously determine the molecular formula for the hexameric macrocycle, which is $[C_{13}H_{15}N_7O_2Zn]_6$. This corresponds to Zn_6(adeninate)$_6$(pyridine)$_6$(carbamate)$_6$. After studying the elemental analysis data and comparing this data to thermogravimetric analysis data, we estimated that approximately 10.5 DMF molecules reside in the cavities that are distributed throughout the 3-D crystal. We note that these estimates are roughly consistent with the relatively conservative electron counts predicted by Platon. Therefore, the formula for the as-synthesized material is predicted to be Zn_6(adeninate)$_6$(pyridine)$_6$(carbamate)$_6$ • 10.5DMF.

All computer programs used in the data collection and refinements are contained in the Bruker program packages SMART (vers. 5.625), SAINT (vers. 6.22), and SHELXTL (vers. 6.14) and Platon (Spek, A.L. (1990) **Acta Cryst. A46**, C34).

Table S28. Crystal data and structure refinement for $Zn_6(adeninate)_6(pyridine)_6(carbamate)_6 \cdot 10.5DMF$.

Identification code		
Empirical formula	C78 H90 N42 O12 Zn6	
Formula weight	2200.14	
Temperature	173(2) K	
Wavelength	0.71073 Å	
Crystal system	Rhombohedral	
Space group	R -3	
Unit cell dimensions	a = 17.780(3) Å	α= 90°.
	b = 17.780(3) Å	β= 90°.
	c = 33.531(7) Å	γ = 120°.
Volume	9180(3) $Å^3$	
Z	3	
Density (calculated)	1.197 Mg/m^3	
Absorption coefficient	1.231 mm^{-1}	
F(000)	3642	
Crystal size	0.30 x .25 x .25 mm^3	
Theta range for data collection	1.80 to 24.99°.	
Index ranges	-21<=h<=21, -21<=k<=21, -39<=l<=39	
Reflections collected	22999	
Independent reflections	3418 [R(int) = 0.0979]	
Completeness to theta = 24.99°	98 %	
Absorption correction	Semi-empirical from equivalents	
Max. and min. transmission	.735 and .685	
Refinement method	Full-matrix least-squares on F^2	
Data / restraints / parameters	3418 / 0 / 208	
Goodness-of-fit on F^2	1.222	
Final R indices [I>2sigma(I)]	R1 = 0.0716, wR2 = 0.2064	
R indices (all data)	R1 = 0.1010, wR2 = 0.2233	
Largest diff. peak and hole	3.227 and -0.793 e.$Å^{-3}$	

Table S29. Atomic coordinates (x 10^4) and equivalent isotropic displacement parameters (Å^{2}x10^3) for Zn_6(adeninate)$_6$(pyridine)$_6$(carbamate)$_6$ · 10.5DMF. U(eq) is defined as one third of the trace of the orthogonalized U_{ij} tensor.

	x	y	z	U(eq)
Zn	2386(1)	9212(1)	471(1)	27(1)
N(1)	2739(3)	10476(3)	379(1)	28(1)
C(1)	3029(4)	11191(3)	621(2)	26(1)
O(1)	1798(3)	8957(3)	987(1)	44(1)
C(2)	3105(5)	11306(4)	1038(2)	37(2)
N(2)	3451(5)	12129(4)	1173(2)	51(2)
O(2)	1792(4)	7724(3)	874(2)	56(1)
C(3)	3647(6)	12773(4)	915(2)	58(2)
N(3)	3590(4)	12753(3)	518(2)	42(2)
N(4)	3112(3)	11670(3)	-9(1)	27(1)
C(4)	3267(4)	11926(4)	385(2)	30(1)
N(5)	2880(5)	10688(4)	1298(2)	58(2)
C(5)	2802(4)	10822(4)	6(2)	29(1)
C(6)	1622(4)	8169(4)	1094(2)	40(2)
N(6)	1269(5)	7908(4)	1457(2)	62(2)
N(7)	3559(3)	9274(3)	500(2)	37(1)
C(7)	1056(8)	8410(7)	1713(3)	111(5)
C(8)	1100(7)	7053(7)	1602(3)	95(4)
C(9)	4301(4)	10033(5)	489(2)	47(2)
C(10)	5104(5)	10093(6)	504(3)	59(2)
C(11)	5150(5)	9358(6)	527(2)	59(2)
C(12)	4408(6)	8580(6)	527(4)	84(3)
C(13)	3619(6)	8541(5)	531(3)	72(3)

Table S30. Bond lengths [Å] and angles [°] for $Zn_6(adeninate)_6(pyridine)_6(carbamate)_6 \cdot 10.5DMF$.

Zn-O(1)	1.952(4)
Zn-N(4)#1	1.973(4)
Zn-N(1)	2.033(5)
Zn-N(7)	2.035(5)
N(1)-C(1)	1.373(7)
N(1)-C(5)	1.374(7)
C(1)-C(4)	1.400(8)
C(1)-C(2)	1.409(8)
O(1)-C(6)	1.323(8)
C(2)-N(5)	1.300(8)
C(2)-N(2)	1.350(8)
N(2)-C(3)	1.334(8)
O(2)-C(6)	1.224(8)
C(3)-N(3)	1.334(8)
C(3)-H(5A)	0.9500
N(3)-C(4)	1.360(8)
N(4)-C(5)	1.324(7)
N(4)-C(4)	1.379(7)
N(4)-Zn#2	1.973(4)
N(5)-H(5B)	0.8800
N(5)-H(3C)	0.8800
C(5)-H(5)	0.9500
C(6)-N(6)	1.341(8)
N(6)-C(7)	1.420(12)
N(6)-C(8)	1.477(12)
N(7)-C(9)	1.335(9)
N(7)-C(13)	1.366(9)
C(7)-H(7A)	0.9800
C(7)-H(7B)	0.9800
C(7)-H(7C)	0.9800
C(8)-H(8A)	0.9800
C(8)-H(8B)	0.9800
C(8)-H(8C)	0.9800

C(9)-C(10)	1.378(10)
C(9)-H(9A)	0.9500
C(10)-C(11)	1.352(11)
C(10)-H(10A)	0.9500
C(11)-C(12)	1.352(11)
C(11)-H(11A)	0.9500
C(12)-C(13)	1.369(11)
C(12)-H(12A)	0.9500
C(13)-H(13A)	0.9500
O(1)-Zn-N(4)#1	116.5(2)
O(1)-Zn-N(1)	103.05(18)
N(4)#1-Zn-N(1)	106.4(2)
O(1)-Zn-N(7)	112.7(2)
N(4)#1-Zn-N(7)	114.2(2)
N(1)-Zn-N(7)	101.9(2)
C(1)-N(1)-C(5)	102.6(5)
C(1)-N(1)-Zn	134.3(4)
C(5)-N(1)-Zn	122.9(4)
N(1)-C(1)-C(4)	109.1(5)
N(1)-C(1)-C(2)	133.3(5)
C(4)-C(1)-C(2)	117.6(5)
C(6)-O(1)-Zn	107.6(4)
N(5)-C(2)-N(2)	118.2(6)
N(5)-C(2)-C(1)	125.2(6)
N(2)-C(2)-C(1)	116.6(5)
C(3)-N(2)-C(2)	119.7(5)
N(2)-C(3)-N(3)	129.7(6)
N(2)-C(3)-H(5A)	115.1
N(3)-C(3)-H(5A)	115.1
C(3)-N(3)-C(4)	110.0(5)
C(5)-N(4)-C(4)	103.9(5)
C(5)-N(4)-Zn#2	128.4(4)
C(4)-N(4)-Zn#2	127.1(4)
N(3)-C(4)-N(4)	125.3(5)
N(3)-C(4)-C(1)	126.2(5)
N(4)-C(4)-C(1)	108.5(5)

C(2)-N(5)-H(5B)	120.0
C(2)-N(5)-H(3C)	120.0
H(5B)-N(5)-H(3C)	120.0
N(4)-C(5)-N(1)	115.9(5)
N(4)-C(5)-H(5)	122.0
N(1)-C(5)-H(5)	122.0
O(2)-C(6)-O(1)	121.1(6)
O(2)-C(6)-N(6)	123.1(7)
O(1)-C(6)-N(6)	115.8(7)
C(6)-N(6)-C(7)	123.8(7)
C(6)-N(6)-C(8)	118.4(8)
C(7)-N(6)-C(8)	117.8(8)
C(9)-N(7)-C(13)	117.2(6)
C(9)-N(7)-Zn	121.5(5)
C(13)-N(7)-Zn	121.3(5)
N(6)-C(7)-H(7A)	109.5
N(6)-C(7)-H(7B)	109.5
H(7A)-C(7)-H(7B)	109.5
N(6)-C(7)-H(7C)	109.5
H(7A)-C(7)-H(7C)	109.5
H(7B)-C(7)-H(7C)	109.5
N(6)-C(8)-H(8A)	109.5
N(6)-C(8)-H(8B)	109.5
H(8A)-C(8)-H(8B)	109.5
N(6)-C(8)-H(8C)	109.5
H(8A)-C(8)-H(8C)	109.5
H(8B)-C(8)-H(8C)	109.5
N(7)-C(9)-C(10)	122.6(8)
N(7)-C(9)-H(9A)	118.7
C(10)-C(9)-H(9A)	118.7
C(11)-C(10)-C(9)	119.2(8)
C(11)-C(10)-H(10A)	120.4
C(9)-C(10)-H(10A)	120.4
C(12)-C(11)-C(10)	119.3(8)
C(12)-C(11)-H(11A)	120.3
C(10)-C(11)-H(11A)	120.3

C(11)-C(12)-C(13)	120.1(8)
C(11)-C(12)-H(12A)	119.9
C(13)-C(12)-H(12A)	119.9
N(7)-C(13)-C(12)	121.3(8)
N(7)-C(13)-H(13A)	119.4
C(12)-C(13)-H(13A)	119.4

Symmetry transformations used to generate equivalent atoms:

#1 y-1,-x+y,-z #2 x-y+1,x+1,-z

Table S31. Anisotropic displacement parameters (Å^{2}x 10^3) for Zn$_6$(adeninate)$_6$(pyridine)$_6$(carbamate)$_6$ · 10.5DMF. The anisotropic displacement factor exponent takes the form: -2p^2 [h^2 a^{*2}U^{11} + ... + 2 h k a* b* U^{12}]

	U^{11}	U^{22}	U^{33}	U^{23}	U^{13}	U^{12}
Zn	33(1)	25(1)	19(1)	-2(1)	-4(1)	11(1)
N(1)	37(3)	31(3)	18(3)	-1(2)	-3(2)	17(2)
C(1)	39(4)	19(3)	20(3)	-4(2)	-9(3)	13(3)
O(1)	60(3)	34(3)	24(2)	-3(2)	4(2)	13(2)
C(2)	65(5)	29(3)	18(3)	0(3)	-7(3)	24(3)
N(2)	99(5)	30(3)	20(3)	-4(2)	-14(3)	28(3)
O(2)	71(4)	34(3)	55(3)	6(2)	19(3)	21(3)
C(3)	109(7)	27(4)	27(4)	-8(3)	-17(4)	25(4)
N(3)	71(4)	25(3)	24(3)	0(2)	-10(3)	19(3)
N(4)	37(3)	30(3)	15(2)	2(2)	-2(2)	18(2)
C(4)	42(4)	34(3)	17(3)	1(3)	-5(3)	22(3)
N(5)	118(6)	35(3)	17(3)	-6(2)	-17(3)	35(4)
C(5)	40(4)	29(3)	21(3)	0(3)	-2(3)	18(3)
C(6)	38(4)	32(4)	29(4)	4(3)	0(3)	2(3)
N(6)	77(5)	54(4)	34(4)	14(3)	17(3)	18(4)
N(7)	38(3)	31(3)	36(3)	1(2)	-5(2)	15(3)
C(7)	145(11)	87(8)	47(6)	-5(5)	44(6)	18(7)
C(8)	90(7)	85(7)	75(7)	51(6)	12(6)	18(6)
C(9)	39(4)	48(4)	45(4)	3(3)	-7(3)	15(4)
C(10)	40(4)	64(5)	72(6)	-1(4)	-8(4)	25(4)
C(11)	51(5)	82(6)	47(5)	12(4)	-5(4)	36(5)
C(12)	56(6)	45(5)	157(11)	19(6)	6(6)	30(5)
C(13)	50(5)	41(5)	129(9)	10(5)	-6(5)	27(4)

Table S32. Hydrogen coordinates (x 10^4) and isotropic displacement parameters (Å^{2}x 10^3) for $Zn_6(adeninate)_6(pyridine)_6(carbamate)_6 \cdot 10.5DMF$.

	x	y	z	U(eq)
H(5A)	3860	13330	1032	70
H(5B)	2954	10812	1555	70
H(3C)	2652	10146	1219	70
H(5)	2634	10472	-228	35
H(7A)	1182	8949	1578	166
H(7B)	1403	8548	1958	166
H(7C)	438	8079	1780	166
H(8A)	1279	6778	1399	143
H(8B)	478	6683	1657	143
H(8C)	1430	7131	1848	143
H(9A)	4275	10553	470	56
H(10A)	5619	10644	498	71
H(11A)	5697	9387	543	71
H(12A)	4435	8059	525	101
H(13A)	3104	7993	555	86

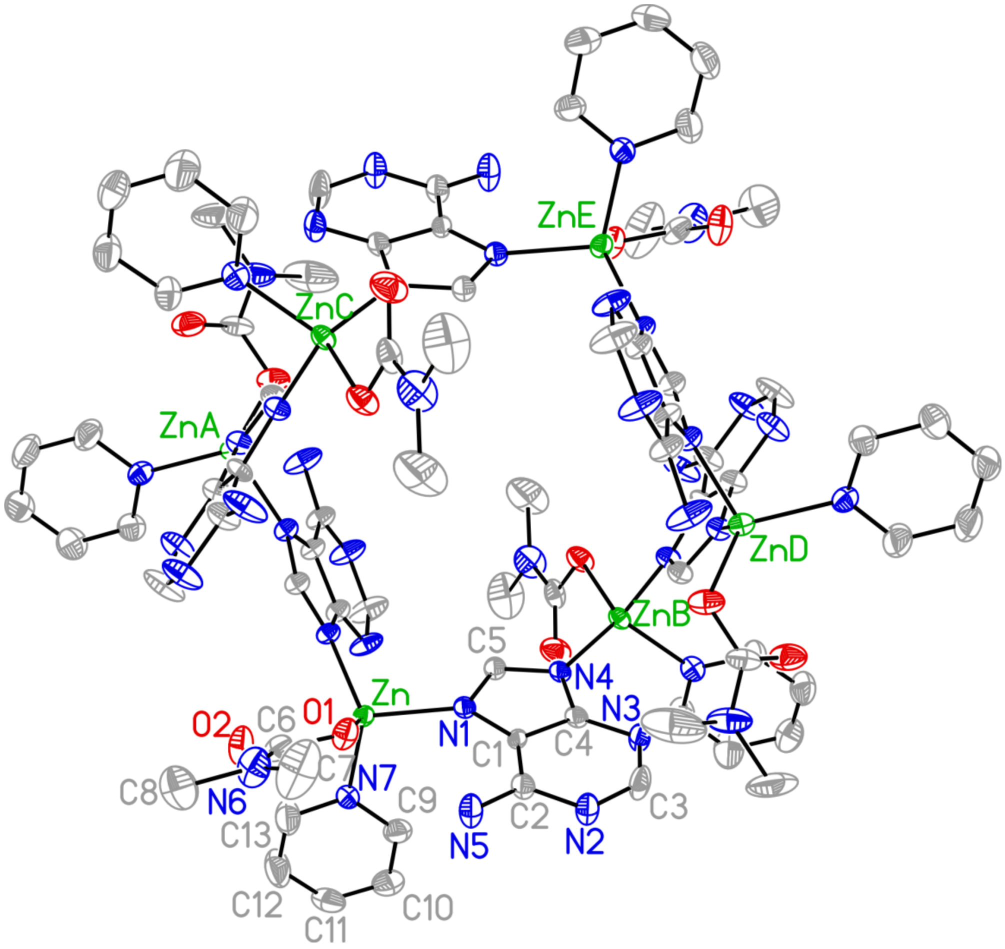

Figure S52. The building unit and asymmetric unit present in crystalline Zn_6(adeninate)$_6$ (pyridine)$_6$(carbamate)$_6$ · 10.5DMF with all atoms of the zinc-adeninate hexameric macrocycle represented by thermal ellipsoids drawn at the 35 % probability level. All hydrogen atoms were omitted for clarity.

Crystallographic data and structure refinements for

(bio-MOF-11)

$Co_2(Ad)_2(CH_3CO_2)_2 \cdot 2DMF, 0.5H_2O$

An X-ray crystal structure was determined for bio-MOF-11 (**6**), using a single crystal on a Bruker Smart Apex CCD diffractometer with graphite-monochromated MoKα (λ= 0.71073 Å) radiation. The parameters used during the collection of diffraction data are summarized in Table S32. The crystal was mounted on a glass loop with fluorolube and placed in a cold N_2 stream (203 K) for data collection.

Unit-cell parameters and systematic absences indicated that bio-MOF-11 crystallized in tetragonal I $4_1/a$. Unit-cell dimensions were derived from the least-squares fit of the angular settings of 534 reflections. Data were corrected for absorption using the Bruker program Sadabs. The crystal was very weakly diffracting with no observed intensities beyond $2\theta = 46^\circ$. The structure was solved via direct methods, which located Co and all of the remaining adenine non-hydrogen atoms. Remaining non-hydrogen atoms from the bridging acetate anion were found from subsequent difference Fourier syntheses. All non-hydrogen atoms were refined anisotropically. Idealized atom positions were calculated for all hydrogen atoms (with d-(C_{methyl}-H) = 0.98 Å, d- ($C_{aromatic}$-H)=0.95 Å, d-(N-H) =0.88 Å , U = $1.2U_{iso}$ of attached atom).

Calculations from Platon Squeeze indicate a large solvent accessible void accounting for 38.7% of the unit-cell volume (one void measuring 2099.7 $Å^3$ with 217 electrons each). The largest difference peak Q1 (1.7 $e^-/Å^3$), is located in the void and only 2.02 Å from H5A (one of the NH_2 hydrogens). Checkcif gives a C-level alert "D-H Without Acceptor N5-H5A". We can assume Q1 is an acceptor atom that is part of a disordered solvate but we are unable to identify or model the specific solvent molecules within the void.

Several checkcif alerts are generated for high GOF values, high R-values, some unusual atomic displacement parameters, and having data with a sin(θ_{max})/wavelength less than 0.575. These are attributable to the diffuse, unresolvable solvate and the low percentage of observed diffraction intensities. There is also a checkcif alert regarding the very large voids. Except for the diffuse solvent, the Co-adenine acetate complex was well-behaved. Bond lengths were typical, and no constraints or restraints were used in the data refinement.

All computer programs used in the data collection and refinements are contained in the Bruker program packages SMART (vers. 5.625), SAINT (vers. 6.22), and SHELXTL (vers. 6.14) and Platon (Spek, A.L. (1990) **Acta Cryst. A46**, C34).

Table S33. Crystal data and structure refinement for $Co_2(Ad)_2(CH_3CO_2)_2 \cdot 2DMF, 0.5H_2O$ (bio-MOF-11).

Identification code	bio-MOF-11	
Empirical formula	C7 H7 Co N5 O2	
Formula weight	252.11	
Temperature	173(2) K	
Wavelength	0.71073 Å	
Crystal system	Tetragonal	
Space group	I 41/a	
Unit cell dimensions	a = 15.4355(18) Å	α= 90°.
	b = 15.4355(18) Å	β= 90°.
	c = 22.775(5) Å	γ = 90°.
Volume	5426.3(16) Å^3	
Z	16	
Density (calculated)	1.234 Mg/m^3	
Absorption coefficient	1.255 mm^{-1}	
F(000)	2032	
Crystal size	0.30 x 0.20 x 0.20 mm^3	
Theta range for data collection	5.28 to 23.26°.	
Index ranges	-17<=h<=17, -17<=k<=17, -25<=l<=25	
Reflections collected	14248	
Independent reflections	1933 [R(int) = 0.0937]	
Completeness to theta = 23.26°	98.8 %	
Absorption correction	Semi-empirical from equivalents	
Max. and min. transmission	0.7873 and 0.7045	
Refinement method	Full-matrix least-squares on F^2	
Data / restraints / parameters	1933 / 0 / 136	
Goodness-of-fit on F^2	2.388	
Final R indices [I>2sigma(I)]	R1 = 0.1047, wR2 = 0.2834	
R indices (all data)	R1 = 0.1371, wR2 = 0.2974	
Largest diff. peak and hole	1.697 and -0.589 e.Å^{-3}	

Table S34. Atomic coordinates (x 10^4) and equivalent isotropic displacement parameters (Å^{2}x10^3) for bio-MOF-11. U(eq) is defined as one third of the trace of the orthogonalized U_{ij} tensor.

	x	y	z	U(eq)
Co(1)	10435(1)	4821(1)	560(1)	35(1)
C(1)	8973(9)	3832(8)	1206(5)	49(3)
N(1)	9266(6)	4204(6)	705(4)	34(2)
O(1)	9878(5)	5955(5)	817(3)	44(2)
C(2)	8566(7)	4151(7)	349(5)	30(3)
O(2)	9194(6)	6154(5)	-23(4)	53(2)
N(2)	8528(6)	4451(7)	-209(4)	45(3)
C(3)	7797(9)	4231(12)	-480(7)	84(5)
N(3)	7126(8)	3781(10)	-274(6)	85(4)
N(4)	8173(6)	3519(6)	1193(4)	33(2)
C(4)	7135(9)	3553(11)	317(7)	77(5)
C(5)	7913(7)	3727(8)	629(5)	40(3)
N(5)	6478(7)	3119(12)	540(6)	125(7)
C(6)	9368(7)	6354(7)	498(6)	41(3)
C(7)	8907(10)	7158(8)	745(8)	78(5)

Table S35. Bond lengths [Å] and angles [°] for bio-MOF-11.

Bond Lengths:

Co(1)-O(2)#1	2.022(9)
Co(1)-O(1)	2.037(8)
Co(1)-N(1)	2.067(9)
Co(1)-N(4)#2	2.069(8)
Co(1)-N(2)#1	2.113(9)
Co(1)-Co(1)#1	2.938(3)
C(1)-N(4)	1.327(15)
C(1)-N(1)	1.356(13)
C(1)-H(1A)	0.9500
N(1)-C(2)	1.353(13)
O(1)-C(6)	1.235(14)
C(2)-N(2)	1.355(13)
C(2)-C(5)	1.360(15)
O(2)-C(6)	1.256(14)
O(2)-Co(1)#1	2.023(9)
N(2)-C(3)	1.330(16)
N(2)-Co(1)#1	2.113(9)
C(3)-N(3)	1.332(17)
C(3)-H(3A)	0.9500
N(3)-C(4)	1.392(17)
N(4)-C(5)	1.385(14)
N(4)-Co(1)#3	2.069(8)
C(4)-N(5)	1.317(17)
C(4)-C(5)	1.420(18)
N(5)-H(5A)	0.8800
N(5)-H(5B)	0.8800
C(6)-C(7)	1.536(16)
C(7)-H(7A)	0.9800
C(7)-H(7B)	0.9800
C(7)-H(7C)	0.9800

Bond Angles:

O(2)#1-Co(1)-O(1)	158.9(3)
O(2)#1-Co(1)-N(1)	90.1(4)
O(1)-Co(1)-N(1)	88.9(3)
O(2)#1-Co(1)-N(4)#2	95.7(4)
O(1)-Co(1)-N(4)#2	105.3(3)
N(1)-Co(1)-N(4)#2	94.6(3)
O(2)#1-Co(1)-N(2)#1	87.3(4)
O(1)-Co(1)-N(2)#1	88.3(4)
N(1)-Co(1)-N(2)#1	165.2(3)
N(4)#2-Co(1)-N(2)#1	100.2(3)
O(2)#1-Co(1)-Co(1)#1	75.2(2)
O(1)-Co(1)-Co(1)#1	83.9(2)
N(1)-Co(1)-Co(1)#1	80.0(2)
N(4)#2-Co(1)-Co(1)#1	169.3(3)
N(2)#1-Co(1)-Co(1)#1	85.3(3)
N(4)-C(1)-N(1)	116.5(10)
N(4)-C(1)-H(1A)	121.7
N(1)-C(1)-H(1A)	121.7
C(2)-N(1)-C(1)	102.3(9)
C(2)-N(1)-Co(1)	129.0(7)
C(1)-N(1)-Co(1)	128.3(8)
C(6)-O(1)-Co(1)	121.9(8)
N(1)-C(2)-N(2)	125.2(9)
N(1)-C(2)-C(5)	109.9(9)
N(2)-C(2)-C(5)	124.9(10)
C(6)-O(2)-Co(1)#1	134.0(8)
C(3)-N(2)-C(2)	112.7(10)
C(3)-N(2)-Co(1)#1	127.1(8)
C(2)-N(2)-Co(1)#1	120.3(7)
N(2)-C(3)-N(3)	128.9(13)
N(2)-C(3)-H(3A)	115.5

N(3)-C(3)-H(3A)	115.5
C(3)-N(3)-C(4)	117.8(12)
C(1)-N(4)-C(5)	101.8(9)
C(1)-N(4)-Co(1)#3	118.9(7)
C(5)-N(4)-Co(1)#3	139.2(7)
N(5)-C(4)-N(3)	119.6(13)
N(5)-C(4)-C(5)	123.7(13)
N(3)-C(4)-C(5)	116.3(12)
C(2)-C(5)-N(4)	109.4(10)
C(2)-C(5)-C(4)	118.9(11)
N(4)-C(5)-C(4)	131.7(11)
C(4)-N(5)-H(5A)	120.0
C(4)-N(5)-H(5B)	120.0
H(5A)-N(5)-H(5B)	120.0
O(1)-C(6)-O(2)	124.7(11)
O(1)-C(6)-C(7)	118.8(12)
O(2)-C(6)-C(7)	116.4(12)
C(6)-C(7)-H(7A)	109.5
C(6)-C(7)-H(7B)	109.5
H(7A)-C(7)-H(7B)	109.5
C(6)-C(7)-H(7C)	109.5
H(7A)-C(7)-H(7C)	109.5
H(7B)-C(7)-H(7C)	109.5

Symmetry transformations used to generate equivalent atoms:

#1 -x+2,-y+1,-z #2 y+3/4,-x+5/4,-z+1/4 #3 -y+5/4,x-3/4,-z+1/4

Table S36. Anisotropic displacement parameters (Å^{2}x 10^3) for bio-MOF-11. The anisotropic displacement factor exponent takes the form: $-2p^2 [h^2 a^{*2}U^{11} + ... + 2 h k a^* b^* U^{12}]$

	U^{11}	U^{22}	U^{33}	U^{23}	U^{13}	U^{12}
Co(1)	31(1)	41(1)	32(1)	13(1)	-4(1)	-4(1)
C(1)	62(9)	41(7)	43(7)	15(6)	-2(6)	-9(7)
N(1)	33(5)	36(5)	34(5)	12(4)	4(4)	-2(4)
O(1)	44(5)	34(4)	55(5)	4(4)	-17(4)	9(4)
C(2)	27(6)	27(6)	35(6)	1(5)	12(5)	4(5)
O(2)	65(6)	56(6)	37(5)	1(4)	-1(4)	-1(4)
N(2)	25(5)	68(7)	43(6)	20(5)	-1(4)	-3(5)
C(3)	44(9)	136(15)	70(10)	52(10)	-18(8)	-30(9)
N(3)	50(7)	135(12)	72(8)	47(8)	-14(6)	-29(8)
N(4)	33(5)	37(5)	30(5)	9(4)	5(4)	0(5)
C(4)	45(9)	116(14)	69(10)	43(9)	-9(8)	-10(9)
C(5)	27(6)	48(8)	47(7)	8(6)	7(5)	7(6)
N(5)	33(7)	260(20)	87(9)	98(12)	-21(6)	-68(10)
C(6)	30(7)	34(7)	58(8)	-1(6)	24(6)	-12(6)
C(7)	75(11)	26(7)	133(14)	-27(8)	9(10)	17(7)

Table S37. Hydrogen coordinates (x 10^4) and isotropic displacement parameters (Å^{2}x 10^3) for bio-MOF-11.

	x	y	z	U(eq)
H(1A)	9323	3797	1549	59
H(3A)	7747	4420	-876	100
H(5A)	6037	2975	315	150
H(5B)	6480	2973	913	150
H(7A)	9089	7252	1152	117
H(7B)	8279	7068	732	117
H(7C)	9060	7666	509	117

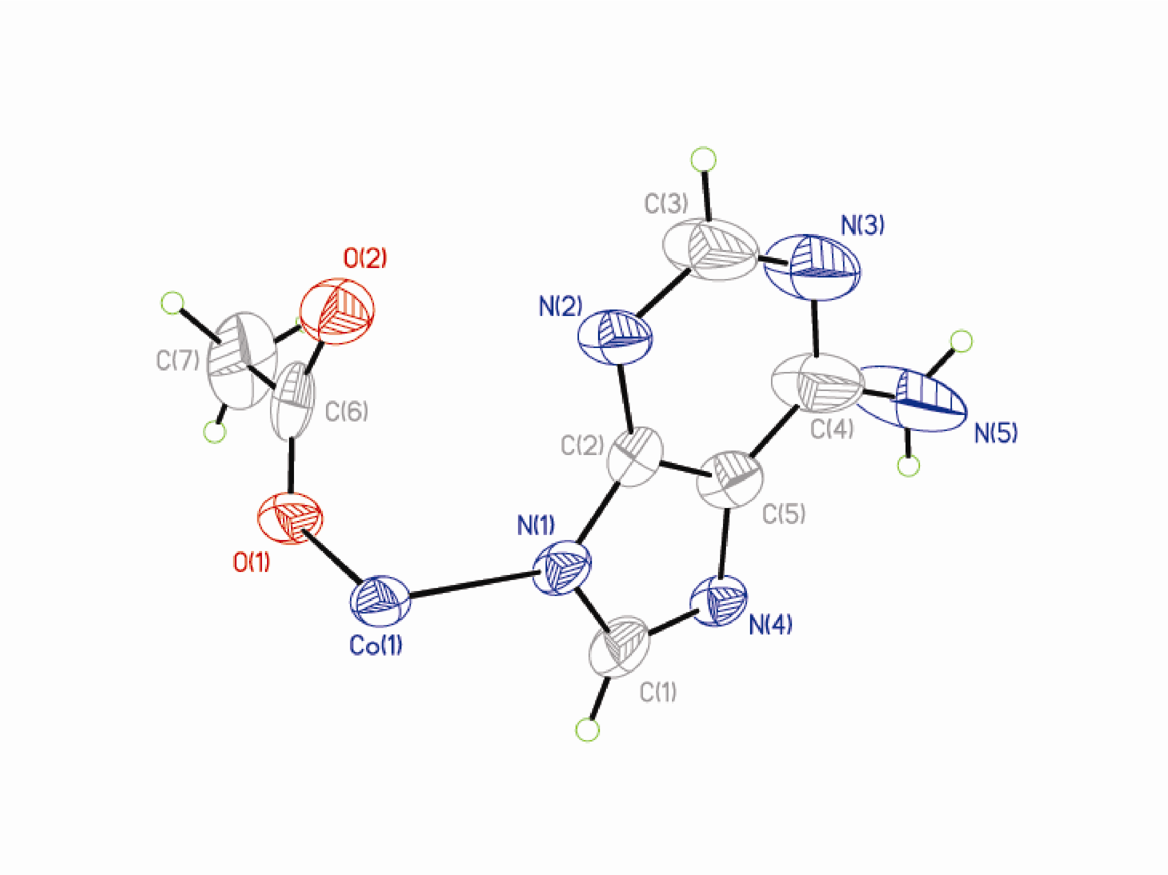

Figure S53. The building unit and asymmetric unit present in crystalline $Co_2(Ad)_2(CH_3CO_2)_2 \cdot 2DMF$, $0.5H_2O$ (bio-MOF-11) with all atoms of bio-MOF-11 represented by thermal ellipsoids drawn at the 35 % probability level.

Single Crystal X-ray Diffraction Studies for bio-MOF-1.

An X-ray crystal structure was determined for bio-MOF-1(**7**) using a single crystal on a Bruker Smart Apex CCD diffractometer with graphite-monochromated MoKα (λ= 0.71073 Å) radiation. The parameters used during the collection of diffraction data are summarized in Table S37. A crystal was mounted in a glass capillary and data were collected at 273 K.

Unit-cell parameters and systematic absences indicated (**7**) crystallized in either tetragonal $I\,4_1$ or $I\,4_122$. $I\,4_122$ was chosen based on *E*-values and the successful solution and refinement of the structure. Unit-cell dimensions were derived from the least-squares fit of the angular settings of 4725 strong reflections from the data collection. Data were corrected for absorption using the Bruker AXS program SADABS.

The structure was solved via direct methods which located the positions of the Zn atoms and most of the non-hydrogen atoms. Remaining non-hydrogen atoms were located from subsequent difference Fourier syntheses. All non-hydrogen atoms were refined anisotropically except for O(1) and a disordered phenyl group (C21 to C26) which was refined as a rigid hexagon (*d*C-C = 1.39 Å). There are two half-occupancy orientations for the disordered phenyl. Hydrogen atom positions were placed in idealized positions.

Final difference Fourier syntheses showed only chemically insignificant electron density (largest difference peak 0.97 Å). However, there is evidence of considerable solvent in the structure. Calculations using Platon show total potential solvent accessible void volume of 7800 Å^3 (out of 16339 Å^3 unit-cell volume) with 1628 e$^-$ per void volume per unit-cell.

The crystal structure did suffer from weak diffraction with few observed reflections at higher 2-theta values and there are a number of checkcif flags which reflect this, including ones for poorly shaped ADP's and unusual U_{eq} values. An inspection of F_o vs. F_c values and trends based upon sin θ, Miller index, or parity group failed to reveal any systematic error in the data. All computer programs used in the data collection and refinements are contained in the Bruker program packages Smart, Saint, and SHELXTL (version 6.14).

Table S38. Crystal data and structure refinement for $Zn_8(Ad)_4(BPDC)_6O \cdot 2(NH_2(CH_3)_2)^+$, 8DMF, $11H_2O$ (bio-MOF-1).

Identification code	bio-MOF-1	
Empirical formula	$C_{104} H_{64} N_{20} O_{25} Zn_8$	
Formula weight	2516.87	
Temperature	273(2) K	
Wavelength	0.71073 Å	
Crystal system	Tetragonal	
Space group	$I\ 4_1\ 2\ 2$	
Unit cell dimensions	a = 38.237(2) Å	α= 90°.
	b = 38.237(2) Å	β= 90°.
	c = 11.1753(12) Å	γ = 90°.
Volume	16339(2) $Å^3$	
Z	4	
Density (calculated)	1.023 Mg/m^3	
Absorption coefficient	1.207 mm^{-1}	
F(000)	5072	
Crystal size	0.20 x 0.16 x 0.16 mm^3	
Theta range for data collection	1.90 to 25.00°.	
Index ranges	-45<=h<=45, -45<=k<=45, -13<=l<=13	
Reflections collected	65848	
Independent reflections	7210 [R(int) = 0.1164]	
Completeness to theta = 25.00°	99.5 %	
Absorption correction	Semi-empirical from equivalents	
Max. and min. transmission	0.8303 and 0.7943	
Refinement method	Full-matrix least-squares on F^2	
Data / restraints / parameters	7210 / 17 / 299	
Goodness-of-fit on F^2	1.528	
Final R indices [I>2sigma(I)]	R1 = 0.0940, wR2 = 0.2376	
R indices (all data)	R1 = 0.1267, wR2 = 0.2501	
Absolute structure parameter	0.56(4)	
Extinction coefficient	0.00012(8)	
Largest diff. peak and hole	0.966 and -0.640 e.$Å^{-3}$	

Table S39. Atomic coordinates (x 10^4) and equivalent isotropic displacement parameters ($Å^2$x10^3) for bio-MOF-1. U(eq) is defined as one third of the trace of the orthogonalized U_{ij} tensor.

	x	y	z	U(eq)
Zn(1)	4592(1)	5006(1)	3965(1)	44(1)
Zn(2)	5883(1)	5883(1)	0	40(1)
Zn(3)	4132(1)	5868(1)	0	40(1)
O(1)	5000	5000	5000	24(2)
O(2)	3919(2)	5016(4)	3267(8)	104(3)
O(3)	4183(2)	4881(3)	4944(8)	93(4)
O(4)	1298(2)	4299(3)	6789(8)	76(3)
O(5)	1516(2)	4016(2)	8269(7)	70(2)
O(6)	3710(2)	5687(3)	840(9)	84(4)
O(7)	3787(4)	6207(5)	1426(15)	190(7)
N(1)	5330(2)	5388(3)	2780(8)	51(3)
N(2)	4715(3)	5414(3)	2752(11)	80(4)
N(3)	4523(2)	5750(2)	1190(11)	64(3)
N(4)	5492(3)	5764(3)	1195(10)	64(3)
N(5)	4999(4)	6081(2)	-175(7)	80(3)
C(1)	5584(4)	5528(4)	2124(13)	75(5)
C(2)	5043(3)	5498(3)	2354(9)	62(3)
C(3)	4451(4)	5556(3)	2098(10)	74(4)
C(4)	4890(2)	5843(3)	777(11)	63(3)
C(5)	5131(3)	5720(3)	1425(10)	71(4)
C(6)	3918(3)	4935(5)	4297(12)	85(5)
C(7)	3267(2)	4906(3)	4228(8)	144(9)
C(8)	2944(2)	4808(3)	4690(9)	161(10)
C(9)	2924(1)	4648(3)	5805(8)	87(4)
C(10)	3228(2)	4586(3)	6457(7)	118(6)
C(11)	3551(2)	4684(3)	5995(8)	115(7)
C(12)	3571(1)	4844(3)	4881(8)	83(4)
C(13)	2286(2)	4725(3)	5933(13)	234(16)
C(14)	1956(2)	4616(3)	6290(13)	222(15)
C(15)	1919(1)	4323(3)	7013(9)	77(4)

C(16)	2214(2)	4138(2)	7379(9)	95(5)
C(17)	2545(2)	4247(3)	7022(9)	110(6)
C(18)	2581(1)	4541(3)	6299(10)	107(6)
C(19)	1559(3)	4195(3)	7399(13)	63(3)
C(20)	3617(4)	5922(5)	1442(16)	164(12)
C(21)	3236(4)	6172(4)	3100(20)	171(18)
C(22)	2923(5)	6158(5)	3729(17)	105(10)
C(23)	2675(4)	5905(5)	3450(20)	151(8)
C(24)	2740(5)	5665(5)	2550(20)	260(30)
C(25)	3053(5)	5678(5)	1915(17)	99(10)
C(26)	3301(3)	5931(4)	2191(15)	131(6)
C(21')	3104(5)	6235(3)	2346(18)	140
C(22')	2798(5)	6224(4)	3016(19)	136(14)
C(23')	2678(4)	5906(5)	3463(16)	151(8)
C(24')	2863(5)	5601(3)	3240(19)	119(11)
C(25')	3170(4)	5612(3)	2570(18)	92(9)
C(26')	3290(3)	5930(4)	2123(12)	131(6)

Table S40. Bond lengths [Å] and angles [°] for bio-MOF-1.

Zn(1)-O(1)	1.9438(8)	N(3)-C(4)	1.521(14)
Zn(1)-O(3)	1.965(7)	N(4)-C(5)	1.414(14)
Zn(1)-N(1)#1	2.028(9)	N(4)-C(1)	1.421(16)
Zn(1)-N(2)	2.119(12)	N(5)-C(4)	1.459(15)
Zn(1)-Zn(1)#1	3.1246(16)	N(5)-H(5A)	0.8600
Zn(2)-O(4)#2	1.906(7)	N(5)-H(5B)	0.8600
Zn(2)-O(4)#3	1.906(7)	C(1)-H(1A)	0.9300
Zn(2)-N(4)#4	2.056(11)	C(2)-C(5)	1.382(15)
Zn(2)-N(4)	2.056(11)	C(3)-H(3A)	0.9300
Zn(3)-O(6)	1.992(9)	C(4)-C(5)	1.262(13)
Zn(3)-O(6)#5	1.992(9)	C(6)-C(12)	1.520(12)
Zn(3)-N(3)#5	2.048(9)	C(7)-C(8)	1.3900
Zn(3)-N(3)	2.049(9)	C(7)-C(12)	1.3900
Zn(3)-O(7)	2.443(15)	C(7)-H(7A)	0.9300
Zn(3)-O(7)#5	2.443(15)	C(8)-C(9)	1.3900
Zn(3)-C(20)#5	2.553(17)	C(8)-H(8A)	0.9300
Zn(3)-C(20)	2.553(17)	C(9)-C(10)	1.3900
O(1)-Zn(1)#6	1.9437(8)	C(9)-C(18)	1.484(7)
O(1)-Zn(1)#7	1.9437(8)	C(10)-C(11)	1.3900
O(1)-Zn(1)#1	1.9439(8)	C(10)-H(10A)	0.9300
O(2)-C(6)	1.193(14)	C(11)-C(12)	1.3900
O(3)-C(6)	1.263(14)	C(11)-H(11A)	0.9300
O(4)-C(19)	1.271(13)	C(13)-C(14)	1.3900
O(4)-Zn(2)#8	1.906(7)	C(13)-C(18)	1.3900
O(5)-C(19)	1.201(13)	C(13)-H(13A)	0.9300
O(6)-C(20)	1.18(2)	C(14)-C(15)	1.3900
O(7)-C(20)	1.265(19)	C(14)-H(14A)	0.9300
N(1)-C(2)	1.268(14)	C(15)-C(16)	1.3900
N(1)-C(1)	1.328(14)	C(15)-C(19)	1.524(12)
N(1)-Zn(1)#1	2.028(9)	C(16)-C(17)	1.3900
N(2)-C(3)	1.361(14)	C(16)-H(16A)	0.9300
N(2)-C(2)	1.371(15)	C(17)-C(18)	1.3900
N(3)-C(3)	1.286(15)	C(17)-H(17A)	0.9300

C(20)-C(26')	1.47(2)
C(20)-C(26)	1.47(2)
C(21)-C(22)	1.3900
C(21)-C(26)	1.3900
C(21)-H(21A)	0.9300
C(22)-C(23)	1.3900
C(22)-H(22A)	0.9300
C(23)-C(24)	1.3900
C(23)-C(23)#9	1.50(2)
C(24)-C(25)	1.3900
C(24)-H(24A)	0.9300
C(25)-C(26)	1.3900
C(25)-H(25A)	0.9300
C(21')-C(22')	1.3900
C(21')-C(26')	1.3900
C(21')-H(21B)	0.9300
C(22')-C(23')	1.3900
C(22')-H(22B)	0.9300
C(23')-C(24')	1.3900
C(23')-C(23')#9	1.50(2)
C(24')-C(25')	1.3900
C(24')-H(24B)	0.9300
C(25')-C(26')	1.3900
C(25')-H(25B)	0.9300

O(1)-Zn(1)-O(3)	107.7(2)
O(1)-Zn(1)-N(1)#1	105.1(3)
O(3)-Zn(1)-N(1)#1	107.5(4)
O(1)-Zn(1)-N(2)	102.1(3)
O(3)-Zn(1)-N(2)	135.4(4)
N(1)#1-Zn(1)-N(2)	95.5(3)
O(1)-Zn(1)-Zn(1)#1	36.51(3)
O(3)-Zn(1)-Zn(1)#1	142.3(2)
N(1)#1-Zn(1)-Zn(1)#1	80.9(2)
N(2)-Zn(1)-Zn(1)#1	77.7(3)
O(4)#2-Zn(2)-O(4)#3	141.6(6)
O(4)#2-Zn(2)-N(4)#4	100.9(4)
O(4)#3-Zn(2)-N(4)#4	104.7(4)
O(4)#2-Zn(2)-N(4)	104.7(4)
O(4)#3-Zn(2)-N(4)	100.9(4)
N(4)#4-Zn(2)-N(4)	95.7(5)
O(6)-Zn(3)-O(6)#5	141.5(5)
O(6)-Zn(3)-N(3)#5	103.4(4)
O(6)#5-Zn(3)-N(3)#5	102.1(4)
O(6)-Zn(3)-N(3)	102.1(4)
O(6)#5-Zn(3)-N(3)	103.4(4)
N(3)#5-Zn(3)-N(3)	95.9(6)
O(6)-Zn(3)-O(7)	55.7(4)
O(6)#5-Zn(3)-O(7)	93.6(5)
N(3)#5-Zn(3)-O(7)	158.2(4)
N(3)-Zn(3)-O(7)	95.0(5)
O(6)-Zn(3)-O(7)#5	93.6(5)
O(6)#5-Zn(3)-O(7)#5	55.7(4)
N(3)#5-Zn(3)-O(7)#5	95.0(5)
N(3)-Zn(3)-O(7)#5	158.2(4)
O(7)-Zn(3)-O(7)#5	81.4(9)
O(6)-Zn(3)-C(20)#5	119.8(5)
O(6)#5-Zn(3)-C(20)#5	26.5(5)
N(3)#5-Zn(3)-C(20)#5	99.8(5)
N(3)-Zn(3)-C(20)#5	129.7(5)
O(7)-Zn(3)-C(20)#5	87.6(5)
O(7)#5-Zn(3)-C(20)#5	29.2(5)
O(6)-Zn(3)-C(20)	26.5(5)
O(6)#5-Zn(3)-C(20)	119.8(5)
N(3)#5-Zn(3)-C(20)	129.7(5)
N(3)-Zn(3)-C(20)	99.8(5)
O(7)-Zn(3)-C(20)	29.2(5)
O(7)#5-Zn(3)-C(20)	87.6(5)
C(20)#5-Zn(3)-C(20)	105.8(8)
Zn(1)#6-O(1)-Zn(1)#7	106.97(5)
Zn(1)#6-O(1)-Zn(1)	109.58(9)
Zn(1)#7-O(1)-Zn(1)	111.90(9)

Zn(1)#6-O(1)-Zn(1)#1	111.90(9)
Zn(1)#7-O(1)-Zn(1)#1	109.58(9)
Zn(1)-O(1)-Zn(1)#1	106.97(5)
C(6)-O(3)-Zn(1)	106.3(7)
C(19)-O(4)-Zn(2)#8	108.3(8)
C(20)-O(6)-Zn(3)	104.4(12)
C(20)-O(7)-Zn(3)	80.2(12)
C(2)-N(1)-C(1)	106.8(11)
C(2)-N(1)-Zn(1)#1	128.4(7)
C(1)-N(1)-Zn(1)#1	123.4(10)
C(3)-N(2)-C(2)	114.2(12)
C(3)-N(2)-Zn(1)	118.2(11)
C(2)-N(2)-Zn(1)	125.9(8)
C(3)-N(3)-C(4)	124.8(11)
C(3)-N(3)-Zn(3)	118.9(9)
C(4)-N(3)-Zn(3)	115.1(8)
C(5)-N(4)-C(1)	91.9(10)
C(5)-N(4)-Zn(2)	148.7(9)
C(1)-N(4)-Zn(2)	115.9(9)
C(4)-N(5)-H(5A)	120.0
C(4)-N(5)-H(5B)	120.0
H(5A)-N(5)-H(5B)	120.0
N(1)-C(1)-N(4)	118.6(13)
N(1)-C(1)-H(1A)	120.7
N(4)-C(1)-H(1A)	120.7
N(1)-C(2)-N(2)	126.2(10)
N(1)-C(2)-C(5)	106.1(8)
N(2)-C(2)-C(5)	127.7(10)
N(3)-C(3)-N(2)	119.8(14)
N(3)-C(3)-H(3A)	120.1
N(2)-C(3)-H(3A)	120.1
C(5)-C(4)-N(5)	116.3(11)
C(5)-C(4)-N(3)	114.4(11)
N(5)-C(4)-N(3)	129.0(11)
C(4)-C(5)-C(2)	118.9(11)
C(4)-C(5)-N(4)	124.3(11)
C(2)-C(5)-N(4)	116.5(8)
O(2)-C(6)-O(3)	126.3(10)
O(2)-C(6)-C(12)	118.4(11)
O(3)-C(6)-C(12)	114.8(12)
C(8)-C(7)-C(12)	120.0
C(8)-C(7)-H(7A)	120.0
C(12)-C(7)-H(7A)	120.0
C(9)-C(8)-C(7)	120.0
C(9)-C(8)-H(8A)	120.0
C(7)-C(8)-H(8A)	120.0
C(8)-C(9)-C(10)	120.0
C(8)-C(9)-C(18)	120.3(6)
C(10)-C(9)-C(18)	119.7(6)
C(11)-C(10)-C(9)	120.0
C(11)-C(10)-H(10A)	120.0
C(9)-C(10)-H(10A)	120.0
C(10)-C(11)-C(12)	120.0
C(10)-C(11)-H(11A)	120.0
C(12)-C(11)-H(11A)	120.0
C(11)-C(12)-C(7)	120.0
C(11)-C(12)-C(6)	122.2(8)
C(7)-C(12)-C(6)	117.7(8)
C(14)-C(13)-C(18)	120.0
C(14)-C(13)-H(13A)	120.0
C(18)-C(13)-H(13A)	120.0
C(15)-C(14)-C(13)	120.0
C(15)-C(14)-H(14A)	120.0
C(13)-C(14)-H(14A)	120.0
C(14)-C(15)-C(16)	120.0
C(14)-C(15)-C(19)	120.8(7)
C(16)-C(15)-C(19)	119.2(7)
C(15)-C(16)-C(17)	120.0
C(15)-C(16)-H(16A)	120.0
C(17)-C(16)-H(16A)	120.0
C(16)-C(17)-C(18)	120.0
C(16)-C(17)-H(17A)	120.0

C(18)-C(17)-H(17A)	120.0
C(17)-C(18)-C(13)	120.0
C(17)-C(18)-C(9)	121.9(7)
C(13)-C(18)-C(9)	117.9(6)
O(5)-C(19)-O(4)	120.3(10)
O(5)-C(19)-C(15)	122.3(10)
O(4)-C(19)-C(15)	117.3(11)
O(6)-C(20)-O(7)	119.6(17)
O(6)-C(20)-C(26')	124.5(17)
O(7)-C(20)-C(26')	115.4(17)
O(6)-C(20)-C(26)	126.1(18)
O(7)-C(20)-C(26)	114.1(18)
C(26')-C(20)-C(26)	3.4(9)
O(6)-C(20)-Zn(3)	49.1(9)
O(7)-C(20)-Zn(3)	70.5(10)
C(26')-C(20)-Zn(3)	171.2(11)
C(26)-C(20)-Zn(3)	174.3(15)
C(22)-C(21)-C(26)	120.0
C(22)-C(21)-H(21A)	120.0
C(26)-C(21)-H(21A)	120.0
C(21)-C(22)-C(23)	120.0
C(21)-C(22)-H(22A)	120.0
C(23)-C(22)-H(22A)	120.0
C(24)-C(23)-C(22)	120.0
C(24)-C(23)-C(23)#9	119.0(19)
C(22)-C(23)-C(23)#9	120.8(17)
C(23)-C(24)-C(25)	120.0
C(23)-C(24)-H(24A)	120.0
C(25)-C(24)-H(24A)	120.0
C(26)-C(25)-C(24)	120.0
C(26)-C(25)-H(25A)	120.0
C(24)-C(25)-H(25A)	120.0
C(25)-C(26)-C(21)	120.0
C(25)-C(26)-C(20)	114.7(16)
C(21)-C(26)-C(20)	125.3(16)
C(22')-C(21')-C(26')	120.0
C(22')-C(21')-H(21B)	120.0
C(26')-C(21')-H(21B)	120.0
C(23')-C(22')-C(21')	120.0
C(23')-C(22')-H(22B)	120.0
C(21')-C(22')-H(22B)	120.0
C(22')-C(23')-C(24')	120.0
C(22')-C(23')-C(23')#9	116.9(5)
C(24')-C(23')-C(23')#9	122.60(16)
C(25')-C(24')-C(23')	120.0
C(25')-C(24')-H(24B)	120.0
C(23')-C(24')-H(24B)	120.0
C(26')-C(25')-C(24')	120.0
C(26')-C(25')-H(25B)	120.0
C(24')-C(25')-H(25B)	120.0
C(25')-C(26')-C(21')	120.0
C(25')-C(26')-C(20)	116.9(12)
C(21')-C(26')-C(20)	123.1(12)

Symmetry transformations used to generate equivalent atoms:

#1 -x+1,-y+1,z+0 #2 x+1/2,-y+1,-z+3/4 #3 -y+1,x+1/2,z-3/4

#4 y+0,x+0,-z+0 #5 -y+1,-x+1,-z #6 -y+1,-x+1,-z+1

#7 y+0,x+0,-z+1 #8 y-1/2,-x+1,z+3/4 #9 -x+1/2,y,-z+3/4

Table S41. Anisotropic displacement parameters (Å^{2}x10^3) for bio-MOF-1. The anisotropic displacement factor exponent takes the form: -2p^2 [h^2 a^{*2}U^{11} + ... + 2 h k a* b* U^{12}]

	U^{11}	U^{22}	U^{33}	U^{23}	U^{13}	U^{12}
Zn(1)	28(1)	64(1)	40(1)	17(1)	-5(1)	4(1)
Zn(2)	36(1)	36(1)	49(1)	2(1)	-2(1)	10(1)
Zn(3)	37(1)	37(1)	47(1)	15(1)	15(1)	22(1)
O(2)	53(4)	167(9)	92(6)	70(9)	18(4)	-22(7)
O(3)	36(4)	164(11)	78(5)	26(6)	-1(4)	-25(5)
O(4)	34(4)	116(8)	79(6)	31(6)	-13(5)	-33(4)
O(5)	58(5)	93(6)	59(5)	18(5)	3(4)	-14(4)
O(6)	65(6)	102(7)	86(7)	55(6)	54(5)	59(5)
O(7)	133(12)	242(18)	196(15)	-37(13)	96(11)	-75(11)
N(1)	28(5)	64(6)	61(7)	13(6)	11(4)	5(4)
N(2)	113(11)	49(6)	79(9)	3(6)	-52(8)	37(6)
N(3)	14(4)	53(6)	124(10)	23(7)	-23(5)	11(4)
N(4)	77(8)	60(7)	55(7)	-18(6)	17(6)	-8(5)
N(5)	117(7)	55(5)	70(5)	40(4)	36(10)	8(7)
C(1)	60(9)	60(9)	105(13)	-19(9)	28(9)	-16(7)
C(2)	81(10)	61(6)	46(6)	-5(5)	34(8)	-25(7)
C(3)	116(12)	57(9)	48(8)	27(7)	-49(8)	-11(7)
C(4)	30(6)	77(8)	82(9)	-30(7)	-19(5)	15(5)
C(5)	87(10)	88(9)	39(6)	2(6)	2(6)	6(7)
C(6)	46(7)	137(15)	73(8)	-19(9)	13(6)	-35(8)
C(7)	49(7)	250(20)	131(13)	133(16)	-13(7)	-20(10)
C(8)	21(6)	320(30)	141(13)	156(16)	-9(7)	-22(9)
C(9)	32(6)	135(13)	95(10)	29(9)	-9(6)	4(7)
C(10)	46(8)	250(20)	63(8)	50(11)	-8(7)	-27(10)
C(11)	49(8)	230(20)	70(9)	19(11)	-3(7)	-54(10)
C(12)	30(6)	115(11)	104(10)	17(8)	-19(6)	-17(5)
C(13)	12(6)	320(30)	370(30)	280(30)	-11(11)	-16(10)
C(14)	29(7)	320(30)	320(30)	260(30)	7(12)	1(12)
C(15)	39(7)	119(11)	74(8)	16(8)	7(6)	-8(6)
C(16)	34(6)	137(13)	114(11)	65(10)	6(7)	8(6)

C(17)	41(7)	211(17)	79(10)	64(11)	3(7)	14(9)
C(18)	47(8)	173(15)	101(12)	71(12)	10(7)	-14(8)
C(19)	29(6)	63(7)	98(10)	6(7)	-4(6)	-10(5)
C(20)	62(11)	280(30)	150(20)	140(20)	33(12)	36(16)

Table S42. Hydrogen coordinates (x10^4) and isotropic displacement parameters (Å^{2}x10^3) for bio-MOF-1.

	x	y	z	U(eq)
H(5A)	5217	6130	-268	96
H(5B)	4845	6172	-642	96
H(1A)	5817	5472	2271	90
H(3A)	4219	5514	2306	88
H(7A)	3281	5013	3482	173
H(8A)	2741	4850	4254	193
H(10A)	3214	4479	7203	142
H(11A)	3753	4642	6432	138
H(13A)	2310	4922	5449	281
H(14A)	1759	4739	6045	266
H(16A)	2190	3942	7863	114
H(17A)	2741	4124	7267	132
H(21A)	3402	6341	3282	205
H(22A)	2880	6319	4335	126
H(24A)	2574	5495	2362	309
H(25A)	3097	5517	1308	118
H(21B)	3185	6447	2047	168
H(22B)	2674	6428	3166	163
H(24B)	2783	5388	3539	143
H(25B)	3294	5408	2421	111

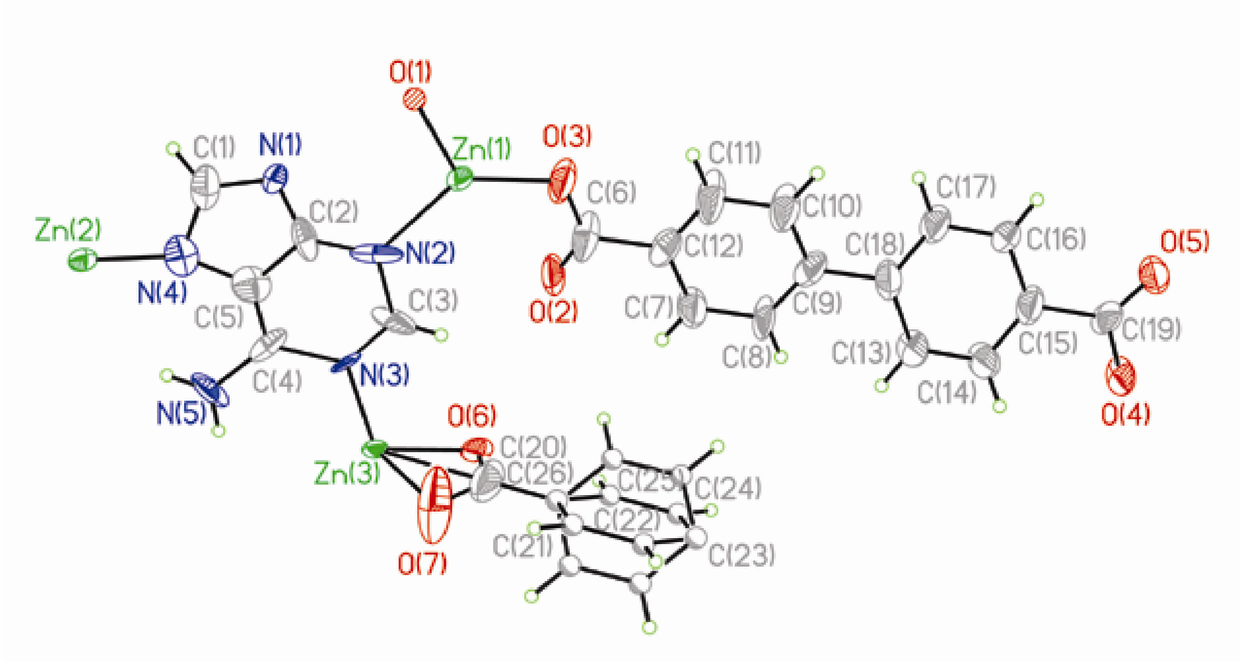

Figure S54. **The building unit and asymmetric unit present in crystalline $Zn_8(Ad)_4(BPDC)_6O \cdot 2(NH_2(CH_3)_2)^+$, 8DMF, $11H_2O$ with all atoms of bio-MOF-1 represented by thermal ellipsoids drawn at the 35 % probability level.**

BIBLIOGRAPHY

1. James, S. L., *Chem. Soc. Rev.* **2003,** *32* (5), 276-288.
2. Eddaoudi, M.; Moler, D. B.; Li, H. L.; Chen, B. L.; Reineke, T. M.; O'Keeffe, M.; Yaghi, O. M., *Accounts Chem. Res.* **2001,** *34* (4), 319-330.
3. Ferey, G., *Chem. Soc. Rev.* **2008,** *37* (1), 191-214.
4. Kitagawa, S.; Kitaura, R.; Noro, S., *Angew. Chem. Int. Edit.* **2004,** *43* (18), 2334-2375.
5. Moulton, B.; Zaworotko, M. J., *Chem. Rev.* **2001,** *101* (6), 1629-1658.
6. Chae, H. K.; Siberio-Perez, D. Y.; Kim, J.; Go, Y.; Eddaoudi, M.; Matzger, A. J.; O'Keeffe, M.; Yaghi, O. M., *Nature* **2004,** *427* (6974), 523-527.
7. Ferey, G.; Mellot-Draznieks, C.; Serre, C.; Millange, F.; Dutour, J.; Surble, S.; Margiolaki, I., *Science* **2005,** *309* (5743), 2040-2042.
8. Koh, K.; Wong-Foy, A. G.; Matzger, A. J., *J. Am. Chem. Soc.* **2009,** *131* (12), 4184-4185.
9. Kumar, J.; Purohit, C. S.; Verma, S., *Chem. Commun.* **2008,** (22), 2526-2528.
10. Wang, X.-S.; Ma, S.; Sun, D.; Parkin, S.; Zhou, H.-C., *J. Am. Chem. Soc.* **2006,** *128* (51), 16474-16475.
11. Beauvais, L. G.; Shores, M. P.; Long, J. R., *J. Am. Chem. Soc.* **2000,** *122* (12), 2763-2772.
12. He, J.; Yu, J.; Zhang, Y.; Pan, Q.; Xu, R., *Inorg. Chem.* **2005,** *44* (25), 9279-9282.
13. Chen, B.; Wang, L.; Zapata, F.; Qian, G.; Lobkovsky, E. B., *J. Am. Chem. Soc.* **2008,** *130* (21), 6718-6719.
14. Rowsell, J. L. C.; Yaghi, O. M., *Angew. Chem. Int. Edit.* **2005,** *44* (30), 4670-4679.
15. Dinca, M.; Long, J. R., *Angew. Chem. Int. Edit.* **2008,** *47* (36), 6766-6779.
16. Morris, R. E.; Wheatley, P. S., *Angew. Chem. Int. Edit.* **2008,** *47* (27), 4966-4981.
17. Lee, J.; Farha, O. K.; Roberts, J.; Scheidt, K. A.; Nguyen, S. T.; Hupp, J. T., *Chem. Soc. Rev.* **2009,** *38* (5), 1450-1459.
18. Ma, L.; Abney, C.; Lin, W., *Chem. Soc. Rev.* **2009,** *38* (5), 1248-1256.
19. Shvareva, T. Y.; Skanthakumar, S.; Soderholm, L.; Clearfield, A.; Albrecht-Schmitt, T. E., *Chem. Mat.* **2006,** *19* (2), 132-134.
20. Horcajada, P.; Chalati, T.; Serre, C.; Gillet, B.; Sebrie, C.; Baati, T.; Eubank, J. F.; Heurtaux, D.; Clayette, P.; Kreuz, C.; Chang, J.-S.; Hwang, Y. K.; Marsaud, V.; Bories, P.-N.; Cynober, L.; Gil, S.; Ferey, G.; Couvreur, P.; Gref, R., *Nat Mater* **2009,** *9,* 172-178.
21. Taylor-Pashow, K. M. L.; Rocca, J. D.; Xie, Z.; Tran, S.; Lin, W., *J. Am. Chem. Soc.* **2009,** *131* (40), 14261-14263.
22. Vaidhyanathan, R.; Bradshaw, D.; Rebilly, J. N.; Barrio, J. P.; Gould, J. A.; Berry, N. G.; Rosseinsky, M. J., *Angew. Chem. Int. Edit.* **2006,** *45* (39), 6495-6499.
23. Ingleson, M. J.; Barrio, J. P.; Bacsa, J.; Dickinson, C.; Park, H.; Rosseinsky, M. J., *Chem. Commun.* **2008,** (11), 1287-1289.

24. Anokhina, E. V.; Go, Y. B.; Lee, Y.; Vogt, T.; Jacobson, A. J., *J. Am. Chem. Soc.* **2006,** *128* (30), 9957-9962.
25. An, H. Y.; Wang, E. B.; Xiao, D. R.; Li, Y. G.; Su, Z. M.; Xu, L., *Angew. Chem. Int. Edit.* **2006,** *45* (6), 904-908.
26. Mantion, A.; Massuger, L.; Rabu, P.; Palivan, C.; McCusker, L. B.; Taubert, A., *J. Am. Chem. Soc.* **2008,** *130* (8), 2517-2526.
27. Lee, H. Y.; Kampf, J. W.; Park, K. S.; Marsh, E. N. G., *Crystal Growth & Design* **2008,** *8* (1), 296-303.
28. Xiao, B.; Wheatley, P. S.; Zhao, X.; Fletcher, A. J.; Fox, S.; Rossi, A. G.; Megson, I. L.; Bordiga, S.; Regli, L.; Thomas, K. M.; Morris, R. E., *J. Am. Chem. Soc.* **2007,** *129* (5), 1203-1209.
29. McKinlay, A. C.; Xiao, B.; Wragg, D. S.; Wheatley, P. S.; Megson, I. L.; Morris, R. E., *J. Am. Chem. Soc.* **2008,** *130* (31), 10440-10444.
30. Verma, S.; Mishra, A. K.; Kumar, J., *Acc. Chem. Res.* **2009,** *43* (1), 79-91.
31. Garcia-Teran, J. P.; Castillo, O.; Luque, A.; Garcia-Couceiro, U.; Roman, P.; Lezama, L., *Inorg. Chem.* **2004,** *43* (15), 4549-4551.
32. Yang, E. C.; Zhao, H. K.; Ding, B.; Wang, X. G.; Zhao, X. J., *New J. Chem.* **2007,** *31* (11), 1887-1890.
33. Navarro, J. A. R.; Lippert, B., *Coord. Chem. Rev.* **1999,** *185-186*, 653-667.
34. Verma, S.; Mishra, A. K.; Kumar, J., *Acc. Chem. Res.* **2009**.
35. Sivakova, S.; Rowan, S. J., *Chem. Soc. Rev.* **2005,** *34* (1), 9-21.
36. Kim, J.; Chen, B.; Reineke, T. M.; Li, H.; Eddaoudi, M.; Moler, D. B.; O'Keeffe, M.; Yaghi, O. M., *J. Am. Chem. Soc.* **2001,** *123* (34), 8239-8247.
37. Vogiatzis, K. D.; Mavrandonakis, A.; Klopper, W.; Froudakis, G. E., *Chemphyschem* **2009,** *10* (2), 374-383.
38. Kintisch, E., *Science* **2007,** *317* (5835), 184-186.
39. White, C. M.; Strazisar, B. R.; Granite, E. J.; Hoffman, J. S.; Pennline, H. W., *J. Air Waste Manage. Assoc.* **2003,** *53* (6), 645-715.
40. Granite, E. J.; Pennline, H. W., *Ind. Eng. Chem. Res.* **2002,** *41* (22), 5470-5476.
41. Strazisar, B. R.; Anderson, R. R.; White, C. M., *Energy Fuels* **2003,** *17* (4), 1034-1039.
42. Li, J. R.; Kuppler, R. J.; Zhou, H. C., *Chem. Soc. Rev.* **2009,** *38* (5), 1477-1504.
43. Banerjee, R.; Furukawa, H.; Britt, D.; Knobler, C.; O'Keeffe, M.; Yaghi, O. M., *J. Am. Chem. Soc.* **2009,** *131* (11), 3875-3877.
44. Arstad, B.; Fjellvag, H.; Kongshaug, K. O.; Swang, O.; Blom, R., *Adsorption* **2008,** *14* (6), 755-762.
45. Caskey, S. R.; Wong-Foy, A. G.; Matzger, A. J., *J. Am. Chem. Soc.* **2008,** *130* (33), 10870-10871.
46. Demessence, A.; D'Alessandro, D. M.; Foo, M. L.; Long, J. R., *J. Am. Chem. Soc.* **2009,** *131* (25), 8784-8785.
47. Bastin, L.; Barcia, P. S.; Hurtado, E. J.; Silva, J. A. C.; Rodrigues, A. E.; Chen, B., *J. Phys. Chem. C* **2008,** *112* (5), 1575-1581.
48. Llewellyn, P. L.; Bourrelly, S.; Serre, C.; Vimont, A.; Daturi, M.; Hamon, L.; De Weireld, G.; Chang, J. S.; Hong, D. Y.; Hwang, Y. K.; Jhung, S. H.; Ferey, G., *Langmuir* **2008,** *24* (14), 7245-7250.
49. Bae, Y. S.; Farha, O. K.; Hupp, J. T.; Snurr, R. Q., *J. Mater. Chem.* **2009,** *19* (15), 2131-2134.

50. Vaidhyanathan, R.; Iremonger, S. S.; Dawson, K. W.; Shimizu, G. K. H., *Chem. Commun.* **2009,** (35), 5230-5232.
51. Vallet-Regi, M.; Balas, F.; Arcos, D., *Angew. Chem. Int. Edit.* **2007,** *46*, 7548-7558.
52. Angelos, S.; Khashab, N. M.; Yang, Y.-W.; Trabolsi, A.; Khatib, H. A.; Stoddart, J. F.; Zink, J. I., *J. Am. Chem. Soc.* **2009,** *131* (36), 12912-12914.
53. Horcajada, P.; Serre, C.; Vallet-Regi, M.; Sebban, M.; Taulelle, F.; Ferey, G., *Angew. Chem. Int. Edit.* **2006,** *45* (36), 5974-5978.
54. Horcajada, P.; Serre, C.; Maurin, G.; Ramsahye, N. A.; Balas, F.; Vallet-Regi, M.; Sebban, M.; Taulelle, F.; Ferey, G., *J. Am. Chem. Soc.* **2008,** *130* (21), 6774-6780.
55. Taylor-Pashow, K. M. L.; Rocca, J. D.; Xie, Z.; Tran, S.; Lin, W., *J. Am. Chem. Soc.* **2009**.
56. Gonzalez-Perez, J. M.; Alarcon-Payer, C.; Castineiras, A.; Pivetta, T.; Lezama, L.; Choquesillo-Lazarte, D.; Crisponi, G.; Niclos-Gutierrez, J., *Inorg. Chem.* **2006,** *45* (2), 877-882.
57. Purohit, C. S.; Verma, S., *J. Am. Chem. Soc.* **2006,** *128* (2), 400-401.
58. Marzotto, A.; Ciccarese, A.; Clemente, D. A.; Valle, G., *J. Chem. Soc.-Dalton Trans.* **1995,** (9), 1461-1468.
59. Suzuki, T.; Hirai, Y.; Monjushiro, H.; Kaizaki, S., *Inorg. Chem.* **2004,** *43* (20), 6435-6444.
60. Prizant, L.; Olivier, M. J.; Rivest, R.; Beauchamp, A. L., *J. Am. Chem. Soc.*: 1979; Vol. 101, pp 2765-2767.
61. Korn, S.; Sheldrick, W. S., *Inorg. Chim. Acta* **1997,** *254* (1), 85-91.
62. Rojas-Gonzalez, P. X.; Castineiras, A.; Gonzalez-Perez, J. M.; Choquesillo-Lazarte, D.; Niclos-Gutierrez, J., *Inorg. Chem.* **2002,** *41* (24), 6190-6192.
63. Dell'Amico, D. B.; Calderazzo, F.; Labella, L.; Marchetti, F., *Inorg. Chim. Acta* **2003,** *350*, 661-664.
64. van der Sluis, P.; Spek, A. L., *Acta. Cryst., Sect. A* **1990,** *46* (3), 194-201.
65. Dewal, M. B.; Lufaso, M. W.; Hughes, A. D.; Samuel, S. A.; Pellechia, P.; Shimizu, L. S., *Chem. Mater.* **2006,** *18* (20), 4855-4864.
66. Lim, S.; Kim, H.; Selvapalam, N.; Kim, K. J.; Cho, S. J.; Seo, G.; Kim, K., *Angew. Chem., Int. Ed.* **2008,** *47* (18), 3352-3355.
67. Dobrzanska, L.; Lloyd, G. O.; Raubenheimer, H. G.; Barbour, L. J., *J. Am. Chem. Soc.* **2005,** *127* (38), 13134-13135.
68. Chatterjee, B.; Noveron, J. C.; Resendiz, M. J. E.; Liu, J.; Yamamoto, T.; Parker, D.; Cinke, M.; Nguyen, C. V.; Arif, A. M.; Stang, P. J., *J. Am. Chem. Soc.* **2004,** *126* (34), 10645-10656.
69. Breck, D. W., *Zeolite Molecular Sieves*. John Wiley & Sons: New York, 1974; p 636.
70. Rowsell, J. L. C.; Yaghi, O. M., *Angew. Chem. Int. Ed.* **2005,** *44* (30), 4670-4679.
71. Zhao, X. B.; Xiao, B.; Fletcher, A. J.; Thomas, K. M.; Bradshaw, D.; Rosseinsky, M. J., *Science* **2004,** *306* (5698), 1012-1015.
72. Choi, H. J.; Dinca, M.; Long, J. R., *J. Am. Chem. Soc.* **2008,** *130* (25), 7848-+.
73. Gregg, S. J.; Sing, K. S. W., *Adsorption, Surface Area, and Porosity*. Academic Press: New York, 1967; p 145.
74. Pan, L.; Adams, K. M.; Hernandez, H. E.; Wang, X. T.; Zheng, C.; Hattori, Y.; Kaneko, K., *J. Am. Chem. Soc.* **2003,** *125* (10), 3062-3067.

75. Cussen, E. J.; Claridge, J. B.; Rosseinsky, M. J.; Kepert, C. J., *J. Am. Chem. Soc.* **2002,** *124* (32), 9574-9581.
76. Hayward, D. O.; Trapnell, B. M. W., *Chemisorption*. Butterworth: Washington, 1964.
77. Chen, B. L.; Ma, S. Q.; Hurtado, E. J.; Lobkovsky, E. B.; Zhou, H. C., *Inorg. Chem.* **2007,** *46* (21), 8490-8492.
78. Ma, S. Q.; Sun, D. F.; Wang, X. S.; Zhou, H. C., *Angew. Chem., Int. Ed.* **2007,** *46* (14), 2458-2462.
79. Banerjee, R.; Phan, A.; Wang, B.; Knobler, C.; Furukawa, H.; O'Keeffe, M.; Yaghi, O. M., *Science* **2008,** *319* (5865), 939-943.
80. Eddaoudi, M.; Kim, J.; Vodak, D.; Sudik, A.; Wachter, J.; O'Keeffe, M.; Yaghi, O. M., *Proc. Natl. Acad. Sci. U. S. A.* **2002,** *99* (8), 4900-4904.
81. Friedrichs, O. D.; O'Keeffe, M. O.; Yaghi, O. M., *Acta Crystallogr.Sect. A* **2003,** *59*, 515-525.
82. da Silva, E. F.; Svendsen, H. F., *Int. J. Greenhouse Gas Control* **2007,** *1* (2), 151-157.
83. Arstad, B.; Blom, R.; Swang, O., *J. Phys. Chem. A* **2007,** *111* (7), 1222-1228.
84. Liu, Y. L.; Eubank, J. F.; Cairns, A. J.; Eckert, J.; Kravtsov, V. C.; Luebke, R.; Eddaoudi, M., *Angew. Chem. Int. Edit.* **2007,** *46* (18), 3278-3283.
85. Rosi, N. L.; Kim, J.; Eddaoudi, M.; Chen, B. L.; O'Keeffe, M.; Yaghi, O. M., *J. Am. Chem. Soc.* **2005,** *127* (5), 1504-1518.
86. Millward, A. R.; Yaghi, O. M., *J. Am. Chem. Soc.* **2005,** *127* (51), 17998-17999.
87. Chen, S. M.; Zhang, J.; Wu, T.; Feng, P. Y.; Bu, X. H., *J. Am. Chem. Soc.* **2009,** *131* (44), 16027-+.
88. Eddaoudi, M.; Kim, J.; Rosi, N.; Vodak, D.; Wachter, J.; O'Keefe, M.; Yaghi, O. M., *Science* **2002,** *295* (5554), 469-472.
89. Wang, Z. Q.; Cohen, S. M., *Chem. Soc. Rev.* **2009,** *38* (5), 1315-1329.
90. Frost, H.; Duren, T.; Snurr, R. Q., *J. Phys. Chem. B* **2006,** *110* (19), 9565-9570.
91. Rezwan, K.; Chen, Q. Z.; Blaker, J. J.; Boccaccini, A. R., *Biomaterials* **2006,** *27* (18), 3413-3431.
92. Giri, S.; Trewyn, B. G.; Stellmaker, M. P.; Lin, V. S. Y., *Angew. Chem. Int. Edit.* **2005,** *44* (32), 5038-5044.
93. Ferrari, M., *Nat. Rev. Cancer* **2005,** *5* (3), 161-171.
94. Zhang, L.; Gu, F. X.; Chan, J. M.; Wang, A. Z.; Langer, R. S.; Farokhzad, O. C., *Clin. Pharmacol. Ther.* **2008,** *83* (5), 761-769.
95. Langer, R., *Nature* **1998,** *392* (6679), 5-10.
96. Rieter, W. J.; Pott, K. M.; Taylor, K. M. L.; Lin, W. B., *J. Am. Chem. Soc.* **2008,** *130* (35), 11584-+.
97. Xie, Y.; Yu, Z. P.; Huang, X. Y.; Wang, Z. Y.; Niu, L. W.; Teng, M.; Li, J., *Chem. Eur. J.* **2007,** *13* (33), 9399-9405.
98. White, K. A.; Chengelis, D. A.; Gogick, K. A.; Stehman, J.; Rosi, N. L.; Petoud, S. p., *J. Am. Chem. Soc.* **2009,** *131* (50), 18069-18071.
99. Rieter, W. J.; Taylor, K. M. L.; An, H.; Lin, W.; Lin, W., *J. Am. Chem. Soc.* **2006,** *128* (28), 9024-9025.
100. Taylor, K. M. L.; Rieter, W. J.; Lin, W., *J. Am. Chem. Soc.* **2008,** *130* (44), 14358-14359.
101. Xie, Z.; Ma, L.; deKrafft, K. E.; Jin, A.; Lin, W., *J. Am. Chem. Soc.* **2009,** *132* (3), 922-923.
102. Sabbatini, N.; Guardigli, M.; Lehn, J. M., *Coord. Chem. Rev.* **1993,** *123* (1-2), 201-228.

103. Parker, D., *Coord. Chem. Rev.* **2000,** *205*, 109-130.

104. Bunzli, J. C. G.; Piguet, C., *Chem. Soc. Rev.* **2005,** *34* (12), 1048-1077.

105. Allendorf, M. D.; Bauer, C. A.; Bhakta, R. K.; Houk, R. J. T., *Chem. Soc. Rev.* **2009,** *38* (5), 1330-1352.

106. White, K. A.; Chengelis, D. A.; Zeller, M.; Geib, S. J.; Szakos, J.; Petoud, S.; Rosi, N. L., *Chem. Commun.* **2009,** (30), 4506-4508.

107. Cross, J. P.; Lauz, M.; Badger, P. D.; Petoud, S. p., *J. Am. Chem. Soc.* **2004,** *126* (50), 16278-16279.

108. Yang, B. B.; Abel, R. B.; Uprichard, A. C. G.; Smithers, J. A.; Forgue, S. T., *J. Clin.Pharmacol.* **1996,** *36* (7), 623-633.

109. Koch-Weser, J.; Klein, S. W., *Jama* **1971,** *215* (9), 1454-60.

110. Sintov, A.; Levy, R. J., *Int. J. Pharm.* **1997,** *146* (1), 55-62.

111. Kerin, N. Z.; Meengs, W. L.; Timmis, G. C.; Salerno, D.; Haber, H. E.; Singer, R. M.; Switzer, D.; Zoble, R.; Carlson, M.; Weidler, D.; Raghavan, P.; Schwartz, K.; Somberg, J. C.; Kereiakes, D.; Ellenbogen, K. A., *Cardiovasc. Drugs Ther.* **1997,** *11* (2), 169-175.

112. Park, Y.; Choi, S.; Kim, H.; Kim, K.; Won, B. H.; Choi, K.; Choi, J. S.; Ahn, W. S.; Won, N.; Kim, S.; Jung, D.; Choi, S. H.; Kim, G. H.; Cha, S. S.; Jhon, Y.; Yang, J.; Kim, J., *Angew. Chem. Int. Edit.* **2007,** *46* (43), 8230-8233.

113. Cairns, A. J.; Perman, J. A.; Wojtas, L.; Kravtsov, V. C.; Alkordi, M. H.; Eddaoudi, M.; Zaworotko, M. J., *J. Am. Chem. Soc.* **2008,** *130* (5), 1560-1561.

114. Alkordi, M. H.; Brant, J. A.; Wojtas, L.; Kravtsov, V. C.; Cairns, A. J.; Eddaoudi, M., *J. Am. Chem. Soc.* **2009,** *131* (49), 17753-17755.

115. Sudik, A. C.; Côté, A. P.; Wong-Foy, A. G.; O'Keeffe, M.; Yaghi, O. M., *Angew. Chem. Int. Edit.* **2006,** *45* (16), 2528-2533.

116. Luo, F.; Yang, Y. T.; Che, Y. X.; Zheng, J. M., *Crystengcomm* **2008,** *10* (11), 1613-1616.

117. Dybtsev, D. N.; Nuzhdin, A. L.; Chun, H.; Bryliakov, K. P.; Talsi, E. P.; Fedin, V. P.; Kim, K., *Angew. Chem. Int. Edit.* **2006,** *45* (6), 916-920.

118. Thushari, S.; Cha, J. A. K.; Sung, H. H. Y.; Chui, S. S. Y.; Leung, A. L. F.; Yen, Y. F.; Williams, I. D., *Chem. Commun.* **2005,** (44), 5515-5517.

119. Nelson, A. P.; Farha, O. K.; Mulfort, K. L.; Hupp, J. T., *J. Am. Chem. Soc.* **2008,** *131* (2), 458-460.

120. Cooper, A. I.; Rosseinsky, M. J., *Nat. Chem.* **2009,** *1* (1), 26-27.

121. Klein, N.; Senkovska, I.; Gedrich, K.; Stoeck, U.; Henschel, A.; Mueller, U.; Kaskel, S., *Angew. Chem. Int. Edit.* **2009,** *48* (52), 9954-9957.

122. DincaÌŒ, M.; Long, J. R., *J. Am. Chem. Soc.* **2005,** *127* (26), 9376-9377.

123. Aebischer, A.; Gumy, F.; Buenzli, J.-C. G., *Physical Chemistry Chemical Physics* **2009,** *11* (9), 1346-1353.

124. Zhang, J.; Badger, P. D.; Geib, S. J.; Petoud, S., *Angew. Chem. Int. Edit.* **2005,** *44* (17), 2508-2512.

125. Petoud, S.; Cohen, S. M.; Buenzli, J.-C. G.; Raymond, K. N., *J. Am. Chem. Soc.* **2003,** *125* (44), 13324-13325.